Model Validation for Air Foil Thrust Bearings

Zur Erlangung des akademischen Grades Doktor-Ingenieur (Dr.-Ing.)
Genehmigte Dissertation von Andre Manuel Theile aus Hagen
Tag der Einreichung: 26.02.2024, Tag der Prüfung: 04.06.2024

1. Gutachten: Prof. Dr.-Ing. Bernhard Schweizer
2. Gutachten: Assist. Prof. Athanasios Chasalevris, PhD
Darmstadt

TECHNISCHE UNIVERSITÄT DARMSTADT

Mechanical Engineering Department

Institute of Applied Mechanics

Model Validation for Air Foil Thrust Bearings

Accepted doctoral thesis by Andre Manuel Theile

1. Review: Prof. Dr.-Ing. Bernhard Schweizer
2. Review: Assist. Prof. Athanasios Chasalevris, PhD

Date of submission: 26.02.2024
Date of thesis defense: 04.06.2024

Darmstadt, Technische Universität Darmstadt
Jahr der Veröffentlichung der Dissertation auf TUprints: 2024

Bitte zitieren Sie dieses Dokument als:
URN: urn:nbn:de:tuda-tuprints-275849
URL: http://tuprints.ulb.tu-darmstadt.de/27584
DOI: https://doi.org/10.26083/tuprints-00027584

Dieses Dokument wird bereitgestellt von tuprints,
E-Publishing-Service der TU Darmstadt
http://tuprints.ulb.tu-darmstadt.de
tuprints@ulb.tu-darmstadt.de

Erklärungen laut Promotionsordnung

§8 Abs. 1 lit. c PromO

Ich versichere hiermit, dass die elektronische Version meiner Dissertation mit der schriftlichen Version übereinstimmt.

§8 Abs. 1 lit. d PromO

Ich versichere hiermit, dass zu einem vorherigen Zeitpunkt noch keine Promotion versucht wurde. In diesem Fall sind nähere Angaben über Zeitpunkt, Hochschule, Dissertationsthema und Ergebnis dieses Versuchs mitzuteilen.

§9 Abs. 1 PromO

Ich versichere hiermit, dass die vorliegende Dissertation selbstständig und nur unter Verwendung der angegebenen Quellen verfasst wurde.

§9 Abs. 2 PromO

Die Arbeit hat bisher noch nicht zu Prüfungszwecken gedient.

Darmstadt, 26.02.2024

A. Theile

Zusammenfassung

In dieser Arbeit wird ein Simulationsmodell für Axialfolienlager, die zur Klasse der hydrodynamischen Gleitlager mit elastischer Lagerfläche gehören, validiert und erweitert. Das Modell ist in der Lage, integrale Größen wie die Tragfähigkeit und die Verlustleistung des Lagers zu bestimmen. Darüber hinaus können Druck- und Temperaturverteilungen sowie Verformungen der einzelnen Komponenten ermittelt werden. Ein validiertes Simulationsmodell ist entscheidend für die Auslegung und das Verständnis der Wirkzusammenhänge der Axiallagerung.
Um die Validität der Simulation bestimmen zu können, werden deren Gültigkeitsbereich und die Aussagekraft der Ergebnisse analysiert. Dazu werden zunächst die wichtigsten Einflussparameter identifiziert. Diese werden in vier Kenngrößen zusammengefasst, die das Lager bestmöglich beschreiben sollen. Sie umfassen die Leistung des Lagers in Bezug auf Tragkraft und Verlustleistung, das thermische Zusammenspiel der einzelnen Komponenten, die Steifigkeit des Lagers und die Schmierfilmverteilung.
Darauf aufbauend werden verschiedene Messgeräte in Betrieb genommen. Die integralen Größen wie Tragfähigkeit und Verlustleistung werden in einem Hochgeschwindigkeits-Prüfstand gemessen. Zur Validierung des thermischen Zustands werden in einem separaten Versuchsaufbau thermische Widerstände bestimmt und Temperaturverteilungen gemessen. Auch die mechanischen Eigenschaften wie Verschleiß, mechanische Reibungskoeffizienten und Steifigkeiten des Lagers werden mit einer Vielzahl von Versuchsaufbauten und geeigneten Messungen untersucht.
Weiterhin wird das Simulationsmodell analysiert und an den entsprechenden Stellen erweitert. Zu diesem Zweck werden CFD-Simulationen der Rotorumgebung durchgeführt und Wärmeübergangskoeffizienten am Rotor in das Simulationsmodell des Lagers implementiert. Weiterhin werden basierend auf der Analyse des Einlaufverhaltens des Lagers ein Verschleißmodell in der Simulation abgebildet. Außerdem wird der thermische Widerstand des Lagers erweitert.
Auf Basis der gemessenen Eingabeparameter des Simulationsmodells können Simulationsunsicherheiten dargestellt werden. Diese sind im Zusammenspiel mit den experimentellen Unsicherheiten entscheidend für die erfolgreiche Validierung des Simulationsmodells.
Der abschließende Validierungsprozess zeigt gute Übereinstimmung des Simulationsmodells mit den experimentellen Ergebnissen in Bezug auf die Kenngrößen des Axiallagers, einschließlich Verlustleistung, Verschleißmuster und thermisches Verhalten. Allerdings ergeben sich Herausforderungen bei der genauen Darstellung der Steifigkeit des Lagers aufgrund des Ausrichtungsprozesses der Bump-Folien.
Diese Forschungsarbeit trägt wesentlich zum Verständnis des Verhaltens und der Komplexität von axialen Folienlagern bei. Die Einführung eines neuartigen Verschleißalgorithmus erhöht die Genauigkeit und den Realismus des Modells. Um eine genaue simulative Darstellung des Verhaltens in der realen Welt zu gewährleisten, unterstreichen die Ergebnisse dieser Arbeit die Bedeutung der Modellverfeinerung und insbesondere die genaue Bestimmung der Eingabeparameter.

Abstract

This work validates and extends a simulation model for an air foil thrust bearing, which belong to the class of hydrodynamic bearings with elastic bearing surfaces. The model can determine integral quantities such as load-carrying capacity and power loss of the bearing. Additionally, it can calculate pressure and temperature distributions as well as deformations of individual components. A validated simulation model is crucial for the design and understanding of the cause effect mechanisms in thrust bearings.
To assess the validity of the simulation, the range of its applicability and the significance of the results are analyzed. Initially, the key influencing parameters are identified and consolidated into four key characteristics aimed at providing the most comprehensive description of the bearing. These metrics encompass the performance of the bearing in terms of load-carrying capacity and power loss, the thermal interaction of individual components, bearing stiffness, and the lubricant film distribution.
Building on this foundation, various measurement devices are put into operation. Integral quantities such as load-carrying capacity and power loss are measured in the newly designed high-speed test rig. To validate the thermal behavior, thermal resistances are determined, and temperature distributions are measured in a separate experimental setup. Mechanical properties such as wear, mechanical friction coefficients, and bearing stiffness are investigated through a variety of test setups and suitable measurements.
Furthermore, the simulation model is analyzed and extended in relevant areas. For this purpose, CFD simulations of the rotor environment are conducted, in order to implement heat transfer coefficients at the rotor. Furthermore, a simple wear model is incorporated into the simulation based on the analysis of the bearing's running-in behavior. Additionally, the formulation of the thermal resistance of the bearing is enhanced.
Simulation uncertainties can be represented based on the measured input parameters of the simulation model. These uncertainties are crucial in cooperation with experimental uncertainties for the successful validation of the simulation model.
The validation process demonstrates good agreement between the simulation model and experimental results regarding the key characteristics of the axial bearing, including power loss, wear patterns, and thermal behavior. However, challenges arise in accurately representing the stiffness of the bearing due to the alignment process of the bump foils.
This research significantly contributes to the understanding of the behavior and complexity of air foil thrust bearings. The introduction of a novel wear algorithm enhances the accuracy and realism of the model. The results emphasize the importance of refining and incorporating precisely determined input parameter into the model to ensure an accurate representation of real-world behavior.

Contents

List of Symbols and Abbreviations

Nomenclature

Symbol	Definition
A_{Block}	Surface area in the thermal resistance test rig.
A_{Bearing}	Surface area of the bearing.
A_{PTFE}	Surface area of the PTFE test specimen in the thermal resistance test rig.
$A_{\mathrm{Rotor,Front}}$	Rotor front face at the drive side.
A_{pad}	Surface area of one pad of the top foil.
b_{i}	Distance of the bump arcs in x_1 direction.
B	Bending stiffness for the shell theory.
c	Penalty stiffness coefficient.
c_{d}	Windage drag coefficient.
c_{p}	Heat capacity of air.
D	Stretching stiffness for the shell theory.
dM	Shear momentum in the air film.
E_{BF}	Elastic modulus of the bump foil.
E_{RD}	Elastic modulus of the top foil.
E_{TF}	Elastic modulus of the top foil.
F_{f}	Friction force.
F_{lc}	Force acting on the torque measurement load cell.
F_{clc}	Force acting on the calibration load cell for the pressure chamber.
F_{g}	Gravitational force due to calibration weights.
F_{N}	Normal force.
$F_{\mathrm{rotor,drag}}$	Drag force on the rotor inside the sealing channels.
F_{thrust}	Thrust force.
F_{s}	Spring force pre-load for torque measurements.
$F_{\mathrm{shear,bearing}}$	Resulting force due to shear stresses from the test bearing.
$F_{\mathrm{shear,periphery}}$	Resulting force due to shear stresses from the periphery.
Gt	Shear stiffness for the shell theory.
$h(r,\varphi)$	Air film height.
$\bar{h}$	Averaged air film height.
h_{BF}	Height of bump foil.
$h_{\mathrm{RD,pre}}(x,y)$	Pre deformation of the rotor disk.
$h_{\mathrm{wave}}(x,y)$	Waviness of the rotor disk.
$h_{\mathrm{cone}}(x,y)$	Run-out of the rotor disk.
$h_{\mathrm{bend}}(r)$	Bending of the rotor disk towards the thrust bearing.
$h_{\mathrm{bowl}}(r)$	Height of bowl shaped pre-deformation of the top foil.
H_{bowl}	Maximum height of bowl shaped pre-deformation of the top foil.
H_{bend}	Maximum bending of the rotor disk towards the thrust bearing.
$H_{\mathrm{coat,nom}}$	Nominal coating thickness.
H_{coat}	Maximum height of coating accumulation.
$h_{\mathrm{coat}}(r,\varphi)$	Coating thickness distribution.
$h_{\mathrm{coat}}(r)$	Coating thickness distribution profile.
$\bar{h}_{\mathrm{coat}}(r)$	Coating thickness distribution averaged over φ.

$h_{\mathrm{coat,\,sim}}(r)$	Simulated coating thickness distribution after wear simulation.
H_{flat}	Maximum waviness height of the rotor disk.
H_{mixed}	Wear parameter.
$\tilde{H}_{\mathrm{shift}}$	Virtual shift of the rotor.
$H_{\mathrm{TF}}(r,\varphi)$	Top foil height profile.
$H_{\mathrm{TF,rm}}(\varphi)$	Top foil height profile evaluated on the middle radius.
$h_{\mathrm{wear}}(r,\varphi)$	Simulated wear height.
h_{wedge}	Film height of a wedge profile.
h_{ww}	Film height without wear.
l_1	Lever arm between bearing center and calibration weights.
l_2	Lever arm between bearing center and load cell.
l_{pad}	Total length of the top foil over the circumferential extend on the middle radius.
L_{B}	Length of contact lines.
L_{BF}	Length of a bump arc.
L_{Br}	Bridge length of bump foils.
$m^{\alpha\beta}$	Moment tensor for the shell theory.
m_{EP}	Mass flow from the aerostatic support thrust bearing.
n	Rotational speed of the rotor.
$n^{\alpha\beta}$	Stress resultant tensor for the shell theory.
p_{applied}	Applied inlet pressure in the test rig.
$p(x,y)$	Pressure in the air film.
p_0	Ambient pressure.
p_{ch}	Pressure in the pressure chamber.
$p(r,\varphi)$	Air film pressure.
$p_{\mathrm{rotor,front}}$	Pressure on the rotor front in the test rig.
P_{loss}	Power loss generated in the foil thrust bearing air film gap.
$P_{\mathrm{shear,periphery}}$	Power losses not belonging to thrust bearing losses.
q^{α}	Traverse shear stress for the shell theory.
$q_{\mathrm{TF,in}}(x,y)$	Incoming heat flux into the top foil.
$q_{\mathrm{TF,out}}(x,y)$	Outgoing heat flux into the top foil.
$Q_{\mathrm{air,in}}$	Integral incoming heat flux from the inner radius into the air film.
$Q_{\mathrm{air,out}}$	Integral outgoing heat flux from the air film into the radial outer periphery.
Q_{Base}	Integral incoming heat flux from the top foil into the base plate.
Q_{Block}	Integral heat flux through the steel block in the thermal resistance test rig.
Q_{Bearing}	Integral heat flux through the test bearing in the thermal resistance test rig.
$Q_{\mathrm{cool,in}}$	Integral incoming heat flux from the cooling flow through the bump foils.
$Q_{\mathrm{cool,out}}$	Integral outgoing heat flux from the cooling flow through the bump foils.
Q_{Dis}	Integral dissipation heat fluxes in the thermal resistance test rig.
Q_{Heater}	Integral heat flux of the heater in the thermal resistance test rig.
Q_{pad}	Integral air heat exchange between the pads.
Q_{RD}	Integral incoming heat flux into the rotor disk.
$Q_{\mathrm{rad,P}}$	Integral outgoing heat flux from rotor disk into the radial outer periphery.
$Q_{\mathrm{ax,P}}$	Integral outgoing heat flux from rotor disk into the axial periphery.
Q_{RR}	Integral outgoing heat flux from rotor disk into the rotor shaft.
Q_{TF}	Integral incoming heat flux into the top foil.
R_{BA}	Bump foil arc radius.

R_{BF}	Thermal resistance of the bump arcs.
$R_{\mathrm{BF,Base,air}}$	Thermal resistance of the air gap between bump foil and base plate.
$R_{\mathrm{i,1}}$	Radius of 1st bump column.
$R_{\mathrm{i,2}}$	Radius of 2nd bump column.
$R_{\mathrm{i,3}}$	Radius of 3rd bump column.
r	Radial coordinate.
r_{i}	Inner radius of the top foil.
r_{m}	Middle radius of the top foil.
r_{o}	Outer radius of the top foil.
R_{R}	Bump foil rounding radius.
r_{step}	Radius of the step.
$r_{\mathrm{RD,o}}$	Outer radius rotor disk.
R_{Block}	Thermal resistance of the steel block in the thermal resistance test rig.
R_{Bearing}	Thermal resistance of the test bearing in the thermal resistance test rig.
$R_{\mathrm{TF,BF,air}}$	Thermal resistance of the air gap between top foil and bump foil.
R_{th}	Total thermal resistance between top foil and bump foil.
$R_{\mathrm{th,air}}$	Air thermal resistance between top foil and bump foil.
R_{z}	Maximum peak to valley height of the profile.
$s_{\mathrm{ce,i}}$	Circumferential extend of the bump foil apexes under the top foil at the inner radius.
$s_{\mathrm{ce,o}}$	Circumferential extend of the bump foil apexes under the top foil at the outer radius.
s_{gimbal}	Gimbal movement of rotation axis B1-B2.
s_{offset}	Offset of the bump foil from the holding arm..
$s_{\mathrm{h}}(r)$	Step-height of the top foil.
$s_{\mathrm{TF,Base}}$	Distance from the top foil to the base plate.
$\bar{s}_{\mathrm{h}}$	Averaged step-height of the top foil.
$s_{\mathrm{w}}(r)$	Step-width of the top foil.
$\bar{s}_{\mathrm{w}}$	Averaged step-width of the top foil.
$S_{\mathrm{a,Base}}$	Surface roughness of the base plate.
$S_{\mathrm{a,BF}}$	Surface roughness of the bump foil.
$S_{\mathrm{a,TF}}$	Surface roughness of the top foil.
S_{q}	Surface roughness parameter (root mean square height).
$T(x,y,z)$	Air field temperature
T_0	Ambient temperature.
T_{f}	Measured torque due to friction.
$T_{\mathrm{m}}(x,y)$	Axial averaged fluid temperature.
$T_{\mathrm{disk,1}}$	Disk temperature (axial position).
$T_{\mathrm{disk,2}}$	Disk temperature (radial position).
T_{Li}	Thermocouple temperatures in layer i the thermal resistance test rig.
$T_{\mathrm{RD}}(r,z)$	Local temperature of the rotor.
$T_{\mathrm{RD,disk}}$	Simulated rotor disk at the outer diameter of the disk.
$T_{\mathrm{TF}}(x,y)$	Local top foil temperature.
T_{TC}	Thermocouple temperature for pyrometer calibration.
$T_{\mathrm{TC,B}}$	Thermocouple base plate temperature.
$T_{\mathrm{TC,H}}$	Thermocouple housing temperature.
t_{Base}	Thickness of the base plate.

t_{BF}	Thickness of the bump disk.
t_{RD}	Thickness of the rotor disk.
t_{TF}	Thickness of the top foil.
$t_{\mathrm{JB,gap}}$	Thickness of the journal bearing gap.
u	Fluid velocity in x-direction
$u_{\mathrm{pyro,1}}$	Output voltage of the pyrometer (axial position).
$u_{\mathrm{pyro,2}}$	Output voltage of the pyrometer (radial position).
v	Fluid velocity in y-direction
$v_{3\mathrm{TF}}$	Displacement of the top foil in 3 direction.
v_{i}	Transnational degree of freedom for the shell theory.
v_{φ}	Circumferential velocity component of the rotor disk.
$v_{\mathrm{RD,\,r}}$	Radial velocity component of the rotor disk.
$v_{\mathrm{RD,\,z}}$	Axial velocity component of the rotor disk.
W	Thrust bearing load capacity.
W_{lim}	Thrust bearing limit load capacity.
w_{α}	Rotational degree of freedom for the shell theory.
w_{i}	Width of i-bump strip.
$x_{1,2}$	Cartesian coordinates.
$x_{\mathrm{TF,BF}}$	Length dimensions for heat diffusion between top foil and bump foil.
$x_{\mathrm{BF,Base}}$	Length dimensions for heat diffusion between bump fol and base plate.
z	Height coordinate.
$\alpha_{\mathrm{ax}}(r)$	Heat transfer coefficient of the rotor disk into the axial periphery.
$\alpha_{\mathrm{rad}}(r)$	Heat transfer coefficient of the rotor disk into the radial periphery.
$\bar{\alpha}_{\mathrm{ax}}$	Averaged heat transfer coefficient of the rotor disk into the axial periphery.
$\bar{\alpha}_{\mathrm{rad}}$	Averaged heat transfer coefficient of the rotor disk into the axial periphery.
α_{RD}	Thermal expansion of the rotor.
$\gamma_{\mathrm{BF,Base}}$	Surface roughness between bump foil and base plate.
$\gamma_{\mathrm{TF,BF}}$	Surface roughness between top foil and bump foil.
γ_{α}	Strain variable for the shell theory.
ϵ_{RD}	Thermal expansion to extension resistance constant of the rotor.
ζ_{RD}	Lamé constant of the rotor.
η	Viscosity of air.
$\kappa_{\alpha\beta}$	Strain variable for the shell theory.
Λ	Mixed lubrication parameter.
λ	Thermal conductivity of air.
λ_{BF}	Thermal conductivity of the bump foil.
λ_{Base}	Thermal conductivity of the base plate.
λ_{Block}	Thermal conductivity of the steel block in the thermal resistance test rig.
$\lambda_{\mathrm{insulation}}$	Thermal conductivity of the insulation of the thermal resistance test rig.
λ_{RD}	Thermal conductivity of the rotor.
λ_{TF}	Thermal conductivity of the top foil.
λ_{JB}	Thermal conductivity of air in the journal bearing gap.
μ_{B}	Friction coefficient between base plate and bump foil.
μ_{T}	Friction coefficient between top foil and bump foil.
ν_{BF}	Poisson's ratio of the bump foil material.
ν_{RD}	Poisson's of the rotor material.
ν_{TF}	Poisson's of the top foil material.

ρ	Density of air.
ρ_{BF}	Density of the bump foil material.
ρ_{TF}	Density of the top foil material.
τ_{RD}	Shear modulus in the rotor
Φ_{Loss}	Loss characteristic of the bearing.
Φ_{St}	Stiffness characteristic of the bearing.
Φ_{Th}	Thermal characteristic of the bearing.
Φ_{Film}	Air film characteristic of the bearing.
φ	Circumferential coordinate.
φ_{i}	Evaluation angle position of top foil WLI measurements.
φ_{negT}	Negative extend of the top foil over the bump foil.
$\varphi_{\alpha\beta}$	Strain variable for the shell theory.
ω	Angular frequency of the rotor.
Θ_{BF}	Nominal angle of the bump arcs.
σ	Surface roughness.

List of abbreviations

Index / Abbreviation	Definit ion
AFTB	Air foil thrust bearing
BF	Bump foil
Br	Bridge
CFD	Computer fluid dynamics
CHT	Conjugate heat transfer
Cool	Cooling
EP	Externally pressurized
JB	Journal bearing
Per	Periphery
PTFE	Polytetrafluoroethylene
SST	Shear stress transport
St	Stiffness
RD	Rotor disk
TC	Temperature calibration
TEHD	Thermo-elasto-hydro-dynamic
TF	Top foil
Th	Thermal
WLI	White light interferometric
acc	Accumulation
aP	Axial periphery
ce	Circumferential extend
coat	Coating
clc	Calibration load cell
ch	Chamber
g	Gravitation
lc	Load cell
lead	Leading
lim	Limit

neg	Negative
nom	Nominal
uncert	Uncertainty
ref	Reference
res	Resulting
rm	Radius middle
sim	Simulation
topo	Topography
trail	Trailing
pyro	Pyrometer
wave	Waviness

List of Figures

List of Tables

1. Introduction

In recent years, the demand for CO2-neutral technologies has increased significantly due to growing concerns about climate change and the urgent need to reduce greenhouse gas emissions. This heightened demand is particularly evident in the field of powertrain solutions. One of the promising technologies in this regard is the fuel cell, which offers clean and efficient energy conversion. To ensure the optimal performance of fuel cells, an efficient and environmentally friendly air supply system is crucial. Oil-free turbomachinery can be utilized for this purpose. Fig. 1.1 depicts a schematic representation of the rotor-bearing system in an air supply unit for a fuel cell.
The air supply unit consists of an electrically driven machine with a permanent magnet embedded within the rotor. It is equipped with a compressor wheel at one end of the rotor to supply air to the fuel cell. Additionally, a turbine wheel is positioned at the other end to enhance the system's efficiency. The rotor is supported by two journal bearings, which guide the rotor and provide radial support against vibrations and external loads. A two-sided thrust bearings, surrounding the runner disk, support the thrust load. These bearings experience variable loads originating from the compressor and turbine wheels, which can change direction. The desired pressure ratio and mass flow requirements dictate rotational speeds of up to 120,000 revolutions per minute (rpm).
In addition to high speeds, achieving oil-free operation is beneficial to ensure an uncontaminated air supply. Gas foil bearings have emerged as a viable option that meet these requirements while also offering cost-effectiveness and robustness. However, due to their complex working principle involving coupled fluid mechanics, thermal dynamics, and tribological interactions, the development of validated predictive tools for gas foil bearings presents a considerable challenge. While detailed numerical investigations are essential, experimental studies play a decisive role in validating simulation models. Hence, this research focuses on experimental investigations and extends simulation models for an air foil thrust bearing (AFTB).

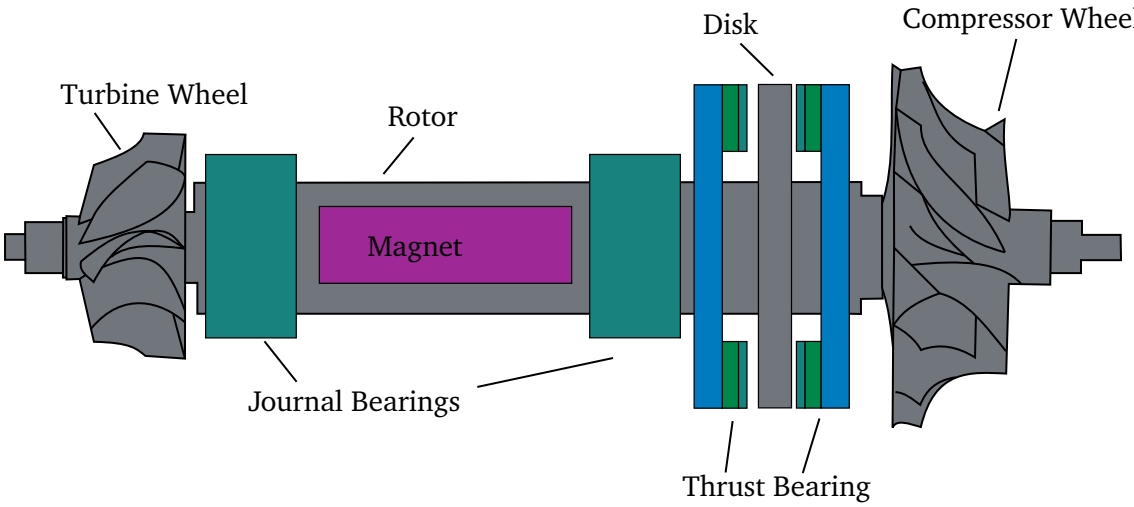

Figure 1.1.: Sketch of the rotor-bearing system of an electric air compressor.

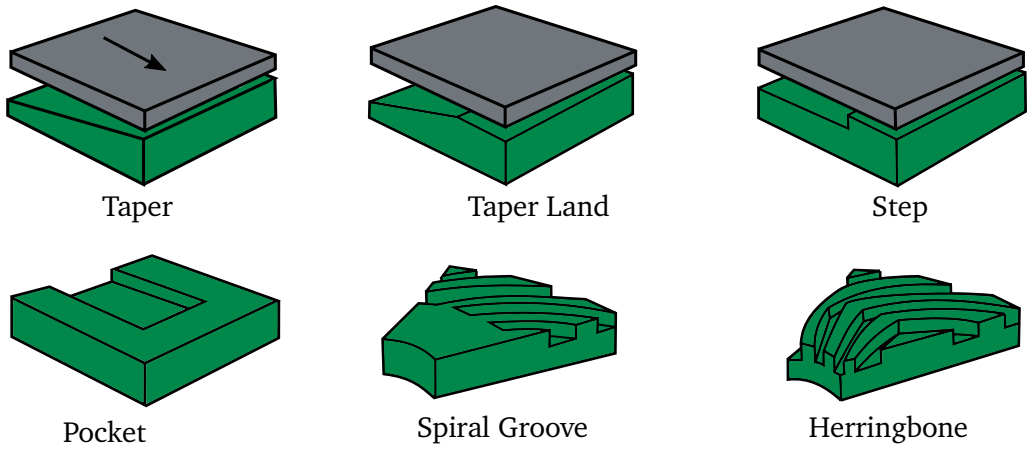

Figure 1.2.: Different bearing concepts from Bisson et. al. [7].

1.1. Motivation

Air bearings are based on the principle of lubrication between two surfaces, which was first theoretically investigated by Reynolds and Tower in the 1880s. Reynolds subsequently developed the differential equation, commonly known as the Reynolds equation, in 1886, providing a foundation for understanding thin fluid films [86, 87, 66]. This principle allows rotating machine parts to generate a pressure within small gaps. When the gap has a convergent shape, pressure is developed to satisfy the conservation of mass and momentum, thereby supporting the rotating shaft. These bearings are known as self-acting fluid film bearings. Fig. 1.2 illustrates various bearing concepts, as presented by Bisson et al. [7]. While solid bearings possess high load capacities, they require high manufacturing precision to account for misalignment, which limits their practicality. Consequently, alternative concepts have been developed.
Foil bearings first appeared in the 1950s and are based on similar principles as those shown in Fig. 1.2. Blok et al. introduced a concept that utilized a cellophane foil and oil to support a rotor; however, this concept was never employed in a machine [8]. Stahler and Huckabay conducted a feasibility study in 1966, presenting similar concepts, which were further investigated by Licht [82, 55]. Nevertheless, these concepts failed to establish rotor support applications. Concurrently, Garett AiResearch developed a different type of foil bearing, which was successfully implemented in air turbines for aircraft air conditioning systems, marking the first serial production of foil bearings [1]. Their design incorporates a bump foil with spring properties to compensate for misalignment and a top foil that shapes the air film to generate pressure. Air foil bearings have become the preferred choice for air conditioning turbines in aircraft and are also employed by companies such as Capstone Turbine Corp in gas turbines and heat engines [43]. In the field of turbomachinery, foil bearings have been explored in various concepts, as documented in patents by Larure [45] and Lubell [56], and discussed in publications by Heshmat [34] and Bonello [9]. Most foil bearings are based on the original concept developed by Garett AiResearch and have undergone further refinements to meet new requirements.
Air bearings offer several advantages over roller bearings or oil-lubricated bearings. Firstly, other concepts necessitate oil lubrication, which must be sealed off from other parts of the machinery. Moreover, the higher viscosity of oil leads to increased friction losses between moving parts, limiting their operational speeds. Air bearings, on the other hand, can operate at higher velocities. Specific advantages of air foil bearings include their low cost compared to rigid air bearings and their ability to compensate for

misalignment and manufacturing inaccuracies. The friction forces between the bump and top foils, as well as between the bump foil and the base plate, contribute to effective damping behavior [40, 48, 71, 44]. Despite these strengths, air foil bearings also have some drawbacks. The aerodynamic film that separates the rotor from the top foil only forms once a certain lift-off speed is achieved, which limits the operating range. Additionally, air foil bearings are more susceptible to wear during start-stop operations. To mitigate these issues, top foils are often coated with low-friction materials like Teflon [10, 15, 16]. Air foil bearings exhibit higher thermal resistance compared to solid bearings and typically require additional air cooling [79, 69, 19].
When considering journal and thrust bearings, air foil bearings face different challenges. For journal bearings, dynamic properties play a crucial role. While dynamical problems can also arise in thrust bearings and have gained attention in scientific literature [62, 3, 26, 60] the high velocities of the rotor disk, shear stress losses, and resulting thermal behavior pose greater challenges for thrust bearings. High temperatures can lead to bearing failures, necessitating cooling measures that reduce overall machine efficiency.
Hence, validated simulation models for thrust bearings play a significant role in the design process of the machine. Once the model is validated, a deep understanding of the causes and effect mechanisms can be created and optimization studies can help to improve the efficiency of the whole machine.

1.2. Objective

The main objective of this work is to validate a simulation model for an air foil thrust bearing using experimental results. The validation process focuses on four crucial characteristics of the bearing: load power loss ration (performance), thermal behavior, stiffness of the bearing system, and film height distribution. To achieve this objective, the subsequent steps are carried out:

- Sensitivity Analysis: Conduct a sensitivity analysis to identify the most influential parameters within the simulation model.
- Test Rig Development: Construct dedicated test rigs specifically designed to measure the key bearing characteristics.
- Measurement Capability Assessment: Determine the measurement capability of the test rigs, including quantifying the uncertainties associated with the measurements.
- Parameter Quantification: Utilize the testing facilities to measure the input parameters required for the simulation model.
- Uncertainty Assessment: Assess the uncertainties associated with the measured input parameters.
- Model Adaptation: Modify the simulation model based on indications and insights gained from the experimental data.
- Validation: Perform the validation process by comparing the simulation results with the experimental measurements, taking into account the associated uncertainties.

By following these steps, this research aims to establish the validity of the simulation model by successfully correlating its predictions with the experimental data. The validated simulation model will contribute to a deeper understanding of the air foil thrust bearing's behavior and enable optimization studies for improved bearing performance in practical applications.

1.3. Structure

In order to carry out the validation, this thesis is divided into the following chapters:

Chapter 2 provides the necessary background on air foil thrust bearings. It begins with an explanation of the design of a typical bearing. A comprehensive overview of the existing literature on air foil bearings is then presented. This chapter also includes an introduction to the basic equations used in the simulation model. Additionally, it introduces the concept of tribological systems. The chapter concludes with an overview of the model validation process tailored specifically to this research topic, including the introduction of output quantities for the sensitivity analysis.

Chapter 3 focuses on the validation test rigs and measurement tools employed in the research. It discusses the measurement capability of the systems and the achievable accuracy of the measurements. The main test rigs presented are the newly developed high-speed test rig for bearing performance measurements up to 120,000 rpm and 100 N, as well as the newly developed thermal resistance test rig for measuring the bump foil's thermal resistance. Existing test beds for assessing the mechanical properties of the bearing are also discussed. Additionally, measurement tools for topography and wear measurements are presented.

Chapter 4 comprises the modeling and adjustment of the air foil thrust bearing model. This chapter is divided into sections focusing on the major components of the bearing: the rotor and its surroundings, bump foils, and the top foil. Each section begins with a sensitivity analysis of the dominant parameters. Geometric properties of the components are then obtained from measurements and thoroughly discussed. Furthermore, the chapter presents model extensions, such as a wear algorithm capable of simulating the running-in process of the foil bearing's coating layer. The chapter concludes with an estimation of the model uncertainties resulting from variations in input variables.

Chapter 5 consolidates all the previous aspects and successfully validates the various parts of the bearing model. It includes a study on bump foil stiffness, followed by the validation of wear simulations using detailed white light interferometric wear measurements. The core of this chapter focuses on the validation of bearing performance through high-speed test rig measurements and a thorough discussion of the simulation model results. Additionally, a validation of the thermal behavior of the bearing system is presented, complementing the chapter.

2. Background

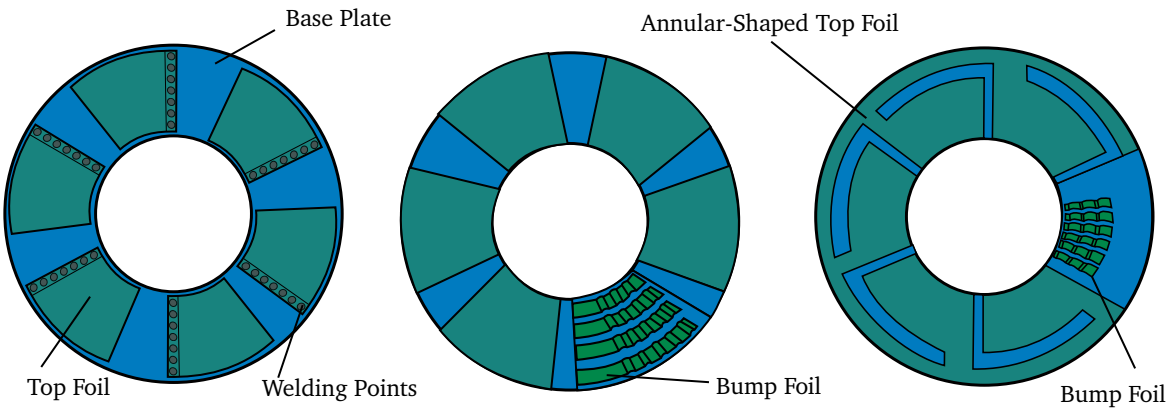

Figure 2.1.: Sketch of different thrust bearing types from literature [19, 20, 46].

This chapter provides an overview of air foil thrust bearings, comprising their historical development in both simulation and experimental investigations. The governing equations for the bearing system, obtained from previous work by Lehn and Rieken [52, 67], are also presented. Additionally, a brief introduction to tribological systems is provided. The final section of the chapter discusses the principles of model validation and the associated challenges.

2.1. Air Foil Thrust Bearings

Air foil thrust bearings typically consist of two main parts: a bump foil and a top foil. The top foil's primary function is to build up fluid film pressure through a convergent gap, thereby counteracting the axial force exerted by the rotor. The bump foil supports the top foil by providing the necessary geometric and design parameters to facilitate the creation of pressure and compensation for misalignment. Consequently, different bearing designs have emerged over the years of development. Fig. 2.1 illustrates three such designs [19, 20, 46]. The first design, known as the type-one air foil bearing, features six individual pads welded onto a base plate, with the underlying bump foil providing support only to a portion of each pad. This arrangement leads to a taper-like air gap when the bearing is unloaded, and the pressure-induced bending of the top foil results in a taper-land configuration when pressure is built up. The second design incorporates six pads mounted into a slit in the base plate, while the underlying bump foils are composed of connected bump arcs separated into four bump strips. The third design, proposed by LaTray et al., arranges the bumps radially, with the top foil consisting of six individual pads connected to an outer ring. Numerous other designs are conceivable, including variations such as the use of metal mesh instead of a bump foil [11]. In the following, a brief historical overview of the research conducted on foil bearings, with a particular focus on air foil thrust bearings, is provided. The theoretical and experimental work is discussed separately.

2.1.1. Simulations of Air Foil Thrust Bearings (AFTBs)

Numerical analysis of air foil bearings can be categorized into two branches: elastohydrodynamic analysis and thermohydrodynamic analysis. Elastohydrodynamic analysis focuses on studying the elastohydrodynamics of the bearing, while thermohydrodynamic analysis examines the thermal behavior. In

recent years, there has been an emergence of combined thermo-elasto-hydrodynamic simulations, which integrate both aspects.

Elastohydrodynamic

The first numerical investigation of air foil thrust bearings was conducted by Heshmat and Gray in 1981-1983 [29, 33]. Their work featured an analytical investigation of the elastohydrodynamics, solving the Reynolds equation for the fluid film and considering a uniform stiffness distribution with a constant value for the bump and top foil. The study aimed to find an optimal geometry for a taper land concept (see Fig. 1.2). The optimal configuration was found to have an r_{o} to r_{i} ratio of 2, a pad angle of $45°$, and a half-taper region. This approach is still used in recent research due to its simplicity [42, 30].
Related to the performance investigations discussed above, Iordanoff published an article in 1998 that compared the load capacity of taper and taper-land configurations for gas lubricated thrust bearings [38]. The study found that the load capacity was better for a taper-land configuration.
In 2004, Peng et al. performed performance investigations on journal bearings, considering compressible air flow and compliance of the bearing surface [61]. They compared their numerical results with experimental data from Dellacorte et. al. [14] and achieved good alignment between the two for load capacity in relation to speed.
Park et. al. performed theoretical considerations of static and dynamic characteristics on an air foil thrust bearing in 2008, including tilt and slip flow [60]. They performed finite element analysis on the bump foil, considering friction forces between the top and bump foils as well as the base plate. The results from the finite element analysis were integrated into their foil bearing model, enabling comprehensive analysis. The study found that the bearing produced more load and torque under tilting conditions.
The first coupled bump and top foil elastohydrodynamic analysis was performed in 2009 by San Andres [73]. In this model, the elastic deformations of the 1D beam-like top foil were coupled with the bump deflections and the gas film hydrodynamics.
Hryniewicz went one step further in 2009 and built a two-dimensional model with a detailed bump foil geometry and considered the interaction between bumps [37]. The model was verified through finite element analysis studies.
Feng performed an analytical investigation in 2010, taking into account the friction and interaction forces between the bump and top foils [22]. In this model, each bump was simplified by two rigid links and a horizontally spaced spring. The local deflection of the top foil was calculated using a finite-element shell model. The deflection was then considered in the local film thickness within the Reynolds equation.
Gad and Koneko introduced a new structural stiffness model in 2014 and 2015, which accounted for the separation of the foils during operation [26, 27, 28]. They coupled this model with the 2D compressible Reynolds equation and solved the fluid-structure interaction iteratively. The simulation results showed good agreement with experimental data from Dickmann [17].
In 2016, Qin et al. developed a 3D flow and structural fully coupled model with a moving mesh to predict the performance of foil thrust bearings for supercritical CO2 cycles [64]. While the Reynolds equation was found to be sufficient for airflow, it was inadequate for supercritical CO2. Therefore, the CFD code EILMER was used to handle the specific fluid properties.
It is worth noting that the previous work primarily focused on the stationary properties of air foil thrust bearings. However, in recent years, researchers have also considered the dynamic interaction between thrust and journal bearings [62].

Thermohydrodynamic

The thermohydrodynamic branch of air foil bearing simulations began approximately 20 years after the elastohydrodynamic branch. In 2001, Salehi et al. presented an investigation on compliant air foil bearings, specifically focusing on their thermal features [72]. They solved a Couette approximation to the energy equation coupled with the compressible Reynolds equation, incorporating thermal properties in the fluid model. The comparison with parallel experimental studies showed an overprediction of 8-19 percent.

In 2010, San Andres presented a thermohydrodynamic model for predicting the performance of gas foil bearings [74]. The model considered the thermal energy transport into the air gap with a cooling gas stream. It also took into account material properties, disk centrifugal effects, and thermal growth. The predictions of the model were compared to published measurements of housing temperatures of an air foil journal bearing.

Lee et al. presented a thermohydrodynamic model for bump air foil journal bearings in 2010 [49]. The model solved the 3D energy equation and Reynolds equation along with temperature distributions in the surroundings. Additionally, it considered the thermal growth of the rotor. The model was extended with measured thermal resistance variables between the top foil and bearing sleeve and was verified through benchmarking against experimental results, showing good agreement.

In 2011, Lee et al. presented the first thermohydrodynamic analysis on air foil thrust bearings [50]. The analysis involved an air foil thrust bearing with radially arranged bumps and a Rayleigh stepped top foil. The temperature distribution in the air foil was computed using the 3D energy equation along with the non-isothermal Reynolds equation. Furthermore, the cooling air flow through the bump foil cooling channels was considered.

Sim et al. published a thermohydrodynamic analysis of bump-type gas foil journal bearings with bump thermal contact and an inlet flow mixing model in 2012 [80]. The analysis took into account energy transport in the air film, heat conduction into the disk, and the thermal resistance of the bump foil. The thermal contact was considered using an analytical model. The simulation results were benchmarked against experimental test data, and the study highlighted the importance of considering the thermal resistance of the bump foils for accurate prediction of bearing performance.

In 2015, Gad et al. adopted the model of Salehi [72] for air foil thrust bearings, including the effects of centrifugal forces on the disk [25].

Thermo-Elastohydrodynamic

Bruckner presented the first thermo-elastohydrodynamic model for bump foil thrust bearings, coupling the hydrodynamic pressure field with the heat generated in the thin film and the elastic deformation of the top and bump film structure [10]. The dissertation also included short test data for an eight-pad generation one thrust bearing. The model simplified heat transfer in the film and adjacent solids by considering constant temperature and constant lubricant properties throughout the film thickness, along with a simple approximation for heat transfer to the adjacent solids.

Lehn developed a fully coupled thermo-elastohydrodynamic model for a thrust foil bearing from 2016 to 2018. The model solved the deformation of the bump and top foils using Reisner-Midlin-Shell theory, incorporating Coulomb friction forces. For the fluid film, the compressible Reynolds equation was solved with the averaged viscosity obtained from a 3D energy equation. The model considered convection and conduction for energy conservation and accounted for the thermal growth and centrifugal deformation of the rotor disk. On the runner's backside, a 2D turbulent flow was solved to handle heat transfer over the disk's backside. Heat transfer from the top foil through the bumps was solved using an analytical thermal resistance model [54, 52, 53].

In 2017, Qin published a thermo-elastohydrodynamic model for air foil thrust bearings operating with supercritical CO2 [63]. To handle this type of fluid, the model considered inertia forces and turbulent flow, which were solved using an in-house tool. A separate finite difference solver for structural deformation solved the Kirchhoff plate equation, coupled by a mapping algorithm.
Overall, these simulation studies and developed models have significantly contributed to the understanding of the behavior and performance of air foil thrust bearings. They have investigated a wide range of factors, including geometric parameters, thermal effects, material properties, and dynamic interactions.

2.1.2. Experimental Studies

First experimental analyses on foil bearings were conducted by NASA researchers in 1977 and 1978 on foil journal bearings [88, 68]. In 1977, Nemeth published a technical paper for NASA that described the first thrust bearing test rig [59]. The test rig utilized an impulse air turbine to drive the rotor, which could reach speeds up to 9 krpm. Thrust loads of up to 80 N were applied through a pressure chamber, while the radial support for the shaft was provided by gas journal bearings.
In 1982, Heshmat et. al. presented a test rig which was able to run up to 80 krpm; externally pressurized journal bearings have been used to mount the shaft in the housing [32]. While the usage of aerostatic journal bearings will basically allow the performance of highly accurate measurements, the running speed of the test rig, which was driven by an impulse turbine, was rather limited.
Iordanoff presented a similar test rig in 1999 [39]. The rotor in this rig was supported by two high-precision ball bearings, and a loading piston supported by aerostatic journal bearings was used to measure the torque. The load was applied through a pressure chamber, allowing for thrust loads up to 900 N and rotor speeds between 20 and 50 krpm. Although this test rig enabled the application of very high loads, the maximum rotor speed was relatively low.
Hryniewicz et al. presented two test rigs for thrust bearings in 2003, featuring a complete oil-free design [36]. With these test rigs, thrust bearings up to a diameter of 102 mm have been analyzed for operating speeds up to 80 krpm and thrust loads up to 1300 N [36]. The rotor shaft was radially supported by two hydrodynamic foil journal bearings, while the rotor was accelerated by an air-driven turbine wheel. The load was applied through an air piston supported by a hydrostatic bearing. This unique design allowed for torque measurements via a torque arm on a calibrated flexure [6]. This test rig has been designed and used to examine rather large bearings at medium rotor speeds. Due to usage of aerostatic bearings for the support of the base plate, very accurate measurements could be carried out.
Dykas also utilized one of the test rigs presented by Hryniewicz et al. for different experimental studies, particularly focusing on cooling conditions [19]. Additionally, Dickman used the same test rig to determine static load deflection curves and for torque measurements at rotor speeds ranging from 5 to 40 krpm [17]. In 2011, Lee presented a test rig capable of running up to 52 krpm [51]. The load was applied through a hand-loading system that pushed the thrust bearing against the rotor disk. The rotor was driven by a 50 kW electric motor, and all moving parts were supported by ball bearings. This test rig investigated thrust bearings with diameters up to 110 mm and thrust loads up to 50 kPa. However, due to the use of ball bearings to support the thrust bearing base plate, the accuracy of the measured friction torque of the foil bearing might be limited.
Balducchi and Arghir conducted experimental analyses on start-up torque in 2013 using a test rig with rotational speeds up to 35 krpm and thrust loads up to 60 N [4]. The test rig was driven by an electric spindle, and the rotor was supported by ceramic ball bearings. The non-rotating part containing the thrust bearing under investigation was radially supported by an aerostatic bearing. The static load was applied by adding weights to the non-rotating component, and the torque was measured using a load cell. Essentially, the test rig may allow the performance of highly accurate measurements. However, the

rotor speed is rather limited due to the spindle drive.
In 2015, San Andres compared his simulated data with the experimental data of Dickmann [75] and found good agreement for drag torque versus shaft speed up to 40 krpm for an applied load of 40 N.
In 2018, LaTray and Kim [47, 46] published a test rig with a Pelton driven rotor, which can run up to 190 krpm. Thrust bearings with an outer diameter of 38 mm have been investigated. The rotor is supported by high-speed angular contact ball bearings. Up to 75 N thrust load can be applied by a pneumatic actuator; the force is measured with a load cell. The base plate of the test bearing is supported by ball bearings; the bearing torque is measured with a load cell. While this test rig allowed for high-speed testing of bearings with moderate loads, the usage of ball bearings may limit the precision of the measured friction torque of the foil thrust bearing.
In 2022, Chen et. al. introduced a test-rig for air foil thrust bearings under dynamic disturbance [12]. The rotor is driven by an electrical motor; rotor speeds up to 25 krpm are considered. The thrust bearing disk has an outer diameter of 30 mm. Loads up to 42 N were applied. The main focus of the work was not on investigating bearing performance but studying the influence of dynamic effects. The rotor disk exhibited a relatively large runner runout error of approximately 12 μm. The usage of ball bearings to support the bearing base plate might limit the accuracy of the measured friction torque.
In 2023, Xu et. al. presented a test rig, which was able to run up to 80 krpm (outer radius of the disk: 35.5 mm; loads up to 120 N) [91, 92]. The rotor is driven by an electric motor; the test bearing is supported aerostatically. The thrust load is applied pneumatically by a cylinder. Due to the aerostatic support of the thrust bearing, the friction torque may be measured with high accuracy. Due to the electric motor, the maximum speed is, however, limited.

In summary, various test rig concepts for air foil thrust bearings have been discussed in the literature. To conduct precise friction torque measurements, reducing friction effects in the support of the thrust bearing base plate is necessary, making aerostatic bearings a suitable choice. Air impulse turbines are a favorable option for achieving high rotor speeds. Another important consideration for high-precision measurements is the reduction of misalignment effects, as misalignment between the runner disk and the foil thrust bearing can significantly influence the friction torque of the bearing. Finally, EP journal bearings proved suitable as well.

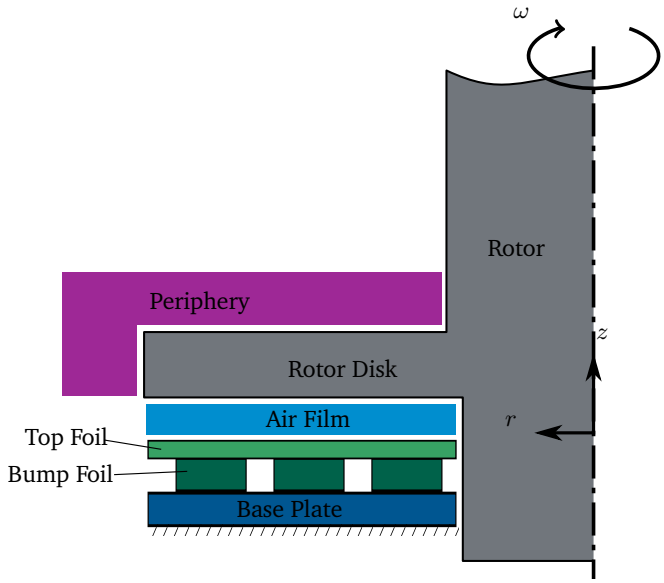

Figure 2.2.: Rotor bearing system of an air foil thrust bearing.

2.2. Governing Equations for the Simulation Model

In this section the equations for the utilized simulation model are presented. These equations are based on the work of Lehn [52] and Rieken [67] and have been adapted in Chapter 4 for the specific type of air foil thrust bearings considered here.
Fig. 2.2 depicts a typical rotor bearing system for an air foil thrust bearing. The rotor and its rotor disk rotate while the bearing remains fixed. The relative movement between the rotor disk and the fixed bearing leads to the formation of an air film between them. The bearing consists mainly of two parts: the bump foil and the top foil. The top foil is positioned on top of the bump foils and can have a pre-deformed shape to facilitate the buildup of pressure in the bearing gap. The bump foil provides spring-like properties to the bearing, allowing it to withstand misalignment and support the top foil at specific locations to restrict its deformation. The bump foil is placed on a base plate. All parts are addressed separately in the following sections.
The following sections address each component separately and provide the corresponding governing equations. The material properties associated with these components can be found in appendix in Tab. A.1.

2.2.1. Rotor

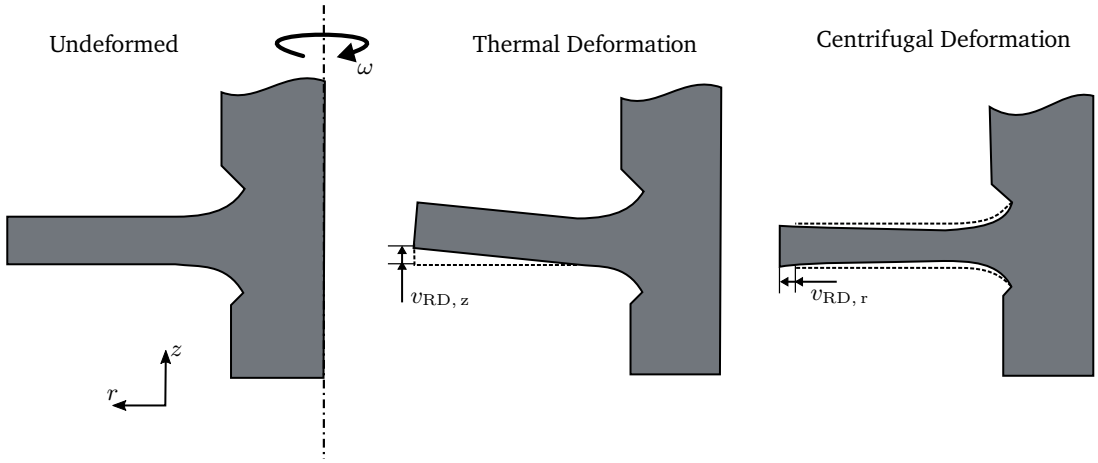

Figure 2.3.: Sketch of the rotor deformation due to centrifugal forces and thermal deflection.

A rotor in a turbomachine consists of a disk and a shaft, as illustrated in Fig. 2.3 on the left side. In the case of the thrust bearing, the rotor disk is of particular interest because the bearing supports the thrust load of the turbomachine on the disk. Due to the high rotational speed ω, the deformation and temperature distribution in the rotor disk can be effectively modeled using an axisymmetric approach. The two deformation modes of the rotor disk are shown in the figure on the right side. In the following equations, all variables related to the rotor are denoted with the subscript RD for rotor disk.
The resulting thermoelastic axisymmetric deformations of the rotor disk, denoted as $v_{\mathrm{RD,r}}$ in the radial direction and $v_{\mathrm{RD,z}}$ in the axial direction, are calculated using the Navier-Lamé equations, which take

into account centrifugal forces and thermal stresses, as described in Ref. [70]:

$$\begin{aligned}
&\tau_{\mathrm{RD}}\left(\nabla^2 v_{\mathrm{RD,r}} - \frac{v_{\mathrm{RD,r}}}{r^2}\right) + (\zeta_{\mathrm{RD}} + \mu_{\mathrm{RD}})\frac{\partial}{\partial r}\left(\frac{1}{r}\frac{\partial}{\partial r}(r v_{\mathrm{RD,r}}) + \frac{\partial v_{\mathrm{RD,z}}}{\partial z}\right) - \epsilon_{\mathrm{RD}}\frac{\partial \Delta T_{\mathrm{RD}}}{\partial r} \\
&= -\rho_{\mathrm{RD}} r \omega^2, \\
&\tau_{\mathrm{RD}}\nabla^2 v_{\mathrm{RD,z}} + (\zeta_{\mathrm{RD}} + \tau_{\mathrm{RD}})\frac{\partial}{\partial z}\left(\frac{1}{r}\frac{\partial}{\partial r}(r v_{\mathrm{RD,z}}) + \frac{\partial v_{\mathrm{RD,z}}}{\partial z}\right) - \epsilon_{\mathrm{RD}}\frac{\partial \Delta T_{\mathrm{RD}}}{\partial z} \\
&= 0.
\end{aligned} \tag{2.1}$$

In these equations, $\zeta_{\mathrm{RD}} = \frac{E_{\mathrm{RD}}\nu_{\mathrm{RD}}}{(1+\nu_{\mathrm{RD}})(1-2\nu_{\mathrm{RD}})}$ represents the Lamé constant and $\tau_{\mathrm{RD}} = \frac{E_{\mathrm{RD}}}{2(1+\nu_{\mathrm{RD}})}$ denotes the shear modulus. Here, E_{RD} is the elastic modulus and ν_{RD} is the Poisson's ratio of the rotor material. The constant ϵ_{RD} is defined as $\epsilon_{\mathrm{RD}} = \frac{E_{\mathrm{RD}}\alpha_{\mathrm{RD}}}{1-2\nu_{\mathrm{RD}}}$, where α_{RD} is the thermal expansion coefficient of the rotor material. The term $\Delta T_{\mathrm{RD}} = T_{\mathrm{RD}} - T_0$ represents the temperature difference of the disk with respect to a reference temperature T_0. This term couples the temperature field to the deformation of the rotor. The centrifugal deformation is taken into account through the inertia force on the right-hand side of the equation, which depends on the rotor's material properties (density ρ) and the rotational speed ω.
The temperature field of the rotor disk, denoted as $T_{\mathrm{RD}}(r, z)$, is obtained by solving the axisymmetric heat diffusion equation:

$$\frac{\partial}{\partial r}\left[\lambda_{\mathrm{RD}} r \frac{\partial T_{\mathrm{RD}}}{\partial r}\right] + \frac{\partial}{\partial z}\left[\lambda_{\mathrm{RD}} r \frac{\partial T_{\mathrm{RD}}}{\partial z}\right] = 0, \tag{2.2}$$

with λ_{RD} representing the thermal conductivity of the rotor material. The boundary and coupling conditions of the rotor disk, as well as its interactions with other components, are discussed in Section 4.1.

2.2.2. Air Film

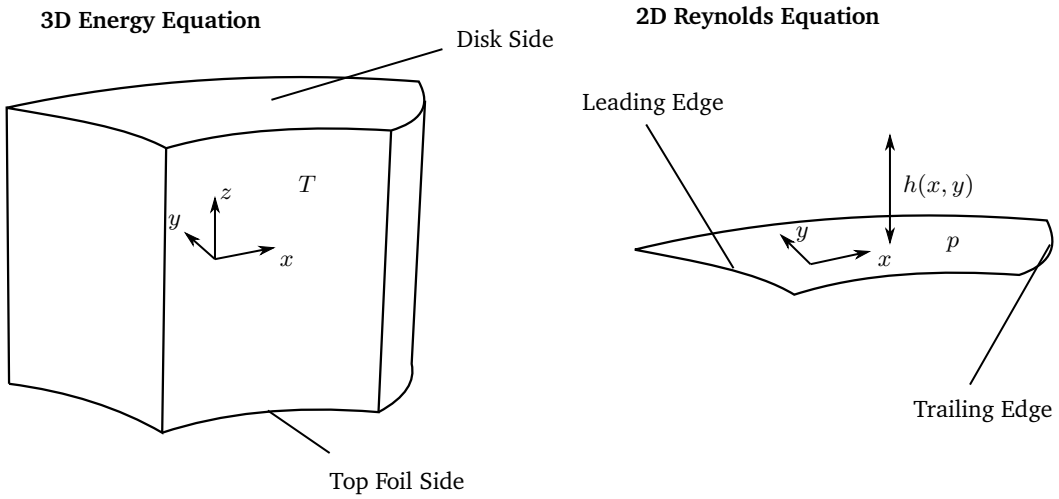

Figure 2.4.: Air film sector of an air foil thrust bearing in 3D for energy equation and 2D for Reynolds equation.

The air film is treated as a 2D field for solving fluid motion and conservation in the x and y directions. For energy conservation, a 3D field is used, where the z coordinate represents the air film height h. Both fields are illustrated in Fig. 2.4. Given the high aspect ratios between typical extensions in lateral (x and y) and film height h direction in z (i.e., $h/x \leq 1000$), the pressure can be assumed to be constant in z direction. Consequently, the air film pressure p is calculated using the generalized Reynolds equation, as

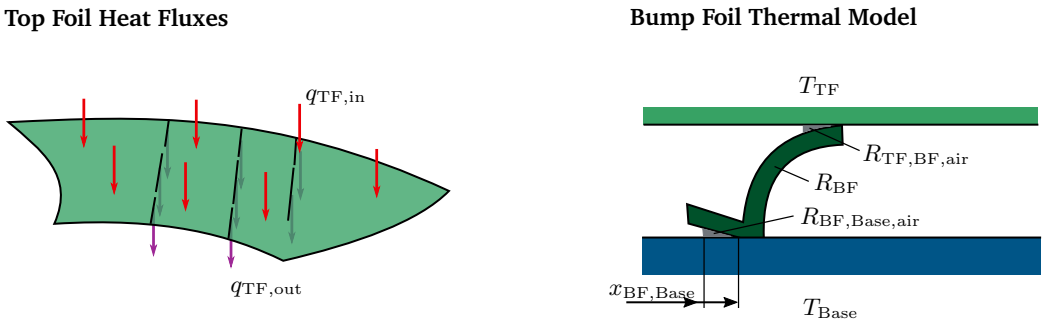

Figure 2.5.: Thermal model of top and bump foil.

described in references such as Dowson et al. [18] and Hamrock et al. [31]. The equation takes into account the averaged fluid temperature $T_{\mathrm{m}}(x, y)$ to determine the density ρ, and viscosity η of the air film (depicted in the Appendix in Eq. A.1-A.3), as reported in previous works by Lee [51] and Mahner [57]:

$$\begin{aligned} &\frac{\partial}{\partial x}\left[\frac{\rho(p,T_{\mathrm{m}})\,h^3}{12\eta(T_{\mathrm{m}})}\frac{\partial p}{\partial x}\right]+\frac{\partial}{\partial y}\left[\frac{\rho(p,T_{\mathrm{m}})\,h^3}{12\eta(T_{\mathrm{m}})}\frac{\partial p}{\partial y}\right] \\ &=\frac{\partial}{\partial x}\left[\frac{\rho(p,T_{\mathrm{m}})U\,h}{2}\right]+\frac{\partial}{\partial y}\left[\frac{\rho(p,T_{\mathrm{m}})V\,h}{2}\right]. \end{aligned} \tag{2.3}$$

The velocities U and V represent the disk velocity in the x and y directions, respectively. The temperature field $T(x, y, z)$ is obtained by solving the energy equation, which can be expressed as follows in thin film flow approximation:

$$\begin{aligned} &\rho c_P\left[u\frac{\partial T}{\partial x}+v\frac{\partial T}{\partial y}\right]=\frac{\partial}{\partial z}\left(\lambda\frac{\partial T}{\partial z}\right) \\ &+\left[u\frac{\partial p}{\partial x}+v\frac{\partial p}{\partial y}\right]+\eta\left[\left(\frac{\partial u}{\partial z}\right)^2+\left(\frac{\partial v}{\partial z}\right)^2\right]. \end{aligned} \tag{2.4}$$

The first term represents convective heat transfer, taking into account the heat capacity c_P (depicted in the Appendix in Eq. A.3) of air. The second term corresponds to diffusive heat transfer, also known as conduction, considering the thermoconductivity λ of air. In the case of air foil thrust bearings (AFTBs), the conductive heat transfer in the axial (z) direction is dominant compared to convective heat transfer. This is due to the small dimensions of the air gap, which are on the order of micrometers or tens of micrometers [52]. Additionally, planar heat diffusion in the lubricating gap can be neglected. The third term in the energy equation accounts for the power of pressure forces, while the last term describes dissipation resulting from shear forces. Since the film height and the air film domain change when the rotational speed or load is varied, a coordinate transformation is performed for the energy equation domain. This transformation converts the range of the gap height from 0 to $-h$ to $z = -1$ to 1, as presented in [52].

2.2.3. Thermodynamics of Top and Bump Foils

The temperature profile $T_{\mathrm{TF}}(x, y)$ of the top foil can be determined using the 2D heat diffusion equation:

$$-\lambda_{\mathrm{TF}} t_{\mathrm{TF}} \nabla T_{\mathrm{TF}} = q_{\mathrm{TF,in}} + q_{\mathrm{TF,out}}, \tag{2.5}$$

where λ_{TF} is the constant heat conductivity and t_{TF} is the thickness of the top foil. The top foil, along with the incoming and outgoing heat fluxes, is illustrated in Fig. 2.5 on the left side. The incoming heat flux can be treated as $q_{\mathrm{TF,in}} = \left(\frac{2\lambda}{h}\frac{\partial T}{\partial z}\right)\Big|_{z=-1}$, coupling the 3D energy equation with the top foil. The outgoing heat flux $q_{\mathrm{TF,out}}$ is represented by the heat going through the bump foils into the base plate, depicted by a thermal resistance R_{th}, presented in Fig. 2.5 on the right side. The thermal resistance R_{th} can be expressed as a series circuit:

$$R_{\mathrm{th}} = R_{\mathrm{TF,BF,air}} + R_{\mathrm{BF}} + R_{\mathrm{BF,Base,air}}, \tag{2.6}$$

where $R_{\mathrm{TF,BF,air}}$ is the thermal resistance of the air gap between the top foil and the bump foil, R_{BF} is the thermal resistance of the bump arc, and $R_{\mathrm{BF,Base,air}}$ is the thermal resistance of the air gap between the bump foil and the base plate. To calculate the individual thermal resistances, certain parameters of the foil bearing geometry and material properties are required. These include the radius of the arc R_{BA}, its nominal angle θ_{BF}, the thickness t_{BF} of the bump foil, the length of the contact lines L_{B}, and the thermal conductivity λ_{BF} of the bump foil. Additionally, the length dimension $x_{\mathrm{TF,BF}}$ or $x_{\mathrm{BF,Base}}$ is needed, which indicates the extent to which the diffusive heat flux is assumed. This is defined as:

$$x_{\mathrm{TF,BF}} = x_{\mathrm{BF,Base}} = 2 \cdot t_{\mathrm{BF}}. \tag{2.7}$$

Furthermore, the thermal conductivity of air λ is given. The roughness value $\gamma_{\mathrm{BF,Base}}$ or $\gamma_{\mathrm{TF,BF}}$ is considered at the contact points to account for surface roughness. It is calculated as the sum of the roughness values of the individual surfaces. As a result, the thermal resistance between the top foil and the bump foil can be obtained.

$$R_{\mathrm{TF,BF,\,air}} = \sqrt{\frac{\gamma_{\mathrm{TF,BF}}}{2R_{\mathrm{BA}}}} \cdot \frac{1}{\lambda_{\mathrm{air}} L_{\mathrm{BF}} \operatorname{atan}\left(\frac{x_{\mathrm{TF,BF}}}{\sqrt{2\gamma_{\mathrm{TF,BF}} R_{\mathrm{BA}}}}\right)}. \tag{2.8}$$

The thermal resistance of a bump foil arc reads:

$$R_{\mathrm{BF}} = \frac{R_{\mathrm{BA}}\theta_{\mathrm{BF}}}{L_{\mathrm{BF}} t_{\mathrm{BF}} \lambda_{\mathrm{BF}}}, \tag{2.9}$$

and the thermal resistance between bump foil and base plate:

$$R_{\mathrm{BF,Base,air}} = \frac{\gamma_{\mathrm{Bb}}}{L_{\mathrm{BF}} x_{\mathrm{Bb}} \lambda_{\mathrm{air}}}. \tag{2.10}$$

Using the analytical thermal resistance quantities, the heat transfer from the top foil to the base plate can be described [52]. These thermal resistances capture the resistance to heat flow at different interfaces, including the air gaps and contact points between the top foil, bump foil, and base plate. By considering these thermal resistances in a series circuit, the overall resistance to heat transfer from the top foil to the base plate can be determined. This provides a quantitative description of the heat transfer process in the foil bearing system.

2.2.4. Mechanics of Top and Bump Foils

The deformations of the top and bump foils are calculated using the Reissner-Mindlin shell theory [5]. This theory allows for three translational degrees of freedom (v_i) and two independent rotational degrees of freedom (w_α) for the foils. The equations governing the deformations depend on the metrical and curvature properties of the shell's middle surface.

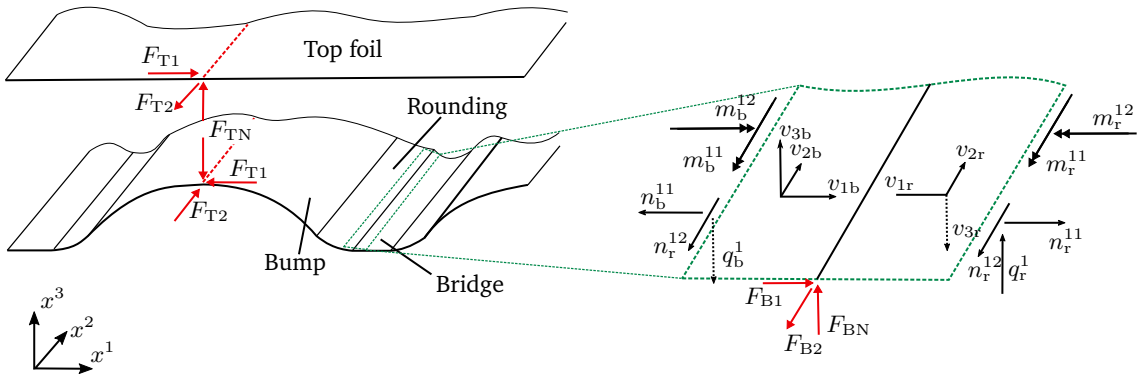

Figure 2.6.: Sketch of the bump mechanics from Lehn [52].

In the case of the top foil, it can be approximated as a planar (flat) shell, and its deformations are governed by the equations for a flat shell. On the other hand, the bump foil is divided into different segments: the bridges between the bumps are modeled as planar shells, while the bumps and their transitions are modeled as cylindrical shells. The deformations of the cylindrical shell segments are governed by a set of five equations [21].
These governing equations describe the deformations of the cylindrical shell without external load, taking into account its radius of curvature R, with the centerline along the y-axis. The specific form of these equations depends on the geometry and properties of the shell, and they are derived based on the principles of the Reissner-Mindlin shell theory.

$$\begin{aligned}&\frac{\partial}{\partial x}\left(D\left(\frac{\partial v_1}{\partial x}+\nu\frac{\partial v_2}{\partial y}+\frac{1}{R}v_3\right)+\frac{B}{R}\left(\frac{\partial w_1}{\partial x}+\nu\frac{\partial w_2}{\partial y}+\frac{1}{R}\frac{\partial v_1}{\partial x}+\frac{1}{R^2}v_3\right)\right)\\&+\frac{\partial}{\partial y}\left(D\frac{1-\nu}{2}\left(\frac{\partial v_2}{\partial x}+\nu\frac{\partial v_1}{\partial y}\right)+\frac{B}{R}\frac{1-\nu}{2}\left(\frac{\partial w_2}{\partial x}+\nu\frac{\partial w_1}{\partial y}+\frac{1}{R}\frac{\partial v_1}{\partial y}\right)\right)\\&=-\frac{Gtk_S}{R}\left(w_1+\frac{\partial v_3}{\partial x}-\frac{1}{R}v_1\right)\end{aligned}\tag{2.11}$$

$$\frac{\partial}{\partial x}\left(D\frac{1-\nu}{2}\left(\frac{\partial v_2}{\partial x}+\nu\frac{\partial v_1}{\partial y}\right)\right)+\frac{\partial}{\partial y}\left(D\left(\frac{\partial v_2}{\partial y}+\nu\frac{\partial v_1}{\partial x}+\frac{\nu}{R}v_3\right)\right)=0\tag{2.12}$$

$$\begin{aligned}&\frac{\partial}{\partial x}\left(Gtk_S\left(w_1+\frac{\partial v_3}{\partial x}+\frac{1}{R}v_1\right)\right)+\frac{\partial}{\partial y}\left(Gtk_S\left(w_2+\frac{\partial v_3}{\partial y}\right)\right)\\&=\frac{D}{R}\left(\frac{\partial v_1}{\partial x}+\nu\frac{\partial v_2}{\partial y}+\frac{1}{R}v_3\right)+\frac{B}{R}\left(\frac{\partial w_1}{\partial x}+\nu\frac{\partial w_2}{\partial y}+\frac{1}{R}\frac{\partial v_1}{\partial x}+\frac{1}{R^2}v_3\right)\end{aligned}\tag{2.13}$$

$$\begin{aligned}&B\left(\frac{\partial}{\partial x}\left(\frac{\partial w_1}{\partial x}+\nu\frac{\partial w_2}{\partial y}+\frac{1}{R}\frac{\partial v_1}{\partial x}+\frac{1}{R^2}v_3\right)+\frac{\partial}{\partial y}\left(\frac{1-\nu}{2}\left(\frac{\partial w_1}{\partial y}+\frac{\partial w_2}{\partial x}+\frac{1}{R}\frac{\partial v_1}{\partial y}\right)\right)\right)\\&=Gtk_S\left(w_1+\frac{\partial v_3}{\partial x}-\frac{1}{R}v_1\right)\end{aligned}\tag{2.14}$$

$$
\begin{aligned}
&B\left(\frac{\partial}{\partial x}\left(\frac{1-\nu}{2}\left(\frac{\partial w_1}{\partial y}+\frac{\partial w_2}{\partial x}+\frac{1}{R}\frac{\partial v_1}{\partial y}\right)\right)+\frac{\partial}{\partial y}\left(\frac{\partial w_2}{\partial y}+\nu\frac{\partial w_1}{\partial x}+\frac{\nu}{R}\frac{\partial v_1}{\partial x}+\frac{\nu}{R^2}v_3\right)\right)\\
&=Gtk_{\mathrm{S}}\left(w_2+\frac{\partial v_3}{\partial y}\right),
\end{aligned}
\tag{2.15}
$$

where $D=\frac{Et}{1-\nu^2}$ is the stretching stiffness, $B=\frac{Et^3}{12(1-\nu^2)}$ is the bending stiffness, and $Gt=\frac{Et}{2(1+\nu)}$ is the shear stiffness. With regard to the Cartesian coordinate system, the 1-, 2-, and 3-direction correspond to the x-,y-, and z-direction, respectively. The underlying constitutive equations for the transverse shear stress q^α is expressed as:

$$
q^\alpha = Gt\cdot a^{\alpha\lambda}\gamma_\lambda\cdot k_S, \tag{2.16}
$$

the moment tensor $m^{\alpha\beta}$ as:

$$
m^{\alpha\beta}=BH^{\alpha\beta\lambda\mu}\left(\kappa_{\lambda\mu}-b^\sigma_\lambda\varphi_{\mu\sigma}\right), \tag{2.17}
$$

and the stress resultant tensor $n^{\alpha\beta}$ as:

$$
n^{\alpha\beta}=DH^{\alpha\beta\lambda\mu}\varphi_{\lambda\mu}-b^\beta_\rho m^{\alpha\rho}. \tag{2.18}
$$

The kinematic relations for the strain variables $\varphi_{\alpha\beta}$, $\kappa_{\alpha\beta}$, and γ_α are:

$$
\varphi_{\alpha\beta}=v_{\beta|\alpha}-v_3b_{\alpha\beta}, \tag{2.19}
$$

$$
\kappa_{\alpha\beta}=\frac{1}{2}\left(w_{\alpha|\beta}+w_{\beta|\alpha}\right), \tag{2.20}
$$

$$
\gamma_\alpha=w_\alpha+v_{3,\alpha}+v_\lambda b^\lambda_\alpha. \tag{2.21}
$$

Finally, the equilibrium equations have the form:

$$
-p^\beta=n^{\alpha\beta}|_\alpha-q^\alpha b^\alpha_\beta, \tag{2.22}
$$

$$
-p^3=n^{\alpha\beta}b_{\alpha\beta}+q^\alpha|_\alpha, \tag{2.23}
$$

$$
0=m^{\alpha\beta}|_\alpha-q^\beta. \tag{2.24}
$$

The contact forces between the top foil and bump foil, as well as between the bump foil and the base plate, are incorporated as external loads on the respective components. In the model, the contacts are approximated as line contacts at the top line of the bump and the corresponding lines on the top foil, as shown in Fig. 2.6.

The normal contact forces, denoted as F_{N}, are modeled using a penalty stiffness approach. They are proportional to the penetration depth Δv_3 and can be calculated as $F_{\mathrm{N}}=c\Delta v_3$, where c is the penalty stiffness coefficient. This formulation allows for only small penetration depths, ensuring that the contact forces act to separate the contacting surfaces. The tangential contact forces, denoted as F_{T}, are formulated using a generalized Coulomb friction approach [90]. The friction force is given by $\mu\cdot\mathrm{step}(\Delta v_\alpha)F_{\mathrm{N}}$, where μ is the coefficient of friction and Δv_α represents the relative tangential displacement between the contacting surfaces. The step function ensures that the friction force only acts when there is relative motion between the surfaces.

This approach captures the contact interactions between the top foil and bump foil, as well as between the bump foil and the base plate, taking into account both normal and tangential forces. It allows for the modeling of contact mechanics and the simulation of the mechanical behavior of the components under contact conditions.

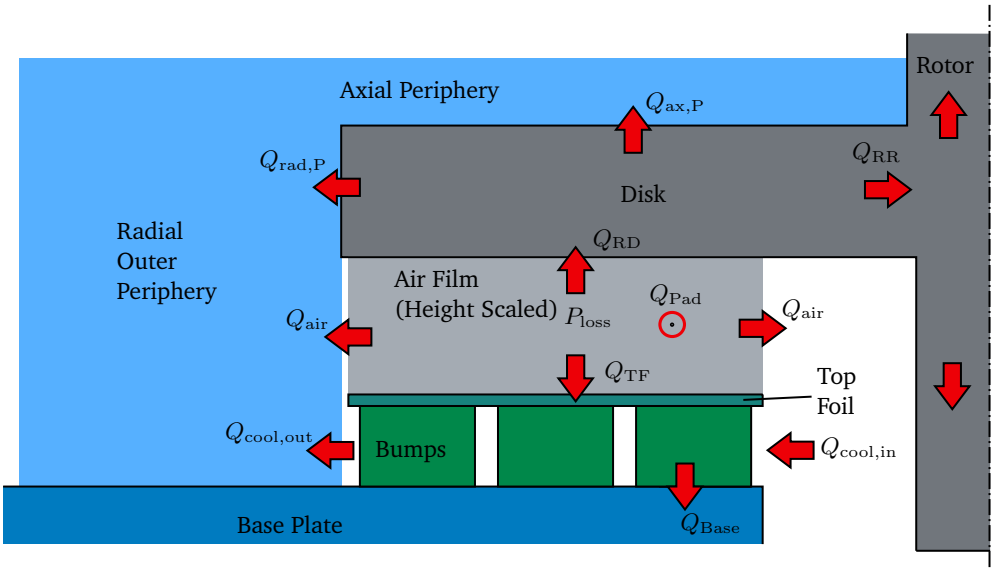

Figure 2.7.: Heat paths in an air foil thrust bearing and its surrounding.

2.2.5. Heat Paths

Heat paths in an air foil thrust bearing and its surroundings play a crucial role in the design and thermal management of the bearing. Fig. 2.7 illustrates the major heat paths involved. The primary heat source is the air film between the top foil and the disk, which generates heat due to shear forces in the fluid. This heat can be distributed through five main paths:

$$P_{\text{loss}} = Q_{\text{TF}} + Q_{\text{RD}} + Q_{\text{air,in}} + Q_{\text{air,out}} + Q_{\text{pad}} \tag{2.25}$$

- Heat conducted into the rotor disk (Q_{RD}): Some of the heat generated in the air film is conducted into the rotor disk, resulting in an increase of its temperature.
- Heat conducted into the top foil (Q_{TF}): Heat can also be conducted into the top foil, leading to an increase in its temperature.
- Heat carried away by air inflow ($Q_{\text{air,in}}$): Fresh air flowing over the inner radius of the air gap absorbs heat from the bearing, helping in the dissipation of thermal energy.
- Heat carried away by air outflow ($Q_{\text{air,out}}$): Air flowing over the outer radius of the air gap carries away heat from the bearing, contributing to heat dissipation.
- Heat exchanged between the pads (Q_{pad}): Heat can be exchanged between the pads of the bearing, which affects the overall thermal behavior of the system.

Heat conducted into the top foil can be further distributed through different paths. It can be carried away by cooling flow or conducted into the bump foils. The bump foil can then conduct heat into the base plate (Q_{Base}), which is often equipped with a water cooling system. Additionally, air cooling can be implemented beneath the top foil, flowing from the inner radius to the outer radius ($Q_{\text{Cool,in/out}}$).
On the other side of the air film, heat conducted into the disk also has various distribution paths. Part of the heat flows throughout the rotor (Q_{RR}) and can be dissipated through convection on the rotating

rotor or conduction in smaller gaps, such as the journal bearings. Heat fluxes towards the periphery can be distributed into radial ($Q_{\mathrm{rad,P}}$) and axial ($Q_{\mathrm{ax,P}}$) components. The amount of heat flowing into the periphery and its effect depend on the surrounding geometry. In some cases, the radial periphery represents a small gap that contributes to additional heat generation in addition to the air film in the bearing. Furthermore, machines often require two axial bearings for each thrust force direction, which means the backside of the disk can also generate additional heat within this second bearing.

2.3. Tribological Systems

In energy-converting machines, tribological contacts between solid bodies, liquids, or gases play a crucial role. These contacts involve the interaction between surfaces and are governed by physical and chemical mechanisms. The field of tribology focuses on studying lubrication, friction, and wear in these contact systems. In the case of aerodynamic thrust bearings, the contact partners are mainly the rotor disk, the bearing surface (represented by the top foil's coating layer), and the air film between them.
One important concept in tribology is the Stribeck curve, which describes the friction behavior of lubricated contacts as a function of the sliding speed [83]. The Stribeck curve, depicted in Fig. 2.8, shows the friction force plotted against the sliding velocity u. Stribeck identified three distinct operating ranges based on the sliding speed:

- Hydrodynamic lubrication: At higher sliding speeds, the lubrication film between the surfaces is thick enough to fully support all normal forces, preventing direct contact between the surfaces. In this range, the friction force increases linearly with the sliding speed due to shear stresses in the lubrication film.
- Mixed lubrication: In the intermediate speed range, the hydrodynamic pressure is not sufficient to fully support the normal load on the contact. As a result, a portion of the normal load is carried by direct contact between solid asperities, leading to the possibility of wear.
- Boundary lubrication: At very low sliding speeds, the normal forces are no longer sustained by the lubrication film, and solid-state friction occurs. In this range, a large portion of the surface area of the two solids is in direct contact with each other.

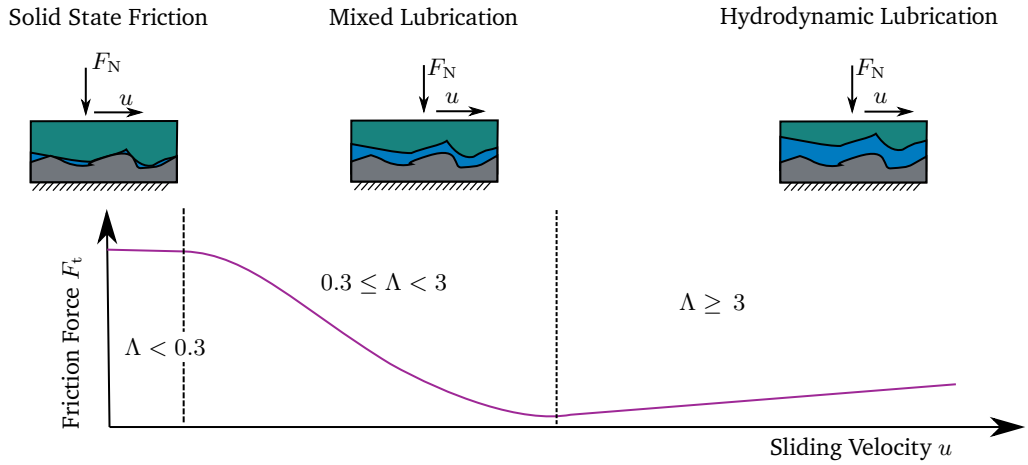

Figure 2.8.: Stribeck curve.

The Stribeck curve is based on the lubricant film thickness parameter Λ, which is defined as the ratio of the gap height h to the combined standard deviation of the surface roughness σ.

$$\Lambda = \frac{h}{\sigma} \tag{2.26}$$

This parameter serves as an indicator of the proportion of solid body contact. For instance, if $\Lambda = 3$ (as in the transition from mixed lubrication to hydrodynamic lubrication), only $1\,\%$ of the surface area of the solids are in contact. On the other hand, if $\Lambda = 0.3$, $99\,\%$ of the surfaces are in contact. It is important to note that real surface roughness profiles can deviate from a normal distribution, leading to variations in the lubricant film thickness parameter for different operating ranges [31].
In the context of foil bearings, the Stribeck curve can be applied to analyze the tribological system. The normal force in this system is exerted by the reaction force of the compressor wheel and is applied to the rotor disk. The rotor disk rotates with a velocity u, while the top foil remains static. Interpreting the Stribeck curve in this context suggests that for a given normal force, there exists a critical rotor velocity at which hydrodynamic lubrication becomes possible. This critical velocity depends on the roughness of the top foil and rotor surfaces, as indicated by the lubricant film thickness parameter Λ and the Reynolds equation. The Reynolds equation calculates the pressure distribution based on the film height, and by adjusting the applied axial force iteratively, the film height and pressure distribution can be obtained. If the velocity is not high enough to establish a lubrication film with sufficient pressure to counteract the normal force, wear can occur. By using a simulation model and known roughness parameters of the contacting surfaces, it is possible to predict this critical point when the local film height h falls below a threshold value, such as $\Lambda = 3$.

2.4. Model Validation

Model validation is an essential step in the development of a simulation model. It involves assessing the accuracy and reliability of the model by comparing its predictions with real-world data. In this section, the concept of model validation, the uncertainty quantification method used for validation, and the concept of sensitivity analysis are discussed.
According to Sargent [76], the concept of model validation and verification can be understood by referring to Fig. 2.9. This figure illustrates the relationships and dependencies between the real world and models. Models should be capable of simulating the physical interrelationships of the real world that correspond to the defined task. In this case, the model is intended to support the design process and facilitate optimization with respect to various output variables. Therefore, the validation and verification process of the model is described in accordance with this task.
The conceptual model in this case represents a logical representation of the system, as depicted in Fig. 2.2. It consists of the bearing itself, its surroundings, and the interactions among all the components. The simulation model is the conceptual model implemented on a computer, incorporating the relevant physical equations and their boundary conditions. To ensure the accuracy of the model, validation and verification processes are applied between these areas.
Model verification is commonly defined as ensuring the correct implementation of the simulation model, while validation involves confirming that the simulation model achieves a satisfactory level of accuracy consistent with its intended application (refer to Schlesinger [77]). Model verification, in our case, has been performed in prior work by Lehn and Rieken [52, 67], confirming that the implementation of the conceptual model aligns with the model specifications. On the other hand, conceptual model validation ensures that the theories and assumptions of the conceptual model are consistent with the system theories of the real world. In this case, the Navier-Stokes equation serves as the system theory for the fluid film in

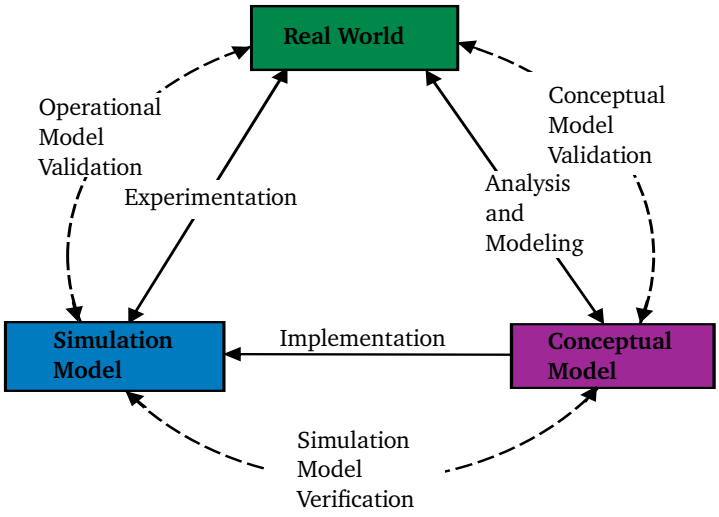

Figure 2.9.: Verification and validation based on Sargent [76].

the bearing, while the conceptual model specifies simplifications leading to the Reynolds equation.
Operational validity guarantees that the behavior of the model's output quantities remains within a defined level of accuracy, accurately representing various conditions of the real world. For instance, if a geometric parameter is changed in both the real world and the simulation, the experiment and simulation results should exhibit the same performance changes. Experimentation is carried out in the real world and can involve multiple levels of abstraction.
Czichos [13] defines six levels of abstraction for the system, ranging from operational trials at level one to abstract model testing at level six. These abstraction levels are necessary for certain studies to identify and exclude parasitic influences. In order to obtain the operational model validation through experimentation, the concept of uncertainty quantification is obtained in this work and described below.

2.4.1. Uncertainty Quantification

The concept of uncertainty quantification is illustrated within the validation process in Fig. 2.10. In order to validate the output of the simulation model, experiments need to be designed and conducted. The results obtained from these experiments can then be compared with the simulation output. Throughout this process, several sources of uncertainty can be identified. First, the experiments themselves are subject to uncertainties, which can be categorized as follows:

- **Systematic errors**: Are predictable and typically constant or proportional to the true value. If the cause of the systematic error can be identified, then it usually can be eliminated, e.g., through calibration and zeroing.
- **Random errors**: Arise from unpredictable fluctuations in the measured output. They manifest as different results for repeated measurements of the same quantity. These errors can be estimated by comparing multiple measurements and can be reduced by averaging them.

In addition to experimental errors, simulation results also encounter uncertainties, which can be classified as follows:

- **Model uncertainties**: These uncertainties arise from the approximations made in modeling the

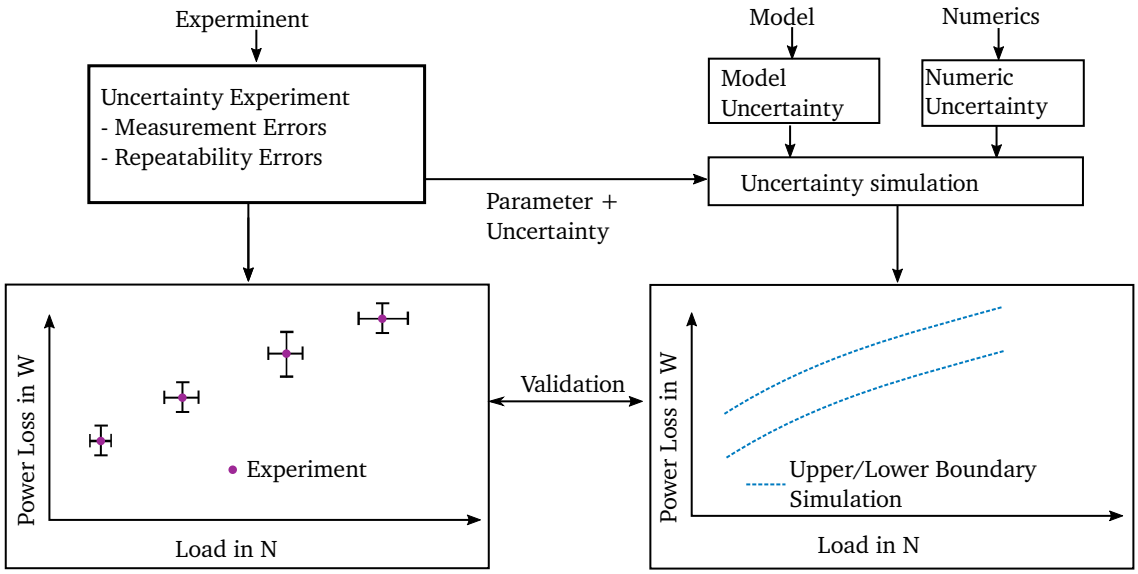

Figure 2.10.: Model validation concept based on Fricke [24].

underlying physical processes. For example, the Reynolds equation is an approximation derived from the Navier-Stokes equation.

- **Numeric errors and uncertainties**: Result from the discretization of the simulation model, leading to rounding or approximation errors. Bugs or coding errors can also lead to numeric errors.
- **Input uncertainties**: All simulation models rely on parameters that must be specified for their use. Differential equations also require initial and boundary conditions to be defined. The process of estimating model inputs based on measured data is often referred to as model calibration, which also faces the measurement uncertainties mentioned above.

Thus, the uncertainty in the simulation can be characterized by considering input uncertainties, model uncertainties, and numeric uncertainties [81].
The goal of the validation in this work is to ensure that model uncertainties are sufficiently small for the simulation to accurately predict the behavior of a real bearing. Since numeric uncertainties can be minimized through the use of fine mesh and high convergence criteria, they can be neglected when considering simulation uncertainties. If all other uncertainties are known, the upper and lower bounds of the uncertainties in both the simulation and the experimental results can be specified. To illustrate the validation process with simple examples, Fig. 2.11 can be consulted. In the figure, three diagrams are presented. In each diagram, a variable denoted as "Quantity 2" is plotted as a function of variable "Quantity 1". Both simulation and experimental results are displayed along with their respective uncertainties.
In case (a) of the figure, all measured quantities fall within the uncertainty range of the simulation results. Both the trend and absolute values closely match. The uncertainty range can be stated as rather small in this case. Thus, it can be concluded that the model uncertainties are smaller than the uncertainties stemming from the simulation inputs. Consequently, the model can be considered validated within the specified parameter space.
Moving on to diagram (b) in the figure, the trend of the experimental results diverges from that of the simulation. This discrepancy suggests that the conceptual model cannot accurately capture the real-world behavior and requires adjustments to achieve a validatable model.
In diagram (c) of the figure, the measured quantities fall within the range of simulation uncertainties,

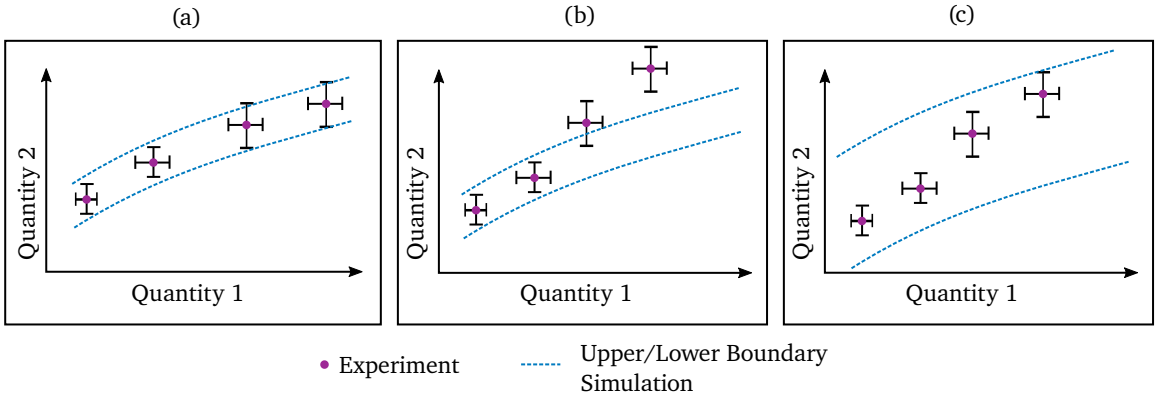

Figure 2.11.: Model validation based on measured data and simulation results.

but the uncertainty range is notably wide. In such cases, achieving a comprehensive validation becomes challenging. Differences in trends cannot be definitively attributed to either inaccuracies in the conceptual model or complex input parameter behavior.
In an additional scenario—not depicted in the figure—experimental uncertainties might be excessively large. In such instances, it is advisable to reconsider the experimental setup and potentially opt for a different level of abstraction to mitigate external factors, as discussed by Czichos [13].
Complex simulation models often depend on numerous input parameters. To identify the most influential parameters, a sensitivity analysis can be applied. This concept will be introduced and applied to the model in the subsequent section.

2.4.2. Sensitivity Analysis

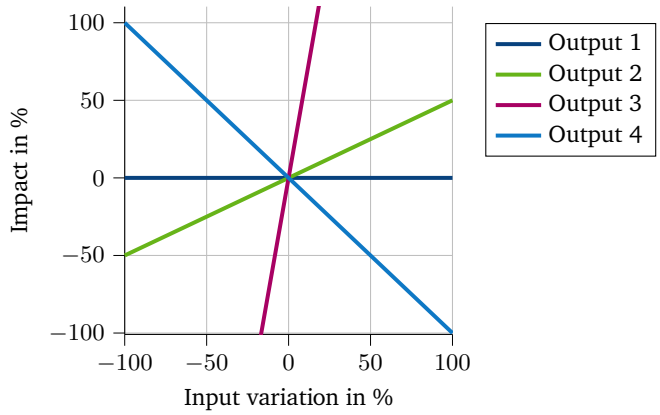

Figure 2.12.: Sensitivity analysis example.

A sensitivity analysis allows us to quantify the relative contributions of individual parameters or inputs to the output of a model. It provides insights into the robustness of the model with respect to different parameters and helps identify insensitive parameters, simplifying the model. Additionally, a sensitivity analysis can guide experimental setups by determining which measurements have a significant impact on the response sensitivity [81]. Fig. 2.12 provides an example of such an evaluation, where the impact of input variations on four evaluation key figures is depicted. On the horizontal axis one example input variation is depicted from -100 to 100 %. The vertical axis shows the input variations impact on four

example evaluation key figures. In this example, the variation of a specific input has no influence on Output 1, but affects the other characteristics in different ways.
To validate the model, output values must be defined, which can also serve as benchmarks for the sensitivity analysis. Since the model is intended to predict the bearing behavior, the selected quantities should be relevant to this purpose.
In this work, four new bearing characteristics are defined and introduced in this section. The first characteristic to be considered is the bearing's performance in terms of load capacity and the power loss. In addition, the design of the bearing depends on how the produced heat is dissipated. Furthermore, the specific bearing load is important to ensure the longevity of the bearing. Moreover, the bearing is dependent on another important design parameter: its stiffness. These four characteristics need to be quantified with respect to simulation and experimental output.
The simulation model provides several output variables, and in this case, the most important ones are interconnected to predict the bearing's performance. These variables include the pressure $p(x, y)$, temperature $T(x, y, z)$, film height $h(x, y)$, and shear momentum dM of the air film. The deformation of the bump and top foil can be combined to determine the resulting top foil deformation $v_{3\mathrm{T}}$ at the bump intersection lines. Moreover, the top foil temperature T_{TF} and the rotor disk temperature T_{RD} are of special interest. Most of these variables can be used to calculate integral quantities, such as the bearing's load capacity given by

$$W = \int_{A_{\mathrm{pad}}} (p - p_0) dA, \tag{2.27}$$

and the power loss

$$P_{\mathrm{loss}} = \omega \int_{A_{\mathrm{pad}}} dM \, dA. \tag{2.28}$$

Calculated temperature gradients are proportional to the heat fluxes going from the air film into the rotor disk Q_{RD} and into the top foil Q_{TF}.
The first characteristic, Φ_{Loss}, quantifies the amount of friction loss generated for a required load in a specific bearing. It is defined as the ratio of power loss P_{loss} to load capacity W:

$$\Phi_{\mathrm{Loss}} = \frac{P_{\mathrm{loss}}}{W}. \tag{2.29}$$

For example, if a bearing produces 300 W of friction losses at 100 N, Φ_{Loss} would be 3 W/N, indicating that every Newton of load produces 3 W of heat in the bearing's fluid film. In most cases, the relationship between power loss and load capacity is nearly linear for a given spinning speed, making this factor an indicator of the bearing's loss behavior and performance.
The generated friction losses dissipate into the air film and are carried away to the surrounding components of the bearing. Understanding how the heat is transported within the system is crucial for the understanding of the bearing. The second bearing characteristic,

$$\Phi_{\mathrm{Th}} = \frac{Q_{\mathrm{TF}}}{P_{\mathrm{loss}}}, \tag{2.30}$$

calculates the ratio between the bearing's power loss and the heat carried into the top foil. It provides a measure of the thermal balance, indicating how much of the dissipated heat goes into the top foil. Φ_{TH} ranges between 0 and 1, with a value of 1 indicating that all the dissipated heat is transferred to the top foil. It is generally beneficial to aim for higher values of this characteristic because lower values indicate

that heat needs to be transferred over the rotor, which is more demanding than transferring heat over the static parts of the bearing system. Therefore, transferring heat over the top foil is preferred.
Due to misalignment in high spinning machinery, the stiffness of the bearing system is important to compensate tilt. The stiffness is also an important design feature for dynamic properties of the rotor bearing system. The stiffness characteristic Φ_{St} is introduced as

$$\Phi_{\mathrm{St}} = \frac{W}{\bar{v}_{\mathrm{RD}}}. \tag{2.31}$$

With W defined as the load capacity and $\bar{v}_{\mathrm{RD}}$ as its corresponding mean of the rotor disk's displacement. It is therefore a global bearing stiffness characteristic and does not take the gradual changes of the local stiffness into account. The order of magnitude for this characteristic is around $1\,\mathrm{N/\mu m}$.
The last characteristic, Φ_{Film}, is determined as the ratio of the minimum film height $min(h)$ to the averaged film height $\bar{h}$:

$$\Phi_{\mathrm{Film}} = \frac{min(h)}{\bar{h}}. \tag{2.32}$$

It describes the local load distribution within the bearing, with a value of 1 indicating even loading across the entire bearing area, which is practically unachievable due to the need for a converging gap to generate pressure. Smaller values imply that certain parts of the bearing experience higher loads than others, which could lead to wear if the local film height falls below the mixed lubrication limit H_{mixed}.

3. Validation Test Rigs and Measurement Tools

To successfully validate the simulation model of the thrust bearing, some preliminary considerations need to be made. The output quantities introduced in the sensitivity analysis (Sec. 2.4.2) form the basis for validating the bearing. The performance of the bearing, described by Φ_{Loss} in terms of load capacity and generated power loss, can only be measured during real operation with a rotating rotor. Therefore, a test rig must be set up to run at 120,000 rpm and apply thrust loads up to 100 N on the bearing. These speed and thrust load values correspond to the maximum values occurring in the real machine.
The thermal characteristic, Φ_{Th}, can also be determined in this test rig by measuring temperatures and corresponding power losses generated in the bearing. As Lehn [52] focused on the thermal resistance of the bump foils, it is important to investigate this aspect more closely. Measuring the thermal resistance requires determining the temperature gradient and power loss. Due to the influence of various parameters in a rotating test rig, a separate test rig dedicated to this purpose is presented in this chapter. It enables the measurement of thermal resistance of the foil package without other influencing effects.
The stiffness characteristic, Φ_{St}, can be straightforwardly determined using standard test beds designed for force-displacement characteristics, also without a spinning rotor.
Measuring the fourth characteristic, Φ_{Film}, directly is challenging. It requires measuring the local film height distribution in an operating bearing, which is a complex task. Alternatively, this question can be addressed indirectly by examining the wear pattern on the coating layer of the top foil. The wear pattern provides insights into the local load distribution within the bearing gap, which is indicative of the local film height. Therefore, this work addresses this bearing characteristic indirectly.
To address these questions, this chapter will present the measurement setups for validating an air foil thrust bearing. First, a new high-speed thrust bearing test rig will be introduced and described in detail. Special attention will be given to the measurement capabilities of non-contact temperature measurements, torque, and axial force measurements, as well as a special gimbal suspension for the base plate in order to provide measurements under aligned conditions. Their functionality will be demonstrated through established measurement setups and simulations. Finally, the test rig's measurability will be evaluated, and the resulting measurement uncertainty will be specified.
Secondly, a thermal resistance test rig will be presented for determining the bump foil's thermal resistance. The design and functionality of the test rig will be discussed, followed by the presentation of its measurement equipment and capabilities.
The subsequent section will focus on the test beds utilized for mechanical property measurements. It will be divided into subsections covering the measurement of mechanical friction coefficients and bump foil stiffness. The friction coefficients will be determined using a test setup in a tribometer where deformation is applied and the reaction force is measured. The bump foil stiffness will be measured using a press with a setup designed for measuring the spring characteristic, where deformation is applied and the reaction force is measured.
Finally, the equipment used for topography and wear measurements in this work will be presented.

3.1. High-Speed Thrust Bearing Test Rig

The high-speed thrust bearing test rig is designed to minimize interfering parameters (such as runner oscillations, soiling, thermal influences, friction in peripheral components, and misalignment) and facilitate precise measurements of the thrust bearing's performance. The basic setup of the test rig is displayed in a simplified sketch in Fig. 3.1. The test rig is divided into two parts so that the thrust bearing can very easily be examined and replaced. The first part—containing the drive and the pressure chamber

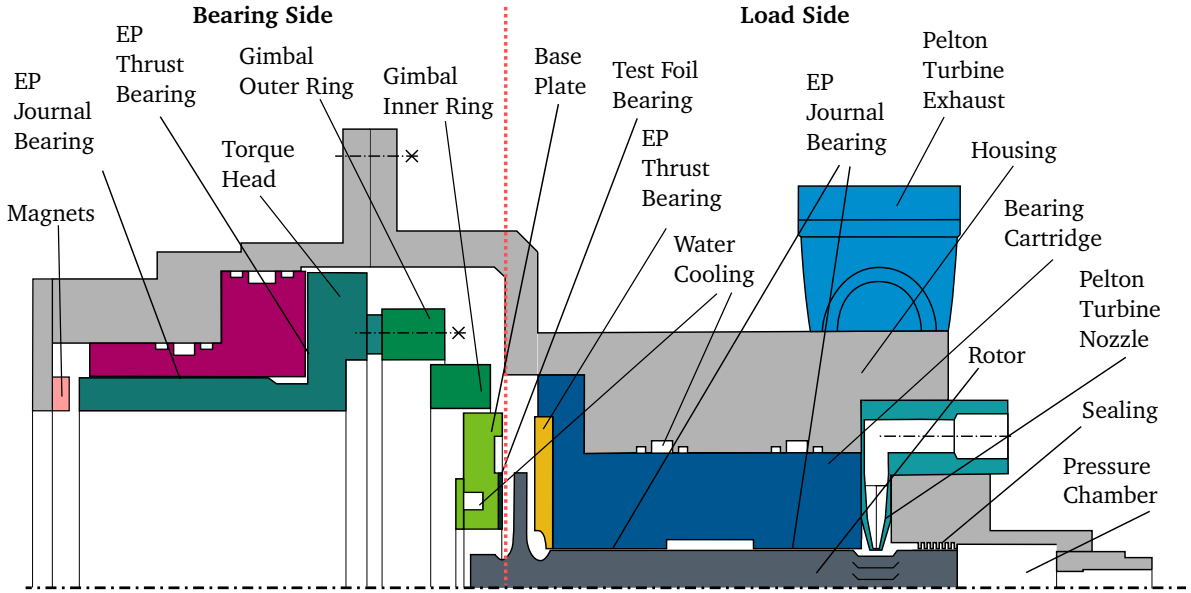

Figure 3.1.: Sketch and basic components of the thrust bearing test rig.

for applying the thrust load—is in the following called the *Load Side*; it can be run autonomously without the test thrust bearing. An image of the load side is displayed in Fig. 3.2 (right side). The second part of the test rig is called the *Bearing Side* and mainly contains the thrust bearing and the gimbal suspension of the base plate on the torque head, see Fig. 3.2 (left side). Both parts can be moved apart and together via a dovetail rail.

The centerpiece of the *Load Side* is the rotor. The rotor—consisting of the Pelton drive, the rotor shaft and the rotor disk—is a single part made of a grinded high-strength steel. This allows very low radial run-out and flatness tolerances of the rotor disk in order to obtain measurements with high-precision. This design, therefore, distinguishes itself from most rotor designs in the literature. The rotor shaft is mounted in two aerostatic, externally pressurized rigid air bearings (EP bearings), which have a supply pressure of 14 bar. As shown in Fig. 3.1, the journal bearing cartridge is cooled by two water cooling channels. Note that at the back side of the rotor disk, an additional aerostatic thrust bearing is used to support possible reverse thrust loads, which may occur if the test rig is used in an inclined position. Hence, the rotor can also be run without the test foil bearing. The two EP bearings for supporting the rotor shaft have small radial clearances (below $10\,\mu\mathrm{m}$) so that the rotor can run very smoothly with small radial oscillations below $1\,\mu\mathrm{m}$ in amplitude. As a consequence, rotor misalignment effects are kept very small. These benefits, along with the ability to support the rotor even at high speeds, are the main reasons EP journal bearings are preferred for this test rig over other bearing concepts in the literature, such as roller bearings or air foil journal bearings. Another important point of the rotor is the drive. Here, an air drive via a Pelton turbine is used to allow high speeds of up to 120 krpm. The shovels of the turbine are milled into the rotor and the air is supplied by six Pelton nozzles. In order to apply an axial force on the rotor, a pressure chamber at the front side of the rotor is used. The chamber is sealed by a labyrinth seal.

The *Bearing Side* of the test rig contains the foil thrust bearing to be investigated as well as several measurement capabilities. The thrust bearing is mounted on a water-cooled base plate. As reported in the literature, misalignment between the rotor disk and the base plate often leads to inaccurate measurements. Therefore, in this design, the base plate is mounted on a special gimbal suspension, which is described in more detail below. The gimbal suspension is connected with the torque head, which is

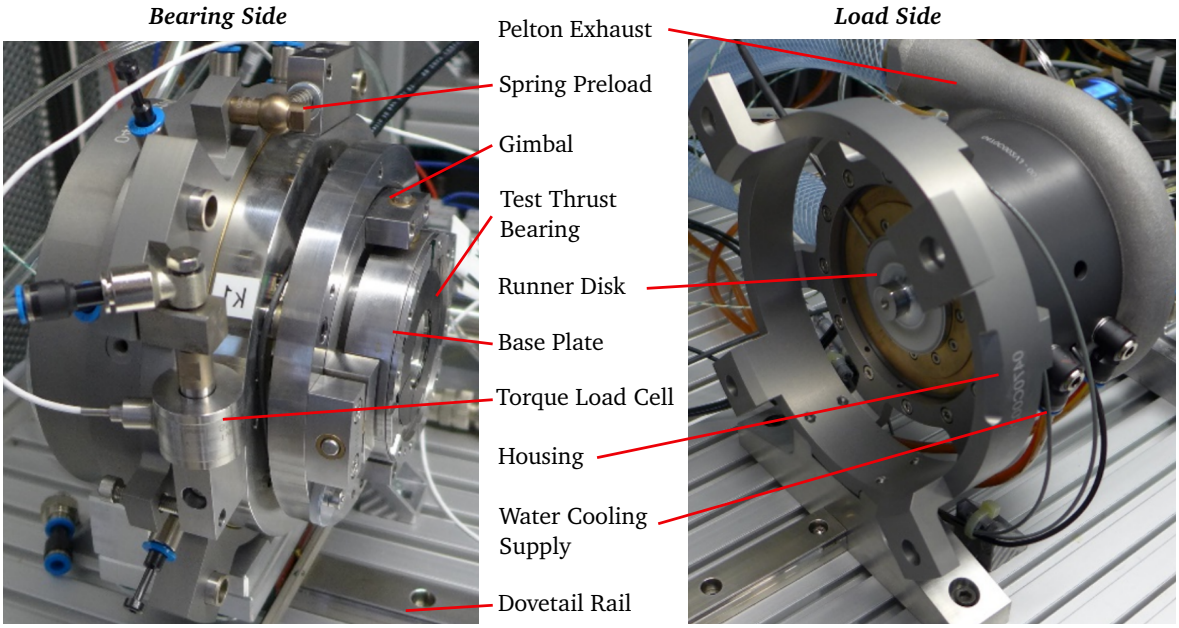

Figure 3.2.: High-speed test rig image.

used to measure the friction torque of the thrust bearing during operation. The torque head is mounted in the housing with the help of two EP bearings; an axial EP bearing and a radial EP bearing. It should be mentioned that the aerostatic thrust bearing is preloaded by magnets at the back side of the test rig. This concept is selected over a base plate support with ball bearings, a design frequently found in the literature. This choice is driven by the fact that an EP-supported base plate can be moved relative to the torque head with nearly zero friction, enabling precise torque measurements.

3.1.1. Measurement and Drive Equipment

In this section, the measurement techniques and the positioning of different sensors are described, as illustrated in the exploded drawing shown in Fig. 3.3.
A pressure chamber located at the right front face of the rotor applies the thrust load directly to the test thrust bearing. The pressure is regulated using an AIRCOM PQ2EE-04 pressure regulator, offering a control range from 0 to 4 bar. To achieve this pressure, the volume flow booster AIRCOM R450 supplies the required air, which is monitored and controlled by the pressure sensor AIRCOM DAV-04H. The pressure can be precisely adjusted within the range of 0 to 4 bar with an accuracy of $0.1\,\%$ at 4 bar. A pressure of 4 bar results in a thrust load of 100 N. It should be noted that pressure adjustments may not result in exactly the same pressure in the chamber due to losses in pipes and valves. However, a specific configured pressure will consistently yield the same pressure in the chamber with a consistent offset.
The rotational speed of the rotor is determined using an optical fiber sensor system consisting of an amplifier (KEYENCE FS-N11CP) and fiber optics (KEYENCE FU-87K). This system utilizes a trigger measurement that points at a mark located at the middle of the rotor. The rotational speed is adjusted by a software PI-control loop that regulates the volume flow of the Pelton nozzle based on the measured spinning speed. The volume flow of the Pelton turbine is controlled by an electric proportional valve (FESTO MPYE). The Pelton drive system is designed to provide up to 3 kW of engine power at a spinning speed of 120 krpm.
For monitoring the dynamics of the rotor in the radial direction, two eddy current distance sensors

High Speed Test Rig - Exterior

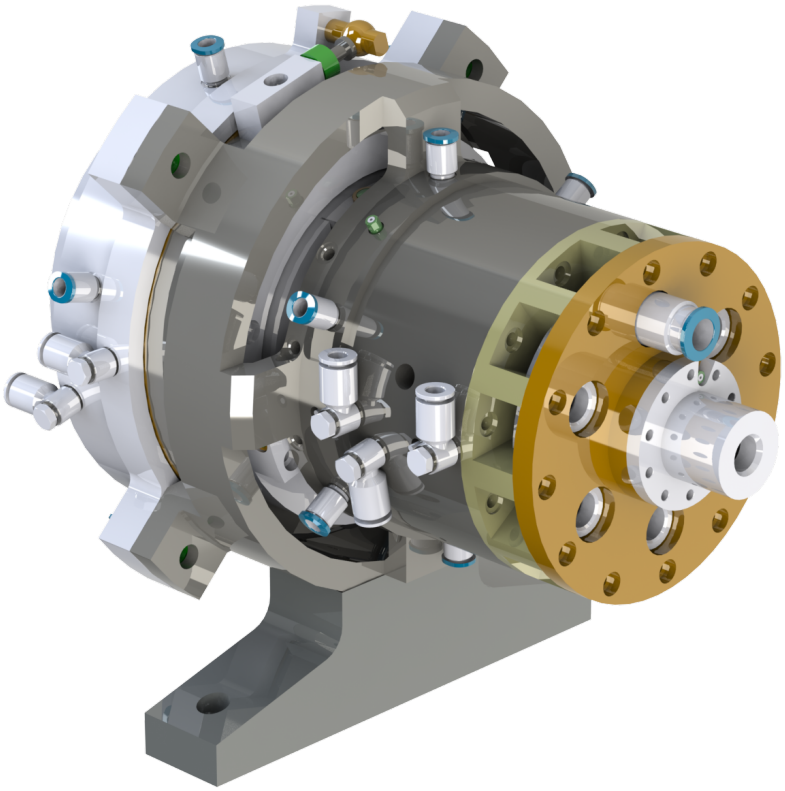

High Speed Test Rig - Explosion

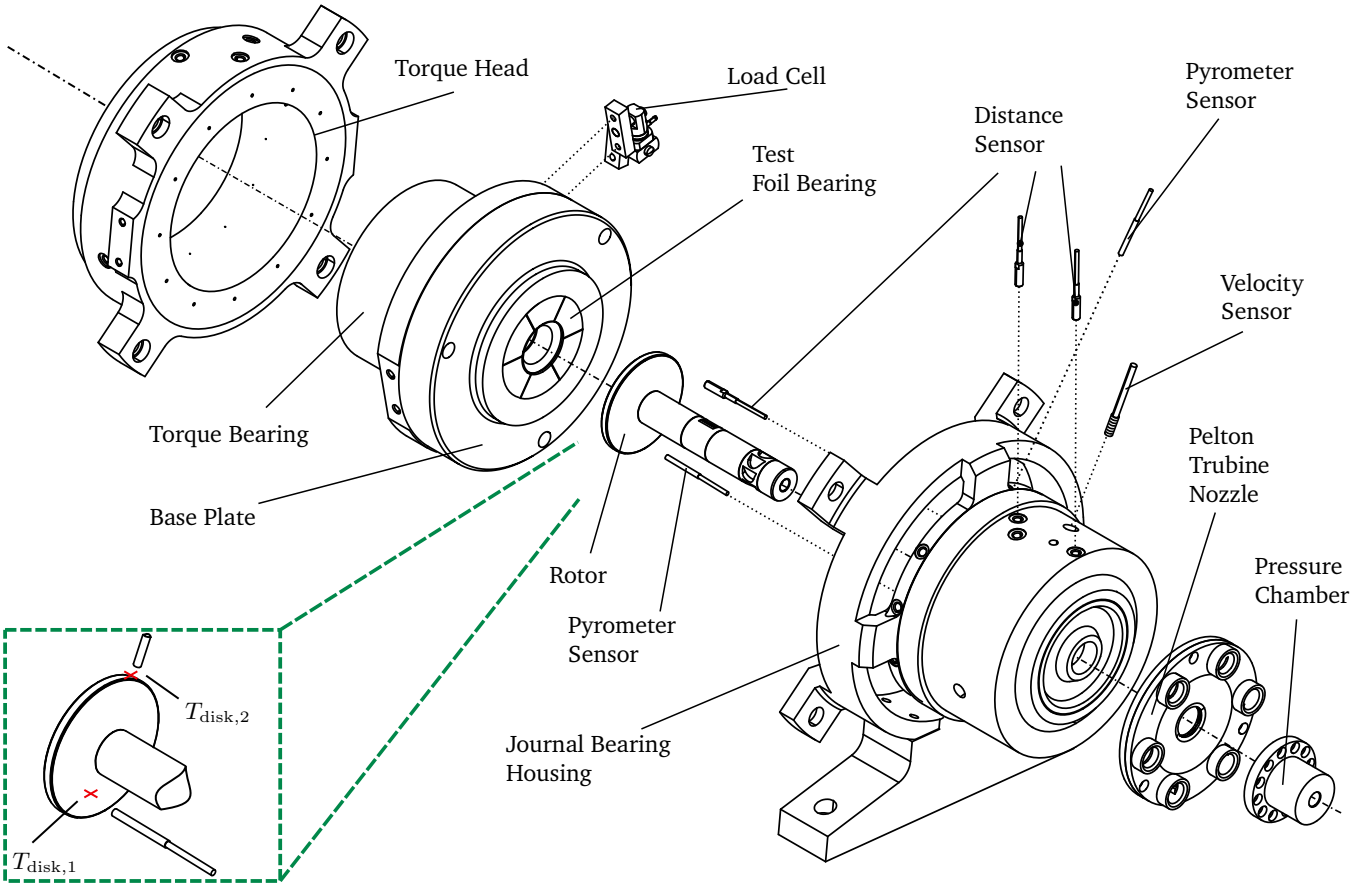

Figure 3.3.: Rendered image of the high-speed test rig and detailed explosion sketch.

(MICRO EPSILON ES04) are employed, strategically positioned near the aerostatic EP journal bearings. Additionally, another eddy current distance sensor (MICRO EPSILON ES08) is placed at the back side of the rotor disk at a diameter of 36 mm to measure the axial displacement of the rotor. These three distance sensors are connected via MICRO EPSILON DT3300 controllers.
To measure the rotor disk temperature without contact, two ADVANCED ENERGY IMPAC IGA 320 pyrometer sensors are used. The first temperature sensor is located at the back side of the rotor disk at a radius of 18.5 mm, providing the measured temperature $T_{\text{disk},1}$. The second pyrometer sensor focuses on the outer perimeter of the rotor disk, offering the measured temperature $T_{\text{disk},2}$, as depicted in Fig. 3.3. Additionally, in the housing close to the journal bearings and in the base plate, ELECTRONIC SENSO DTE 02 type K thermocouples are used to determine the surrounding temperature.
To determine the power loss of the thrust bearing, the friction torque generated in the thrust bearing is measured. The torque head, which transfers the forces and torques acting on the thrust bearing into the housing, is mounted almost frictionless in EP bearings (one radial and one axial EP bearing). The friction torque generated in the test thrust bearing is transferred into the housing by a torque arm. Between the torque arm and the housing, a load cell (BURSTER TYPE 8411) is inserted; the measured force allows the calculation of the bearing torque of the test bearing.
The following sections describe the main features of the test rig in more detail.

Disk Temperature

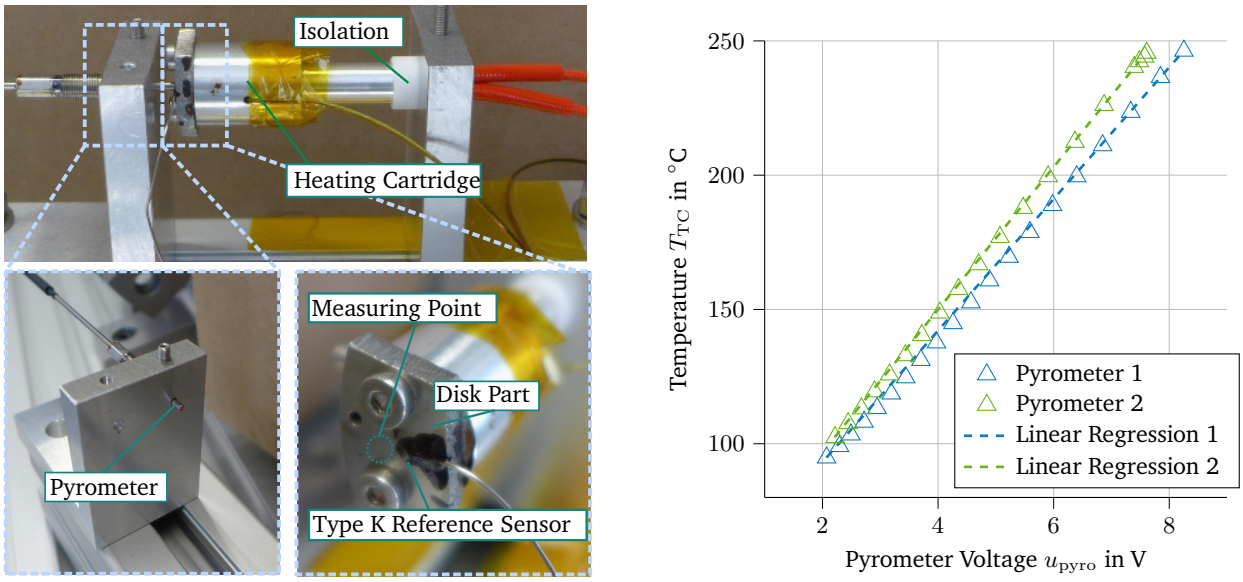

(a) Pyrometer sensor calibration setup.

(b) Pyrometer sensor calibration measurements.

Figure 3.4.: Calibration setup and measurements for the non-contact pyrometer disk temperature measurements.

Two non-contact pyrometers are used to measure the rotor disk temperature at two positions ($T_{\text{disk},1}$ and $T_{\text{disk},2}$, see Fig. 3.3). The controller of the temperature sensor emits infrared light through a 1 mm thick fiber optics to the desired measurement position in order to enable precise local temperature measurements. The fiber optics are glued into a 3 mm metal tube in order to protect the sensor from disturbing environmental influences (ambient light). Due to the metal tube and due to the distance of the sensors to the measurement object, the sensors need to be calibrated.
The calibration setup for the temperature sensors is depicted in Fig. 3.4a. It consists of an electric heater

in a heating cartridge, a square-shaped metal part (of rotor disk material) equipped with a Type K reference temperature sensor T_{TC} close to the measurement point and the pyrometer, which is placed in a specified distance from the measurement point. During the calibration measurements, the heater is warmed up until the reference temperature sensor shows a temperature of $250\,^{\circ}\mathrm{C}$. The heater is then switched off and the temperature curve detected by the reference sensor is recorded. Simultaneously, the electrical current provided by the pyrometer is measured and recorded. The current is then converted into a voltage signal ($u_{\mathrm{pyro},1,2}$). The result of the calibration measurements for both pyrometers are shown in Fig. 3.4b. The output signals of both sensors exhibit a linear behavior with respect to the reference temperature. Note that the rotor disk material (steel) has a rather low emissivity. Therefore, and because of the small sensor dimensions, there exists a limit temperature that can be measured with the sensors applied here. Temperatures below the limit temperature cannot be detected with the pyrometers used here. As can be seen in Fig. 3.4b, the limit temperature for the axial temperature sensor ($T_{\mathrm{disk},1}$) is $94\,^{\circ}\mathrm{C}$; for the radial temperature sensor ($T_{\mathrm{disk},2}$) it is $102\,^{\circ}\mathrm{C}$. The slopes of the two curves are slightly different, which can be traced back to the gluing process of the fiber optics into the metal tube. Carrying out a linear regression, the subsequent relationships are obtained

$$T_{\mathrm{disk},1} = 24.88\,\mathrm{K/V} \cdot u_{\mathrm{pyro},1} + 40.12\,\mathrm{K} \text{ and} \tag{3.1}$$

$$T_{\mathrm{disk},2} = 26.71\,\mathrm{K/V} \cdot u_{\mathrm{pyro},2} + 41.89\,\mathrm{K}, \tag{3.2}$$

where $u_{\mathrm{pyro},1}$ and $u_{\mathrm{pyro},2}$ denote measured output voltages of the pyrometers. The accuracy of the measurements is approximately $\pm 1\,\mathrm{K}$ with a repeatability error of $\pm\,1\,\%$.
Concluding comment: the calibration of the pyrometers has been carried out with a stationary target. The pyrometers are, however, used to measure the temperature of the rotating rotor disk. Therefore, the question may arise, how rotation of the thrust disk may affect the reading of the sensor. According to the manufacturer, rotation of the thrust disk will only affect the reading of the sensor, if the distance between the pyrometer and the target is larger than approx. 500 mm. In our test rig, the distance between the rotor disk and the pyrometers is, however, smaller than 5 mm. Hence, the influence of disk rotation on the measured temperatures may be considered of minor importance.

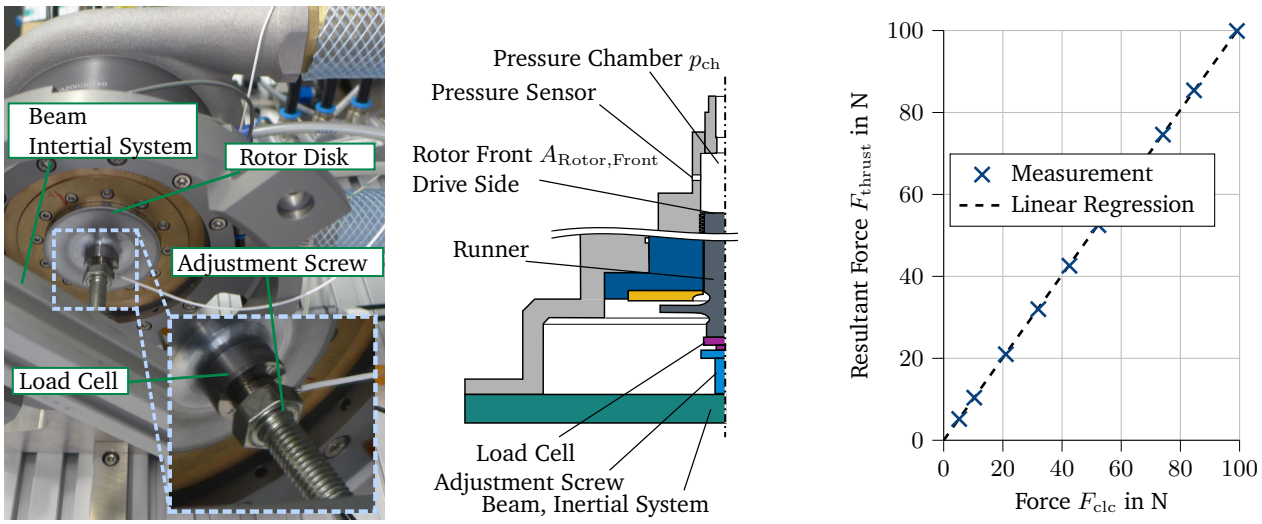

(a) Calibration measurement pressure chamber setup.

(b) Pressure chamber calibration measurement.

Figure 3.5.: Pressure chamber functionality and calibration test.

Pressure Chamber

As mentioned above, the axial load on the rotor is applied by a pressure chamber at the front face of the rotor. The load system is checked for functionality and calibrated with the help of a load cell (BURSTER 8416). The setup for this functionality test is shown in Fig. 3.5a. The load applied on the rotor via the pressure chamber (at the drive side of the rotor) is supported at the left front face of the rotor (disk side of the rotor) by a screw (inertial system). Between the screw and the front face of the rotor, a calibration load cell is inserted. Hence, the axial force generated in the pressure chamber is transferred via the load cell and the screw into the inertial system (note that the beam segment in Fig. 3.5a is fixed in the inertial system). By increasing the pressure p_{ch} in the pressure chamber, the corresponding reaction force in the load cell can be measured and compared with the resulting measured pressure force, which is given by

$$F_{\mathrm{thrust}} = p_{\mathrm{ch}} \cdot A_{\mathrm{Rotor,Front}}, \tag{3.3}$$

where $A_{\mathrm{Rotor,Front}}$ is the area of the rotor front face. The result of this calibration measurement is depicted in Fig. 3.5b, where the measured force F_{thrust} in the pressure chamber is plotted as a function of the force F_{clc} detected in the calibrated load cell. As can be seen, an almost linear relationship is identified in the force range from 1 to 100 N with a maximum error of ± 0.3 N (the repeatability error is $\pm 0.1\,\%$). These calibration measurements can only be performed with a non-spinning rotor. To estimate the influence of the spinning rotor, CFD analyses are obtained in ANSYS CFX. The simulation setup, as illustrated in Fig. 3.6, consists mainly of a chamber with a height of 25 mm and a diameter of 20 mm. The geometry of the chamber is simplified, and for this analysis, there is no additional hole for the pressure sensor, only a simplified inlet (p_{applied}) is considered. At the bottom of the chamber, the rotor is spinning, and moving wall boundary conditions are applied. The touchless sealing is also simplified, represented by a small gap with a height of $50\,\mu\mathrm{m}$. One side of this channel has a fixed wall boundary condition, representing the housing, while the other side, which is the moving rotor face, has a moving wall boundary condition with $v_\varphi = \omega\, r$ as the velocity component in the circumferential direction. The length of this channel is set to 20 mm according to the sealing in the high-speed test rig. At the end of the channel, outlet boundary conditions with atmospheric pressure p_0 of 1 bar are applied.

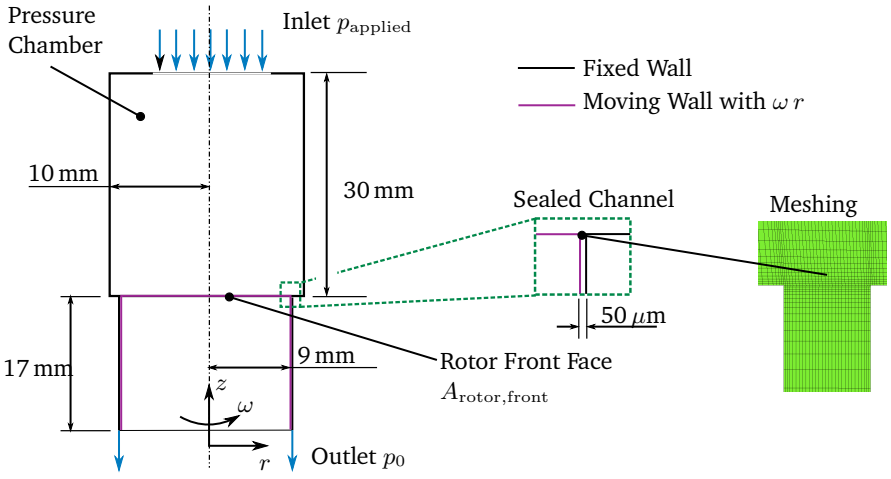

Figure 3.6.: CFD simulation setup for the high-speed test rig's pressure chamber.

The results of the simulations for three applied pressures and two spinning speeds are listed in Tab. 3.1.

Table 3.1.: CFD results for high-speed test rig pressure chamber with a spinning rotor.

Pressure p_{applied}	Force rotor face $F_{\text{rotor, front}}$	Inlet Force $F_{\text{rotor, inlet}}$	Drag Force Rotor $F_{\text{rotor, drag}}$
1 bar 2000 Hz	25.43 N	24.43 N	0.18 N
2 bar 2000 Hz	50.87 N	50.89 N	0.27 N
4 bar 2000 Hz	101.88 N	101.78 N	0.42 N
4 bar 1000 Hz	101.92 N	101.78 N	0.41 N

The reaction force on the rotor is evaluated for a given inlet pressure using the following formula:

$$F_{\text{rotor, front}} = p_{\text{rotor, front}} \cdot A_{\text{rotor, front}}, \tag{3.4}$$

where $A_{\text{rotor, front, drive}}$ represents the area of the rotor's front face in contact with the chamber. This force can be compared with a virtual force generated by the applied inlet pressure, defined as:

$$F_{\text{rotor, inlet}} = p_{\text{applied}} \cdot A_{\text{rotor, front}}. \tag{3.5}$$

The comparison indicates that these two forces are almost equal for the investigated operational states. Furthermore, the drag force $F_{\text{rotor,drag}}$ on the rotor inside the channel due to Poiseuille flow is evaluated. The drag force on the rotor is weakly dependent on the spinning speed but more influenced by the pressure in the chamber. In general, its influence is smaller than 1%. Therefore, it can be concluded that the pressure chamber is capable of building up pressure on the rotor's end face and applying a reaction force towards the thrust bearing both at downtime and with a spinning rotor, without significant errors and losses.

Torque Measurements

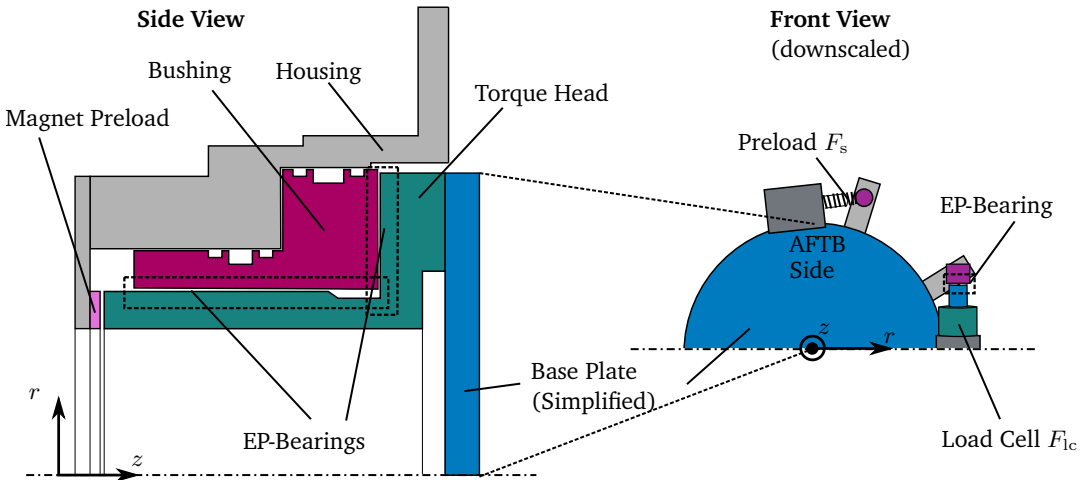

Figure 3.7.: High-speed test rig torque measurement system.

The measurement system for torque measurements is displayed in Fig. 3.7. On the left side, a sectional side view is shown. On the right side, a front view is shown to get a better understanding of the torque measurement system. The test bearing is assembled on a frictionless mounted bushing. This is realized by an axial and radial externally pressurized (EP) aerostatic bearing. The axial bearing is preloaded in

negative z direction by magnets that hold the torque head in place. The applied torque from the test bearing is supported by a load cell which pushes against a fixed arm. Between the load cell and this arm, another EP-bearing guarantees that no friction forces are transferred into the load cell due to axial movements of the measurement system to avoid disturbance on the measured force. The load cell is preloaded by a spring with around $F_\mathrm{s} = 1\,\mathrm{N}$ to hold the torque bearing in place.

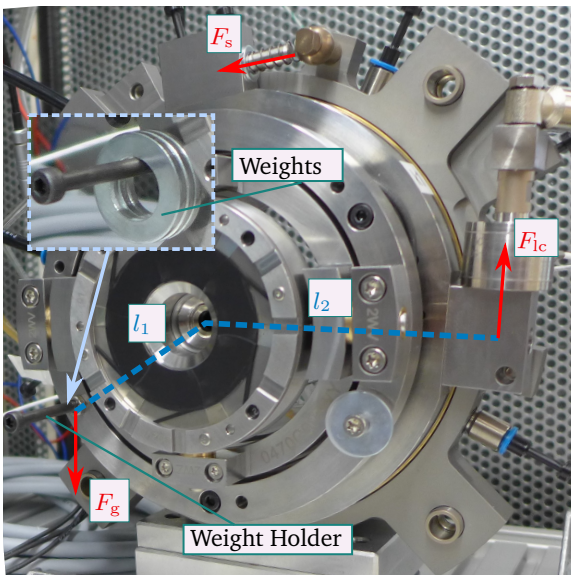

(a) High-speed test rig torque measurement system calibration setup. With $l_1 = 52.3\,\mathrm{mm}$ and $l_2 = 87\,\mathrm{mm}$.

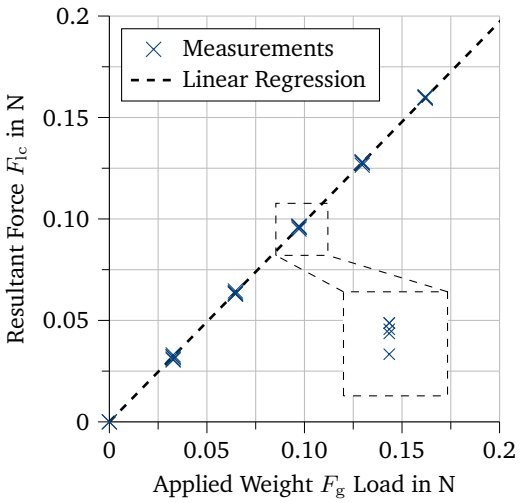

(b) High-speed test rig torque measurement system calibration measurements.

Figure 3.8.: Torque system functionality and calibration setup and measurements.

To calibrate this load cell, an external force is applied at the base plate with the help of ring-shaped weights, which are connected with the base plate using a screw fixed at the base plate, see Fig. 3.8a. The magnitude of the weights (gravitational force F_g) and the corresponding lever arm define the applied torque, which presents the friction torque. For the calibration of the load cell, different weights are fixed at the screw. The result of the calibration tests is depicted in Fig. 3.8b, where the measured force F_lc in the load cell is displayed as a function of the applied weight load F_g. The load cell is preloaded with a spring force of $F_\mathrm{s} 1\,\mathrm{N}$. In addition to the preload generated by the spring, the connected wires and cooling channels as well as the tilting of the gimbal may add a further preload to the measured force F_lc. All preload effects are zeroed before each calibration measurement. The calibration tests are repeated five times. As can be seen in Fig. 3.8b, the relationship between the F_lc and F_g is almost linear. Hence, the power loss can be simply determined by multiplying the measured force in the load cell by the lever arm l_2 and the angular frequency ω of the rotor, i.e.,

$$P_\mathrm{loss} = F_\mathrm{lc} \cdot l_2 \cdot \omega. \tag{3.6}$$

The calibration measurements show a maximum error of $4.5 \cdot 10^{-3}\,\mathrm{N}$, which is subsequently converted into a power loss value using Eq. 3.6. This conversion results in a range of $\pm 5\,\mathrm{W}$ at 120 krpm (the repeatability error is $\pm 3\,\%$).

An important aspect, which has to be considered in connection with the measurement of the friction torque at the base plate, is the air flow outside the bearing gap induced by the spinning rotor. Due to the fact that the rotor is spinning with high angular velocities, the air at the rotating surfaces is set into

motion, also in regions with comparatively large air gaps. Of special importance is the rotation-induced air flow in the regions of the base plate outside the bearing foils (i.e., outside the bearing gap). Note that F_{lc} measures the resultant friction torque due to shear stresses acting at the complete base plate, i.e., not only the torque resulting from the shear stresses in the bearing gap. Hence, the resultant force F_{lc} can be decomposed into two parts according to

$$F_{\mathrm{lc}} = F_{\mathrm{shear,bearing}} + F_{\mathrm{shear,periphery}}. \tag{3.7}$$

$F_{\mathrm{shear,bearing}}$ denotes the force due to the friction forces in the bearing gap; $F_{\mathrm{shear,periphery}}$ represents the force due to friction forces acting at the base plate outside the bearing gap. Measuring only $F_{\mathrm{shear,periphery}}$ without a bearing in the test rig is challenging because the rotor lacks a defined position without bearing support from both sides. Additionally, even without a bearing, shear losses would occur between the rotating rotor and the empty bearing area on the base plate.
To quantify the amount of those losses, a CFD analysis is therefore performed in ANSYS CFX. The simulation has two objectives. First, the side losses of the test rig rotor are to be quantified, and second, the simulation serves for the subsequent determination of heat transfer coefficients for the AFTB-simulation model. The latter aspect is discussed in more detail in Sec. 4.1.3. In the following, the simulation setup of the CFD analysis is shown and the evaluation focuses on the peripheral side losses. The total friction

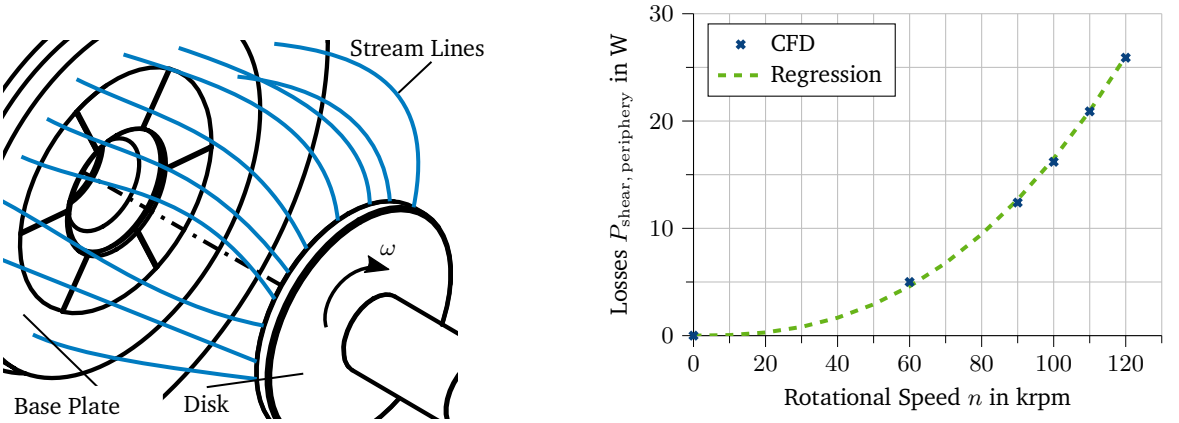

(a) High-speed test rig rotor disk sketch of side losses due to peripheral fluid set in motion.

(b) Simulated peripheral losses for the high-speed test rigs rotor disk.

Figure 3.9.: Peripheral side losses of the rotor disk on the bearing's base plate.

torque results from the shear stresses acting in the fluid film gap (region II, see Fig. 3.10a) and from the shear stresses acting at the remaining part of the base plate. The remaining part can be subdivided into

- the region below the air gap (region I), i.e. the region between the rotor nose and the inner radial surface of the base plate and
- the region above the air gap (region III).

To characterize and determine the friction losses of the thrust bearing, the losses resulting from the fluid gap are of main interest, since the other losses generated in region I and region III usually depend on the current design of the rotor. Hence, the question arises as to how large the proportion of the individual friction losses to the total friction loss is. Since it is difficult to measure the friction losses separately in the three regions, a CFD analysis is carried out in order to answer this question.
The shear forces increase at least quadratically with respect to the fluid velocity. In turbulent boundary

layers, for instance, usually higher-order dependencies exist (see e.g. [65], where different windage power loss models are compared). The fluid velocity is, however, increasing linearly with respect to the radial distance from the rotor axes. The radius of the inner radial surface of the base plate at the rotor nose is 8 mm, whereas the outer radius of the rotor disk is 27 mm. It can therefore be assumed that the resulting shear forces and friction losses below the air gap at the rotor nose in region I are an order of magnitude smaller than the losses in region III above the air gap. The shear forces acting in region III can generally not be neglected. Note that the air in region III is mainly set into motion by the outer radial surface of the rotor disk with velocities up to $\omega \cdot r = 2\,\pi \cdot 2000\,\mathrm{Hz} \cdot 27 \cdot 10^{-3}\,\mathrm{m} \approx 340\,\mathrm{m/s}$. These high velocities result in drag coefficients, which are approximately one order of magnitude larger than the corresponding drag coefficients resulting from the air flow in region I.
Hence, the main task is to determine the shear forces and corresponding friction torque on the base plate generated in region III, which is here accomplished with the help of a detailed CFD model of region III. With the total friction torque obtained by the measurement and with the help of the simulated friction torque in region III resulting from the CFD analysis, it is then possible to validate the multi-physical model with respect to the predicted friction losses of the bearing. Therefore, the simulated friction torque in region III is subtracted from the measured total friction torque. This difference can then directly be compared with the simulated friction torque in the air gap resulting from the multi-physical model.
To determine the friction forces in region III, a detailed CFD model is used (ANSYS CFX). Therefore, the air flow in the area marked in red is considered, see Fig. 3.10a. Since rotational symmetry can be assumed, a 2D-approach is sufficient. The mesh is illustrated in Fig. 3.10b. It should be mentioned that cell heights of $0.5\,\mu\mathrm{m}$ are used at all boundaries to achieve values for y+ below 1 (y+ represents the dimensionless wall coordinate, see [78]). The cell growth rate has been set to a maximum value of 1.2. Air is modeled as a compressible fluid with a SST turbulence approach. Values for y+ below 1 in combination with a SST turbulence may provide rather accurate simulation results near the fixed walls [58].
The boundary conditions are illustrated in Fig. 3.10c. At the interface of the rotor disk, the fluid velocity is assumed to be known, namely the corresponding velocity of the rotor disk (no-slip moving wall boundary condition), i.e., the velocity in circumferential direction is prescribed by $v_\varphi = \omega \cdot r$. The outer boundary is an opening, which is modeled as an entrainment boundary condition under the assumption of ambient pressure ($p_0 = 1\,\mathrm{bar}$). At the back side of the rotor disk at the inner radius there is also an opening. Here, ambient pressure can be assumed, since there are ventilation holes for the EP bearing, which are not shown in the sketch. This second opening is represented by an entrainment boundary condition. All other boundaries are fixed walls, where zero slip boundary conditions are applied. Fig. 3.10c shows the absolute value $U = \sqrt{u^2 + v^2 + w^2}$ of the fluid velocity, calculated for a rotor speed of $n = 2000\,\mathrm{Hz}$. As can be seen, the fluid is set into motion by the rotor disk and tossed into the regions at the base plate with velocities larger than 100 m/s. These high fluid velocities are forced to become zero at the base plate due to the no-slip boundary condition so that large shear stresses are produced. With the shear stresses acting at the base plate in region III, the peripherical losses $P_{\mathrm{shear,periphery}}$ can be calculated.
Fig. 3.10d depicts the absolute value of the velocity gradient $\nabla \vec{U}$. As can be seen, rather steep velocity gradients exist in region III, which produce an appreciable friction torque at the base plate.
The resulting shear losses that are evaluated at all fixed walls belonging to the bearing's base plate are shown in Fig. 3.9b on the vertical axis as a function of the spinning speed n of the disk on the horizontal axis. At 120 krpm they amount to 26 W and are therefore significant for further evaluation of the measured power losses of the test rig. A regression can be placed through the evaluated points with a dependency on the spinning speed of $c_\mathrm{d}\,\omega^{2.8}$, which is reasonable compared to literature results on windage power losses. Raymond et. al. compared several windage power loss empirical models, presented by White et. al. [89], and all had exponents between 2.5 and 3 of the spinning speed ω [65].

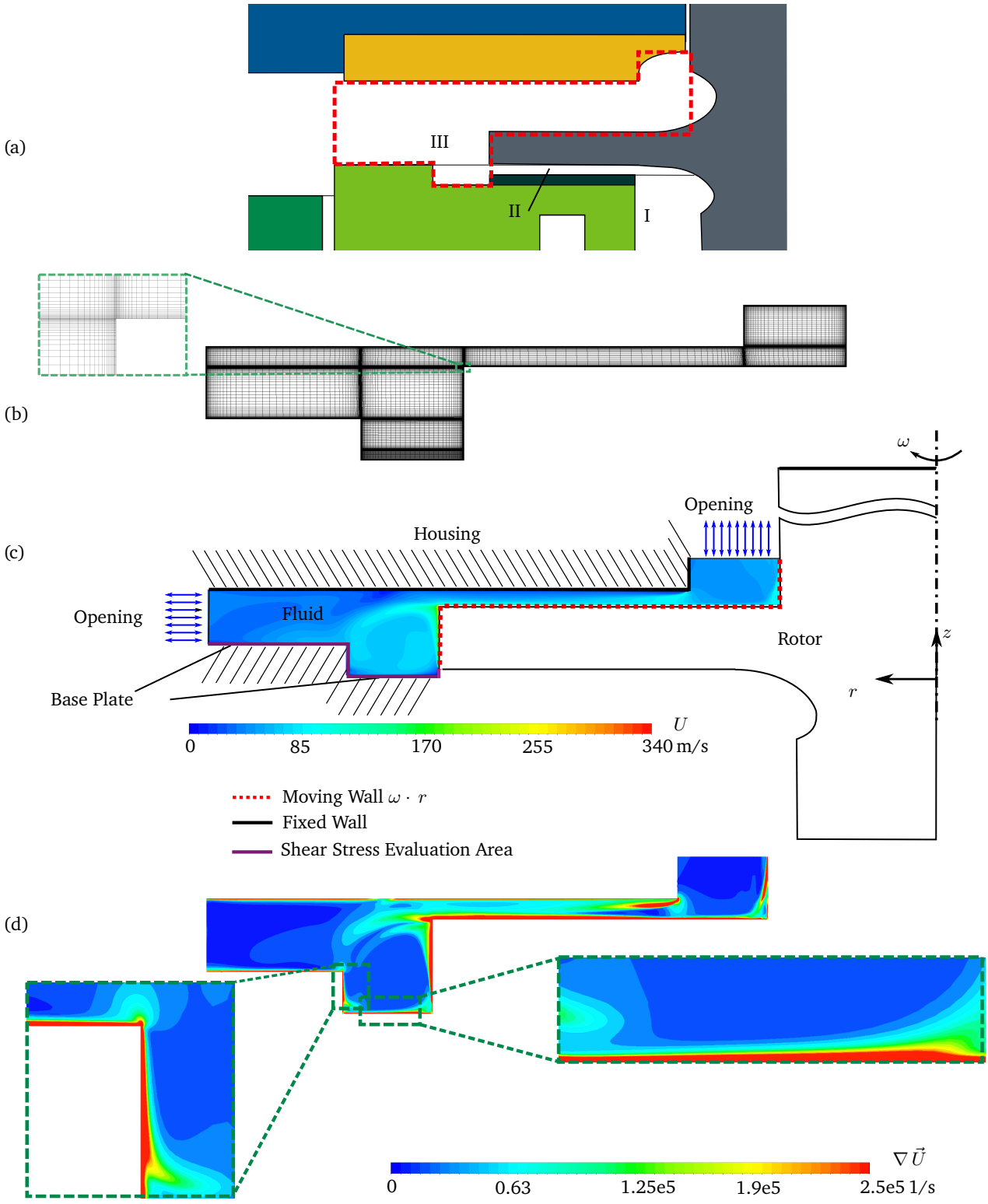

Figure 3.10.: (a) Sketch of the simulation domain; (b) mesh for the CFD analysis; (c) boundary conditions and CFD configuration as well as simulated fluid velocity $U = \sqrt{u^2 + v^2 + w^2}$ for $n = 2000$ Hz; (d) absolute value of the velocity gradient $\nabla \vec{U}$ for $n = 2000$ Hz.

Vrnacik showed similar results in a NASA research paper with a correlation of $P \sim c_\mathrm{d}\,\omega^3$ and $c_d \sim \frac{1}{\sqrt{\omega}}$, and hence a similar exponent [41]. The simulated c_d-value is $9 \cdot 10^{-11}$. Therefore, the shear losses at the periphery can be addressed by

$$P_{\mathrm{shear,\,periphery}} \approx 9 \cdot 10^{-11}\,\omega^{2.8}. \tag{3.8}$$

Combining the measured resultant force in the load cell F_lc with the rotational speed n in order to get the resulting measured power loss with the shear losses of the periphery yields

$$P_\mathrm{Loss} = F_\mathrm{lc}\,l_2\,\omega - P_{\mathrm{shear,\,periphery}}, \qquad \text{with } \omega = 2\,\pi\,n. \tag{3.9}$$

Pelton System and Rotational Speed

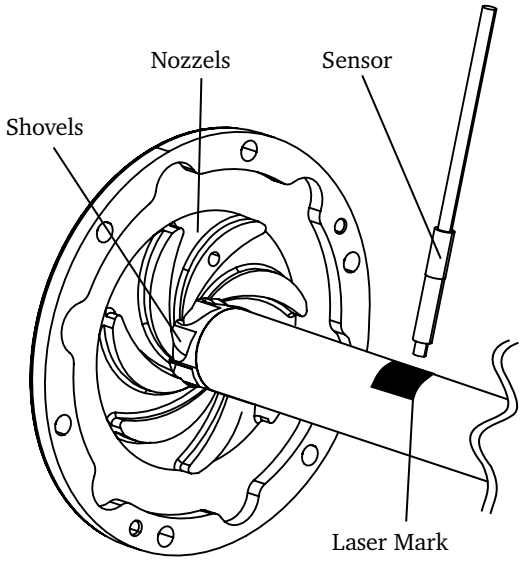

Figure 3.11.: High-speed test rig control loop for rotational speed.

The adjustment of the rotational speed of the high-speed test rig is achieved through a software PI-control loop that regulates the Pelton nozzle volume flow based on the measured spinning speed. The system is illustrated in Fig. 3.11, where six nozzles direct air jets at the rotor shovels, propelling the rotor. The Pelton system is designed to deliver up to 3 kW of engine power at a spinning speed of 120 krpm, operating with a supply pressure of 5 bar and a total nozzle cross-section of $50\,\mathrm{mm}^2$, resulting in a mass flow rate of approximately $m_\mathrm{Pelton} = 60\,\mathrm{g/s}$.
The controllability of the spinning speed is quite sensitive due to the almost continuously adjustable opening position of the valve. Consequently, the accuracy achieved is below 100 rpm, which corresponds to about $0.1\,\%$ of the spinning speed at 120 krpm. To verify this level of accuracy, the velocity signal derived from the laser marks to the main frequency oscillation of the rotating rotor, specifically the unbalance-excited oscillation at the first order of rotational frequency, as recorded by the distance sensors in the two journal bearings are compared. Notably, the measured rotational speed determined via the laser mark trigger measurement perfectly correlates with the unbalance-excited oscillation. Therefore, the laser mark trigger measurement is well-suited for accurately quantifying the rotor's rotational speed n.

Gimbal Suspension

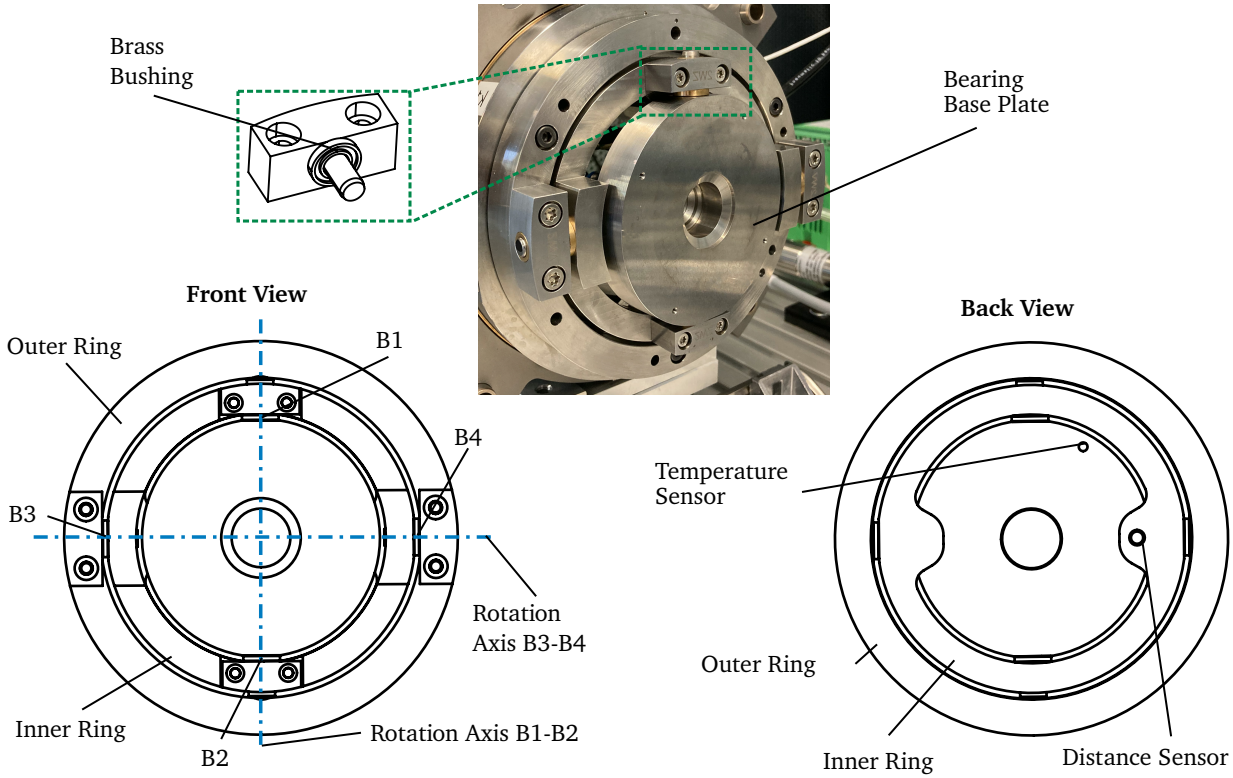

Figure 3.12.: Test bearing gimbal suspension in the high speed test rig.

The gimbal suspension is a critical feature of the high-speed test rig, designed to enable the bearing to align itself with the rotor disk or apply defined tilt. In an actual turbomachine, the bearing is typically tilted towards the rotor disk due to tolerances, and the amount of misalignment is often unknown. To validate a one-pad simulation model, the rotor disk and the bearing must be aligned, as only tilt-free conditions can be simulated. On the other hand, to validate a full bearing model with tilt conditions, the amount of tilt must be known.

The concept behind the gimbal suspension is that it aligns itself as the axial force increases, ensuring that the axial bearing remains free of misalignment at higher loads. The cardanic gimbal suspension of the base plate, where the foils of the thrust bearing are mounted, is displayed in Fig. 3.12. The upper part of the figure shows a photo of the gimbal in the test rig. Below the photo, the front view is depicted on the left side. On the right side, the back view of the gimbal suspension is presented. The gimbal consists of two rings: the inner ring, which is connected with the base plate of the thrust bearing and the outer ring, which is rigidly fixed to the torque head. At the top and bottom of the inner ring, two brass bushings (B1 and B2) are rigidly fixed. The pins of the two bushings are connected with the base plate. Hence, the base plate can rotate around the vertical B1-B2 axis relative to the inner gimbal ring. Also at the left and right side of the outer ring, two brass bushings (B3 and B4) are rigidly fixed. The pins of these two bushings are connected with the inner ring so that the inner ring may rotate around the horizontal B3-B4 axis relative to the outer ring. Altogether, the base plate has two rotational degrees of freedom with respect to the torque head. Hence, the base plate will always be aligned with the rotor disk during the operation, even if the rotor and torque head are misaligned with respect to the space-fixed system. Note that a distance sensor is used to measure the tilting of the base plate with respect to the inner ring,

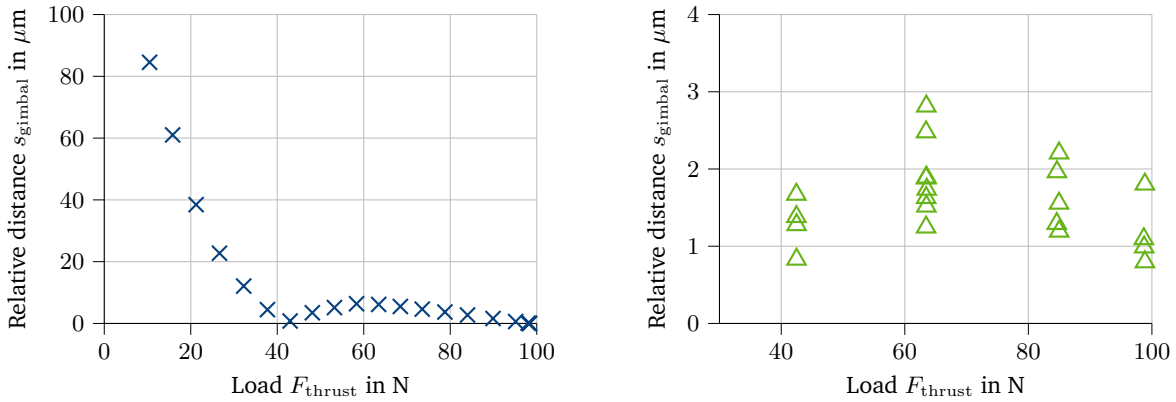

Figure 3.13.: Gimbal movement of rotation axis B1-B2 - functionality measurement.

see Fig. 3.12.
Test measurements were conducted to verify the functionality of this relative movement concerning the applied load on the base plate, assembled in the high-speed test rig (Fig. 3.13). At 100 N, the relative distance s_{gimbal} of the sensor with respect to the base plate is set to $0\,\mu\text{m}$. It is evident that for loads below 40 N, the relative distance increases with decreasing load, reaching over $80\,\mu\text{m}$ at 10 N and even higher tilts for lower loads. However, above 30 N, the changes are below $6\,\mu\text{m}$. Repeated measurements of six test runs conducted within the load range of 40 to 100 N exhibit a consistent behavior, which is depicted in Fig. 3.13 on the right-hand side. The measured relative distance, and consequently, the gimbal's displacement under load, remains below $3\,\mu\text{m}$. As a result, the bearing performance (load capacity, power loss, temperatures) can be measured with high precision, with only small misalignment between the thrust bearing and the rotor disk for thrust forces exceeding 30 N. It should be mentioned that the gimbal cannot guarantee tilt-free measurements due to many influencing parameters such as bearing manufacturing inaccuracies, disk misalignment, and base plate tilt. The gimbal will always align with the averaged height of the bearing pads, which does not necessarily mean it is tilt-free.
To further assess the proper functionality of the gimbal suspension, the wear of the complete top foil can be analyzed. If the gimbal suspension effectively reduces misalignment effects, the wear marks observed on the six pad segments of the top foil should be similar. Fig. 3.14 shows a microscopic image of the same top foil after the running-in process. The wear pattern of a single pad segment of this top foil has been analyzed in detail in Sec. 5.2.1. The analysis will show that three characteristic wear areas exist, namely wear area I (located at the inner radius r_{i} in the center of the pad segment), wear area II (located at the inner radius at the trailing edge), and wear area III (located at the outer diameter in the center of the pad segment). As can be seen in Fig. 3.14, all six bearing pad segments show the three characteristic wear areas. For a detailed description of the quantitative amount of wear in the three wear areas, refer to the measurement results presented in Sec. 5.2.1.

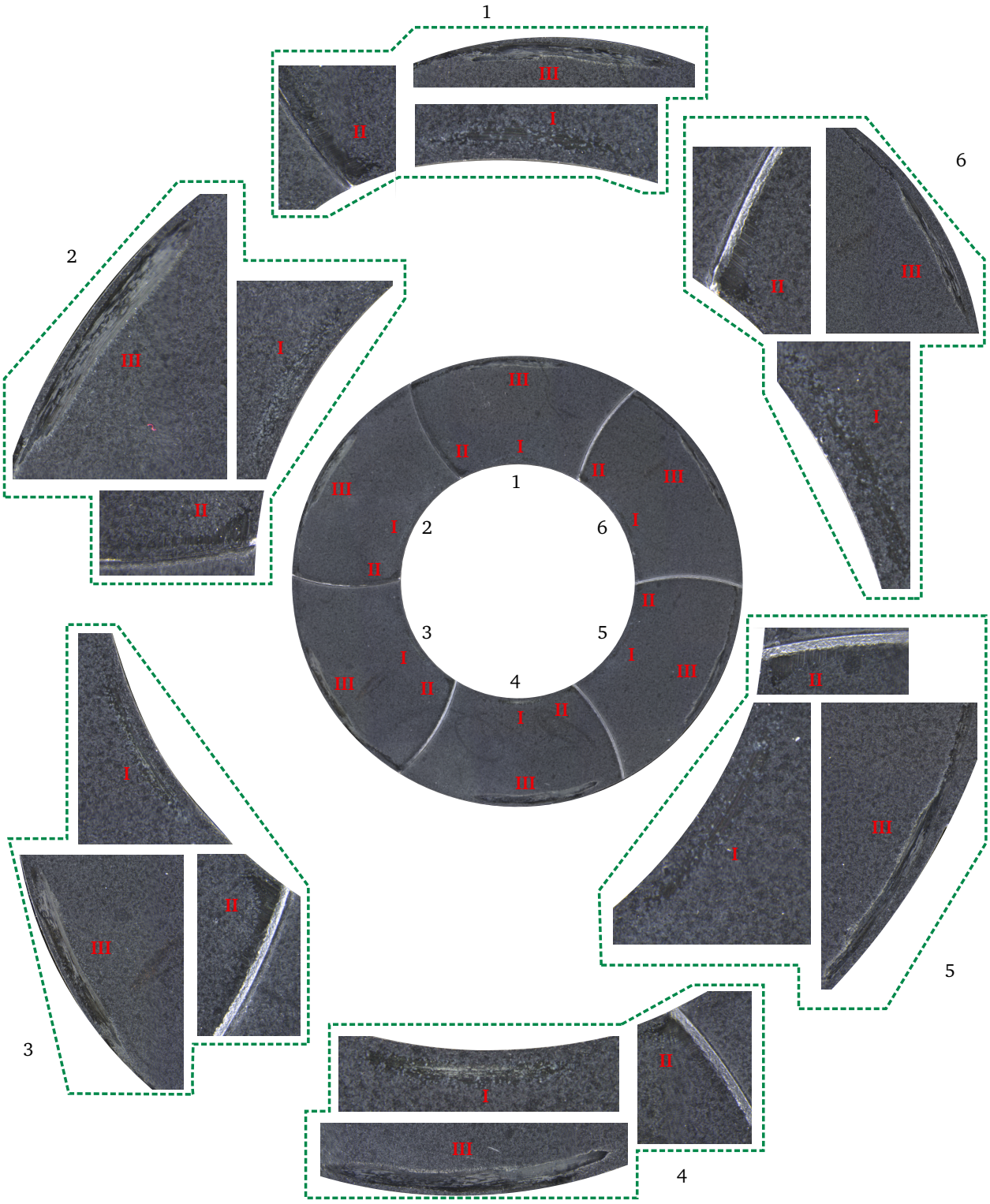

Figure 3.14.: Microscopic image of all six pad segments of the top foil used during experiments. Zoom images for the three wear areas for each pad segment.

3.1.2. Measuring Ability

In this section, the measuring ability of the high-speed test rig is summarized, and the resulting measurement uncertainty is provided.
The test rig can accurately determine the thrust load F_{thrust} and power loss P_{loss} as critical thrust bearing performance parameters. The thrust load is determined and regulated by the pressure chamber, which exhibits good linearity and is calibrated for the non-spinning rotor. A Computational Fluid Dynamics (CFD) analysis of the pressure chamber shows that the influence of the spinning rotor on this measurement system is less than $1\,\%$. Hence, the pressure measurement in the chamber is a suitable quantity for accurately determining the thrust load. The torque, measured by a load cell supported by a spring and the shear stress on the bearing, is also found to precisely measure the bearing's power loss. When considering peripheral losses $P_{\mathrm{shear,\,periphery}}$ of the rotor disk through Computational Heat Transfer (CHT) analysis, the measurement system fully describes the power loss P_{loss} of the bearing.
The thermal behavior can also be evaluated by the test rig. Two contactless pyrometers measure the temperatures on the rotor disk, namely $T_{\mathrm{disk,\,1}}$ and $T_{\mathrm{disk,\,2}}$, as well as the base plate's temperature $T_{\mathrm{TC,\,B}}$. These pyrometers are calibrated with a separate setup using a heating cartridge. Both sensors exhibit a linear behavior with different slopes and have a starting range of around $100\,°\mathrm{C}$.
One essential capability of the test rig is the ability to measure thrust bearing performance under aligned conditions. Calibration measurements show that this condition can only be achieved with thrust loads exceeding 30 N. Therefore, measurements with higher loads can be compared with a one-pad simulation model.

Resulting Measurement Uncertainty

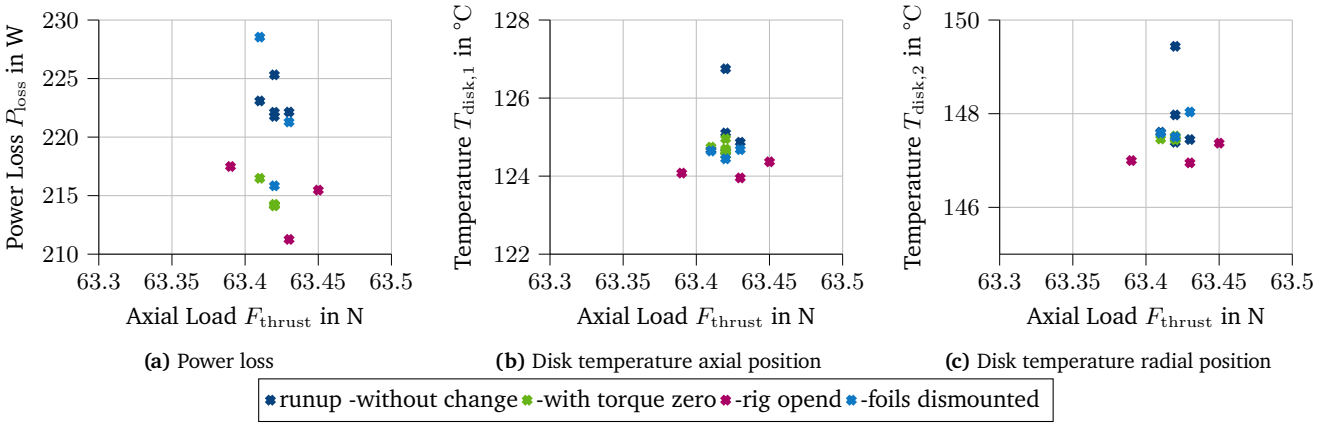

(a) Power loss **(b)** Disk temperature axial position **(c)** Disk temperature radial position

Figure 3.15.: Repeatability through different top foils at the same operating point.

The resulting measurement uncertainty of the high-speed test rig is a combination of sensor accuracy and a repeatability error of the test rig (compare Sec. 2.4.1). To determine this repeatability error, measurements are repeatedly performed with the same top foil or different top foils under various conditions.
For each case, a run-up is conducted from a standstill to the desired spinning speed and load condition. This involves zeroing the preload on the torque sensor at standstill, setting the spinning speed to 120 krpm, and gradually increasing the load in 5 N steps until approximately 60 N is reached. After reaching a thermal steady point, an average over 1 s of all values is saved. This specific operating point is chosen to minimize the influence of running-in wear and other performance-critical factors of the bearing (refer to

later evaluations in Sec. 5.2.2), despite the top foils being previously run-in in other experiments.
Four cases are examined with the same top foil. In the first case, five run-ups, as described above, are performed without zeroing the torque sensor between run-ups, i.e., zeroing it only once at the beginning of this test. In the second case, the torque sensor is zeroed between the five run-ups. Case number 3 describes three run-ups with the test rig opened between the measurements, moving the torque head away from the drive side over the dovetail. The torque sensor was zeroed in this test case between each run-up. This case is chosen to determine the influence of the cooling flow pipes and sensor cables hanging at the backside of the base plate, which can affect the torque sensor's preload. The fourth case describes three run-ups with the same foil package dismounted and remounted between each run-up. The measured power loss, disk temperature (axial and radial positions), and axial load for these four cases are shown in Fig. 3.15. In Fig. 3.15a the measured power loss, and in Fig. 3.15b and Fig. 3.15c the measured disk temperature are shown as a function of the axial load.
For the first case, the measured power loss ranges from 222 to 225 W. With zeroing the torque sensor between the run-ups in the second case, the range reduces further to 214 to 216 W. The third case, involving opening the test rig, results in a range of 211 to 215 W, indicating an influence on repeatability. The largest influence on the repeatability error is observed in the fourth case, where the foils are dismounted and mounted again, resulting in a range of 215 to 229 W. Across all four cases, the measured load falls between 63.39 and 63.45 N, which is much less than $1\,\%$ and well within the sensor's accuracy. This applies to all subsequent evaluations. The measured axial force is not considered in greater detail in other repeat measurements. It can be concluded that the power loss measurement repeatability error for one top foil is $\pm\,4\,\%$ (two standard deviations from the mean value).
A similar analysis is performed for the measured temperatures. The repeatability error is estimated to be $\pm\,0.5\,\%$ for the axial position and $\pm\,0.4\,\%$ for the radial position, resulting in a smaller repetition error than the power loss measurement.
Additionally, five top foils from the same batch are evaluated at the same operating point described above — after run-up. The measured power loss and pyrometer's temperature concerning load are displayed in Fig. 3.16. The range of the measured power loss is between 223-231 W, which corresponds to a deviation of $\pm\,1.8\,\%$. For the axial position, the measured range is between 122.3 and 128.8 K, indicating a deviation of $\pm\,2.5\,\%$. The radial position exhibits a range of 147.6 to 156.8 K, representing a deviation of $\pm\,3\,\%$.
Upon closer inspection, there seems to be no correlation between the measured power loss and temperature. For example, for TF1, the highest power loss is measured, but not the highest temperatures. Therefore, it can be concluded that the deviation does not stem from different top foils or running-in conditions but rather from a repeatability error. This shows that the repeatability error for power loss measurement is not increased by considering multiple comparable top foils. However, the measured temperature range increases with multiple top foils.
In summary, the repeatability error for power loss measurements can be given as $\pm\,4\,\%$, and for temperature measurements as $\pm\,3\,\%$. The axial load repeatability error is taken into account with $\pm\,0.1\,\%$. The housing temperatures $T_{\mathrm{TC,B}}$ and $T_{\mathrm{TC,H}}$ also have comparable small repeatability errors of $\pm\,0.1\,\%$. These errors can be added to the sensor inaccuracies or the inaccuracies of the calibration sensors. The derived inaccuracies will serve as measurement uncertainties for the high-speed test rig measurement evaluation in Chapter 5. The resulting uncertainty is presented in Tab. 3.2. Note that all repeatability errors are given for two standard deviations from the mean value.

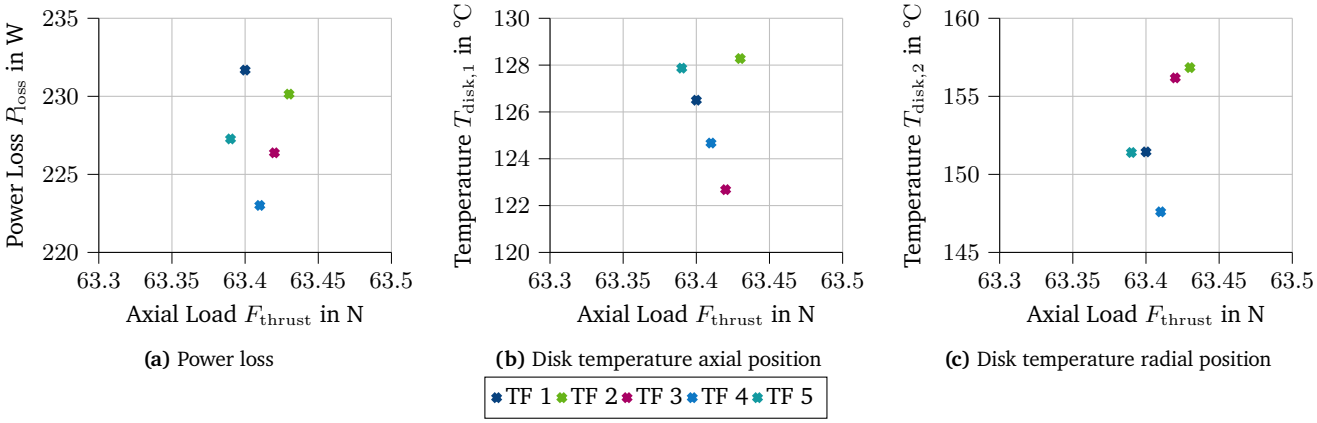

(a) Power loss

(b) Disk temperature axial position

(c) Disk temperature radial position

Figure 3.16.: Repeatability through different top foils at the same operating point.

Table 3.2.: High speed test rig resulting measurement uncertainties for individual measurement systems.

Quantity	Value
Power Loss P_{loss}	$\pm 4\,\% \pm 5\,\text{W}$
Load F_{thrust}	$\pm 0.1\,\% \pm 0.3\,\text{N}$
Pyrometers $T_{\text{disk},1}$ and $T_{\text{disk},2}$	$\pm 3\,\% \pm 1\,\text{K}$
Type K $T_{\text{TC,B}}$ and $T_{\text{TC,H}}$	$\pm 0.1\,\% \pm 2\,\text{K}$

3.2. Thermal Resistance Test Rig

The fluid film within the bearing gap generates heat due to friction losses. This heat follows two main paths (see Sec. 2.2.5). The first path leads into the rotor disk, while the second path traverses through the foil package. The latter path, concerning the foil package, is described by an analytical thermal resistance model in Sec. 2.2.3. Results obtained from this resistance model, applied to the current foil bearing design, indicate that only a minimal amount of heat is transferred through the foil package ($\leq$ 30%). To validate these findings and the underlying approach, a new test rig has been designed, capable of determining thermal resistance without a rotating rotor.

3.2.1. Design and Functionality

The test rig is illustrated in Fig. 3.17. On the left side of the figure, a rendered picture of the assembly is presented, while the right side shows an exploded sketch highlighting all essential components. The test rig is mounted on a steel plate, supported by four feet to allow accessibility from below. To ensure safety, the exterior is enclosed within an acrylic glass box. Unlike typical setups where heat is generated within an air film, this test rig employs an electric heater ring, eliminating the need for rotating parts. The electric heat intensity can be adjusted using a DC power source. The heater is situated in a movable isolation block, which can be vertically adjusted to apply axial loads on the bearing package. The applied load can be fine-tuned using a micrometer screw and is measured with a load cell connected in series between the micrometer screw and the movable heat block. The axial force on the base of the test rig is supported by three fixation rods, allowing a bearing load of up to 200 N. The foil bearing package is positioned on the base plate, which is also insulated. The internal structure is depicted in a cross-section

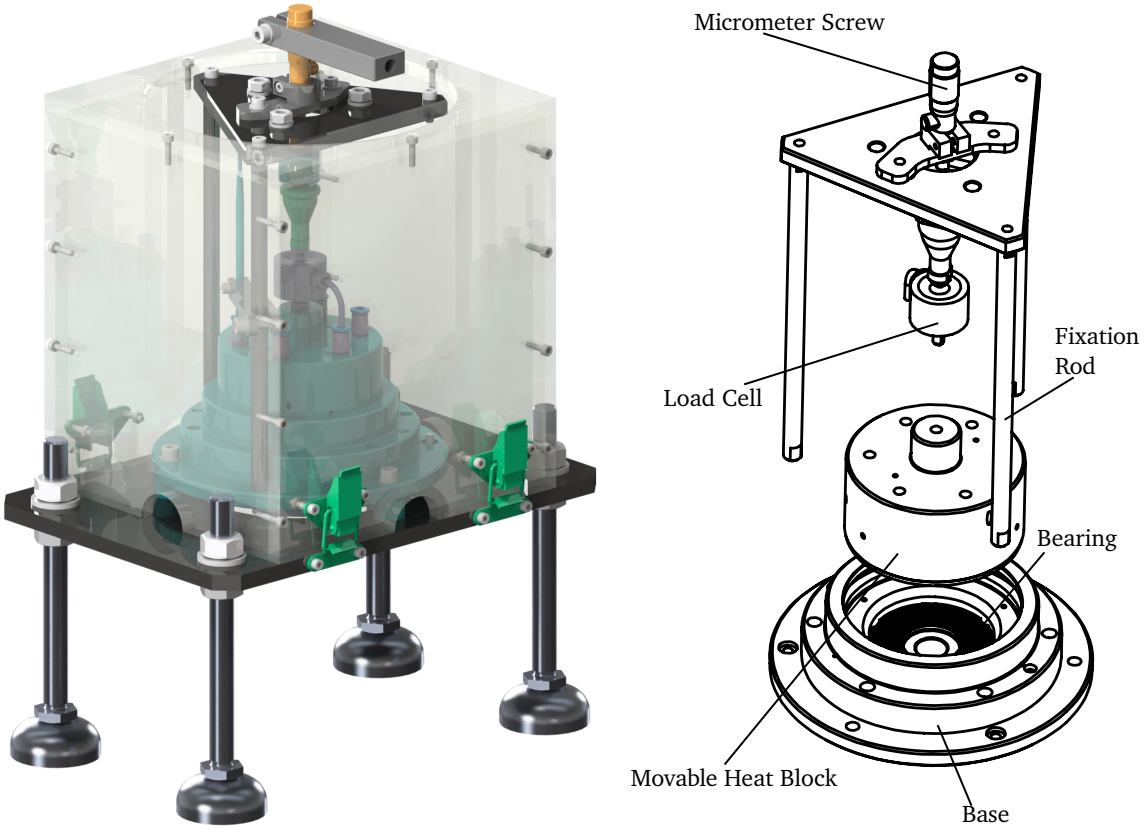

Figure 3.17.: Thermal resistance test rig assembly rendering image on the left side and on the right side with an explosion view (without temperature sensors).

sketch in Fig. 3.18. To facilitate steady-state conditions at the base plate, the heat is dissipated using cooling fins and an air blower. The test rig is equipped with three main temperature measurement layers: T_{L1} located 1 mm below the heater, T_{L2} above the test bearing, at the bottom of the steel block, and T_{L3} beneath the test bearing within the base plate. This setup enables the determination of temperature gradients between these layers. An energy balance of the test rig yields the heat energy conducted into the bearing:

$$Q_{\mathrm{Heater}} = Q_{\mathrm{Block}} + Q_{\mathrm{Dis}}. \tag{3.10}$$

In Eq. 3.10, Q_{Dis} represents the sum of all dissipative heat fluxes over the insulation.
The surrounding insulation is made of a duroplastic material called Doglas 250G, designed to withstand temperatures up to $250\,^{\circ}\mathrm{C}$. This material has a thermal conductivity of $\lambda_{\mathrm{insulation}} = 0.23\,\mathrm{W/m/K}$, as stated in the material sheet. On the other hand, the base plate and the steel block possess a thermal conductivity of $\lambda_{\mathrm{Block}} = 15\,\mathrm{W/m/K}$, also as indicated in the material sheet. The steel block serves to homogenize the temperature from the heater and to quantify the heat flux into the test bearing, using the relation:

$$Q_{\mathrm{Block,\,L1L2}} = \frac{\Delta T_{\mathrm{L1,L2}}}{R_{\mathrm{Block}}}, \qquad \text{with } R_{\mathrm{Block}} = A_{\mathrm{Block}}\,\lambda_{\mathrm{Block}}. \tag{3.11}$$

Here, R denotes the thermal resistance, and $A_{\mathrm{Block}} = \pi(r_{\mathrm{o}}^2 - r_{\mathrm{i}}^2)$ is the cross-sectional area of the lower face of the block connected with the bearing. The heat conducted through the test bearing can be

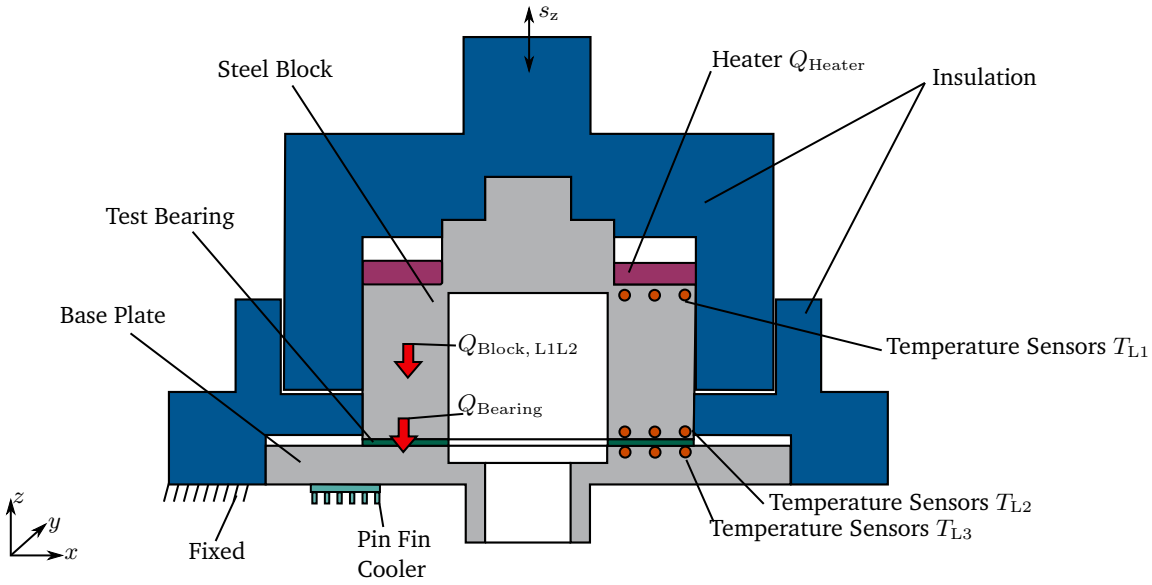

Figure 3.18.: Thermal resistance cross section of the movable heat block and the base.

determined as follows:

$$Q_{\text{Bearing}} = \frac{\Delta T_{\text{L2,L3}}}{R_{\text{Bearing}}}. \tag{3.12}$$

It is assumed that the heat in the block in the L1-L2 direction is transferred into the bearing without significant losses. Therefore:

$$Q_{\text{Block, L1L2}} = Q_{\text{Bearing}}. \tag{3.13}$$

By combining the above equations, the unknown thermal resistance of the bearing R_{Bearing} can be calculated using the measured temperature gradients in the test rig:

$$R_{\text{Bearing}} = \frac{\Delta T_{\text{L2,L3}}}{\Delta T_{\text{L1,L2}}} R_{\text{Block}}. \tag{3.14}$$

This calculated value can be directly compared with the thermal resistance obtained from the empirical thermal resistance model (see Sec. 2.2.3). In the following section, the measurement equipment and the measuring capabilities are discussed.

3.2.2. Measurement Equipment and Measuring Abilities

The test rig is equipped with nine temperature sensor positions within the test environment and seven positions outside to determine dissipative thermal fluxes. All temperature sensors are ELECTRONIC-SENSOR class 1 Typ-K sheath thermocouples with an accuracy of $\pm 2\,\text{K}$, calibrated in a boiling water bath. The load cell is calibrated with a calibrated load cell in a bench vise, offering an accuracy of $\pm 1\,\text{N}$.

Linearity and Repeatability Error

Since the thermal resistance determined by Eq. 3.14 is independent of the injected heat, there should be linearity between the input power and the measured temperatures. To confirm this, tests with different

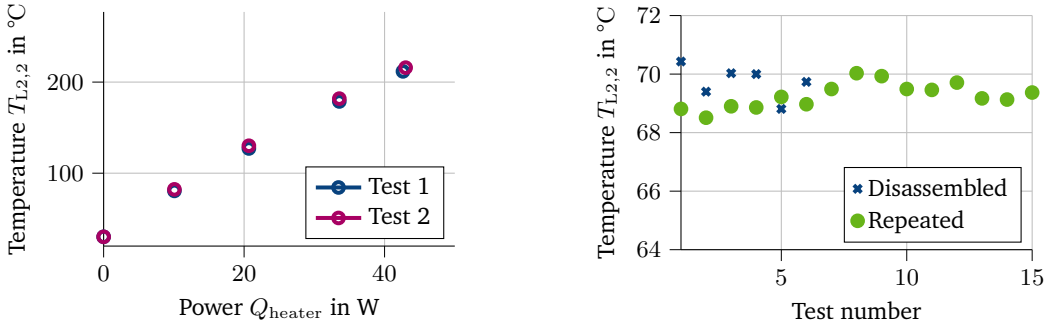

(a) Linear behavior between applied heat and measured temperature.

(b) Thermal resistance repeatability error.

Figure 3.19.: Thermal resistance test rig and repeatability error measurements.

input powers Q_{Heater} from the electric heater were conducted. As shown in Fig. 3.19a for one sensor (second layer, second sensor $T_{\mathrm{L2,2}}$), and for two repetitions, it is evident that the test rig exhibits a linear behavior between these two quantities. Therefore, it is sufficient to evaluate tests with only one input power.
Additionally, repeatability measurements were performed. Fig. 3.19b presents the measured temperature as a function of the repeatability tests for one sensor $T_{\mathrm{L2,2}}$. The first test accounts for the error in the test rig due to assembling and disassembling, showing a maximum deviation of 1.25 K. The second test is carried out without any changes to the test rig but by cooling down and heating up again 15 times with the same input power. This leads to a maximum deviation of $0.48\,\mathrm{K}$. Based on these measurements, a repeatability error of two times the standard deviation can be concluded, amounting to $\pm\,1.5\,\%$ concerning the average measured temperature.

Calibration Test Object

To verify the capability of the test rig in determining thermal resistance, a calibration test object with a known thermal resistance is employed. The test object is a PTFE disk with a thickness of 1 mm and a thermal conductivity of $0.24\,\mathrm{W/m/K}$. With its cross-section of $A_{\mathrm{PTFE}} = 0.0017\,\mathrm{m}^2$, a thermal resistance of $2.21\,\mathrm{K/W}$ can be calculated. The resistance of the block is $0.91\,\mathrm{K/W}$. During a stationary operation point with an input power of 30 W, temperature gradients for the layers can be measured: $\Delta\,T_{\mathrm{L2,L3}} = 15.5\,\mathrm{K}$ for the gradient within the steel block and $\Delta\,T_{\mathrm{L1,L2}} = 36.4\,\mathrm{K}$ over the test object. By inserting these measured quantities into Eq. 3.14, a resistance of the test object of $2.14\,\mathrm{K/W}$ is obtained. Compared to the $2.21\,\mathrm{K/W}$ calculated with the given material's properties, this demonstrates the capability of the test rig to determine the thermal resistance of a test object within a deviation of $3.5\,\%$. It is reasonable that the resistance determined from the measurements is slightly smaller than the actual one because the calculation in Eq. 3.14 assumes that all heat from the block goes into the bearing without any heat losses through the insulation, which is a simplified steady-state condition. However, it is evident that this approximation leads to only a small inaccuracy, and dissipative thermal fluxes can be safely neglected.

3.3. Test Beds for Mechanical Properties

This section describes two test beds used for measuring the mechanical properties of the foil bearings. Both test beds are based on standard industrial testing facilities. The first test bed measures the mechanical

friction coefficients between the top foil and bump foil, as well as between the bump foil and base plate, using a BRUCKER UMT TriboLab. The second test bed determines the stiffness of the bump foils, employing a ZWICK ROLL Multipress Proline.

3.3.1. Mechanical Friction Coefficients

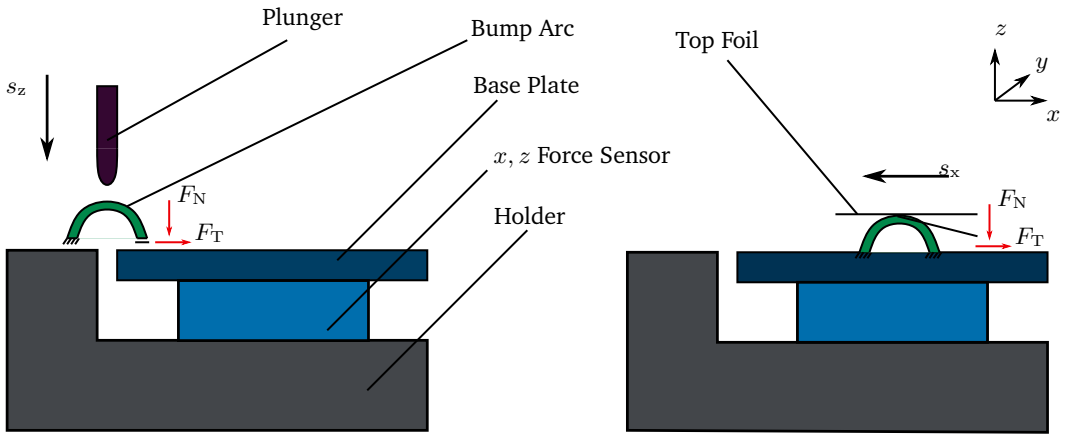

Figure 3.20.: Test setup to determine friction coefficients between the bump foil and the base plate on the right side and on the left side to determine the friction coefficient between top and bump foil.

As described in Sec. 2.2.4, the friction coefficient between bump foil and base plate, and bump foil and top foil are essential input parameters for the simulation model to calculate Coulomb friction forces. To measure these coefficients, a test setup is constructed within a BRUCKER UMT TriboLab. The TriboLab is capable of precise movement of a carrier with a resolution of $0.5\,\mu\mathrm{m}$, and reaction forces can be measured using a precise ATI-Nano43 6-axes load cell. The load cell is calibrated with another calibrated load cell specifically for this test setup. Two distinct friction coefficients are determined: μ_{TF}, representing the friction coefficient between the top foil and the bump foil, and μ_{BF}, representing the friction coefficient between the bump foil and the base plate (see Fig. 2.6).
The dominant movement of the bump foil with respect to the base plate is due to the normal force F_{TN} acting on the bump arc. Therefore, the bump arc enlarges and a tangential reaction force—mainly F_{B1} will occur. The second orthogonal part of the tangential force F_{B2} is negligible in this case. In case of top foil movement relative to the bump foil, also x_1-directed movement is the dominant one. Pressure forces on the top foil—especially between two neighboring bumps—will pull the top foil down in x_3 direction. This leads to normal force F_{TN} and to a movement in x_1 direction relative to the bump foil; this causes a tangential reaction force F_{T1}.
For the test involving the friction coefficient μ_{BF} (left side in Fig. 3.20), the holder and the base plate have the same height, and the left side of a bump foil arc is fixed to the holder. The right side of the bump arc can move horizontally in the x-direction on the base plate. The base plate is supported by the force sensor to measure the normal force F_{N} and the tangential force F_{T}. The plunger is connected to the Tribolab's carrier and can apply a displacement s_{z} in the z-direction on the bump strip.
For the friction coefficient between the top and bump foil, denoted as μ_{TF}, the top foil is glued to the carrier, and the bump foil is fixed on the base plate in all directions. A displacement in the z-direction is applied to put a normal force F_{N} on the bump foil over the top foil. The top foil is then moved horizontally by a small amount of $2\,\mu\mathrm{m}$ in the x-direction. The reaction tangential force F_{T} is measured by the sensor. The friction coefficient can be determined for both cases by dividing the tangential force by the normal

force:

$$\mu = \frac{F_\mathrm{T}}{F_\mathrm{N}}. \tag{3.15}$$

3.3.2. Stiffness of the Bump Foils

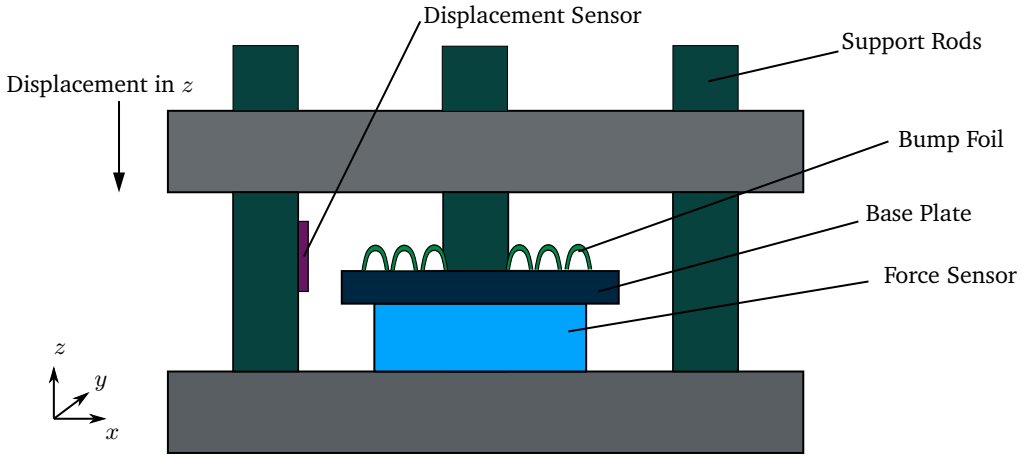

Figure 3.21.: Bump foil stiffness measurement setup.

The integral stiffness Φ_St of the bump foil is the quotient of its integral deformation and the integral force acting on it. It can be determined through force-displacement measurements. For this purpose, a test setup is integrated into a ZWICK Multipress Proline (Fig. 3.21). This setup is originally designed for stiffness measurements of springs. It consists of three stable support rods on which a plate can be lowered onto the test object to ensure high test rig stiffness compared to the measured stiffness. The z-displacement of the upper plate is measured with an additional displacement sensor, while the reaction force is measured by a calibrated force sensor under the test object. Prior to testing, the setup's deformation is calibrated and accounted for in the measurements. The measurement results and their comparison with the simulated stiffness of the bump foils are discussed in Sec. 5.1.

3.4. Topography and Wear Measurements

This section introduces the measurement equipment used for analyzing topography and wear, with a special emphasis on the evaluation of white light interferometric (WLI) top foil measurements. For all other devices, a concise description along with a brief use-case scenario is provided.

White light interferometric measurements

Later evaluations, such as the ones concerning the top foil modeling parameters in Sec. 4.3.2, reveal the significant influence of these parameters on the bearing's performance (compare Sec. 4.3.1). Thus, topography measurements are essential to determine the top foils' pre-deformations and other topographic details. For this purpose, a ZYGO Nexview NX2 white light interferometer (WLI) is utilized, equipped with a 200x200 mm lateral measurement table and magnification options ranging from 1x to 100x. To strike a balance between accuracy and evaluation time, a lateral resolution of $17\,\mu\mathrm{m}$ is chosen, resulting in 3500

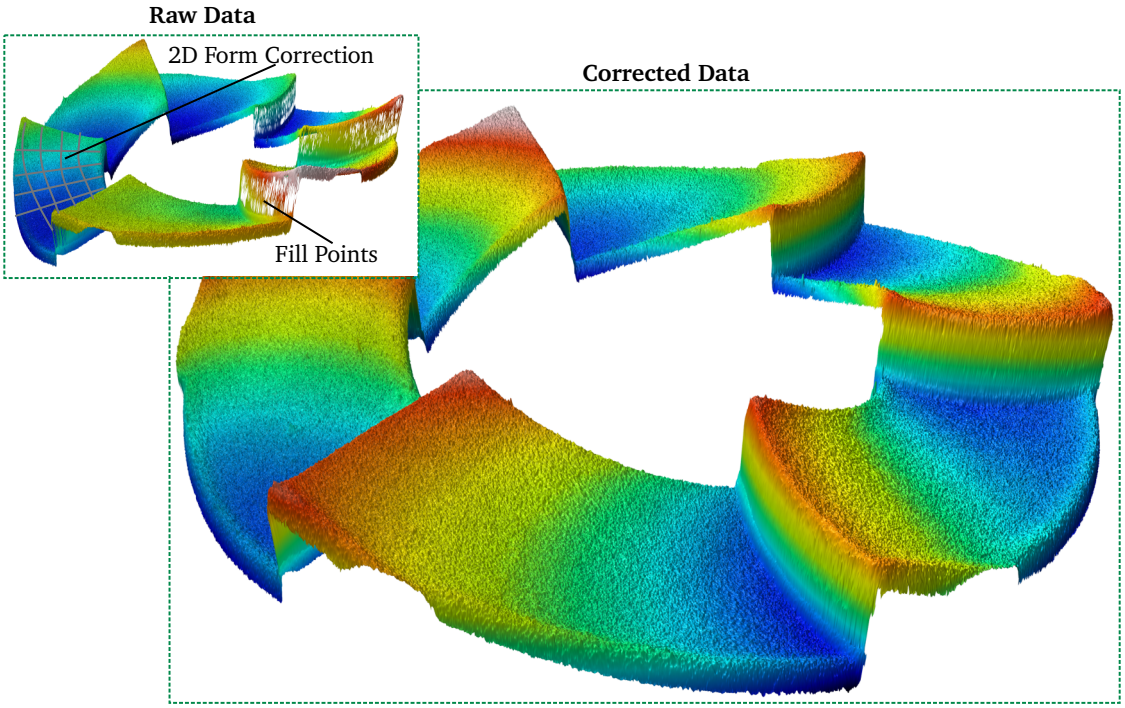

Figure 3.22.: Visualization of measured top foil data of WLI measurements.

data points in both x and y directions, thus providing 12 million data points for each measurement. To facilitate proper comparison between individual measurements, the measured data needs to be aligned using an evaluation algorithm, owing to the complex geometry. The alignment process involves the following steps:

- **Determination of the center point of the top foil**: The center point of the top foil is geometrically determined by estimating a center point. Based on this estimated point, the inner radius of the top foil is located by randomly exploring points up or down and left or right from this estimated point. Three points found on the inner radius are then connected with lines, and a perpendicular line is drawn from the center of each line. The intersection of these perpendicular lines yields the center P_{c} of the inner circle of the top foil. This process is repeated eight times, and the resulting points are averaged.

- **Delete and fill measurement errors:** Gradient barriers are employed to identify and rectify measurement errors. The barriers are determined based on a factor of the standard deviation.

- **Alignment of measurement data:** To align the measured data, the steps of the top foil are searched on a circumferential profile on the middle radius. This profile is depicted in Fig. 3.23, where the circumferential height profile H_{TF} on the middle radius r_{m} is presented in the upper graph with respect to the circumferential angle φ. The lower graph illustrates the gradient of the height profile. Whenever a step occurs, the gradient exhibits significant changes, surpassing the 3 times standard deviation barrier. By detecting these steps, the entire measurement data can be rotated using a rotation matrix based on the center point, thereby aligning it with other measurements.

- **Form corrections**: The data can be further aligned based on the circumferential profiles. To visualize this evaluation process, an example top foil is shown in Fig. 3.22, with both raw and

corrected data.

With the aforementioned evaluation procedure, the complete top foil can be scanned before and after experiments. Additionally, the backside of a top foil, denoted as $\mathrm{WLI}_{\mathrm{back}}$, can be scanned to obtain additional information. Thanks to the alignment process, the backside measurements can be subtracted from the top $\mathrm{WLI}_{\mathrm{top}}$ side measurements, enabling a clearer depiction of coating layer information. The results and conclusions drawn from these evaluations are discussed in Sec. 4.3.2.

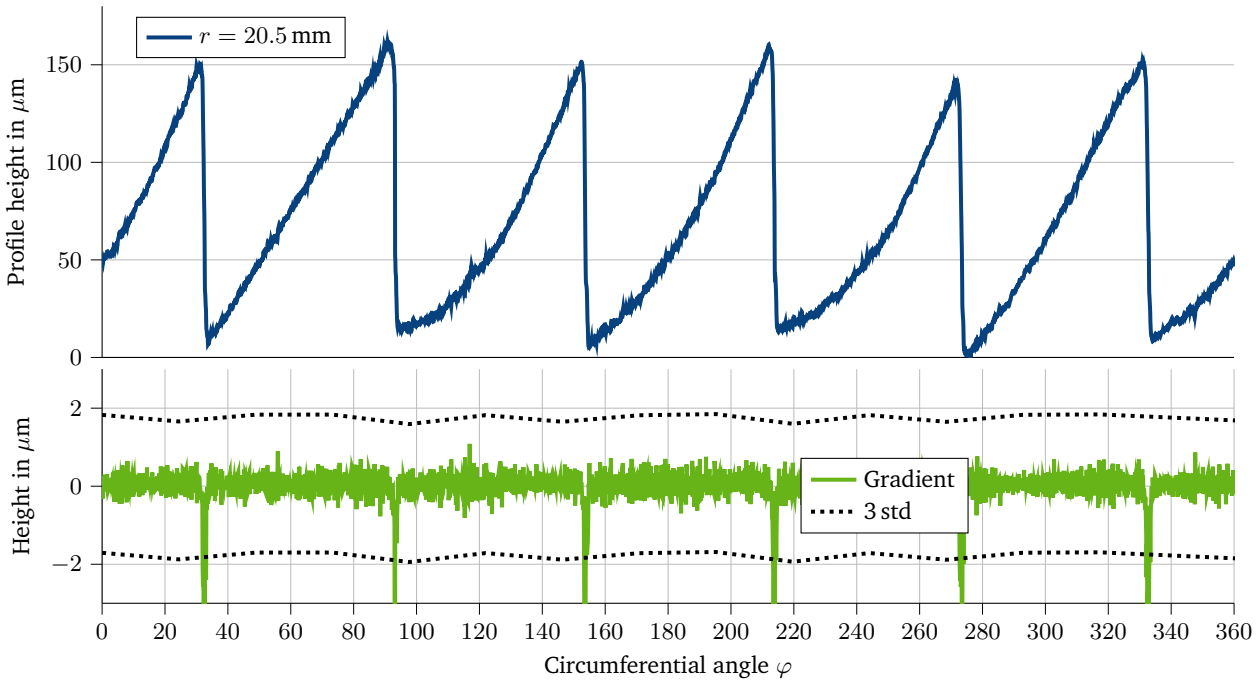

Figure 3.23.: Determination of the rotation matrix in order to align top foil measurements. Based on gradient barrier.

Confocal Microscope Measurements

Due to the coarse x, y resolution of the WLI measurements described above, higher-resolution measurements are necessary to determine surface roughnesses accurately. For this purpose, a NANOFOCUS μsurf Custom equipped with the MountainsMap software is employed. Smaller areas (below $1\,\mathrm{mm}^2$) of the examined parts are evaluated to obtain surface roughness information. The used 50x optic provides x, y resolution of $0.25\,\mu\mathrm{m}$ and a z-resolution of 0.0267 nm.

Microscopic Measurements

In this work two different kinds of microscopic measurements are utilized:
Cross section measurements
In order to microscopically determine the coating thickness or other geometrical properties in a cross-section, the cross-section must first be exposed and prepared. For this purpose, a specimen is taken from the component to be examined using a precision cut-off grinder, embedded in an investment material, ground, and finally polished. Microscopic pictures of these cross-section probes are taken with a LEICA DMI5000, which is capable of automatically stitching multiple pictures to create an overview image.
Reflected-light microscope

In addition to the cross-section measurements, basic top-view microscopic images are required in this work. A LEICA M205C microscope with a 10x optic is employed for this application.

3.5. Summary and Conclusion

In this chapter, various test stands and measuring equipment used in the thesis are introduced. A new high-speed test rig capable of loading thrust bearings with diameters of up to 55 mm and rotating at 120 krpm, with the ability to apply up to 100 N thrust load, was presented. The rig allows for automatic alignment of the thrust bearing with the rotor disk through a gimbal suspension. Emphasis was placed on the measurement capability, explaining the calibrations of load application and torque measurement, along with the non-contact temperature measurement. A CHT simulation in Ansys CFX was performed to analyze the torque measurement system, identifying peripheral losses that can be considered in further analyses. The repeatability of power loss determination was found to be within $\pm 3\,\%$, while the thrust load determination exhibited a repeatability error of $\pm 0.1\,\%$.
Furthermore, an additional test rig was introduced, designed to measure the thermal resistance of the bump foils. This setup allows for the application of a heat flux to the thrust bearing without rotating parts using a heating element and enables the imposition of various axial loads. The functionality of the rig was verified through a test object with known thermal resistance, demonstrating good accuracy.
Additionally, two test setups for mechanical properties were presented. The first setup is employed to determine friction values between the foils, while the second setup is used to measure the stiffness of the bump foils.
Lastly, the devices used for determining the topographical properties of the components and conducting wear measurements were discussed. Primarily, white light interferometric (WLI) measurements were considered, and their complex evaluation method was explained.
In conclusion, the extensive array of measuring instruments allows for a thorough analysis of the physical relationships in the thrust bearing. The high accuracy of power loss measurement in the high-speed test rig enables a precise analysis of the bearing's performance. These measurement capabilities contribute significantly to the comprehensive understanding of the thrust bearing and its behavior under various operating conditions.

4. Modeling and Model Adjustments

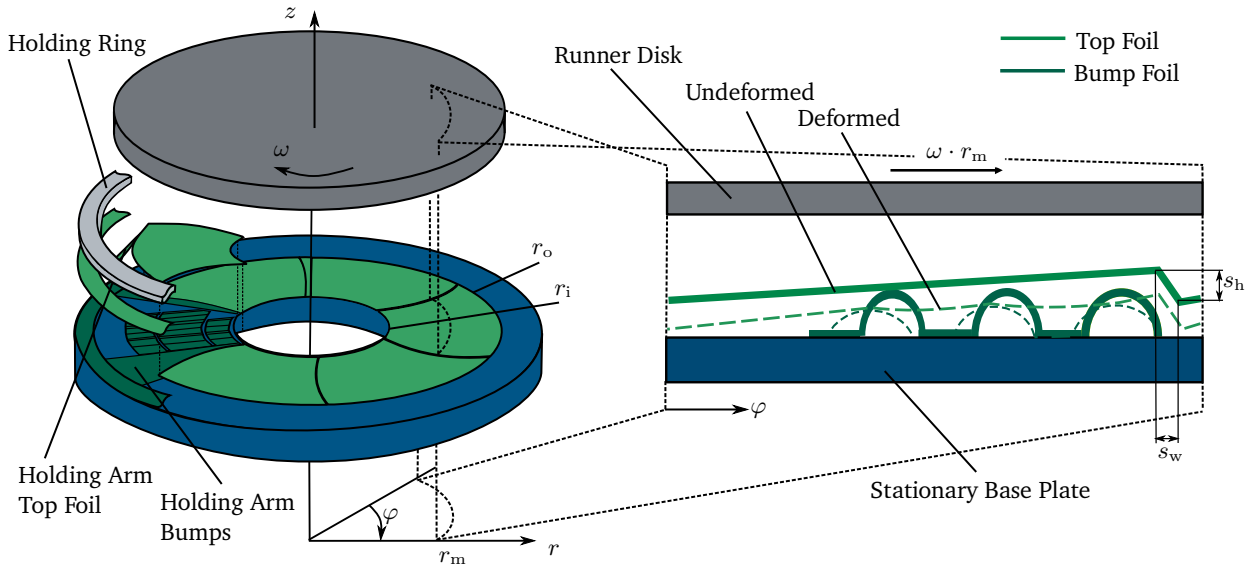

Figure 4.1.: Sketch of the foil bearing assembly. Consisting of stationary surface as base plate, bump foil, top foil, and disk.

To validate the simulation model, a validation bearing design is required. The bearing design for this work is depicted in Fig. 4.1, illustrating its main components. It comprises a stationary base plate on which the bump and top foils are mounted, and a rotating runner disk. The bump foil consists of six individual pads made from a single stamped annular foil. Positioned above the bump foil is the top foil, also composed of an annular foil with six stamped steps that separate the pads.
On the right side of Fig. 4.1, a circumferential cut through the bearing system of one pad at the middle radius r_m is displayed. In its undeformed state, the top foil maintains a constant slope from one step to another. The step is characterized by a step height S_h and a step width S_w. When the rotor disk begins to spin, the convergent gap generates pressure, resulting in the rotor lifting off when a certain lift-off speed is achieved. The applied load F_thrust on the disk reduces the gap height h_nom, leading to a higher pressure buildup within the fluid flow, corresponding to the force exerted on the disk. As a consequence of this pressure buildup, the top foil can deform over the bumps to create a taper land region, and the bumps themselves deform under the pressure exerted by the top foil.
Accurately modeling the interaction of these components is essential for minimizing uncertainties in the model (see Sec. 2.4). Hence, this chapter discusses all relevant parameters, primarily focusing on geometric properties, and divides them into three main sections: one for the rotor and the bearing system's surroundings, another for the bump foil, and the last one for the top foil. These parameters are presented and analyzed based on sensitivity analysis for each parameter.
Based on the results of the sensitivity analysis and the behavior of the measured quantities, simulation model adjustments are presented in this chapter. These adjustments encompass modifications to the air foil bearing's geometry and its periphery, as well as extensions of the current model. Ultimately, the chapter concludes by evaluating the uncertainties arising from inaccuracies in the input parameters. These evaluations form the foundation for the validation process in the subsequent chapter.

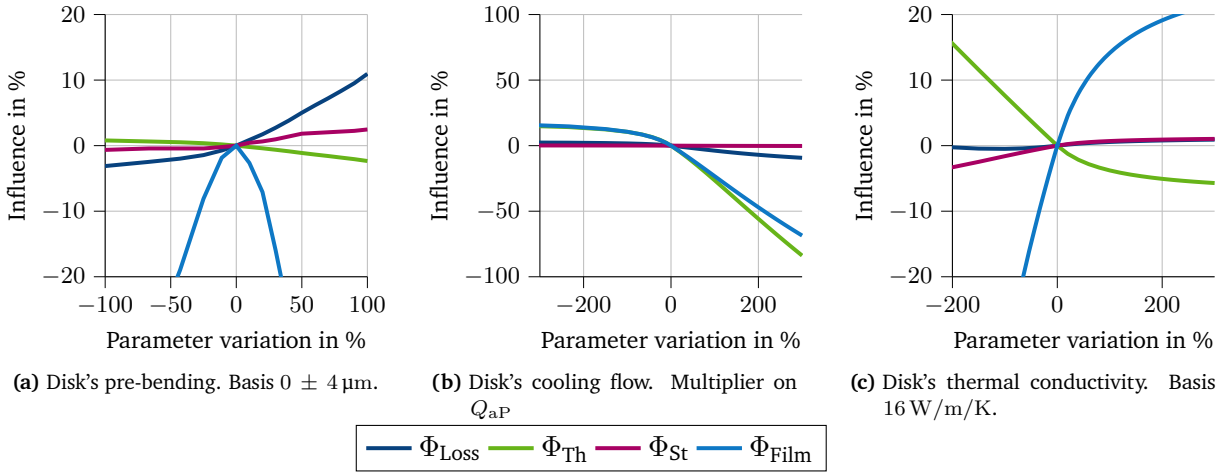

(a) Disk's pre-bending. Basis $0 \pm 4\,\mu\text{m}$.

(b) Disk's cooling flow. Multiplier on Q_{aP}

(c) Disk's thermal conductivity. Basis $16\,\text{W/m/K}$.

Figure 4.2.: Sensitivity analysis on disk properties.

4.1. Rotor and Surroundings

In this section, the rotor and its surroundings are discussed based on a sensitivity analysis. Afterward, the modeling is described with an extension of the film thickness as well as rotor boundary conditions based on the high-speed test rig's properties. Special attention is paid to a CHT simulation, which is used to describe the heat transfer coefficients of the side of the disk facing away from the bearing.

4.1.1. Sensitivity Analysis of Rotor and Environmental Parameters

The sensitivity analysis is based on the four evaluation quantities introduced in 2.4.2. The simulation is performed with a spinning speed n of 120 krpm and a thrust load $F_{\text{thrust}} = 100\,\text{N}$, serving as the baseline for the following investigations.
Three significant disk properties are analyzed in this section and displayed in Fig. 4.2. The parameter variation shown in the first plot in Fig. 4.2a is a surface property of the disk. It introduces a disturbing term in the film height h of the Reynolds equation, virtually bending the disk towards or away from the thrust bearing by $h_{\text{cone}}(x,y) = H_{\text{bend}}\left(1 - \frac{r-R_{\text{iT}}}{R_{\text{iT}}}\right) - H_{\text{bend}}$, with H_{bend} varying from -4 to $+4\,\mu\text{m}$. This parameter variation leads to a strong non-linearity in the film height quantity Φ_{Film} and significantly affects the loss quantity. The conclusion drawn from this observation is that surface properties of the disk, as long as they are in the same dimension as the fluid film height, can influence the bearing's behavior in terms of performance and wear patterns. Changes in the disk deformation directly impact the film height, resulting in a different bearing load distribution. Thus, accurate knowledge about the actual properties of the disk surface is crucial for correct modeling.
The second parameter analyzed in Fig. 4.2b involves varying the amount of heat carried away from the backside of the disk. Increasing this heat removal effectively reduces the thermal quantity Φ_{Th}, indicating that more heat is conducted into the disk and less into the top foil. It also decreases the film quantity Φ_{Film} by a similar amount. This can be attributed to a reduced temperature gradient over the disk, resulting in a smaller thermal deflection (compare Fig. 2.3), which, in turn, reduces the loss quantity Φ_{Loss} and improves performance. However, the influence of this parameter is not as strong as the disk pre-bending mentioned earlier. Nevertheless, it has a significant impact on the bearing's behavior, especially concerning the thermal aspects. Consequently, a Computational Heat Transfer (CHT)

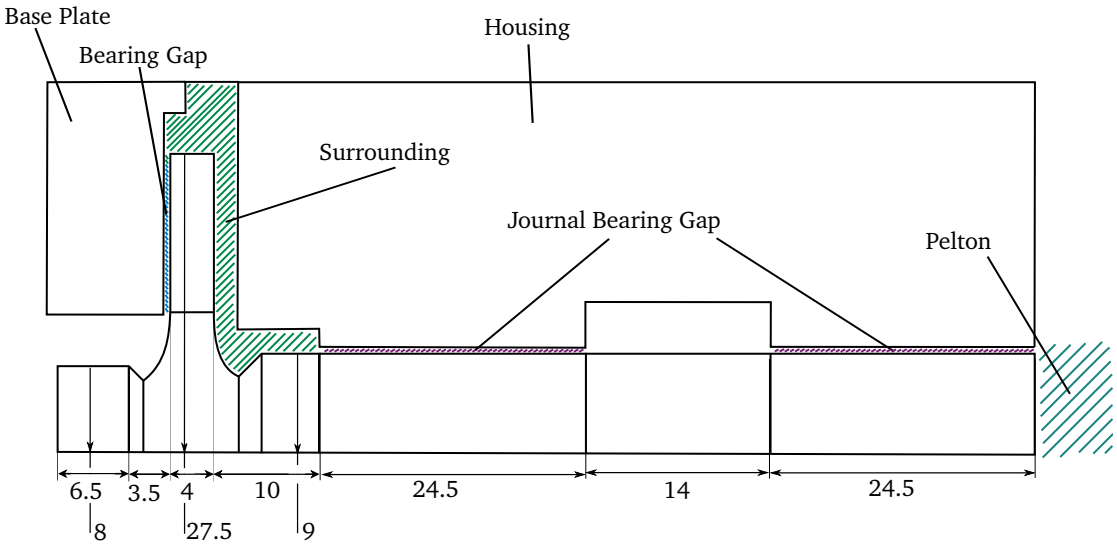

Figure 4.3.: Sketch of disk dimensions of the high-speed test rig modeled in the TEHD model.

simulation of the disk surroundings is set up for further investigations and to establish accurate boundary conditions.
The third parameter analyzed, displayed in Fig. 4.2c, pertains to the disk's thermal conductivity. It describes the thermal behavior of the disk itself and provides insights into the importance of other boundary conditions of the disk, aside from the cooling flow on the backside. Notably, an increase in thermal conductivity leads to a decrease in the thermal quantity Φ_{Th}, similar to the parameter in Fig. 4.2b. However, it also results in an increase in the film quantity and subsequently leads to an increase in the loss quantity. This observation highlights the importance of carefully setting up boundary conditions to accurately model the bearing's behavior and to establish the correct material properties.

4.1.2. Modeling Based on Measured Input

Fig. 4.3 illustrates the test rig's rotor and its surroundings. The disk has a thickness t_{RD} of 4 mm and an outer radius $r_{\mathrm{RD,o}}$ of 27.5 mm. The left end of the rotor has a diameter of 6.5 mm, and the edge of the disk features roundings to better withstand centrifugal tensions. On the right side of the disk, the radius gradually increases to 9 mm. The rotor shaft radius remains at 9 mm till the end of the rotor. The first journal bearing gap is located 10 mm away from the disk, and between both journal bearings, there is a 14 mm segment with a larger gap. After the second bearing, the Pelton turbine shovels follow, although in the simulation model, this part is not fully respected for.
The thermal conductivity is set to $\lambda_{\mathrm{RD}} = 16\,\mathrm{W/m/K}$, and the thermal expansion coefficient is $\alpha_{\mathrm{RD}} = 10.9 \cdot 10^{-6}\,1/\mathrm{K}$, based on the material sheet of the rotor. These macroscopic parameters play a crucial role in heat transfer and correct centrifugal deformation of the disk. The rotor is modeled using the Navier-Lamè equation presented in Sec. 2.2.1. Alongside macroscopic dimensions, the microscopic properties are of special interest as they can influence the local film height in the bearing gap. These microscopic properties are described in the following.

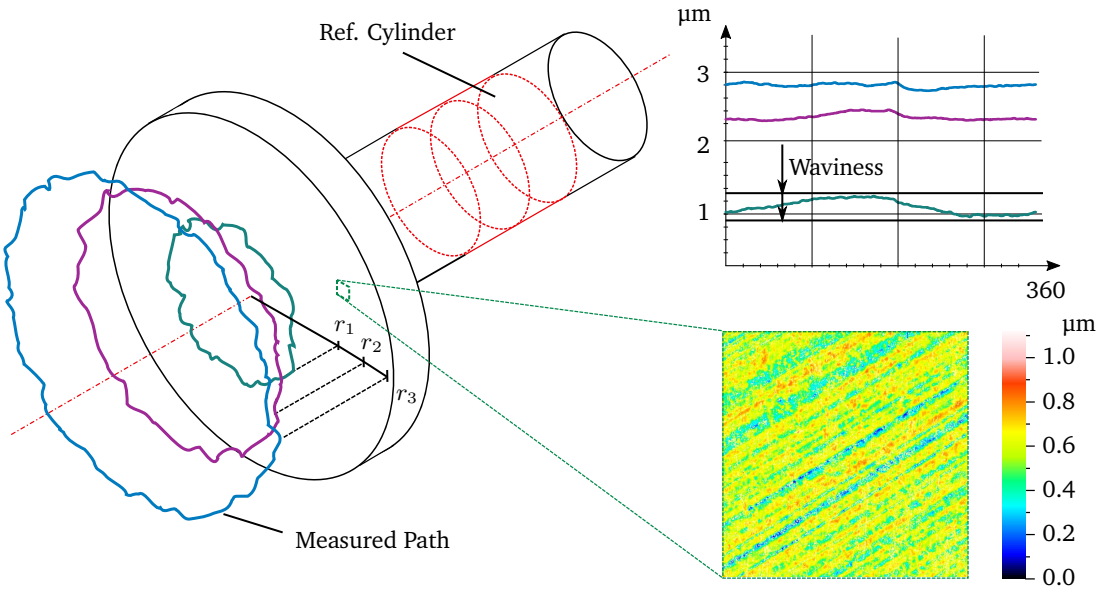

Figure 4.4.: Rotor disk surface measurements of waviness, parallelism and roughness.

Surface Properties of the Disk

The surface properties of the disk are taken into account for film height investigation. The sensitivity analysis indicates that the pre-deformation of the disk significantly affects the bearing performance, particularly concerning film height behavior. To take this into account, the film height is extended with a field variable $h_{\mathrm{RD,pre}}(x, y)$. It consists of two components based on the run-out and flatness tolerances of the disk, denoted as h_{wave} and h_{cone}, defined as follows:

$$h_{\mathrm{wave}}(x, y) = \frac{1}{2}\sin(n\,\varphi) H_{\mathrm{flat}} + \frac{1}{2}\sin\left(n\,\frac{r}{r_{\mathrm{o}}}\right) H_{\mathrm{flat}} \tag{4.1}$$

$$h_{\mathrm{cone}}(x, y) = H_{\mathrm{bend}}\left(1 - \frac{r - r_{\mathrm{i}}}{r_{\mathrm{i}}}\right) - H_{\mathrm{bend}}. \tag{4.2}$$

Here, H_{flat} represents the maximum waviness height, and H_{bend} represents the maximum pre-bending of the disk towards or away from the bearing. Consequently, the pre-deformation of the rotor disk can be expressed as:

$$h_{\mathrm{RD,pre}}(x, y) = h_{\mathrm{wave}} + h_{\mathrm{cone}}. \tag{4.3}$$

Analyses for the waviness show a negligible small influence on the bearing performance and are therefore not considered in more detail in the following. However, thermal bending plays a significant role in the bearing performance and has been found to range from $0\,\mu\mathrm{m}$ to $8\,\mu\mathrm{m}$ with respect to the outer radius of the disk, as reported by Rieken et al. [67]. This range is similar to the pre-bending arising from grinding errors, and the tolerance for this pre-bending in the test rig's rotor is set to $\pm 2\,\mu\mathrm{m}$. The direction of the actual pre-bending of the test rig's disk is of particular interest since it can either compensate for or support thermal bending, significantly influencing the bearing performance, as observed in the sensitivity analysis in Fig. 4.2a. The actual values can be derived from measurements, and Fig. 4.4 helps to illustrate this process. Based on two reference cylinders measured along the journal bearing positions on three different circles, a middle line is drawn. A plane with the middle line as a normal vector is then placed

on the disk. The heights of three different radii ($r_1,\ r_2,\ r_3$) with respect to the plane are measured and shown in the sketch on the left side. These measurements indicate a cone-like behavior with a maximum height at $r_3 = 2.4\,\mu\mathrm{m}$. The waviness, representing the deviation of each line from its mean value, is below $1\,\mu\mathrm{m}$ for all lines, in accordance with expectations from the manufacturing process. Therefore, it can be concluded that the actual pre-deformation of the rotor disk compensates for the thermal bending by a maximum amount of $2.4\,\mu\mathrm{m}$, thus improving the bearing performance by approximately $2\,\%$.
Additionally, surface roughness is important for later wear simulations and can be derived from confocal surface measurements. The test window is also shown in Fig. 4.4. The measurements reveal roughness peaks next to some straight grooves, with a maximum height of $1\,\mu\mathrm{m}$, resulting from the grinding process of the disk. The root mean square surface value is $S_\mathrm{q} = 0.19$ for the disk.

4.1.3. Analysis of Rotor Surroundings

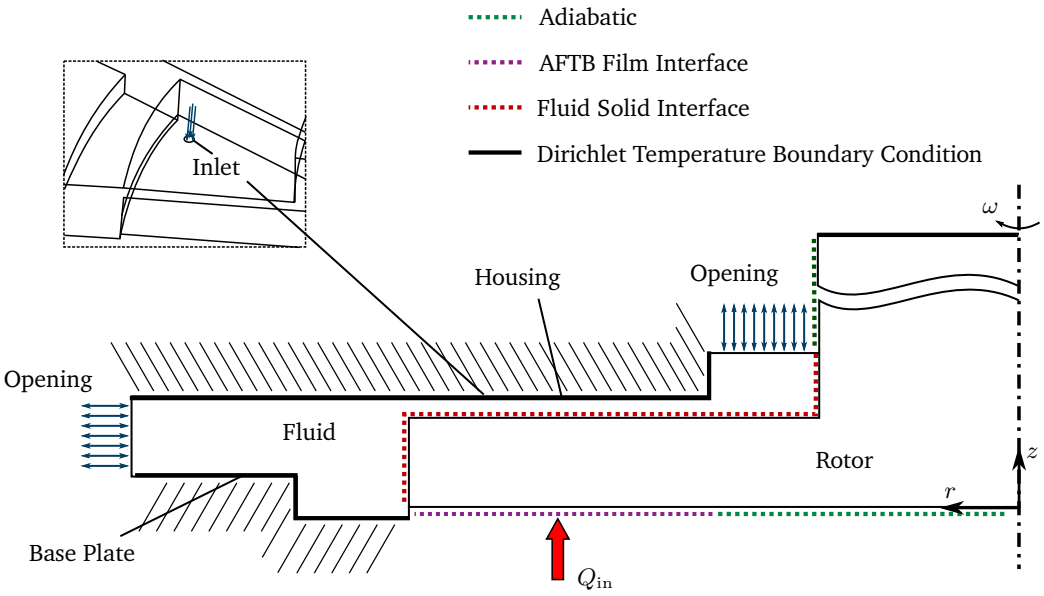

Figure 4.5.: Simulation configuration of the rotor disks peripheral flow.

Based on the sensitivity analysis of the rotor parameters, it is evident that peripheral heat transfer plays a crucial role in determining the thermal behavior of the rotor-bearing system. In the dissertation by Lehn [52], a heat transfer turbulent model is described for a one-sided axial bearing case. However, the given model differs from the test rigs setup in the following aspects:

- The original model has included free flow on the backside of the disk. Whereas here, the height of the flow in the test rig surrounding of the rotor disk is given as 1 mm and bounded by a solid wall, and therefore 0 velocity at $z = 1\,\mathrm{mm}$ in all directions (see Fig. 4.6).
- The externally pressurized thrust bearing induces cooling at the upper wall.
- Due to the bounding walls, the flow exhibits pipe flow-like behavior pulling air from the inside to the outside, with no connection to the atmosphere except for the two openings at the inner radius and the outer periphery (see Fig. 3.10).
- The original model offers two individual approaches for the radial and for the axial periphery. In the given test rig configuration, the radial periphery is connected to the axial periphery.

As a consequence, the given model does not accurately represent the rotor environment. Another drawback is the computational effort required to calculate the runner environment velocities and temperatures. One possible approach to address these issues and improve the model would be to explore existing Nusselt correlations. An overview of such correlations is provided in an article by Fénot [23]. However, due to high spinning speeds and the geometry of the disk, no known correlation seems to be suitable. Alternatively, setting up the environment in a commercial CFD solver and obtaining heat transfer coefficients from it could be more effective. This approach would involve a one-time computational effort, and subsequently, the bearing simulation could benefit from reduced computation time. One drawback of this approach is that it only represents the test rig rotor environment. When the configuration changes, such as in the real machine environment, a new model needs to be set up. However, for this work, this drawback is of minor relevance since it only requires validation of the test rig measurements. Thus, a conjugate heat transfer simulation is performed in ANSYS CFX. The model is set up to derive heat transfer coefficients for the TEHD bearing simulation. The same model as described in Sec. 3.1, which accounts for the measured side losses of the test rig, is used for this purpose. In this section, the CHT configuration is presented, along with a description of the heat transfer boundary conditions.
The 3D simulation configuration is depicted in Fig. 3.10. Furthermore, the CHT setup is presented in Fig. 4.5. The geometry aims to closely resemble the test rig setup while keeping the computational cost manageable. The configuration mainly consists of two parts: the rotor and the surrounding fluid. Each part is modeled with the following properties:

- The rotor is treated as a solid with heat diffusion and the following boundary conditions:
  - The shaft and the lower end are adiabatic, as heat transfer over these faces is expected to be lower due to their smaller radius r.
  - An air film interface Q_{in} is implemented to allow inward heat flux, representing the thrust bearing connection to the rotor.
  - Fluid-solid interfaces are applied along the interfering boundaries to the fluid domain.
  - The temperature boundary condition at the shaft's upper end is set to the fixed surrounding temperature T_0 to represent the Pelton turbine.
  - The rotor is modeled with a 30° sector and is periodic in the circumferential direction.
- In the fluid region, the total energy equation and a shear stress transport (SST) turbulent compressible air modeling are solved, along with the following boundary conditions:
  - Moving walls with $v_\varphi = \omega\, r$ are applied at all fluid-solid interfaces to account for the velocity and heat transfer to the rotor, representing the interaction with the rotor and the surrounding air.
  - Two openings with entrainment boundary conditions at atmospheric pressure p_0 are included.
  - One inlet is modeled to simulate the fluid flow of the aerostatic support thrust bearing with $m_{\mathrm{EP}} = 1\,\mathrm{g/s}$.
  - The remaining boundaries are assumed to be fixed walls with a fixed surrounding temperature T_0.

The solid part is automatically meshed within Ansys ICEM using free tetrahedral elements, while the fluid part is manually meshed. Refinement is applied to all walls, both movable and fixed, with a first layer of $3\,\mu\mathrm{m}$ thickness and a growth rate of 1.2 to ensure adequate y+ values. This results in 8 million elements in the fluid region. The height of the fluid region above the disk is set to 1 mm, which is an average value for medium to high thrust bearing loads. In such cases, the support thrust bearing at this

side of the rotor has no load-carrying capacity anymore, but its airflow is considered for cooling purposes using the inlet m_{EP}. The incoming heat flux from the air film interface is approximated by the equation:

$$Q_{\mathrm{in}} = \frac{\eta\,\omega^2\,r^2}{h\,k_{\mathrm{lf}}} dA. \tag{4.4}$$

This equation is valid for power loss estimation for flow between parallel plates, where one is spinning with ω and the other one is fixed with a distance of $h = 10\,\mu\mathrm{m}$ and a fixed viscosity η at $T = 370\,\mathrm{K}$ (see Eq. A.1). This equation grants a good distribution of applied heat dependent on the radius. The loss factor k_{lf} serves as a parameter to adjust the amount of heat that goes into the disk as a fraction of the total power loss generated in such a gap.
The simulations are performed for four different spinning speeds: 90, 100, 110, and 120 krpm. For each spinning speed, three different loss factors k_{lf} (1,1.5,2) of Eq. 4.1.3 are considered to simulate various load situations in the thrust bearing gap. It is important to note that the thrust bearing itself is not explicitly simulated, but approximate shear losses are applied on the disk. This results in a total of 16 different scenarios. Fig. 4.6 shows the resulting temperature distribution and velocity for the operating point at the maximum speed of 120 krpm with an applied loss of 220 W in the disk (with $k_{\mathrm{lf}} = 1$). The temperature distribution in the disk exhibits a radial increase from approximately $100\,^{\circ}\mathrm{C}$ at the inner radius to $204\,^{\circ}\mathrm{C}$ at the outer radius. The temperature gradient over the shaft is smaller, reaching around $20\,^{\circ}\mathrm{C}$ at the Pelton interface. The fluid temperature follows the velocity streamlines, indicating dominant convection. The velocity profile shows a maximum velocity of 340 m/s at the outer disk interface. The velocity is forced to become zero at all fixed walls, such as the upper wall above the disk and the base plate. Due to centrifugal forces, the fluid is pulled outwards over the disk, leading to a pipe-like flow from the inner to the outer diameter of the disk. To maintain mass conservation, fluid is pulled through the inner opening and then ejected at the outer opening. A vortex is visible at the radial periphery, similar to Taylor vortices described in literature for incompressible flow [35].

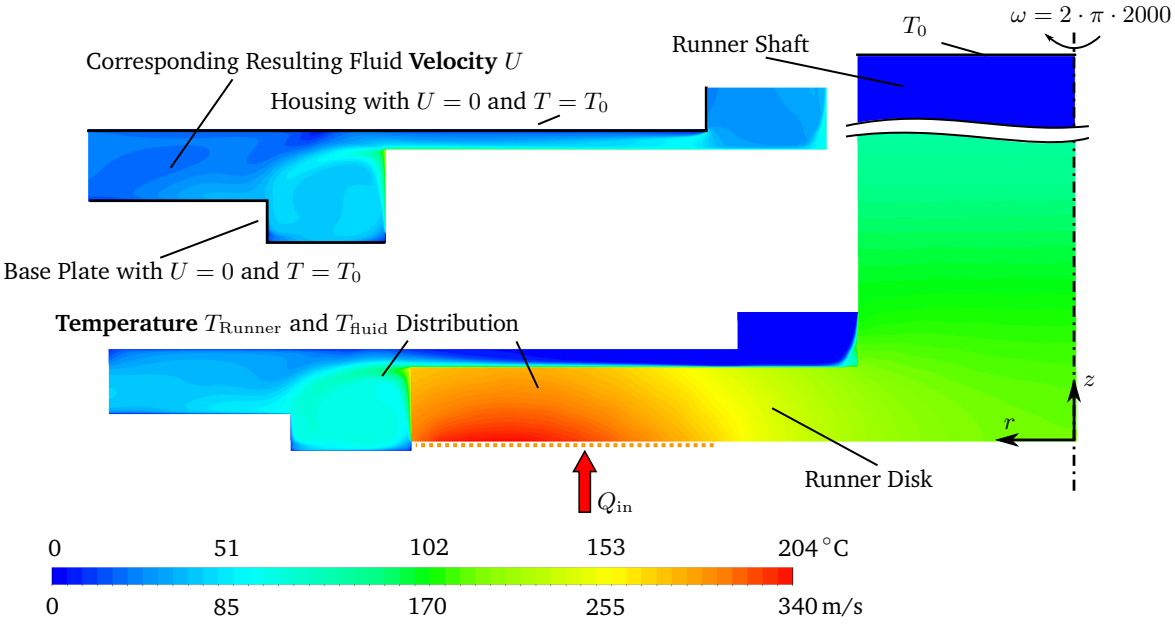

Figure 4.6.: CHT results of the rotor disk and its environment. Fluid velocity and temperature evaluation.

An energy balance evaluation can be performed to analyze the results for all heat fluxes at the rotor's

boundaries, which are based on Fig. 2.7. The heat fluxes are composed as follows:

$$Q_{\mathrm{RD}} = Q_{\mathrm{ax,P}} + Q_{\mathrm{rad,P}} + Q_{\mathrm{RR}} = 157\,W + 44\,W + 17\,W. \tag{4.5}$$

This indicates that around 70 % of the applied loss is carried away by the surrounding fluid in the axial periphery, while 20 % is carried away over the radial periphery. Q_{RR} can be further divided into 13 W (6 %) flowing over the Dirichlet boundary condition at the rotor's end, and the remaining 4 W (2 %) flowing over the rotor at the small fluid region below the first journal bearing. Additionally, the simulated

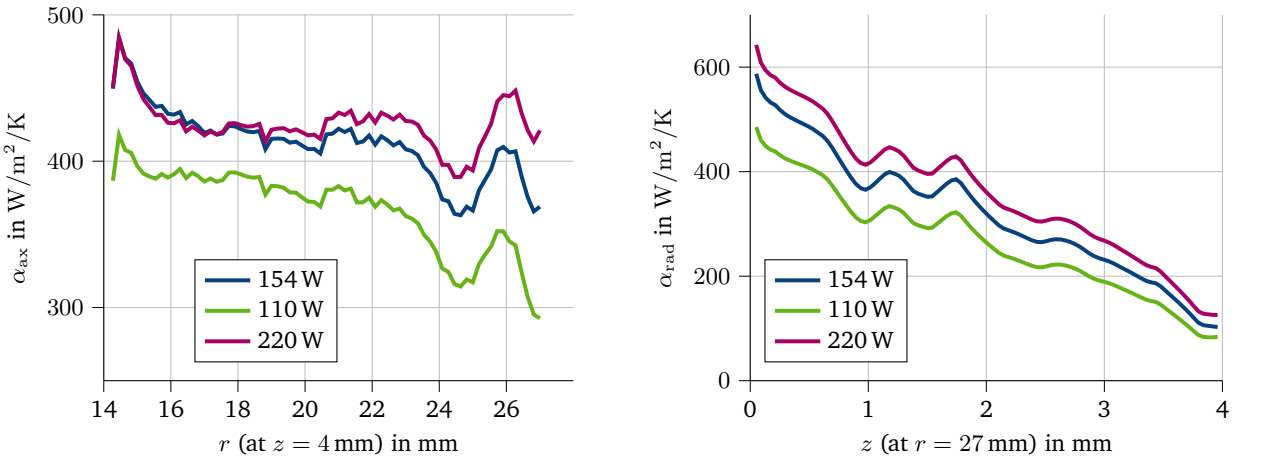

(a) CHT resulting heat transfer coefficient over the r-coordinate at the axial disk surface.

(b) CHT resulting heat transfer coefficient over the z-coordinate at the radial disk surface.

Figure 4.7.: CHT results of α-values.

heat transfer coefficients are analyzed. Fig. 4.7 displays three scenarios to examine the heat transfer coefficients more closely. On the left side (Fig. 4.7a), the heat transfer coefficient is plotted over the radius r of the disk at the axial periphery. It can be observed that higher applied losses result in more heat being carried away in this area, which is reasonable since temperature gradients are higher for higher applied losses. The heat transfer coefficient fluctuates along the radius r primarily because of the highly turbulent flow induced by the EP-inlet mass flow of the EP thrust bearing (refer to Fig. 4.5). On the right side (Fig. 4.7b), the heat transfer coefficient at the radial periphery is plotted over the disk height coordinate z. The dependencies appear to be clearer than for the axial one. The alpha values increase with higher power loss conducted into the disk, and a linear dependency on the z-coordinate is evident. This section aims to determine simple heat transfer coefficients and reduce complexity of modeling the heat exchange of the rotor. At this point, the heat transfer coefficients seem to be dependent on power loss and the geometry coordinate. The first simplification is to calculate average heat transfer coefficient for both axial and radial periphery. These average values are taken into account instead of both linear functions. The relationship between the heat transfer coefficient and power loss is discussed further below. However, the dependency on the power loss is more complicated, as it is a result of the complex gap function, spinning speed, and fluid temperatures. In order evaluate these dependencies, the applied loss can be plotted as a function of the resulting temperature $T_{\mathrm{RD,disk}}$ in Fig. 4.8 for all simulated scenarios (spinning speed $n = 90...120$ krpm, $k_{\mathrm{lf}} = 1...2$). The temperature is evaluated at the same position where the radial pyrometer is located in the high-speed test rig (compare Sec. 3.1.1). The plot reveals an almost perfect linear correlation between the radial temperature $T_{\mathrm{RD,disk}}$ and the applied heat Q_{RD}. The speed seems to have a negligible influence on the temperature; for example, the two points at 150 W produce almost the same temperature, despite a speed difference of 20 krpm between them.

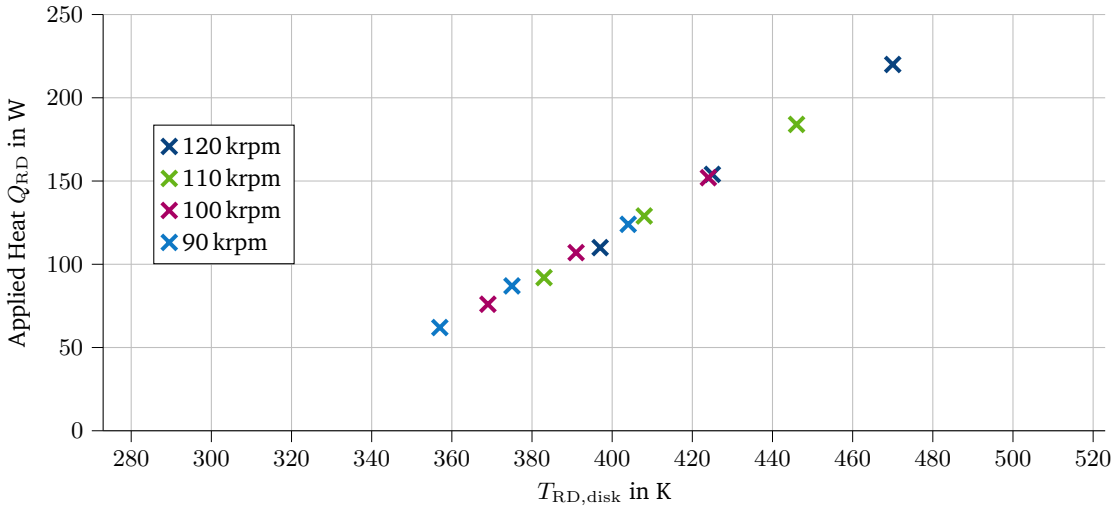

Figure 4.8.: Induced power loss into the rotor disk over radial mean disk temperature.

Next, mean values ($\bar{\alpha}_{\mathrm{ax}}$, $\bar{\alpha}_{\mathrm{rad}}$) of $\alpha_{\mathrm{ax}}(r)$ and $\alpha_{\mathrm{rad}}(z)$ are calculated for each operating point, resulting in the following plot in Fig. 4.9, where the mean α-values for the axial and radial periphery are plotted as a function of the radial disk temperature $T_{\mathrm{RD,disk}}$. The simulated average heat transfer coefficients behave

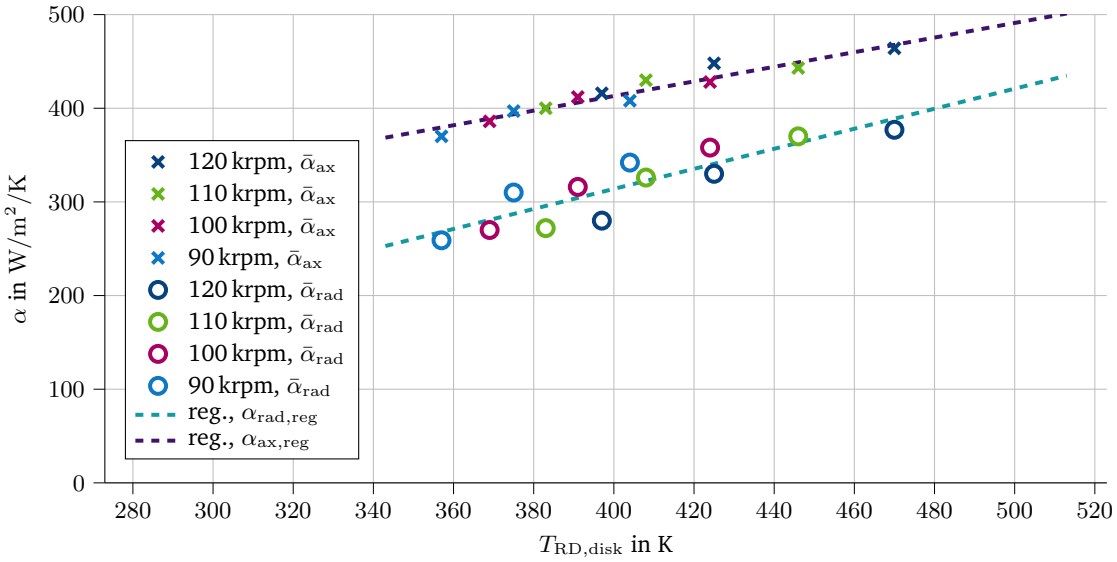

Figure 4.9.: CHT Resulting heat transfer coefficient as a function of the simulated radial disk temperature.

almost linearly with increasing simulated temperature. Therefore, a linear regression can be applied for both positions:

$$\alpha_{\mathrm{rad,reg}}(T_{\mathrm{RD,disk}}) = 1.07\,\mathrm{W/m^2/K^2} \cdot T_{\mathrm{RD,disk}} + 178\,\mathrm{W/m^2/K} \tag{4.6}$$

$$\alpha_{\mathrm{rad,reg}}(T_{\mathrm{RD,disk}}) = 0.78\,\mathrm{W/m^2/K^2} \cdot T_{\mathrm{RD,disk}} + 314\,\mathrm{W/m^2/K}. \tag{4.7}$$

Thus, the heat transfer from the disk into the surrounding periphery depends only on the disk temperature, which, in turn, is proportional to the conducted heat from the thrust bearing gap.
Based on this CHT analysis, it can be concluded that a proper heat transfer model is crucial for correct

disk modeling, as almost 90 % of the thrust bearing's power loss carried into the disk is dissipated through convection at the axial and radial periphery surfaces. Consequently, both derived heat transfer coefficients serve as input for the rotor boundary conditions in the adapted AFTB-TEHD-simulation model.

4.1.4. Derived Rotor Boundary Conditions

As demonstrated in the sensitivity analysis in Fig. 4.2c, accurately modeling the runner environment is crucial for achieving an accurate thermal analysis. In this section, adjustments are made to the runner modeling to better represent the test rig design. The modeled disk with its interfaces is shown in Fig. 4.10, where seven different boundaries are labeled. The interface boundary conditions are set as follows:

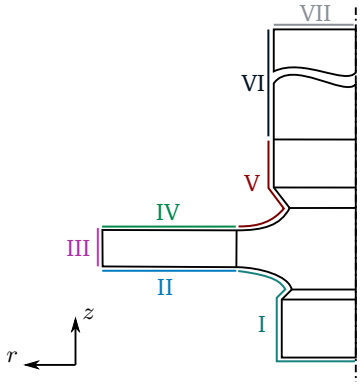

Figure 4.10.: Labels for rotor TEHD simulation boundary conditions.

I and V: Zero Flux

Based on the CHT analysis, it can be concluded that the heat fluxes over these boundaries are negligibly small. Therefore, these boundaries are set as adiabatic (zero flux).

II: Thrust Bearing Air Film Interface

The thrust bearing air film interface is defined by taking the mean heat flux over the circumference of the energy equation at its upper boundary:

$$-n\,\Gamma_{\mathrm{II}} = \frac{n_{\mathrm{pad}}}{\varphi_{\mathrm{pad}}} \int_0^{\varphi_{\mathrm{pad}}} \frac{2\,\lambda\,r}{h} \frac{\partial\,T}{\partial z} d\varphi. \tag{4.8}$$

It is assumed that the high spinning speed of the disk leads to temperature averaging effects over the circumference, allowing the rotor geometry to be considered as 2D rotationally symmetric [52].

III and IV: Periphery CHT

The runner periphery is treated with Neumann heat transfer coefficient interface values obtained from CHT calculations. Based on the investigations in Sec. 4.1.3, the boundary conditions are set to:

$$-n\Gamma_{\mathrm{rad,P}} = \alpha_{\mathrm{rad,P}}\ (T_{\mathrm{RD}} - T_0) \tag{4.9}$$

$$-n\Gamma_{\mathrm{ax,P}} = \alpha_{\mathrm{ax,P}}\ (T_{\mathrm{RD}} - T_0)\,. \tag{4.10}$$

These correlations are only valid for this specific rotor, its surroundings, and spinning speed over 90 krpm, as they are solely dependent on the temperature and not the spinning speed.

VI: Aerostatic Journal Bearings

The two EP journal bearings are supported by a constant flow of fresh air and also experience dissipation heat flux due to shear stresses in the small gap. It is assumed that the fresh air flow compensates for the dissipated fluxes. Consequently, the journal bearings can be modeled as having a conductive heat flux over a small gap. The gap height of the test rig's journal bearing is determined from the manufacturing measurement sheet and set to a constant value of $t_{\mathrm{JB,gap}} = 12\,\mu\mathrm{m}$ for the used rotor housing combination. The applied Neumann conditions read as follows:

$$-n\Gamma_{\mathrm{VI}} = \frac{\lambda_{\mathrm{JB}}\left(T_{\mathrm{RD}} - T_0\right)}{t_{\mathrm{JB,gap}} - v_{\mathrm{RD,r}}}, \tag{4.11}$$

where $v_{\mathrm{RD,r}}$ is the radial displacement component of the rotor, and λ_{JB} is the mean thermal conductivity of the air in the journal bearing's gap.

VII: Pelton Drive

The Pelton drive interface is set as a constant temperature Dirichlet boundary condition.
In summary, this section models the rotor with the actual dimensions of the test rig. An extension to the film height due to manufacturing errors is introduced. Additionally, the boundary conditions are established, with many of them derived from the CHT simulation.

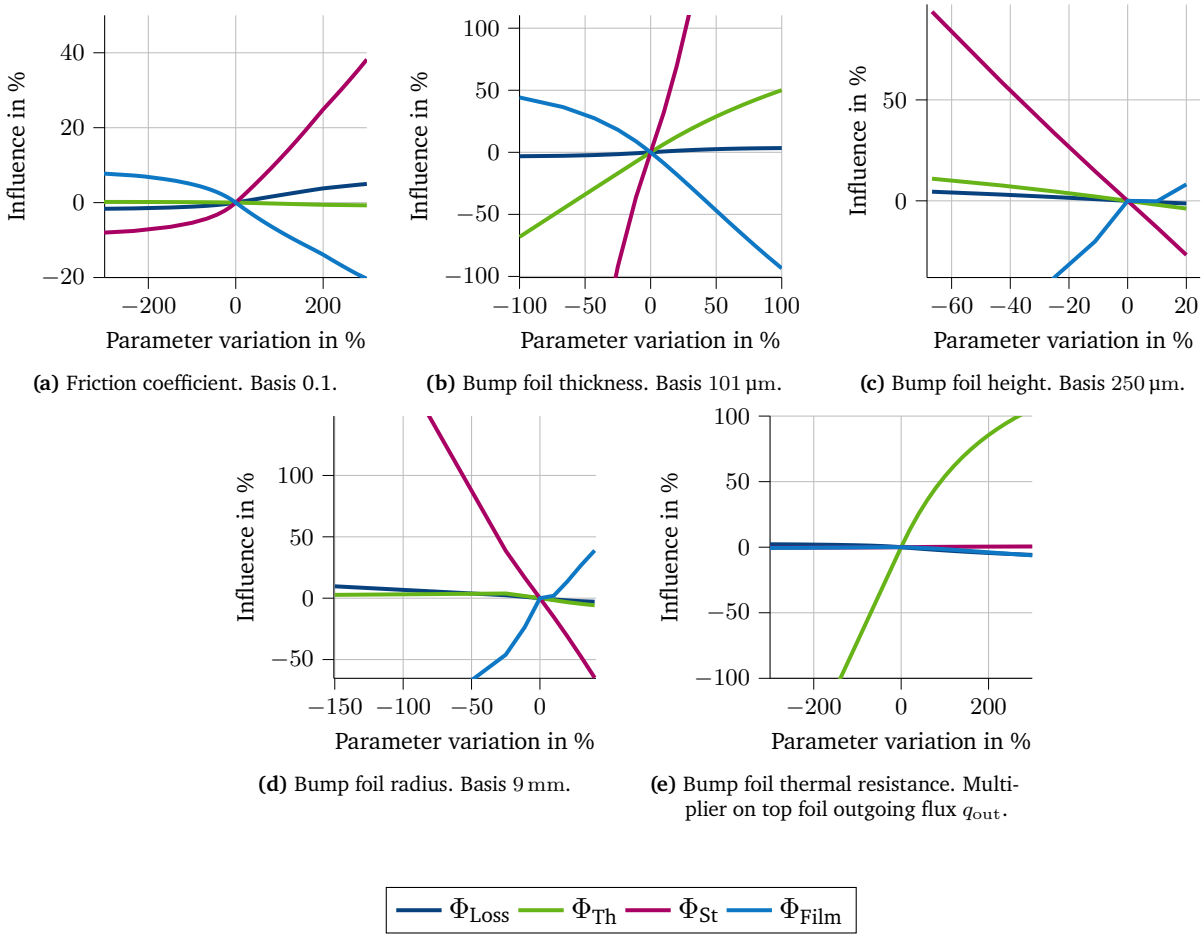

(a) Friction coefficient. Basis 0.1.

(b) Bump foil thickness. Basis 101 µm.

(c) Bump foil height. Basis 250 µm.

(d) Bump foil radius. Basis 9 mm.

(e) Bump foil thermal resistance. Multiplier on top foil outgoing flux q_{out}.

Figure 4.11.: Sensitivity analysis on bump foil parameters.

4.2. Bump Foil

This section discusses the bump foil based on a sensitivity analysis. It presents the geometry, measured input, and associated uncertainties. Moreover, an extension to the basic thermal resistance model is presented using the sensitivity analysis results. Finally, the friction coefficients between the bump foil and the base plate, and the bump foil and the top foil are measured and discussed.

4.2.1. Sensitivity Analysis on Bump Foil Parameters

The sensitivity analysis of bump foil input parameters is depicted in Fig. 4.11, simulated using the original model introduced in Sec. 2.2, with a thrust load $F_{\text{thrust}} = 100\,\text{N}$ and a spinning speed n of 120 krpm. The first parameter examined is the friction coefficient, as shown in Fig. 4.11a. Changes in this parameter influence all evaluation metrics except for the thermal property. The stiffness metric Φ_{st} is particularly affected. Alterations in the friction coefficient not only lead to variations in integral stiffness but also influence the individual stiffness of the interconnected bump arcs due to their connections. This phenomenon can explain the changes in the film quantity Φ_{Film}, which, albeit minor, could still impact the bearing's performance. While substantial variations of 200 % are not anticipated, classification of the friction value suitable to the given material pairing is essential. Hence, friction coefficients for this

bearing setup are measured as discussed in Sec. 4.2.4.
The second parameter investigated is the bump foil's thickness, as shown in Fig. 4.11b. In terms of stiffness, a sensitivity analysis is unnecessary due to the cubic dependence between thickness and stiffness derived from the governing equations in Chap. 2.2.4. However, the analysis reveals the impact of thickness changes on the thermal quantity Φ_{Th} and the film quantity Φ_{Film}. The bump foil's thickness emerges as a highly sensitive parameter, necessitating careful determination to avoid simulation result uncertainties in light of even minor inaccuracies in the micron range. Conversely, the bump foil thickness's influence on the loss quantity Φ_{Loss} remains limited. This indicates that bump foil stiffness plays a minor role in bearing performance under aligned conditions.
Similar observations arise when considering radii and height changes in Fig. 4.11d and Fig. 4.11c. The system's stiffness undergoes significant changes, while the loss quantity remains relatively constant over a wide range. The thermal parameter also exhibits minimal variation. As with most other parameters, the film quantity proves highly sensitive.
The final parameter under investigation is the bump foil's thermal resistance, depicted in Fig. 4.11e. The thermal resistance in the top foil's flux (cf. Sec. 2.2.3) is scaled by a factor. This underscores the criticality of knowing the bump foil's thermal resistance for accurate thermal modeling of the rotor-bearing system. Other metrics display weaker sensitivity, emphasizing the insufficiency of solely examining bearing performance to fully comprehend its behavior.
Numerous other geometrical parameters relate to bump foils. However, these display lower sensitivity concerning the considered metrics. Nonetheless, they are evaluated based on measurements and accurately incorporated into the simulation model (see Tab. 4.2).

4.2.2. Modeling Based on Measured Input

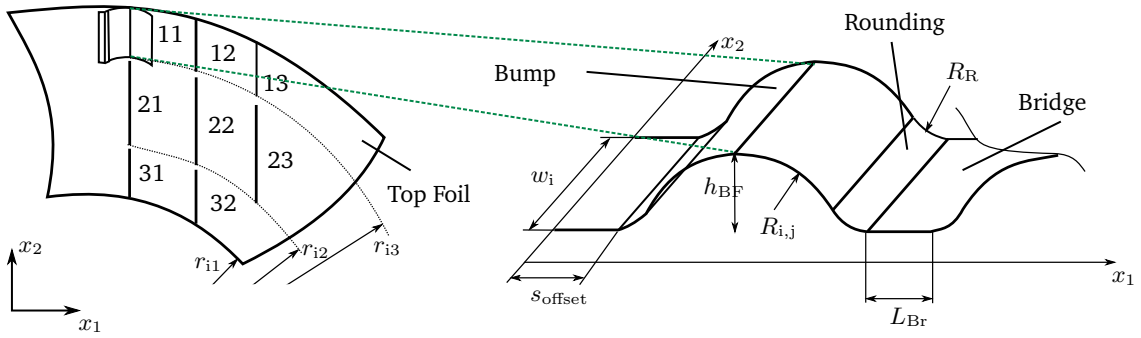

Figure 4.12.: Bump foil geometry sketch. Positions and of the bump foil as well as geometric properties.

Each bump foil segment comprises three bump strips: the outer strips house three bumps each, while the inner strip features two bumps. These strips connect via holding arms, attached to the base plate. Fig. 4.12 illustrates the geometry. Each bump consists of a bridge, a rounding, the bump arc, and a final rounding. The three strips connect at the first bridge with an offset s_{offset}. Measured input parameters are used to determine all essential values. For precision, a microscopic image of the middle strip's cross-section, presented in Fig. 4.13, is analyzed. Given that cross-section measurements are destructive, three bumps from the same batch, not employed in test rig measurements, are used. Key measurements are summarized in Tab. 4.1. The roughness parameters are input for the thermal resistance model (cf. Eq. 2.2.4). The "Variation" column represents standard deviations from mean measurements, crucial for the uncertainty estimation (Sec. 4.4).

Table 4.1.: Bump foil measured parameters.

Parameter	Value	Variation	Description
$R_{\mathrm{i},1}$	9.13 mm	$\pm 3\,\%$	radius of 1st bump
$R_{\mathrm{i},2}$	8.87 mm	$\pm 3\,\%$	radius of 2sd bump
$R_{\mathrm{i},3}$	5.32 mm	$\pm 3\,\%$	radius of 3rd bump
w_1	3.37 mm	-	width of 1st strip
w_2	5.75 mm	-	width of 2sd strip
w_3	3.373 mm	-	width of 3rd strip
R_{R}	0.15 mm	-	radius of the roundings
L_{Br}	0.561 mm	-	length of the bridges
h_{BF}	0.255 mm	$\pm 8\,\%$	height of bump foil
t_{BF}	0.101 mm	$\pm 0.5\,\%$	thickness of bump foil
s_{offset}	0.118 mm	-	offset of the bumps
$r_{\mathrm{i}1}$	14 mm	-	starting radius of the first bump strip
$r_{\mathrm{i}2}$	17.63 mm	-	starting radius of the second bump strip
$r_{\mathrm{i}3}$	23.63 mm	-	starting radius of the third bump strip
$S_{\mathrm{a,Base}}$	$0.35\,\mu\mathrm{m}$	-	surface roughness of the base plate
$S_{\mathrm{a,BF}}$	$0.3\,\mu\mathrm{m}$	-	surface roughness of the bump foil
$S_{\mathrm{a,TF}}$	$0.63\,\mu\mathrm{m}$	-	surface roughness of the top foil

4.2.3. Thermal Resistance

As evident from the sensitivity analysis in Fig. 4.11e, the thermal resistance significantly affects the thermal behavior. Therefore, this section focuses on an in-depth investigation of the foil package's thermal resistance. Thermal resistance measurements are conducted on the thermal resistance test rig detailed in Sec. 3.2 and evaluated in Sec. 5.4.1, based on geometric properties outlined in Sec. 4.2.2. The benchmark thermal resistance for the test bearing is $R_{\mathrm{th}} = 4.16\,\mathrm{K/W}$, considering the measured bump geometry and surface roughness (simulated with the basic model from Sec. 2.2). Examining the bearing topology (e.g., Fig. 2.5), it is evident that contact lines are fewer compared to other bearing types in literature. This prompts investigation into other possible heat paths for this bearing type and its surroundings.
Initially, a limit value analysis helps assess the situation: Assuming the region beneath the top foil contains only air and no steel from the bump foil, yields the worst-case conductivity scenario. Fig. 4.14a illustrates the thermal resistance $R_{\mathrm{th,air}}$ of the air gap under the top foil against the distance from the top foil to the base plate $s_{\mathrm{TF,Base}}$. The resistance can be expressed as:

$$R_{\mathrm{th,air}} = \frac{s_{\mathrm{TF,Base}}}{\lambda_{\mathrm{Air}}\, A_{\mathrm{Bearing}}}. \tag{4.12}$$

For $s_{\mathrm{TF,Base}} \leq 400\,\mu\mathrm{m}$, the thermal resistance is below 10 K/W, similar to the model's thermal resistance ($R_{\mathrm{th}} = 4.16\,\mathrm{K/W}$). Given the bump height and bump foil thickness are both below $400\,\mu\mathrm{m}$, an extension to the model is necessary. Defining the distance from the top foil to the base plate as:

$$s_{\mathrm{TF,Base}} = v_{3\mathrm{TF}} + h_{\mathrm{BF}} + t_{\mathrm{BF}} + h_{\mathrm{Shape}}. \tag{4.13}$$

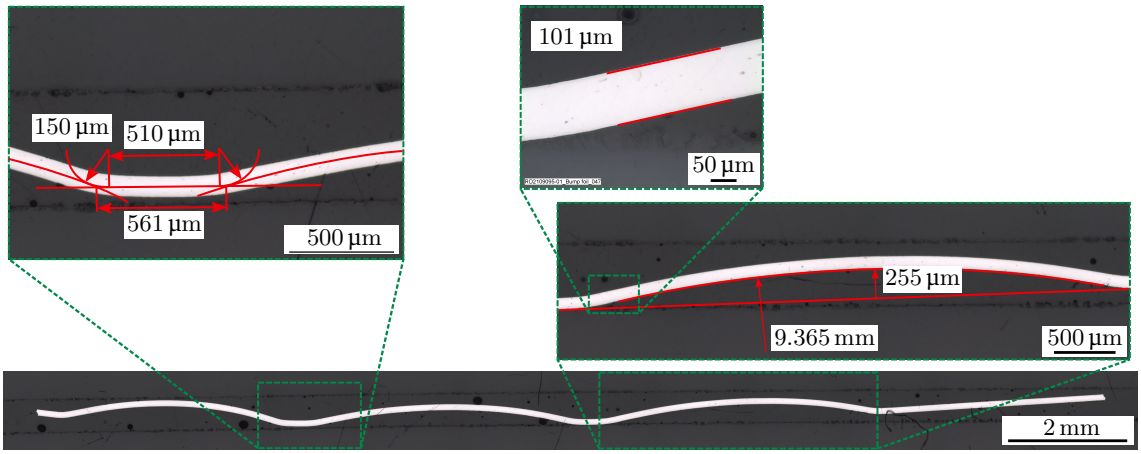

Figure 4.13.: Bump foil cross-section microscopic image of one bump strip. With zoom boxes for detailed geometric properties.

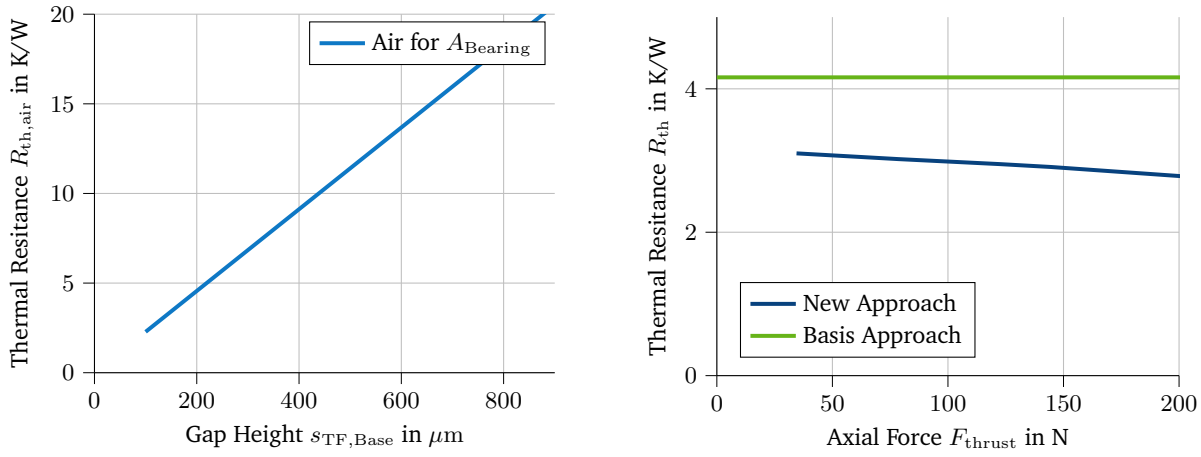

(a) Thermal resistance of the air gap under the top foil, dependent on the bump height.

(b) Simulated thermal resistance with the basis approach and the extended bump foil thermal resistance approach.

Figure 4.14.: Thermal resistance calculations under the top foil.

Here, h_{Shape} is defined later in Sec. 4.3.5, involving the pre-deformation of the top foil. The thermal resistance can then be defined as:

$$R_{\mathrm{Th,Air}} = \begin{cases} 0 & \text{Contact Locations of Bumps} \\ \frac{2\,s_{\mathrm{TF,Base}}}{\lambda_{\mathrm{TF,Air}}+\lambda_{\mathrm{Base,Air}}} & \text{Locations between Bumps.} \end{cases} \tag{4.14}$$

In this context, $\lambda_{\mathrm{TF,Air}}$ and $\lambda_{\mathrm{Base,Air}}$ represent the heat transfer coefficients of air calculated at the top foil and base plate, respectively. Therefore, the above equation uses an average heat transfer coefficient of air, assuming a linear temperature profile between the top foil and the base plate. Lehn's heat resistance model is extended by incorporating $R_{\mathrm{Th,Air}}$ as an outward heat flux on the top foil:

$$-n\Gamma = -\frac{T_{\mathrm{TF}} - T_{\mathrm{Base}}}{R_{\mathrm{Th,Air}}}. \tag{4.15}$$

Simulation results of this extension are shown in Fig. 4.14b, where the calculated thermal resistance R_{th} is shown as a function of the thrust force F_{thrust}. It can be seen, that the basis approach is not dependent

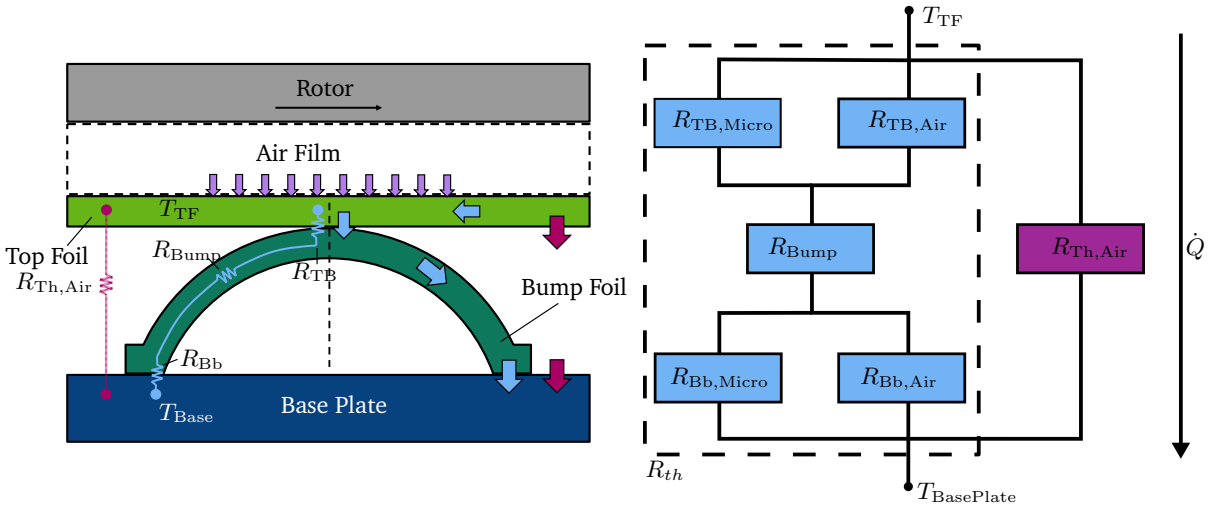

Figure 4.15.: Extended thermal resistance model based on the work of Lehn [53].

on the thrust force, whereas the new approach is. This can simply be explained by the decreasing distance from the top foil to the base plate with increasing thrust force. Thus, the resulting thermal resistance can be $25\,\%$ lower with the new approach compared to the basis approach for a thrust load of 100 N.
Additionally, the base plate temperature is often assumed constant. Yet, real-world observations indicate a different scenario where the base plate is water-cooled. While the cooling liquid's temperature remains constant, the cooling channel is often at a finite distance from the base plate surface, incurring a thermal resistance. The resistance approximates as:

$$R_{\mathrm{th,Base}} = \frac{t_{\mathrm{Base}}}{\lambda_{\mathrm{Base}}\, A_{\mathrm{base}}}. \tag{4.16}$$

For the test rig's base plate with $t_{\mathrm{Base}} = 12\,\mathrm{mm}$ thickness and $\lambda_{\mathrm{Base}} = 30\,\mathrm{W/m/K}$ thermal conductivity, $R_{\mathrm{th,Base}} = 0.24\,\mathrm{K/W}$. This must be factored in for validation and comparison with measurements in Sec. 5.4.2.

4.2.4. Friction Coefficient

The friction coefficient between the top and bump foil, and between the bump foil and base plate, is determined through tangential and normal force measurements in the BRUKER Tribolab test bench (cf. Sec. 3.3.1). Tests between base plate and bump foil involve three different single bumps, each repeated 30 times for robust statistics. This process is repeated thrice to account for assembly uncertainties. Fig. 4.16a presents the resulting friction coefficients for these tests, using a normal load of 0.5 N. The mean coefficient over all tests is 0.17, with a standard deviation of 0.04 or $\pm 23\,\%$ for the bump foil and base plate contact.
The contact between the bump arc and the lower side of the top foil is investigated similarly, as detailed in Sec. 3.3.1. Fig. 4.16b illustrates results for tests between three bump arcs and three positions on the top foil. The mean coefficient is 0.1, with a smaller standard deviation of 0.006, attributed to the anti-friction effect of the coating layer on the top foil, since droplets of the coating layer are also visible on the back side of the top foil from the coating process of the front side.
The presented results are assessed at one normal force. To eliminate normal force dependency on the friction coefficient, tests are conducted at different forces. Fig. 4.17 displays the averaged friction

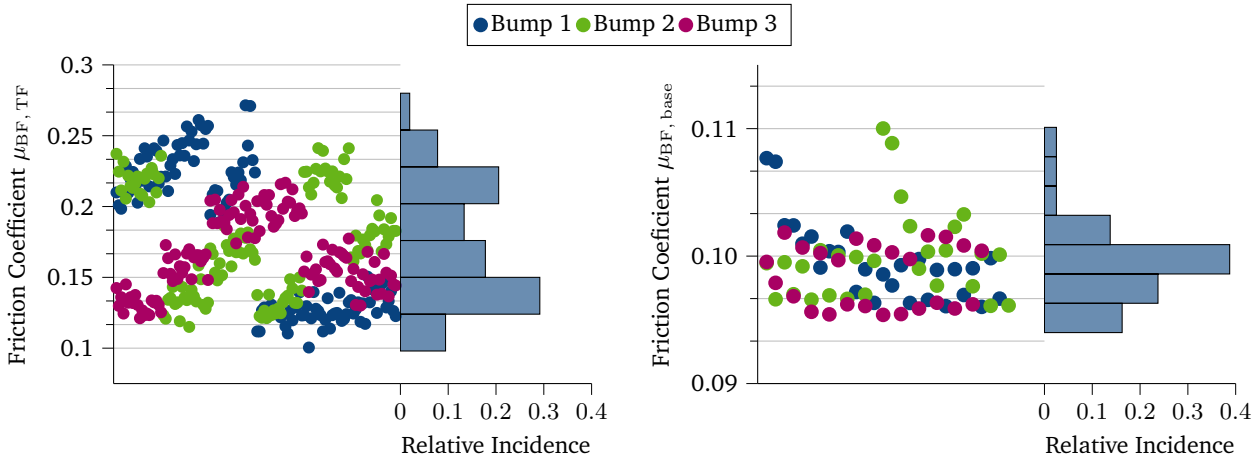

(a) Friction coefficient between bump foil and base plate with a mean value of 0.17 and a standard deviation of 0.04

(b) Friction coefficient between top foil and bump foil with a mean value of 0.1 and a standard deviation of 0.006.

Figure 4.16.: Measured friction coefficients of the air foil thrust bearing.

coefficient and standard deviation for the bump foil and base plate contact. A negligible dependency on the normal force is observed, maintaining similar standard deviation magnitude across all forces. Consequently, fixed values for the tested parameter space can be established for both contact pairs, yielding:

$$\mu_{\mathrm{BF,TF}} = 0.1 \tag{4.17}$$

$$\mu_{\mathrm{BF,base}} = 0.17. \tag{4.18}$$

The associated standard deviation is incorporated into the uncertainty estimation (Sec. 4.4).

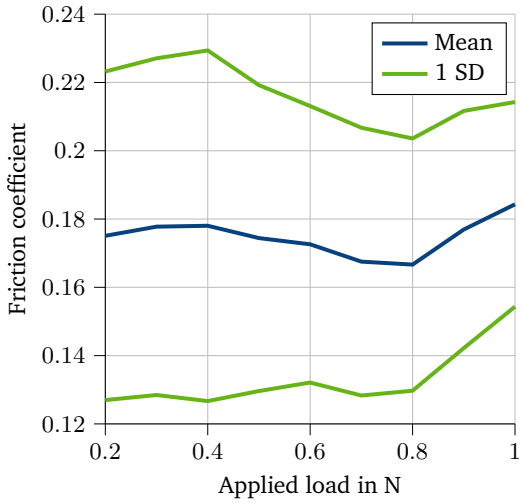

Figure 4.17.: Friction coefficient measurements with respect to the applied load.

4.3. Top Foil and Air Film Height

This section presents the modeling and adjustments conducted for the top foil and film height. At first a sensitivity analysis is performed to identify influential inputs for top foil modeling. Subsequently, the modeling process based on measured inputs is discussed, with a focus on the top foil step and coating distribution. Given the unique step's extent, the continuous top foil is modeled differently from other top foils, elaborating on the chosen approach's advantages and disadvantages. Additionally, a wear algorithm is introduced to address coating distribution wear during running-in processes. The section concludes by summarizing film height variables and parameters.

4.3.1. Sensitivity Analysis on Top Foil Parameters

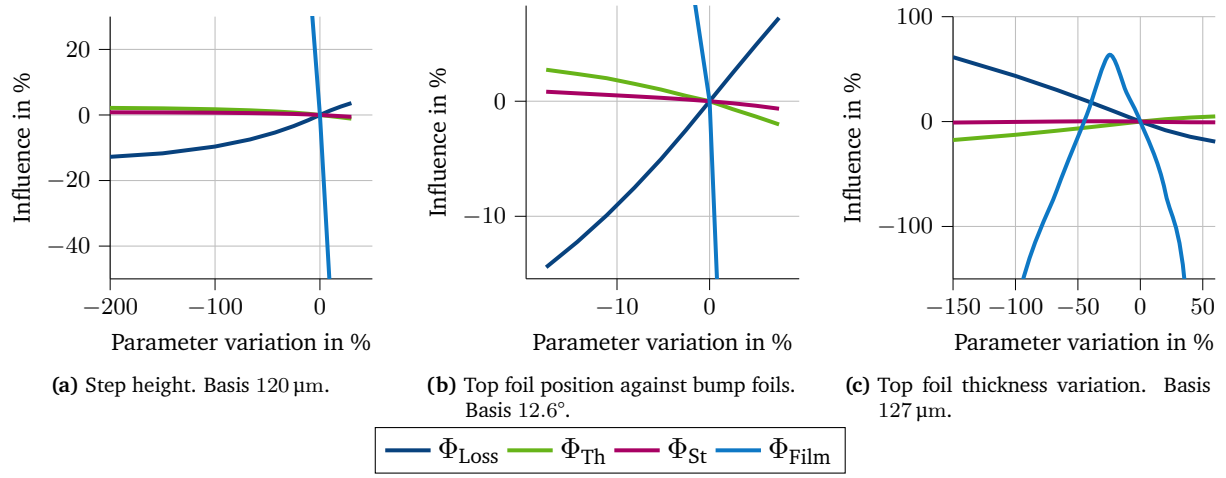

(a) Step height. Basis 120 µm.

(b) Top foil position against bump foils. Basis 12.6°.

(c) Top foil thickness variation. Basis 127 µm.

Figure 4.18.: Sensitivity analysis on top foil parameters.

Fig. 4.18 illustrates the sensitivity analysis of top foil parameters. Three parameters are varied to assess their impact on four output quantities (introduced in Section 2.4.2). These analyses use the simulation model from Section 2.2, with a thrust load of $F_{\mathrm{thrust}} = 100\,\mathrm{N}$ and a spinning speed n of 120 krpm.
The first parameter studied is the step height of the annular-shaped top foil. The results are shown in Fig. 4.18a. This parameter has a limited effect on thermal behavior Φ_{TH} and stiffness Φ_{St}, but significantly influences performance by decreasing the loss factor Φ_{Loss}. Notably, the film height factor Φ_{Film} exhibits the highest sensitivity, making step height a critical geometric parameter that requires thorough evaluation. This conclusion is reinforced by the analysis of the φ_{negT} parameter graph in Fig. 4.18b, where the influence is pronounced within the range of $-20\,\%$ to $5\,\%$. Finally, the third parameter investigated is the top foil's thickness t_{TF}, shown in Fig. 4.18c. This parameter significantly affects the loss factor Φ_{Loss} and has a non-linear impact on the film factor Φ_{Film}.

4.3.2. Modeling Based on Measured Input

The topography of the top foil is presented in Fig. 4.19. The examined top foil is a continuous annular foil with six interconnected pad segments, separated by a stamped step defined by a curvature radius $r_{\mathrm{step}} = 13\,\mathrm{mm}$, centered at the outer radius $r_{\mathrm{o}} = 27\,\mathrm{mm}$, and an inner radius $r_{\mathrm{i}} = 14\,\mathrm{mm}$. Other input parameters are determined using white-light interferometric (WLI) measurements of the entire top foil.

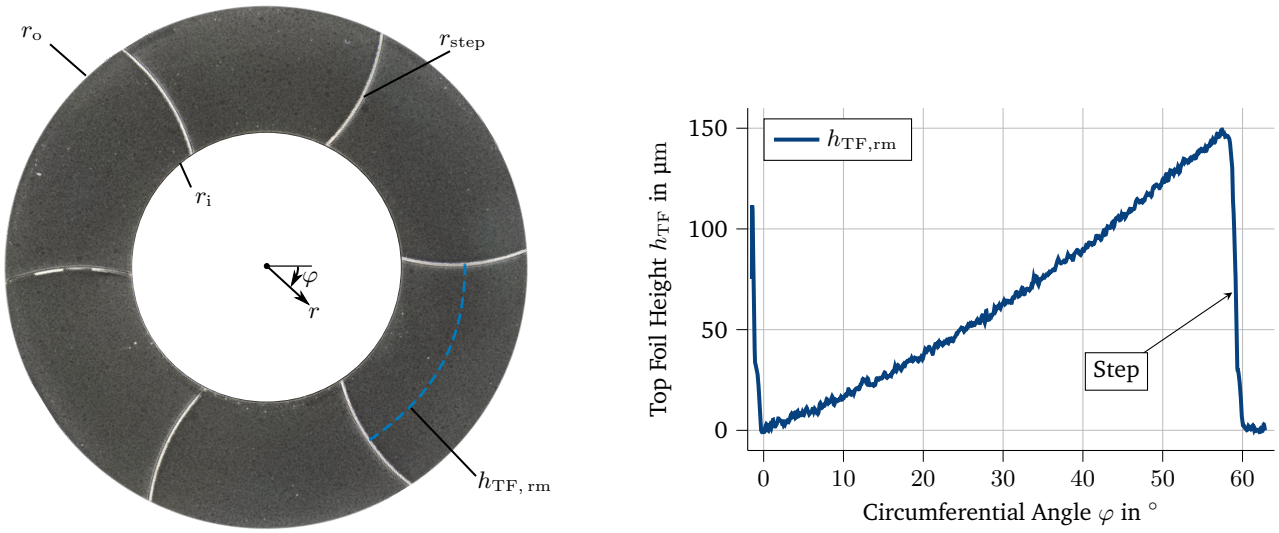

Figure 4.19.: Microscopic image of the top foil and a measured height profile (WLI measurement) of the top foil on its middle radius ($r_m = 20.5\,\text{mm}$).

Detailed analysis of the geometry, described in Section 3.4, relies on ZYGO Nexview NX2 WLI images acquired from both the back side (WLI_{back}) and coating side (WLI_{top}).

Top Foil Slope

The measured height profile of a pad along its middle radius $r_m = 20.5\,\text{mm}$ across the circumferential angle φ is displayed in Fig. 4.19. This profile exhibits a continuous slope from 0 at $\varphi = 0\,°$ to $147\,\mu\text{m}$ at $\varphi = 58.05\,°$, returning to 0 at $\varphi = 60\,°$. This implies a step width $s_w(r = r_m)$ of $1.95\,°$ or $700\,\mu\text{m}$ and a step height $s_h(r = r_m)$ of $147\,\mu\text{m}$ on the middle radius r_m. An analysis of height profiles on various radii examines the complete top foil's relation to the step height and width. They are discussed in the following.

Top Foil Step

The step's importance in the top foil's geometry is evident from the sensitivity study. In order to analyze the complete top foil with respect to the step-height and step-width, several height profiles on different radii are evaluated. The results of these measurements are displayed in Fig. 4.20a and Fig. 4.21a, which depict step-width and step-height as a function of the radius r for all six steps of the top foil segments. Note that the number of measurement points in radial direction was rather large in order to precisely detect the step-width as a function of the radius r (height measurements from the inner top foil radius r_i to the outer radius r_o in 0.01 mm steps along the curvature of the step).
In connection with the measurement of step-width and step-height, it should be pointed out that the step connecting two adjacent pad segments is not a straight line in radial direction, which can clearly be seen in Fig. 4.19. Hence, the step-widths and step-heights depicted in Fig. 4.20a and Fig. 4.21a have not been evaluated at a constant angle φ, but along the curvature of the steps by means of a comparatively elaborate analysis. Based on the WLI measurements of the complete top foil, the step-width and step-height have been determined—for each of the six pads individually—along the curvature of the corresponding step. For that purpose, the difference between the highest and the lowest point of the profile has been determined along the curvature of each step. The step-width is the circumferential

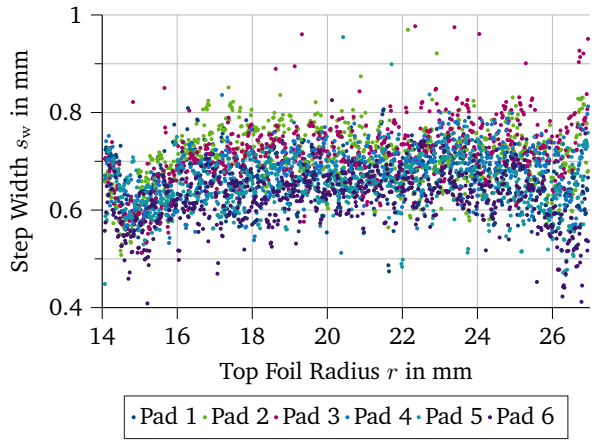

(a) Measured step width of the specimen of all 6 pads.

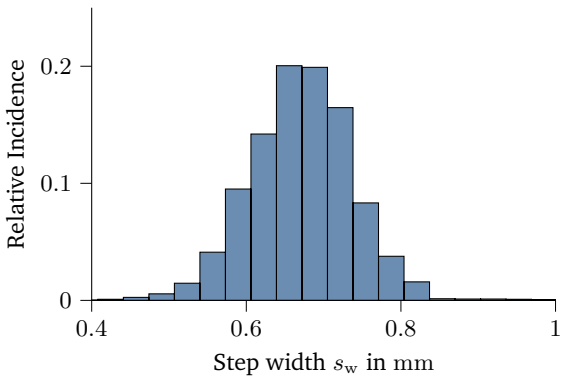

(b) Mean value of 0.67 mm and a standard deviation of 0.068 mm.

Figure 4.20.: Top foil measured step height and width.

distance between these two points; the step-height is just the height difference between the two points. As can be seen in Fig. 4.20a, the measured step-width is almost constant with respect to the radius r for all segments. The minimal step-width is 0.6 mm and the maximal value is 0.8 mm; the overall mean value is $\bar{s}_w = 0.66$ mm and a standard deviation of 0.068 mm. The measured step-height s_h as a function

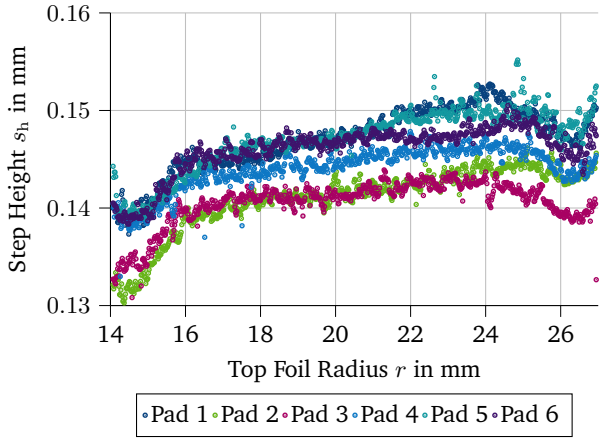

(a) Measured step height of the specimen of all 6 pads.

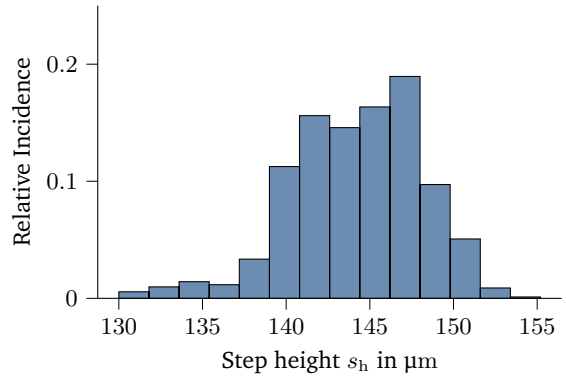

(b) Step height mean value 144 µm and a standard deviation of 4 µm.

Figure 4.21.: Top foil measured step height and width.

of the radius r along the curvature of the step is illustrated in Fig. 4.21a for the six segments. Small differences are detected between the different segments. The variation of the step heights between the pad segments - evaluated at the middle radius r_m - is rather small: 142 µm (Segment 2) and 147 µm (Segment 5). Concerning the variation of the step-height along the step curvature in radial direction, the minimum step-height can be detected near the inner radius r_i and the maximum near the outer radius r_o. At the inner and outer radius, the variation of the step-height between the different pad segments is a little bit larger than at the middle radius r_m, namely up to 10 µm. The differences in step-height along the curvature of the step and between the different pad segments stem from the stamping process and are not intended. The numerical analysis with the multi-physical thrust bearing model within the sensitivity study has, however, shown that the influence of the step-height variations on the performance of the

bearing is $\approx \pm 2\,\%$ on the performance. The overall mean value of the step-height is $\bar{s}_\mathrm{h} = 0.145\,\mathrm{mm}$. The standard deviation over all pads is $4\,\mu\mathrm{m}$ and serves as uncertainty of the measured step height.

Top Foil Pre-Deformation

An additional important geometrical property of the top foil can be derived from the back side measurements ($\mathrm{WLI_{back}}$). The top foil shows a bowl-like (parabolically-shaped) deformation as a function of the radius r due to the manufacturing process (stamping). The measurements show that the bowl-height is almost constant in circumferential direction. The measured bowl profile $h_\mathrm{bowl}(r)$ (averaged in circumferential direction) is displayed in Fig. 4.22a as a function of the radius r. On the middle radius of the top foil at $r = r_\mathrm{m}$, the bowl has its minimum. The bowl height is growing towards the inner radius r_i and outer radius r_o and has a parabolically shaped contour with a maximum value of $20\,\mu\mathrm{m}$. The distribution of the maximum bowl height—evaluated on different circumferential positions over the top foil—is shown in Fig. 4.22b. It is evident, that the maximum height does not fluctuate much for one top foil. Therefore, the bowl-like pre-deformation $h_\mathrm{bowl}(r)$ is considered as a function of the radius only. The standard deviation over the top foil is $1.3\,\mu\mathrm{m}$ and serves as the uncertainty of the bowl height.

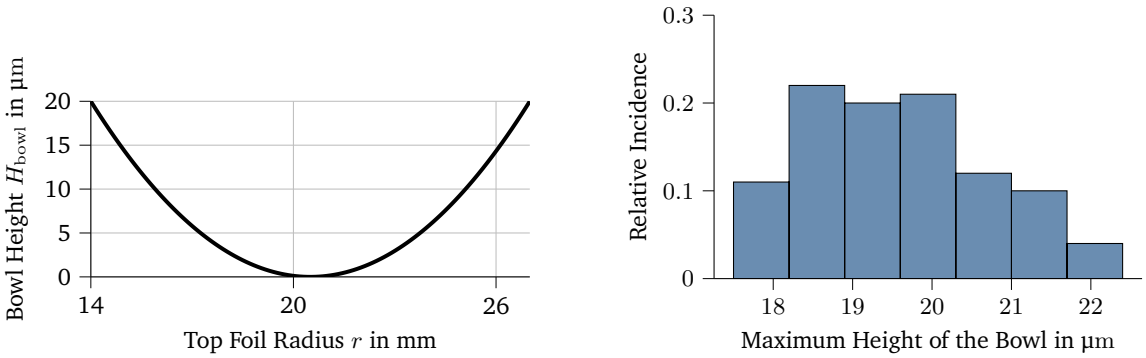

(a) Averaged profile of the foils bowl like pre-deformation.

(b) Maximum height of the bowl over a whole pad. With a mean value of $19.7\,\mu\mathrm{m}$ and a standard deviation of $1.3\,\mu\mathrm{m}$.

Figure 4.22.: Top foil pre-deformation measurements with respect to the bowl like shape.

These effects need to be taken into account in the simulation and are implemented into the film height variable in Sec. 4.3.5. With these three properties—the step height, width, and the bowl like deformation—all mechanic foil parameters are addressed. Further analyses are performed from measurements of the coating layer.

Coating Layer Distribution

The measurement procedure employed here aims to determine the relative coating thickness. This process consists of two steps:

- In the first step, the pre-deformation resulting from the manufacturing process is determined according to Sec. 4.3.2. The observed pre-deformation exhibits a parabolic shape in the radial direction. Given its nearly uniform circumferential distribution, it can be considered a function solely dependent on the radius r and independent of the circumferential angle φ. The pre-deformation is quantified using a White Light Interferometry (WLI) measurement from the back side of the top foil ($\mathrm{WLI_{back}}$), yielding the function $h_\mathrm{bowl}(r)$.

- The second step entails conducting a WLI measurement from the top side of the top foil ($\mathrm{WLI_{top}}$) to establish the relative coating thickness in relation to the central radius r_m. Detailed measurements indicate that the coating thickness primarily varies with the radius r, with the circumferential variation being negligible. Subsequent to the $\mathrm{WLI_{top}}$ measurement, the bowl-shaped pre-deformation $h_\mathrm{bowl}(r)$ is subtracted, yielding the relative coating thickness as a function of the radius r. For clarity in presentation, the relative coating thickness is set to zero at the central radius r.

Fig. 4.23a illustrates a characteristic WLI measurement of the coating side ($\mathrm{WLI_{top}}$) of a top foil segment. The plot shows that the height is $0\,\mu\mathrm{m}$ at $\varphi = 0°$ and $s_\mathrm{h} = 147\,\mu\mathrm{m}$ (step-height), as well as at $\varphi = 60°$ (measured at r_m). Notably, the figure reveals the presence of coating accumulations at the inner and outer radii, attributed to the coating process. To validate the measurement procedure, cross-section images of the top foil were generated. These images provide precise information about absolute coating thicknesses. In Fig. 4.23a, cross-section images at the inner radius, center radius, and outer radius are depicted. Cross-section image I and, especially, cross-section image III exhibit non-uniform coating thicknesses, reaching up to $50\,\mu\mathrm{m}$ in height. Cross-section image II, acquired at the center radius, displays an almost uniform coating thickness of approximately $30\,\mu\mathrm{m}$. These images support the projections of relative coating accumulations made using the $\mathrm{WLI_{back}}$ and $\mathrm{WLI_{top}}$ measurements. A comprehensive comparison of the WLI measurements with cross-section images demonstrates the precision of the described measurement procedure using WLI techniques in determining the relative coating thickness both qualitatively and quantitatively.
In Fig. 4.23b, multiple height profiles from $\varphi = 0 - 55°$ were extracted from the coating measurements and plotted as a function of the radius r. For ease of comparison (also see Fig. 4.19), the different height profiles were normalized to zero at r_m. The maximum coating accumulation is approximately $20\,\mu\mathrm{m}$ relative to the coating thickness at the central radius r_m. The height profiles remain remarkably consistent for various angles. This consistency enables the use of an averaged function, calculated by circumferential averaging, to describe the coating distribution. The resulting averaged height distribution $\bar{h}_\mathrm{coat}(r)$—representing the average value across all six pad segments—as a function of the radius (r) is presented in Fig. 4.23c. The height is set to zero at the central radius r_m, with a maximum height of $12\,\mu\mathrm{m}$ detected at $r = 14.8\,\mathrm{mm}$ and $r = 26.2\,\mathrm{mm}$. Notably, the accumulation peaks near the inner and outer top foil radii occur approximately 0.8 mm away from these radii. The standard deviation of the coating distribution along the radius r, derived from the measured height profiles, remains almost constant across the radius r.
Given the significant accumulations, in comparison to standard local film heights of $2\,\mu\mathrm{m}$ to $20\,\mu\mathrm{m}$, accounting for the resulting averaged height distribution $\bar{h}_\mathrm{coat}(r)$ in the simulation model is necessary. The implementation is elaborated further in Sec. 4.3.5. The standard deviation serves as input uncertainty for this parameter. It is important to note that the averaging process eliminates roughness. This aspect is explored in greater detail in the validation section regarding the film variable H_mixed (Sec. 5.2.1). The contribution $\bar{h}_\mathrm{coat}(r)$ to the film height variable $h(r, \varphi)$ will undergo closer analysis in the validation section regarding wear (Sec. 5.2).

Top Foil Thickness

The foil thickness t_TF is indicated on the drawings but can exhibit a relatively broad range due to manufacturing variations between batches. The objective is to investigate the potential variance in foil thickness for an individual top foil, as well as across different foils within a single batch. This determination holds significance for uncertainty assessment since this parameter notably influences the evaluation variables, as detailed in Sec. 4.3.1. The method employed for assessment involves cross-section analysis. Hence, being a destructive test, the tested foils are unsuitable for further use in the high-speed

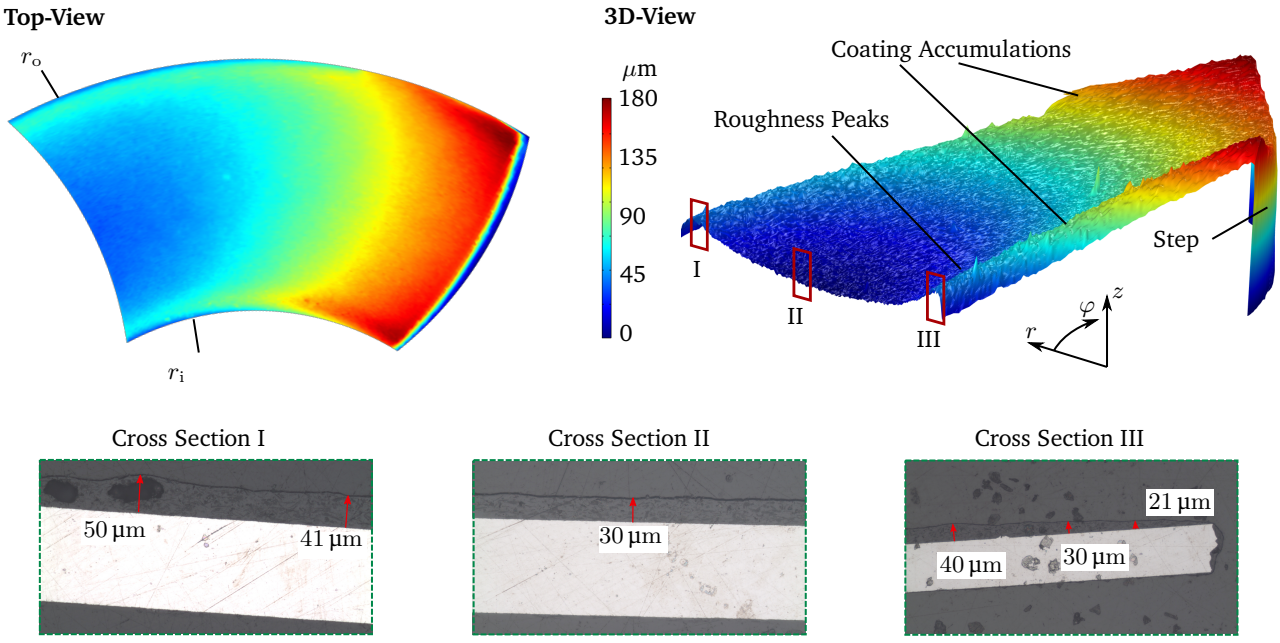

(a) Measured top foil height (height of the top foil without the bowl-shaped pre-deformation). Left: top-view, right: 3D-view, and, bottom: three measured cross sections.

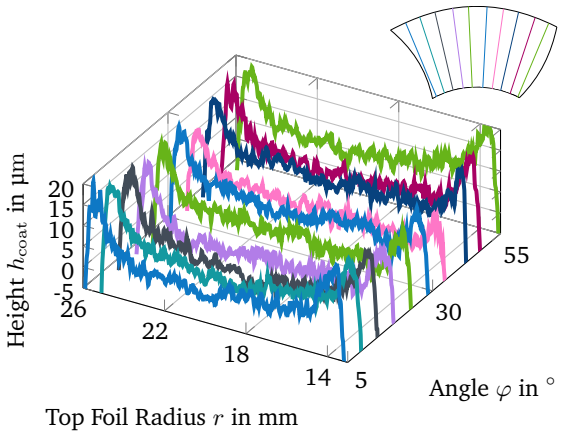

(b) Coating height profiles as a functions of the radius r at several circumferential angles (from $\varphi_1 = 5°$ to $\varphi_{10} = 55°$, positions of the radial cuts are indicated in the sketch).

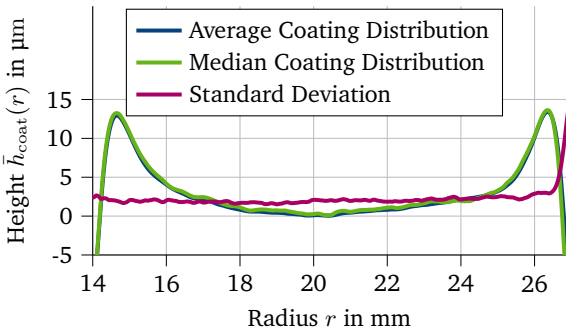

(c) Coating distribution in radial direction (averaged in circumferential φ-direction).

Figure 4.23.: WLI measurements of the top foil.

test rig.
Cross-sections are created on five foils, with each foil being evaluated at three positions: two along the radial direction and one circumferential position on a medium radius. Each of these cross-sections undergoes evaluation at three distinct points using high magnification. The mean value across all these measurements yields t_{TF} =132 µm, accompanied by an uncertainty of ±1 µm.

Top Foil Position

As shown in Sec. 4.3.1, the precise determination of the top foil position φ_{negT} relative to the bump foil location is of paramount importance due to its high sensitivity. Although this parameter could be

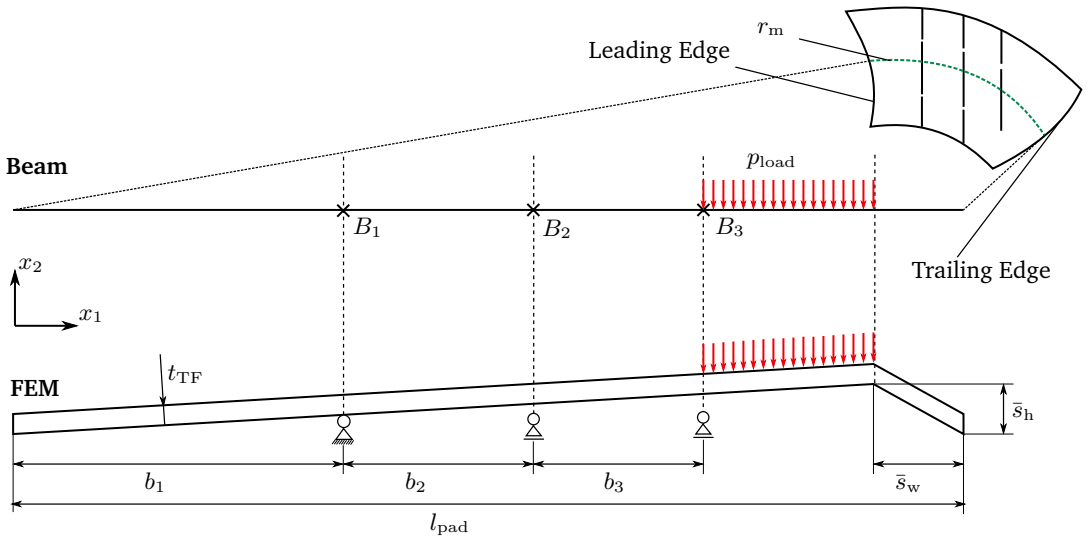

Figure 4.24.: Simulation setup for top foil bending. Represented as beam and 2D FEM.

inferred from the drawings, the investigations have unveiled the step width as a new significant parameter. This parameter, in turn, could impact the accurate alignment of the foil's position in simulations. The position is secured by three pins at the outer bearing ring of both the top and bump foils. The measured clearance for the pin hole positioning is $0.16°$, serving as the uncertainty associated with this parameter. The relative positioning of the top foil concerning the bump foils can be determined through microscopic measurements, yielding $\varphi_\mathrm{negT} = 12.4°$.

4.3.3. Continuous Top Foil

As described in Sec. 4.3.2, the transition at the border of adjacent pads isn't vertical; rather, it extends over a significant region. Given that the observed step width $s_\mathrm{w}(r)$ averages at 0.66 mm – four times the top foil thickness t_TF – further adjustments are required for incorporating this foil type into an appropriate model. To gain deeper insight into the mechanics of deformations in the top foil, a 1D Timoshekov beam simulation alongside a 2D Finite Element Method (FEM) is established. The setup is depicted in Fig. 4.24. The 1D beam setup represents the top foil at its middle radius r_m. Consequently, its length l_pad corresponds to the extent of one pad at its middle radius. The beam exhibits continuity boundary conditions for displacement and rotation at its ends, aligning with the periodic nature of the annular-shaped top foil. At bump positions (B_1, B_2, B_3), a prescribed displacement is applied to model the top foil slope from leading to trailing edge across the step. Specifically, at position B_1, the displacement is set to 0 in both directions with unrestricted rotation. At B_2, the displacement in the x_2 direction equals $h_\mathrm{b2} - h_\mathrm{b1}$, where

$$h_\mathrm{b1} = \frac{\bar{s}_\mathrm{h}}{l_\mathrm{pad} - \bar{s}_\mathrm{w}}\, b_1 \quad \text{and} \tag{4.19}$$

$$h_\mathrm{b2} = \frac{\bar{s}_\mathrm{h}}{l_\mathrm{pad} - \bar{s}_\mathrm{w}}\, (b_2 + b_1), \tag{4.20}$$

with the x_1 direction left unrestricted. The displacement at B_3 follows a similar pattern in the x_2 direction while leaving the x_1 direction unrestricted. A line load p_load is applied between B_3 and the start of the step.

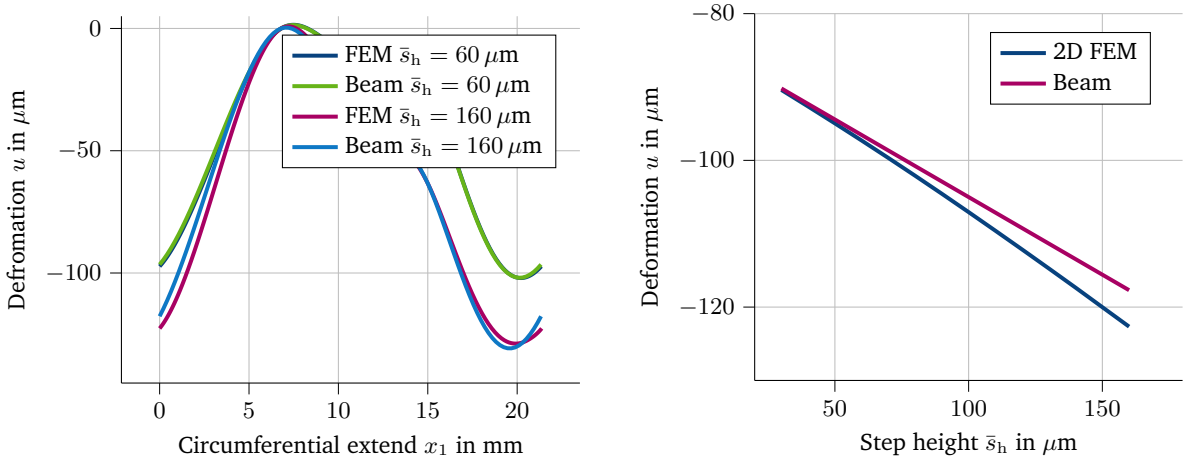

(a) Deformation dependent on step height.

(b) Deformation dependent on step height.

Figure 4.25.: Simulation results FEM vs Beam.

The 2D FEM setup is structurally similar, with the distinction being that the step's pre-deformation is already accounted for in the geometry. Periodic boundary conditions for displacement and rotation are applied between the leading and trailing edges. The cross-section width is defined as $r_\mathrm{o} - r_\mathrm{i}$, with a thickness of $t_\mathrm{TF} = 132\,\mu\mathrm{m}$ in both FEM and beam models.
Fig. 4.25a displays the simulation results for the deformation u in the x_2 direction as a function of circumferential extent x_1 for two different step heights: $60\,\mu\mathrm{m}$ and $160\,\mu\mathrm{m}$. The step height $\bar{s}_\mathrm{h}$ not only influences the step's height but also the slope of the top foil between pads due to continuity. Thus, the prescribed displacements at B_2 and B_3 depend on the step height to ensure contact between bump points and the top foil. For a step height of $\bar{s}_\mathrm{h} = 60\,\mu\mathrm{m}$, the Beam and FEM results align perfectly, while for $\bar{s}_\mathrm{h} = 160\,\mu\mathrm{m}$, differences emerge. The key disparity lies in the rise following the step to the first bump. The rise in the FEM is gentler, affecting the ending angle on the right side, whereas the steeper slope in the beam simulation enforces an angle at the step's pad end. This difference stems from the FEM geometry being pre-deformed from $x_1 = 0$ to B_1, while the beam's geometry remains flat. Nonetheless, the deviation remains relatively modest for a step height of $\bar{s}_\mathrm{h} = 160\,\mu\mathrm{m}$. To highlight the difference, Fig. 4.25b plots the deformation u at the trailing edge against various step heights $\bar{s}_\mathrm{h}$. The growing disparity between the beam and 2D FEM results becomes more pronounced as the step height increases. The discrepancy in deformation reaches $5\,\mu\mathrm{m}$ for a step height of $\bar{s}_\mathrm{h} = 160\,\mu\mathrm{m}$. Therefore, it can be inferred that as the step height increases, so does the deviation. This introduces inaccuracies in the beam theory modeling for larger step heights. Consequently, it's reasonable to assume that the same trend applies to shell theory and the 2D top foil model. However, given the step height range of the top foils used in this thesis, any errors can be deemed negligible. Therefore, the subsequent considerations treat the top foil as a plane shell, and the step height and width only factor into the fluid film. This forms the basis for discussing boundary conditions of the top foil in the following section.

Continuous Top Foil Boundary Conditions

Drawing from the preceding considerations, continuous boundary conditions from the trailing edge to the leading edge can be established to effectively represent the annular-shaped top foil. Specifically, this translates to the following mechanical conditions based on the shell equations (2.11-2.15) outlined in

Sec. 2.2.4:

$$\begin{aligned}
\vec{n}_l v_{\alpha,\mathrm{l}} &= \vec{n}_t v_{\alpha,\mathrm{r}} \\
v_{3,\mathrm{l}} &= v_{3,\mathrm{r}} \\
\vec{n}_l w_{\alpha,\mathrm{l}} &= \vec{n}_t w_{\alpha,\mathrm{r}} \\
\vec{n}_l n_{\mathrm{l}}^{\alpha\beta} &= \vec{n}_t n_{\mathrm{r}}^{\alpha\beta} \\
q_l^{\alpha} &= q_t^{\alpha} \\
\vec{n}_l m_{\mathrm{l}}^{\alpha\beta} &= \vec{n}_t m_{\mathrm{r}}^{\alpha\beta}.
\end{aligned} \tag{4.21}$$

The heat equation's (3.10) boundary conditions are established as:

$$\begin{aligned}
T_{\mathrm{TF,in}}(x,y) &= T_{\mathrm{TF,out}}(x,y) \\
-\vec{n}\nabla T_{\mathrm{TF}}(x,y)|_l &= \vec{n}\nabla T_{\mathrm{TF}}(x,y)|_t \,.
\end{aligned} \tag{4.22}$$

Zero flux boundary conditions are applied at the inner and outer radii.
For the Reynolds equation (2.3), the boundary conditions at the leading and trailing edges are similarly set:

$$\begin{aligned}
p_{\mathrm{l}}(x,y) &= p_{\mathrm{t}}(x,y) \\
-\vec{n}\nabla p(x,y)|_l &= \vec{n}\nabla p(x,y)|_t \,.
\end{aligned} \tag{4.23}$$

It's worth noting that this also leads to the velocities u and v being identical at the leading and trailing edges, given that the velocity components are determined by pressure gradients and rotor velocity. At the inner and outer radius, the pressure is set to ambient pressure.
For the 3D energy equation (Eq. 2.4) solved in the air film, adjustments are made for numerical stability. The continuous boundary conditions for the 3D energy equation at the leading and trailing edges are:

$$\begin{aligned}
T_{\mathrm{l}}(x,y,z) &= T_{\mathrm{t}}(x,y,z) \\
-\vec{n}\nabla T(x,y,z)|_l &= \vec{n}\nabla T(x,y,z)|_t \,.
\end{aligned} \tag{4.24}$$

However, this equilibrium of forced flux isn't a stringent condition since the energy equation in the x and y directions doesn't have a flux component. To enhance stability, the energy equation is expanded with planar diffusion, resulting in the following form:

$$\begin{aligned}
\rho c_P \left[u\frac{\partial T}{\partial x} + v\frac{\partial T}{\partial y}\right] &= \left[\frac{\partial}{\partial x}\left(\lambda\frac{\partial T}{\partial x}\right) + \frac{\partial}{\partial y}\left(\lambda\frac{\partial T}{\partial y}\right) + \frac{\partial}{\partial z}\left(\lambda\frac{\partial T}{\partial z}\right)\right] \\
+ \left[u\frac{\partial p}{\partial x} + v\frac{\partial p}{\partial y}\right] &+ \eta\left[\left(\frac{\partial u}{\partial z}\right)^2 + \left(\frac{\partial v}{\partial z}\right)^2\right].
\end{aligned} \tag{4.25}$$

4.3.4. Wear Simulation

In the results obtained from the original TEHD simulation model, the maximum thrust load F_{thrust} is approximately 40 N, achieved at a minimum gap height of $H_{\mathrm{min}} = 3\,\mu\mathrm{m}$ and a spinning speed n of 120 krpm. Incorporating the coating distribution $h_{\mathrm{coat}}(r)$ and the bowl-like pre-deformation $h_{\mathrm{bowl}}(r)$ as contributions to the local film height $h(r,\varphi)$ (as discussed in Sec. 4.3.5), leads to a further reduction of the maximum thrust load to $F_{\mathrm{thrust}} = 7\,\mathrm{N}$, again at a minimum gap height of $H_{\mathrm{min}} = 3\,\mu\mathrm{m}$ and a spinning speed of 120 krpm. However, experimental tests on the test bench have demonstrated forces of up to 100 N. This discrepancy arises due to wear occurring on the coated surface of the top foil, particularly

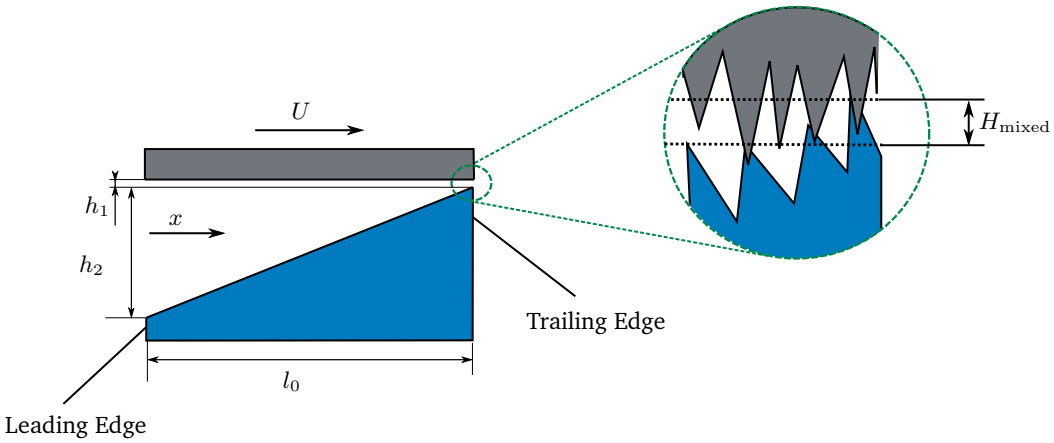

Figure 4.26.: Sketch of a wear example setup with a taper and a slider.

during running-in conditions and at low speeds [4, 11, 46]. To account for this aspect in the simulation, a wear approach must be incorporated into the TEHD model.
The following section outlines a simple approach for simulating wear. This approach is valid for tribological hard-soft contact conditions, where one contact partner is significantly harder than the other. In such cases, it is reasonable to assume that wear occurs predominantly on the softer surface, which, in this context, is the coated top foil. The approach is briefly introduced in Theile et. al. [85]. A second, but slightly different approach is utilized in Eickhoff et. al. [21]. In their approach the coating is worn away in iterative steps, whereas this approach is calculating the wear pattern for a specific load case in one solution step.

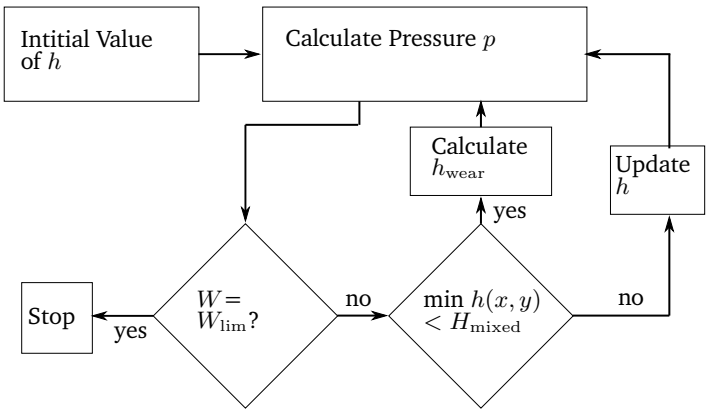

Figure 4.27.: Flowchart of the wear simulation approach.

To introduce the algorithm, a basic 1D model is established. Fig. 4.26 illustrates the model, which simulates a wedge-shaped profile. The profile consists of an infinite slider moving at velocity U, with a varying distance h_1 to the highest point of the wedge profile. If the gap height at the trailing edge becomes small, mixed lubrication might arise, initiating a surface abrasion process. In this case, the wedge profile represents the softer contact partner. Within the lubrication gap, the Reynolds equation is

calculated. For an ideal gas, the 1D Reynolds equation can be expressed as:

$$\nabla \left(\frac{h^3}{12\,\mu} p \frac{\partial\, p}{\partial\, x} - \frac{U}{2}\, h\, p \right) = 0. \tag{4.26}$$

The film height h_{wedge} is defined as:

$$h = h_{\mathrm{wedge}} = h_1 + h_2 \left(1 - \frac{x}{l_0} \right). \tag{4.27}$$

The wear algorithm is depicted in the flow chart shown in Fig. 4.27. The approach employs a limit force F_{lim} at a specific speed n and a minimum gap height $H_{\mathrm{min}} = H_{\mathrm{mixed}}$. Starting with an initial gap height h, the pressure is obtained from the Reynolds equation. Integrating the pressure across the wedge profile yields the thrust force F_{thrust} acting on the bearing. If this force is equal to or exceeds the designated limit force F_{lim}, the simulation terminates. If not, it checks whether the minimum gap height within the fluid domain is below the mixed lubrication limit. If it isn't, the film height is updated, and the pressure calculation process restarts. This cycle continues until certain areas of the minimum film thickness fall below the mixed lubrication limit. At this point, the wear process initiates.
In this approach, the areas below the limit are virtually removed from the wedge profile, which is expressed through the variable h_{wear} defined as:

$$h_{\mathrm{wear}} = \begin{cases} 0, & h_{\mathrm{ww}} \geq H_{\mathrm{mixed}} \\ H_{\mathrm{mixed}} - h_{\mathrm{ww}}, & h_{\mathrm{ww}} < H_{\mathrm{mixed}}. \end{cases} \tag{4.28}$$

Here, the film height variable h_{ww} denotes the film height without wear and is analogous to the actual film height h, defined as:

$$h_{\mathrm{ww}} = h_{\mathrm{wedge}} + \tilde{H}_{\mathrm{shift}} \tag{4.29}$$

$$h = h_{\mathrm{wedge}} - h_{\mathrm{wear}} + \tilde{H}_{\mathrm{shift}}. \tag{4.30}$$

A global variable $\tilde{H}_{\mathrm{shift}}$ is introduced, which virtually shifts the slider until a condition is satisfied. This adjustment is performed iteratively within the solver until the load capacity F_{thrust} reaches the limit force F_{lim}, by incrementally increasing h_{wear} in regions where the film height is too small. This process calculates and stores the accumulated wear in the variable h_{wear} for subsequent simulations.
Results from this simulation approach, based on the discussed wedge example, are presented in Fig. 4.28. The left graph shows the height profile before and after the wear simulation, with h_1 and H_{mixed} set to $3\,\mu\mathrm{m}$. The corresponding pressure p is displayed on the right side. In this example, the solver is manipulated to enhance the resulting load capacity while maintaining a limit film height of $H_{\mathrm{mixed}} = 3\,\mu\mathrm{m}$. Consequently, the wedge profile experiences abrasion at the trailing edge, leading to the formation of a taper land profile with a maximum abrasion of $2\,\mu\mathrm{m}$. This, in turn, leads to a higher pressure buildup at the end of the taper region, resulting in an increased load capacity. The stopping criterion in this case was the resulting load capacity, but it could also be replaced with other criteria, such as a maximum allowable wear height.
This wear simulation approach is subsequently applied to the air foil thrust bearing in the TEHD simulation model to replicate running-in wear on the coating layer of the top foil.

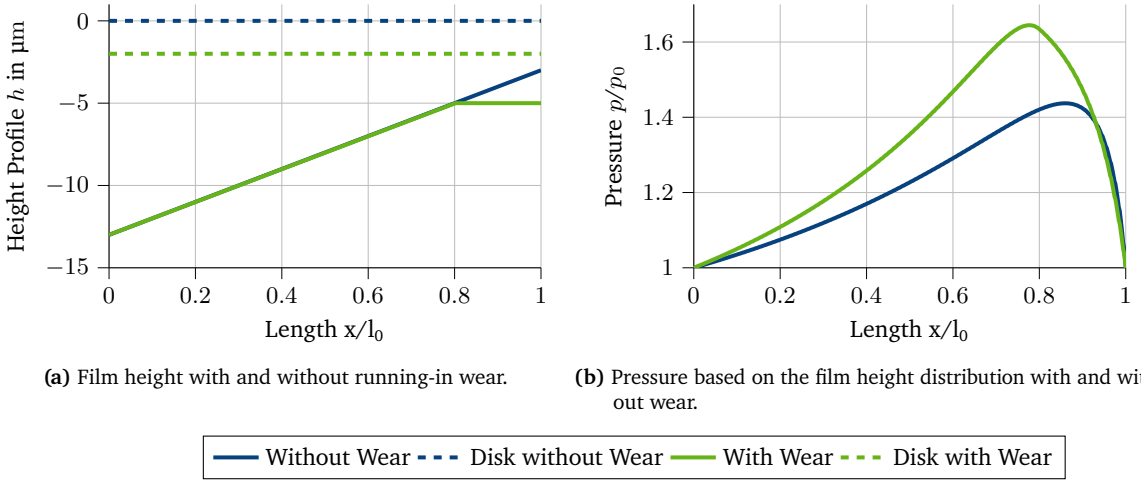

(a) Film height with and without running-in wear.

(b) Pressure based on the film height distribution with and without wear.

Figure 4.28.: Simulation results of the wear example calculation for the height profile and the pressure distribution.

4.3.5. Film Height Expression

The film height, within the context of air foil bearings, is composed of various contributions from the rotor-bearing system. Each component contributes fixed values, such as pre-deformation, and variable values, like the actual deformation of components during the calculation process. This section details the implementation of these contributions into the film height h of the thrust bearing TEHD simulation model.
First, the contributions from the rotor are revisited, as discussed in Sec. 4.1.2. These contributions involve the runner deformation $v_{\mathrm{RD,z}}$ and the pre-deformation $h_{\mathrm{RD,pre}}$, resulting in:

$$h_{\mathrm{disk}} = h_{\mathrm{RD,pre}} + v_{\mathrm{RD,z}}. \tag{4.31}$$

The pre-deformation is predetermined and does not change, while the deformations of the disk depend on factors such as temperature and rotational speed.
Secondly, the contributions to the film height from the top foil are addressed. These contributions can be summarized as topographical contributions h_{topo} and a deformation variable $v_{3\mathrm{TF}}$ of the top foil in the film height direction z. The deformations of the top foil result from pressure forces calculated using the compressible Reynolds equation (see Eq. 2.3). The film height expression for the top foil is thus given by:

$$h_{\mathrm{TF}} = h_{\mathrm{topo}} + v_{3\mathrm{T}}. \tag{4.32}$$

The topographical contributions h_{topo} for the top foil are more involved than that for the disk. It can be split into two main parts:

$$h_{\mathrm{topo}}(r,\varphi) = h_{\mathrm{shape}}(r,\varphi) + h_{\mathrm{coat}}(r), \tag{4.33}$$

with the coating distribution $h_{\mathrm{coat}}(r)$ representing the measured coating distribution, as discussed in Sec. 4.3.2 (see Fig. 4.23c). This distribution consists of 1000 data points interpolated linearly between r_{i} and r_{o}. The variable $h_{\mathrm{shape}}(r,\varphi)$ can be further divided into:

$$h_{\mathrm{shape}}(r,\varphi) = h_{\mathrm{bowl}}(r) + h_{\mathrm{taper}}(r,\varphi). \tag{4.34}$$

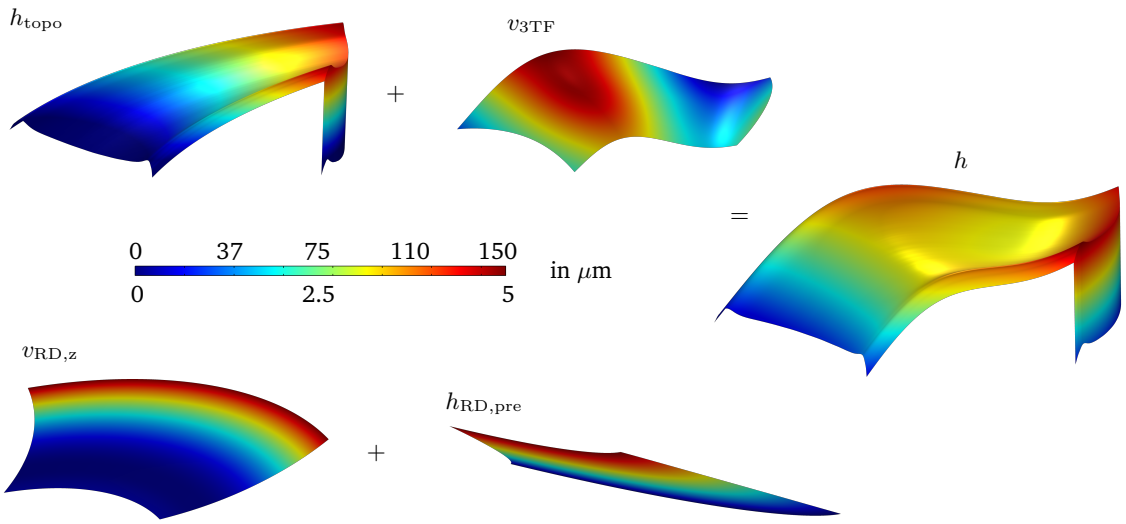

Figure 4.29.: Simulation input parameter for film height. Height scaled 50x.

The bowl-like shape in terms of radius r is given by:

$$h_{\mathrm{bowl}}(r) = \bar{H}_{\mathrm{bowl}} \frac{(r - r_{\mathrm{m}})^2}{(r_{\mathrm{i}} - r_{\mathrm{m}})^2}, \tag{4.35}$$

where $r_{\mathrm{m}} = \frac{r_{\mathrm{i}}+r_{\mathrm{o}}}{2}$ and $\bar{H}_{\mathrm{bowl}} = 20\,\mu\mathrm{m}$ is determined from measurements. The variable $h_{\mathrm{taper}}(r, \varphi)$ comprises two contributions:

$$h_{\mathrm{taper}} = h_{\mathrm{step}} + h_{\mathrm{slope}}. \tag{4.36}$$

In this simulation approach, the step is modeled only within the film height expression for the Reynolds equation. This approach assumes that the step transitions behave more rigidly than the actual film and do not experience bending at the transitions, as discussed in more detail in Sec. 4.3.3. Consequently, the step itself can be modeled as a plane within the shell theory, deformed by the pressure of the air film. The slope of the shape film height variable h_{slope} is therefore determined by

$$h_{\mathrm{slope}} = \bar{s}_{\mathrm{h}} \frac{\varphi - \varphi_{\mathrm{negT}}}{\varphi_{\mathrm{step}} - \varphi_{\mathrm{lead}}}, \tag{4.37}$$

with φ_{lead} defined as the angle running along the curvature of the leading edge. φ_{step} is also a circular arc with the same center like the leading edge but with a smaller radius defined as

$$r_{\mathrm{step}} = r_{\mathrm{curvature}} - \bar{s}_{\mathrm{w}}. \tag{4.38}$$

The constant parameters $\bar{s}_{\mathrm{h}}$ and $\bar{s}_{\mathrm{w}}$ are taken from measurements described in Sec. 4.3.2. The film height over the step h_{step} is derived similarly as

$$h_{\mathrm{step}} = \bar{s}_{\mathrm{h}} \frac{\varphi_{\mathrm{step}} - \varphi}{\varphi_{\mathrm{step}} - \varphi_{\mathrm{trail}}}, \tag{4.39}$$

with φ_{trail} being the circular arc described by φ_{lead} rotated by an angle of $360/n_{\mathrm{pad}}$ around the center of the bearing, where n_{pad} is the number of pads.
The complete film height expression can be written as the sum of contributions from the rotor disk and the top foil:

$$h = h_{\mathrm{nom}} + h_{\mathrm{TF}} + h_{\mathrm{disk}}. \tag{4.40}$$

When applying the wear algorithm discussed in Sec. 4.3.4, the expression becomes:

$$h = h_{\mathrm{nom}} + h_{\mathrm{TF}} + h_{\mathrm{disk}} + h_{\mathrm{wear}} + \tilde{H}_{\mathrm{shift}} \tag{4.41}$$

$$h_{\mathrm{ww}} = h_{\mathrm{nom}} + h_{\mathrm{TF}} + h_{\mathrm{disk}} + \tilde{H}_{\mathrm{shift}}. \tag{4.42}$$

The resulting film height accounts for variables $v_{3\mathrm{TF}}$ and $v_{\mathrm{RD,z}}$, as well as all pre-deformations and topographical contributions. Fig. 4.29 displays the resulting film height considering these variables, with the height scaled by a factor of 50.

4.4. Model Uncertainty Estimation

Table 4.2.: Uncertainty results of important input parameters.

Parameter	Variation	Res. uncert.: Φ_{Loss}	Φ_{TH}	Φ_{St}
Friction coefficient μ	$\pm 25\,\%$	$\pm 0.4\,\%$	$\pm 0.05\,\%$	$\pm 2.6\,\%$
Step height $\bar{s}_{\mathrm{h}}$	$\pm 2\,\%$	$\pm 0.5\,\%$	$\pm 0.06\,\%$	$\pm 0\,\%$
Bump height h_{B}	$\pm 8\,\%$	$\pm 0.6\,\%$	$\pm 1.5\,\%$	$\pm 10.5\,\%$
Bump radius R_{ij}	$\pm 3\,\%$	$\pm 0.3\,\%$	$\pm 0.5\,\%$	$\pm 4.5\,\%$
Top foil thickness t_{tT}	$\pm 0.5\,\%$	$\pm 0.34\,\%$	$\pm 1.5\,\%$	$\pm 1.5\,\%$
Pos. top foil φ_{negT}	$\pm 0.16\,\%$	$\pm 0.16\,\%$	$\pm 0.04\,\%$	$\pm 0\,\%$
Ambient temp. T_0	$\pm 20\,\%$	$\pm 0.05\,\%$	$\pm 0.3\,\%$	$\pm 0\,\%$
Step width $\bar{s}_{\mathrm{w}}$	$\pm 6\,\%$	$\pm 0.2\,\%$	$\pm 0.03\,\%$	$\pm 0\,\%$
Bowl $h_{\mathrm{bowl}}(r)$	$\pm 25\,\%$	$\pm 0.7\,\%$	$\pm 0\,\%$	$\pm 0\,\%$
Coating acc. $h_{\mathrm{coat}}(r)$	$\pm 25\,\%$	$\pm 3\,\%$	$\pm 0\,\%$	$\pm 0\,\%$
Resulting uncertainty		$\pm 5.45\,\%$	$\pm 3.98\,\%$	$\pm 17.6\,\%$

For validating the simulation model, it is crucial to estimate the model's uncertainty. As depicted in Fig. 2.10, the simulation uncertainty is the aggregate of model uncertainties arising from inaccurate conceptual modeling, numerical uncertainties due to solving errors or coarse mesh, and uncertainties stemming from measured input. This section focuses on the latter category, summarizing the uncertainties associated with essential input parameters. These parameters are listed in Tab. 4.2, along with their measured variations and the simulated uncertainties. This uncertainty is extracted from the sensitivity analysis conducted in the preceding sections of this chapter. Notably, the sensitivity analysis was performed for a spinning speed of 120 krpm and a load of 100 N, representing the highest load point. The assumption for the further course of this work is that the uncertainty remains constant for all lower load points and other examined spinning speeds.

It becomes apparent that most parameter variations have only a weak influence on the output quantities. Among the parameters, the coating accumulation on the top foil exhibits the highest impact on the loss quantity, contributing an uncertainty of 3 %. Summing up all uncertainties yields a resulting uncertainty of $\pm 5.45\,\%$ for the loss quantity and $\pm 3.98\,\%$ for the thermal quantity. However, the stiffness quantity's resulting uncertainty is notably higher at $\pm 17.6\,\%$.
The objective of validation is to quantify the accuracy of the simulation model based on the conceptual model. Consequently, based on the uncertainty estimation, it can be inferred that this work can only detect inaccuracies in modeling beyond $\pm 5.45\,\%$ influence on power loss. Similarly, for thermal flow, deviations in modeling can only be detected beyond $\pm 3.98\,\%$. Within these ranges, the presence of significant inaccuracies in the modeling cannot be firmly established.

4.5. Summary and Conclusion

This chapter focuses on the modeling and adjustments made for the air foil thrust bearing, building upon the detailed simulation model developed by Lehn and Eickhoff [52, 67, 21]. The chapter is organized into four major sections. Firstly, the rotor and its surrounding environment are analyzed using measured input. The rotor is represented based on dimensions from the high-speed test rig's rotor, and a comprehensive conjugated heat transfer analysis is conducted using Ansys CFX to derive heat transfer coefficients for the rotor disk.
The subsequent section focuses on the analysis of the bump foil. Initially, geometric properties are determined through measurements. This is followed by an extension of the existing thermal resistance modeling approach, incorporating conduction over the top foil surface and through the air into the base plate.
The third section is dedicated to modeling the top foil. In this work, the top foil takes the form of an annular foil with six embossed steps, dividing the foil into six interconnected pads. A white light interferometric analysis is performed on the top foil, yielding the following conclusions:

- The top foil exhibits a continuous slope from pad to pad, rising to the step height S_h after each step.
- The step has a circumferential extent $s_\mathrm{w}(r)$ and maintains an almost constant height.
- A bowl-like pre-deformation $h_\mathrm{bowl}(r)$ is present in the top foil, reaching a maximum height of $20\,\mu\mathrm{m}$ at the inner and outer radii.
- The coating layer $h_\mathrm{coat}(r)$ is unevenly distributed, with accumulations around $12\,\mu\mathrm{m}$ in height at the inner and outer radii.

These findings are integrated into the local film height of the Reynolds equation. Additionally, a finite element analysis (FEM) is performed on the annular top foil to assess the accuracy of the provided shell modeling. Based on these results, continuous boundary conditions are formulated for the given top foil. To account for wear on the top foil's coating layer, a wear algorithm is introduced. This extension enables the thrust bearing model to simulate the running-in process of the bearing, incorporating these simulated wear patterns for further bearing simulations.
Finally, model uncertainty estimation is conducted to determine the prediction accuracy of the modeling. Based on this uncertainty estimation, it is established that this work can only detect modeling inaccuracies beyond $\pm 5.45\,\%$ influence on power loss, and $\pm 3.98\,\%$ influence on thermal flow, and $\pm 17.6\,\%$ for the stiffness.

5. AFTB-Simulation Model Validation

This chapter presents the final validation of the air foil thrust bearing (AFTB) model. The validation process is organized into four primary aspects, corresponding to the quantities introduced in Section 2.4.2. The first aspect pertains to the stiffness of the bump foil, denoted as Φ_{St}. In this section, a comparison is made between the measured bump foil stiffness and simulated values. Subsequently, an investigation into the wear occurring on the top foil's coating layer is conducted. This investigation aligns with the film quantity Φ_{Film}, which characterizes the strain on the bearing caused by applied loads. Following this, the validation of bearing performance, represented by Φ_{Loss}, involves comparing simulated power loss and load data with measurements from the high-speed test rig. This section delves into a more detailed analysis of simulation results. The concluding part of this chapter addresses the thermal behavior, denoted as Φ_{Th}, and its validation. Initially, the thermal resistance of the bump foil is validated using a dedicated thermal resistance test rig. Additionally, temperature measurements from the high-speed test rig are compared with simulation results.

5.1. Stiffness of the Bump Foil

The stiffness of the bump foil is measured using ZWICK measurements, as described in Section 3.3.2. The measured force-displacement relationship is depicted in Fig. 5.1. The stiffness measurement system is calibrated, ensuring high accuracy. The presented data are averaged results from five measurements, with a repeatability error of less than 1 %. Notably, a pronounced non-linearity in the force-displacement curve is observed between 0 and 40 N. This phenomenon is attributed to the alignment processes of the bump arcs with the base plate. Beyond 40 N, the bump stiffness Φ_{St} continues to exhibit a slightly progressive behavior.
In the simulation model, all bump arcs maintain contact with the base plate from zero load to high loads. This discrepancy results in a distinct stiffness characteristic in the simulation. The uncertainty-quantified simulation results, as discussed in Section 4.4, incorporate an uncertainty of $\pm 17.6\,\%$. The simulation involves lowering a flat and rigidly modeled top foil in the z-direction towards the base plate, mirroring the measurement setup. Comparing the measured data to the simulation results reveals a discrepancy in the progressive behavior. Notably, the simulation results do not precisely replicate the measured behavior, not even beyond 40 N. Consequently, it can be inferred that an accurate prediction of the real stiffness is not possible. This highlights the limitations of the current simulation setup in accurately reflecting real-world conditions regarding the stiffness of this type of an AFTB. Compared to Fig. 2.11, the validation process of the stiffness of the bump foils reveals case b.) behavior, indicating a not accurate enough conceptual model of the bump foil.
Given that sensitivity studies discussed in Section 4.2.1 already indicate a minor influence of the stiffness parameter Φ_{St} on other core bearing characteristics (Φ_{Loss}, Φ_{Th}, and Φ_{Film}), no adjustments are proposed for the simulation model in this work. The reason for this independence can be attributed to the rigidity of the top foil (compare Fig. 5.17 in Sec. 5.4). Once the top foil has taken shape in a taper land like bearing (from approximately 30 N), its form remains constant even under higher loads.
Future investigations in this domain could concentrate on comprehending the contact mechanism of this specific embossed bump foil type, aiming to more precisely model the bump foil alignment process.

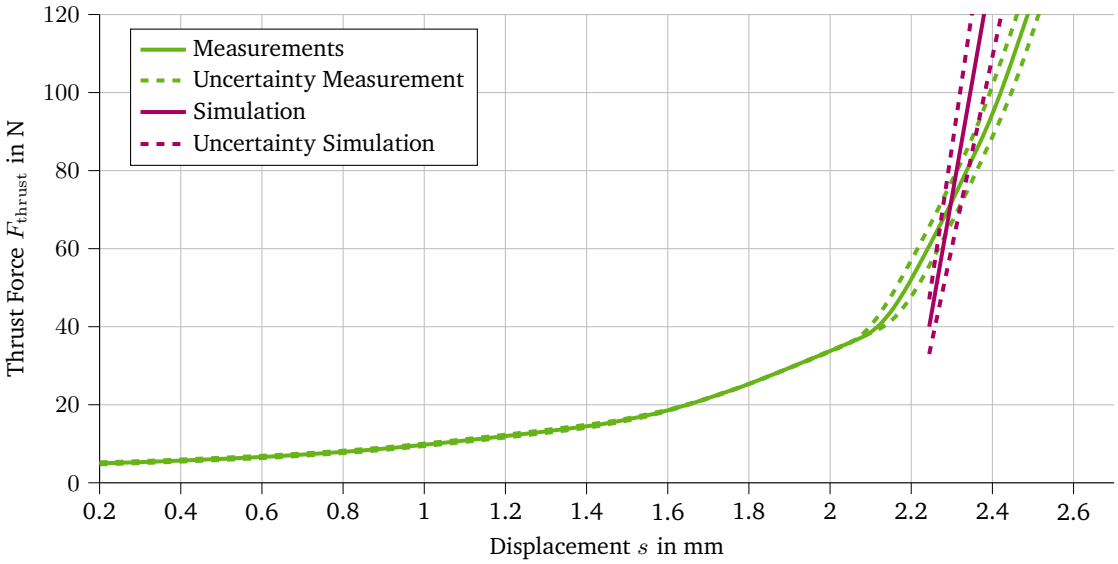

Figure 5.1.: Stiffness test of the bump foil. Zwick measurements compared to simulation results.

5.2. Validation of Wear Simulations

This section presents and discusses the results of wear simulations based on wear measurements conducted on the top foil's coating layer. The validation process for the wear simulations involves the following steps:

- Examination and discussion of the mixed lubrication parameter H_{mixed} through detailed wear measurements using White Light Interferometry (WLI) on the top foil and corresponding wear simulations.
- Comparison of the loss factor Φ_{Loss} and disk temperatures T_{disk} to refine the mixed lubrication parameter H_{mixed}.
- Analysis of the running-in wear process in different stages.

5.2.1. Determining the Mixed Lubrication Limit

During operation, considerable wear in the Teflon layer occurs at different locations of the top foil. Occurrence of strong wear during the running-in process is characteristic for the here considered annular-shaped top foil design. It's worth noting that wear of the top foil is also observed in connection with the classical multi-pad thrust bearing design, see, e.g., [4, 11, 46].
However, for the annular-shaped design investigated here, the occurring wear is usually markedly larger than for the classical multi-pad design. Regarding the classical multi-pad bearing design, the different pad segments are not connected. As a result, the pads can very simply align with the rotor disk under load so that the influence of wear on the bearing performance is reduced. Considering the annular-shaped top foil design, however, the pad segments are stiffly connected so that the alignment of the pad segments with the rotor disk under load is reduced. As a consequence, the influence of wear on the bearing performance is significantly larger in comparison to the classical multi-pad bearing design [21].
The objective of this section is to establish the mixed lubrication limit variable H_{mixed}, as introduced in

Section 4.3.4, through comparison with measurements. Consequently, measurement results are presented as follows.

Wear of the Top Foil's Coating Layer

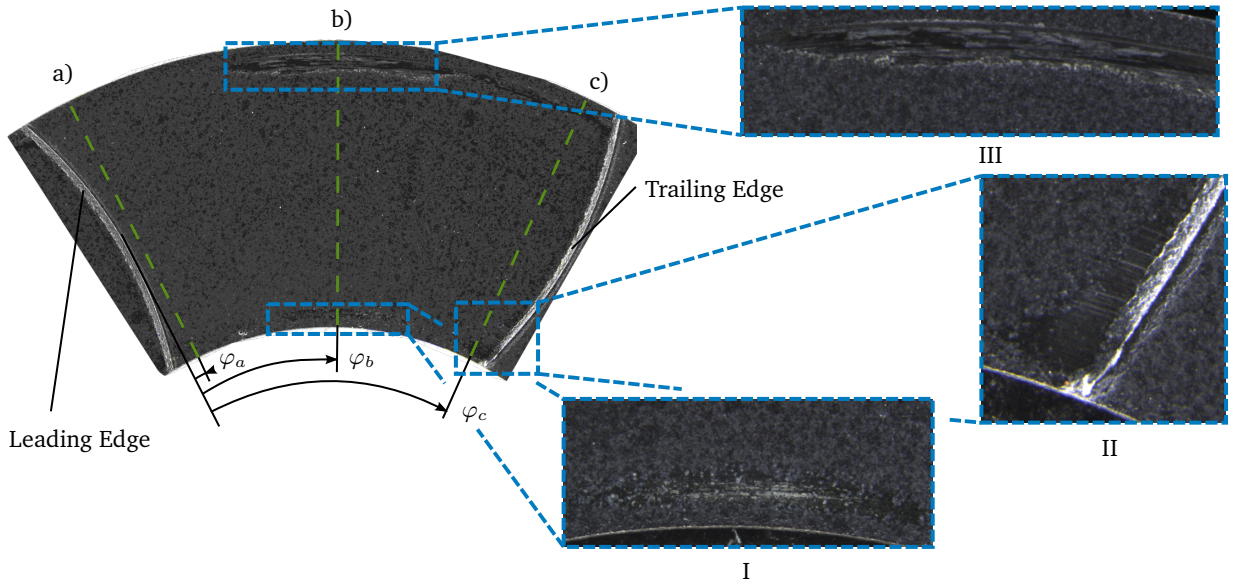

Figure 5.2.: Image of one top foil pad after testing. Dotted lines indicate positions of height profiles for Fig. 5.3a.

This section aims to identify wear areas and quantify the extent of wear. Microscopic images are employed to pinpoint wear areas on the top foil. Additionally, wear depth is quantified through precise WLI measurements in the worn areas. Roughness parameters in the worn region are assessed using confocal measurements.
Fig. 5.3 displays a microscopic image of a worn top foil segment, revealing three main wear areas:

- The first wear area—area I—is located at the inner radius r_i in the center of the segment.
- The second wear area —area II—is also at the inner radius, but at the trailing edge.

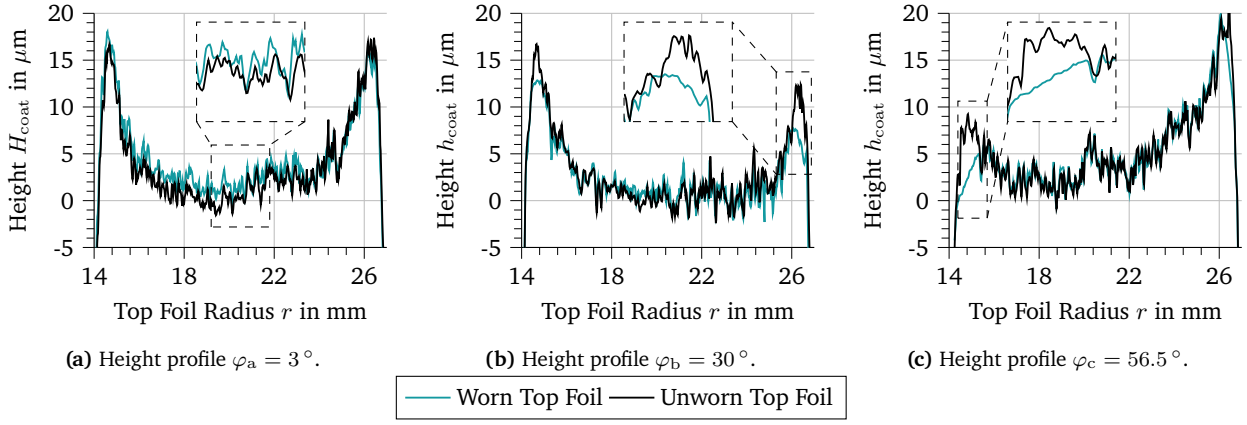

(a) Height profile $\varphi_\mathrm{a} = 3\,°$.

(b) Height profile $\varphi_\mathrm{b} = 30\,°$.

(c) Height profile $\varphi_\mathrm{c} = 56.5\,°$.

Figure 5.3.: Height profiles from WLI measurements. New and used test top foil compared.

- The third wear area—area III—is at the outer diameter of the center of the segment.

From a microscopic image, it is not possible to obtain any quantitative information on the wear depth. To get quantitative information, WLI measurements are performed with the top foil after the running-in process. Therefore, radial height profiles of the coating height $h_{\mathrm{coat}}(r)$ are measured at three different angles, see Fig. 5.3. The locations of the three angles are indicated in Fig. 5.3 by the green dashed lines and are defined by the three angles $\varphi_{\mathrm{a}} = 3°$, $\varphi_{\mathrm{b}} = 30°$, and $\varphi_{\mathrm{c}} = 56.5°$. Note that $\varphi = 0°$ is located at the leading edge at the middle radius r_m, i.e., right after the step of the top foil.
WLI measurements have been carried out before the running-in procedure with a new top foil and—at the same positions—after the running-in process. It should be mentioned again that WLI surface measurements have to be carried out from the coated top side of the top foil ($\mathrm{WLI}_{\mathrm{top}}$) as well as from the uncoated back side ($\mathrm{WLI}_{\mathrm{back}}$) in order to determine the coating layer distribution, see Sec. 4.3. Although these measurements are rather expensive and complex, very detailed and exact information on the coating layer thickness can be determined for the unworn and for the worn top foil.
The height profiles $h_{\mathrm{coat}}(r)$ for $\varphi_{\mathrm{a}} = 3°$ (close to the leading edge) for the unworn top foil (new top foil) and for the worn top foil (after the running-in process) are almost identical, see Fig. 5.3. As can be seen, the coating has accumulations of approximately $17\,\mu\mathrm{m}$ close to the inner and outer radius, see Sec. 4.3. Comparing both curves, it can be concluded that wear does not occur in the area close to the leading edge. Note that even the roughness peaks are visible at the same positions before and after the running-in procedure, which also illustrates the high accuracy of the measurement technique.
Corresponding height profiles $h_{\mathrm{coat}}(r)$ for $\varphi_{\mathrm{b}} = 30°$ are depicted in Fig. 5.3. Comparing the curves before and after the running-in process, wear can be detected at the inner and outer radius in the regions with the coating accumulations (see Sec. 4.3.2). The amount of wear at the inner radius is approximately $4\,\mu$m and at the outer radius approximately $7\,\mu$m.
By comparing the measurement curves close to the trailing edge at $\varphi_{\mathrm{c}} = 56.5°$, wear of $7\,\mu$m with a maximum width of 2 mm can be identified close to the inner radius (Fig. 5.3). At the outer radius, just one single roughness peak has been worn. The zoom plot depicts the abrasion at the inner radius in more detail. The worn profile in Fig. 5.3 for φ_{c} shows a slope of $5\,\mu\mathrm{m}$ per mm in radial direction close to the inner radius, which can, however, not be explained by thermo-elastic rotor deformations. To

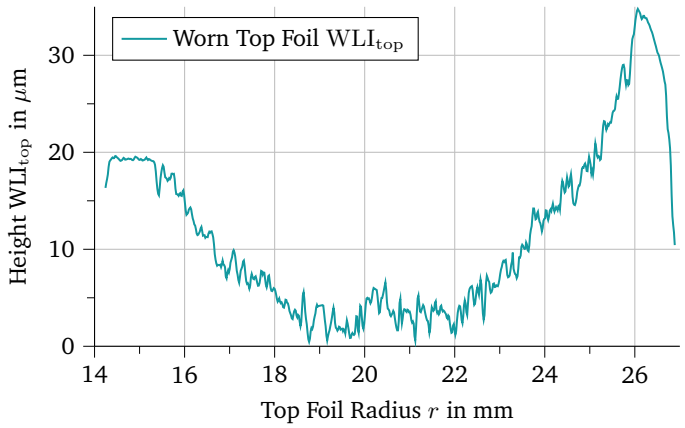

Figure 5.4.: Height profile (compare Fig. 5.3c) near trailing edge without back fit.

explain the above mentioned wear effect, the WLI measurement $\mathrm{WLI}_{\mathrm{top}}$ of the top side of the worn foil at $\varphi_{\mathrm{c}} = 56.5°$ is examined more closely, see Fig. 5.4. Starting from the middle radius r_{m}, the height is increasing towards the inner and outer radius: close to the outer radius r_{o} a maximum value of $\approx 34\,\mu\mathrm{m}$ is observed and at the inner radius r_{i} a value of $\approx 19.5\,\mu\mathrm{m}$. This curve can be explained by the bowl-shaped

pre-deformation of the foil, which has been described in detail in Sec. 4.3. Obviously, the bowl-shaped pre-deformation entails a straightening of the abrasion at the inner radius. This indicates that the bowl-shaped pre-deformation of the top foil is noticeably influencing the bearing behavior. Apparently, the bowl-shaped pre-deformation is not markedly flattened due to pressure in the air film; otherwise, the height profile for φ_c in Fig. 5.3 would not show the above mentioned slope at the inner radius. In contrast to the classical multi-pad top foil, the annular-shaped top foil has a significantly increased bending stiffness, which reduces the displacement, the deformation, and therefore the alignment of the bearing pads with the rotor disk under load.

Short remark on the observed wear pattern: The reason for the occurrence of the three characteristic wear areas I, II and III may be explained as follows. The wear areas I and III can simply be traced back to the coating accumulations close to the inner and outer radius of the top foil, see Sec. 4.3.5, and the parabolic (bowl-shaped) pre-deformation of the top foil resulting from the manufacturing process. Note that these two wear areas are found where the top foil is supported by the bump foils and not in the taper part of the sector near the leading edge. The physical reason for the occurrence of wear area II lies in the rather complex bending deformation of the top foil close to the trailing edge under load, which is bent upwards under load because of the rather stiff connection between the different bearing segments. Each top foil sector transforms from the initial taper-step topology towards the taper-land topology due to the developing air pressure. Based on the connection of each trailing edge to the neighboring leading edge, the trailing edge tends to bend upwards, causing additional wear with the center located near the inner radius. A detailed analysis of the wear, highlighting the development of the described wear pattern with the help of a numerical TEHD bearing model can be found in part I of the paper [21].
Summarizing, it can be concluded from the WLI measurements that the maximum wear depth is $\approx 7\,\mu$m, since the abrasion occurs at the locations with the coating accumulations, which have a maximum height of $20\,\mu$m, see Fig. 4.23b. It can furthermore be observed that there are no spots where the entire Teflon layer has been worn. However, wear entails a smoothing of the top foil and a kind of self-optimization effect, since the worn top foil shows a significantly larger load capacity than the unworn new foil. This running-in effect is characteristic for thrust bearings with an annular-shaped top foil geometry.

Roughness of the Coating Layer

The radial height profiles depicted in Fig. 4.23a indicate that the Teflon layer has a large roughness. WLI measurements are, however, not suitable for determining the roughness parameters with high accuracy. Therefore, a confocal surface measurement with a NANOFOCUS[1] μsurf has been performed close to area II of the worn top foil (see Fig. 5.3). An image of the intensity layer of the confocal microscopy measurement is shown in Fig. 5.5.
Close to the inner radius r_i at the trailing edge, a heavily worn region II can be observed (red dashed rectangle). The green dashed region above is, however, almost unworn. In the heavily worn region, the grinding grooves from the rotor disk are clearly visible. In both regions—heavily worn red region and almost unworn green region—roughness evaluations have been carried out. The root mean square value of the roughness height in the unworn region I is $S_\mathrm{q} = 0.72\,\mu\mathrm{m}$; in the heavily worn region II the measurement yields the value $S_\mathrm{q} = 0.193\,\mu$m.
Fig. 5.5 shows 1-dimensional height profiles measured within the two regions. In the unworn region I the roughness is $R_\mathrm{z} = 5.5\,\mu\mathrm{m}$; in the worn region II the roughness is $R_\mathrm{z} = 1\,\mu\mathrm{m}$. Note that in the worn region, not only the roughness peaks are removed, but also the surface is smoothed. Corresponding roughness measurements have also been carried out at the surface of the rotor disk, where a roughness

[1] https://www.nanofocus.com

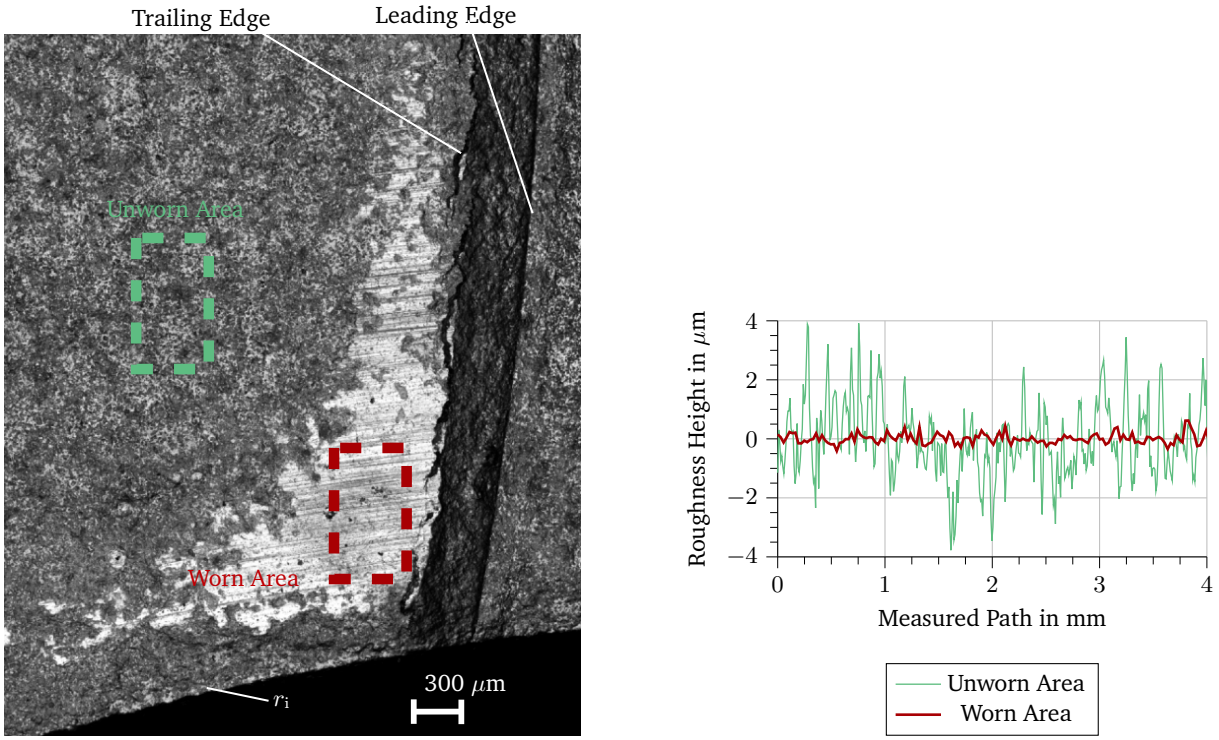

Figure 5.5.: Confocal microscope (left side intensity layer image) roughness measurements of the coating layer in the heavily worn area I and in the almost unworn area II: roughness parameter $R_z = 5.5\,\mu m$ in the unworn area and $R_z = 0.9\,\mu$m in the worn area; root-mean square height $S_q = 0.715\,\mu$m in the unworn area and $S_q = 0.193\,\mu$m in the worn area.

value of $S_{q,Disk} = 0.19\,\mu m$ has been measured. This roughness value is very similar to the value measured on the top foil in the heavily worn region.

Tuning of the Mixed Lubrication Limit

A wear simulation with the model of Sec. 4.5 has been carried out with the following input data: $n = 120$ krpm and $F_{thrust} = 100$ N. To run the wear simulation, the critical gap parameter H_{mixed}, which specifies the onset of wear, has to be defined. In literature, different criteria for the onset of mixed lubrication and wear have been formulated. Arghir [2] suggests that mixed lubrication can be assumed if the film thickness becomes smaller than three times the standard deviation of the combined roughness of rotor and top foil, which yields $H_{mixed} = 3\sqrt{S_{q,foil}^2 + S_{q,disk}^2} = 3\sqrt{0.72^2\,\mu m + 0.19^2\,\mu m} = 2.2\,\mu m$ for the considered rotor/bearing system. Szeri claims that mixed lubrication occurs if the film thickness gets smaller than $H_{mixed} = 2.5\,\mu$m [84]. Hamrock introduces the special parameter $\Lambda = \frac{H_{mixed}}{R_q}$ and states that wear will occur for $\Lambda \leq 3$ [31].
Based on these criteria, the here used parameter H_{mixed} is varied between 1 and 5 μm in order to determine—via a comparison with the experiment—the onset of mixed lubrication for the current problem. As can be seen in Fig. 5.3, wear only occurs at the coating accumulations at the inner and outer radius in the center of the segment (areas I and III) and at the trailing edge at the inner radius (area II). Therefore, measured radial wear profiles for $\varphi_b = 30°$ and $\varphi_c = 56.5°$ (see Fig. 5.3) are compared with simulated radial wear profiles carried out with different parameters H_{mixed}. Based on these comparisons, the correct value for H_{mixed} can be determined.

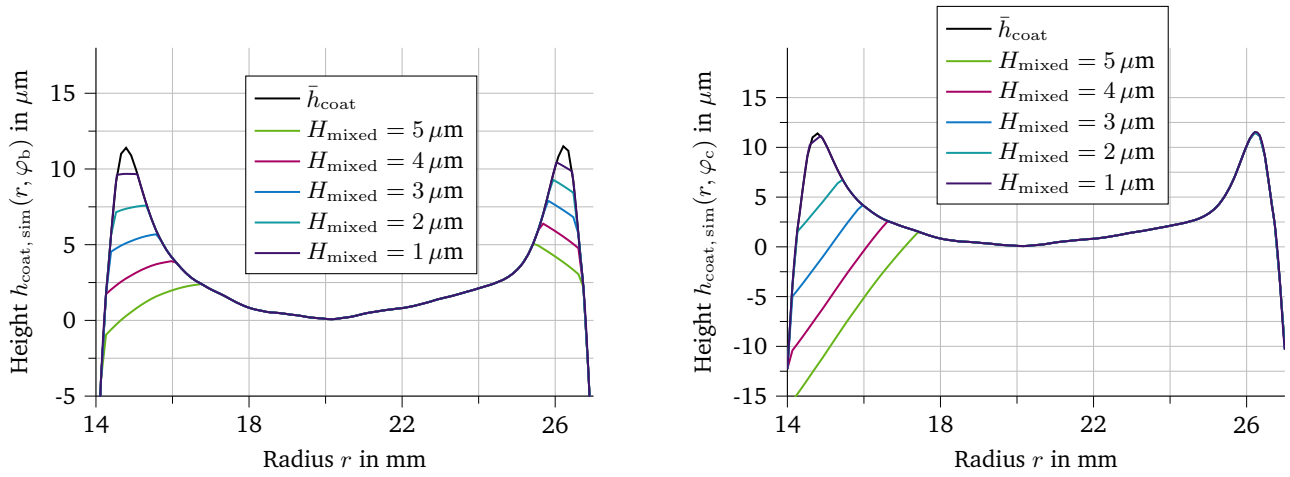

(a) Simulation result for height profiles in the middle of the pad for different mixed lubrication parameters H_{mixed}. Measurements are found in Fig. 5.3b. The location is indicated in Fig. 5.2 line b.).

(b) Simulation results for height profiles near the trailing edge of the pad for different mixed lubrication parameters H_{mixed}. Measurements are found in Fig. 5.3c. The location is indicated in Fig. 5.2 line c.).

Figure 5.6.: Simulated wear height profile on two different locations.

In Fig. 5.6a, simulated wear profiles $h_{\mathrm{coat,\,sim}}(r,\varphi_{\mathrm{b}}) = \bar{h}_{\mathrm{coat}}(r) - h_{\mathrm{wear}}(r,\varphi_{\mathrm{b}})$ are depicted for different values of H_{mixed} at $\varphi_{\mathrm{b}} = 30°$. The black curve $\bar{h}_{\mathrm{coat}}(r)$ shows the unworn profile from the measurement. The other five curves depict the simulated thickness of the worn Teflon layer. It is evident that with increasing H_{mixed}, wear will also increase. Compared to the measured profile in Fig. 5.3, the simulations show qualitatively quite similar and reasonable results. For wear parameters $H_{\mathrm{mixed}} = 2 - 3\,\mu\mathrm{m}$, a good quantitative correlation can be achieved. The amount of wear is, however, overestimated for $H_{\mathrm{mixed}} \leq 3\,\mu\mathrm{m}$ at the inner radius and underestimated at the outer radius.
In Fig. 5.6b, corresponding wear simulation results are depicted for the radial cut at $\varphi_{\mathrm{c}} = 56.5°$. Again, a good qualitative correlation with the measurement of Fig. 5.3 is observed.
Recapitulating: the simulation with all five wear parameters show a similar qualitative abrasion behavior. For $H_{\mathrm{mixed}} = 3\,\mu\mathrm{m}$, the width of the worn area is predicted to be 2 mm and seems to fit best with the measurements; also the height of the worn profile shows a good agreement with the measurements for this wear parameter.
The bearing performance can simply be characterized by determining the loss factor Φ_{Loss}, i.e., by dividing the power loss by the applied load. Simulated loss factors for different values of H_{mixed} are depicted in Fig. 5.7a. It is obvious that for higher values of H_{mixed}, the loss factor is decreasing, i.e., the bearing performance is increasing. The difference between $H_{\mathrm{mixed}} = 1\,\mu\mathrm{m}$ and $H_{\mathrm{mixed}} = 5\,\mu\mathrm{m}$ is approximately $12\,\%$. It can therefore be concluded that wear will lead to a higher performance of the bearing, which is typical for the running-in process of this bearing design. The measured loss factor and its uncertainty is also displayed in the figure. Comparing the measured loss factor with the simulated factors, a good agreement can be observed for $H_{\mathrm{mixed}} \leq 3\,\mu\mathrm{m}$. Hence, the wear simulation model is able to predict the performance of the worn bearing.
Furthermore, measured disk temperatures are compared with simulated disk temperatures. In Fig. 5.7b, the simulated disk temperatures $T_{\mathrm{disk},1}$ and $T_{\mathrm{disk},2}$ (see Fig. 3.1) are depicted as a function of H_{mixed}. Obviously, the wear parameter H_{mixed} has a noticeable influence on the calculated disk temperatures. For lower values of H_{mixed}, the temperatures are also lower. This effect can be explained by the improved thermal conduction of the air film at lower values of H_{mixed} because lower values of H_{mixed} correspond

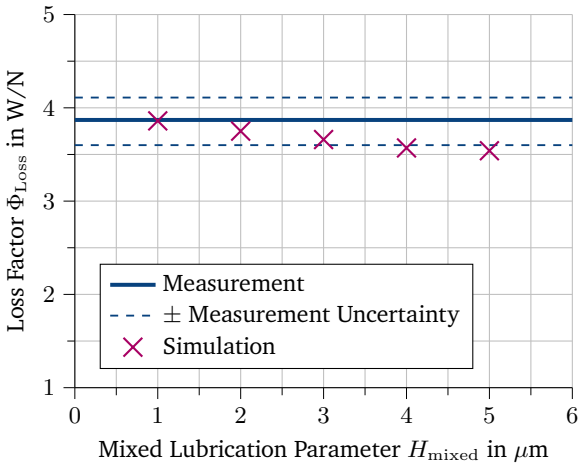

(a) Power loss divided by applied load simulation results for 120 krpm and 100 N.

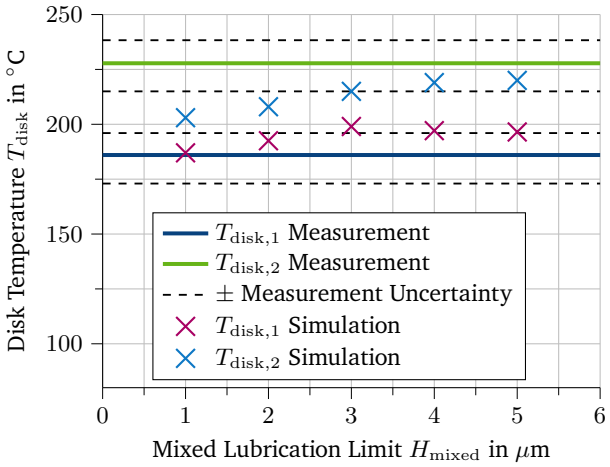

(b) Simulated disk temperature compared to measurements for 120 krpm and 100 N.

Figure 5.7.: Calibration of the numerical parameter H_{mixed} through comparison with measured data.

to a reduced average gap height. As a result, there is a higher temperature diffusion capability of the air film (compare with Eq. 2.4). Compared with the measurements, it can be concluded that a value of $H_{\mathrm{mixed}} \approx 3\,\mu\mathrm{m}$ yields a good correlation with the two measured temperatures.
Summarizing all the above results and comparisons, it can be concluded that parameter values for H_{mixed} in the range of $2\,\mu\mathrm{m}$ to $3\,\mu\mathrm{m}$ yield a good correlation with the WLI wear measurements and also with the test rig performance measurements. Wear parameters H_{mixed} in the range of $2\,\mu\mathrm{m}$ to $3\,\mu\mathrm{m}$ are also in good accordance with corresponding parameters in literature. In the subsequent simulations, $H_{\mathrm{mixed}} = 3\,\mu\mathrm{m}$ has been chosen.

5.2.2. Running-in Wear

The topography of the coating layer distribution, coupled with the annular shape of the foil, leads to wear on the coating of the top foil during the running-in process. This running-in process is evaluated using the torque measurement system in the high-speed test rig. To analyze the running-in process and its effects, a series of eight run-ups are conducted using the same top foil. The test procedure is as follows: In the initial run, the test rig is accelerated to $n = 120\,\mathrm{krpm}$ without applying an axial load to the bearing. The torque is calibrated to zero once thermal equilibrium is reached. Subsequently, the load is incrementally increased up to 10 N. After reaching 10 N, the test rig is shut down, and the top foil is removed for microscopic examination before being reinstalled (details of wear assessments are presented in the following section). The second run involves accelerating the test rig to 120 krpm again, and the force is gradually raised to 10 N. Subsequent load increases are in increments of 5 N until reaching 60 N. The third run-up involves load increments beyond 85 N. The subsequent five run-ups are all conducted with the same load steps towards a load of 100 N, without removing the top foil between run-ups.
The measured torque $T_{\mathrm{f}} = F_{\mathrm{lc}}\, l_1$ is plotted as a function of the test time t_{test} for all running-in runs in Fig. 5.8 on the left vertical axis. On the right vertical axis, the applied load F_{thrust} is shown, with consistent progression across all runs.
During the first run, no abnormalities can be detected in the torque signal or are smaller than the measurement resolution. Its measured torque is extracted in a zoom box in Fig. 5.8 on the right side. Small steps in the signal are noticeable. In the second run (till 60 N), torque abnormalities arise after the

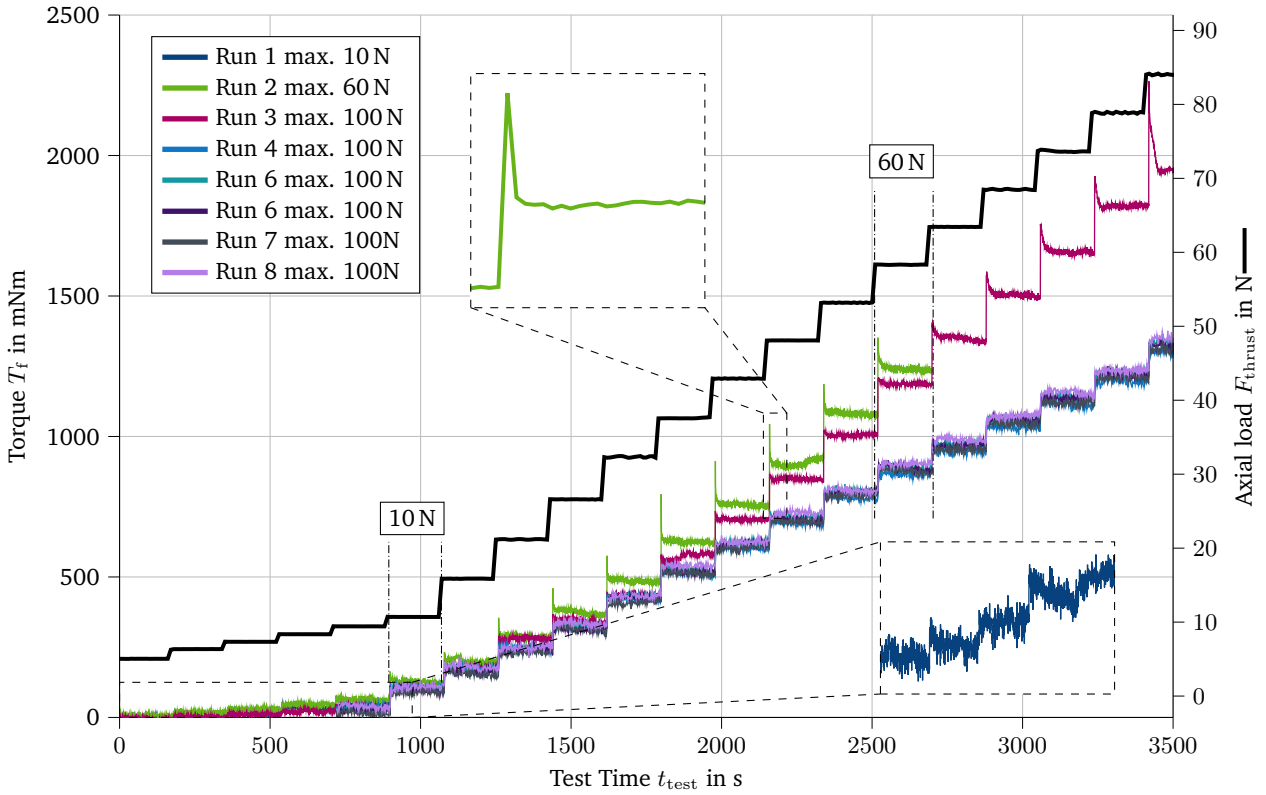

Figure 5.8.: Torque measurements of a running-in process of one top foil with eight subsequent runs.

load jump from 15 to 20 N. The torque momentarily overshoots before stabilizing at a lower level. This behavior is present for each load step. A zoom box for run 2 at the load step from 30 to 40 N represents this behavior clearly. For the third run, which reaches up to 85 N, no torque overshoot is observed within the load range of 60 N (maximum load for run 2), only manifesting beyond that point. Notably, the Pelton turbine of the test rig was unable to withstand the mixed lubrication occurring at 85 N, causing a torque overshoot that led to reduced spinning speed and an emergency stop. Consequently, the bearing had to support 90 N at around 60 krpm, resulting in more wear than usual due to compromised lubrication. This phenomenon arises when wear surpasses a certain threshold, and the Pelton turbine cannot promptly provide the additional torque. Despite this, the bearing remains usable for further investigation and comparison with simulations.

The subsequent five runs, all carried out at 100 N, unveil distinct aspects of the run-in process of the previous cycles. Firstly, the maximum torque during these five runs is notably lower than in previous cycles. Secondly, torque overshoots are absent. Furthermore, the torque curves exhibit a gentler slope after around 40 N.

From these observations, several conclusions can be drawn: During running-in, a portion of the coating layer smoothes in, explaining the torque overshoots as the fluid film remains below the mixed lubrication threshold in specific regions. Once the interfering layer elements have been smoothed away, the bearing can operate beyond the mixed friction condition in the fluid friction range, resulting in decreased measured torque (compare Fig. 2.8). A comparison between the third and second runs up to 60 N underscores the distinction between the running-in process and recurrent wear. After the bearing's coating layer has worn to match the loading requirements concerning the fluid film, subsequent runs can apply the load without causing wear. Additionally, the bearing appears to optimize itself during the run-in process, exemplified

in the third and fourth runs. This running-in effect can be attributed to reduced coating accumulations' height due to wear at specific locations (refer to Sec. 5.2.1). Consequently, it can be deduced that smaller coating accumulation enhances bearing performance.
Another insight from the five subsequent runs is that the running-in process appears complete after the third run, as indicated by the absence of torque overshoots or inter-run torque fluctuations. This suggests a steady state in terms of wear. Notably, all top foils examined in this study were run-in until reaching this steady state, allowing for meaningful comparisons among them.
Based on that, the bearing's running-in behavior can be examined in the simulation model and wear pattern comparisons can be performed with microscopic images.

Evaluation of Running-in Stages

Microscopic images are utilized to depict the resulting top foil wear state, which is then compared with simulation results for h_{wear} computed using $H_{\mathrm{mixed}} = 3\,\mu\mathrm{m}$. Fig. 5.9 illustrates this comparison. Starting with images of the new state, both the top foil picture and simulation result show no wear. At 10 N, minor wear is evident at the trailing edge on the inner radius (area II) of the top foil. The simulation result similarly demonstrates smoothing at the upper portion of the inner radius coating accumulation, precisely at the trailing edge. With a 60 N thrust load, abrasion is observable at the inner radius in the middle section of the pad (area I). Wear at the trailing edge also increases in size and depth. This wear pattern is qualitatively consistent in the simulation. Running-in wear at 90 N and 60 krpm leads to wear on the outer radius in area III. Wear increase is smaller but detectable at the inner radius, and the trailing edge also experiences heightened wear. The simulation closely aligns with the microscopic image, with minor discrepancies at the inner radius and trailing edge. This supports the assertion that the running-in process and its stages in the annular-shaped top foil can be effectively captured using the adjusted simulation model.
With the help of simulation results, the running-in conditions of the bearing can be further analyzed. Simulation results for film height in the discussed load cases are illustrated in Fig. 5.10 as a 3D-height representation. The simulation indicates that at 10 N, only the first row of bumps makes contact with the top foil, leaving the remaining pad unengaged. The minimum film height of $3\,\mu$m is observed in a small region at the inner radius, specifically at the trailing edge near the coating accumulation. At 60 N thrust load, pressure build up results in a tapered land topology, with all bumps in contact and slight top foil sagging. Coating accumulations remain dominant, framing the pad at both inner and outer radii. Between 60 N and 100 N, topological changes are minimal. Wear-related height changes occur primarily at accumulations and the trailing edge, leading to a flatter film height topology. However, the coating accumulations are far from completely wearing off. In summary, for this bearing concept, considering the given step height, width, coating accumulation, and mixed lubrication limit, the bearing can sustain only 7 N without wear. Even with a uniform coating distribution, this bearing geometry is limited to carrying a maximum of 20 N before experiencing wear, particularly at the leading edge. Further discussion on this aspect is provided in Sec. 5.3.2.

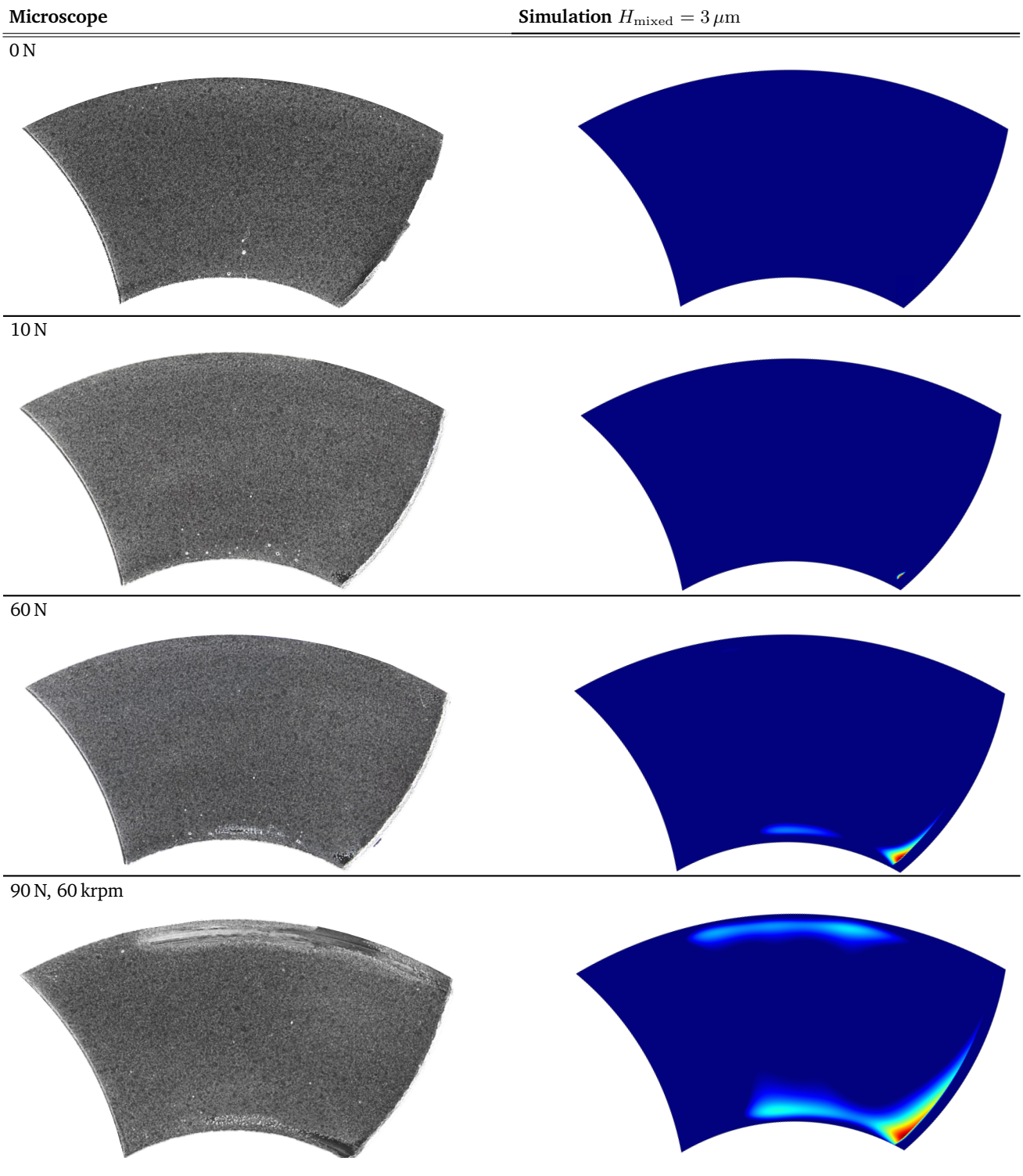

Figure 5.9.: Running-in wear shown for one top foil (TF_3) on the left side in microscopic images and on the right side in simulation results.

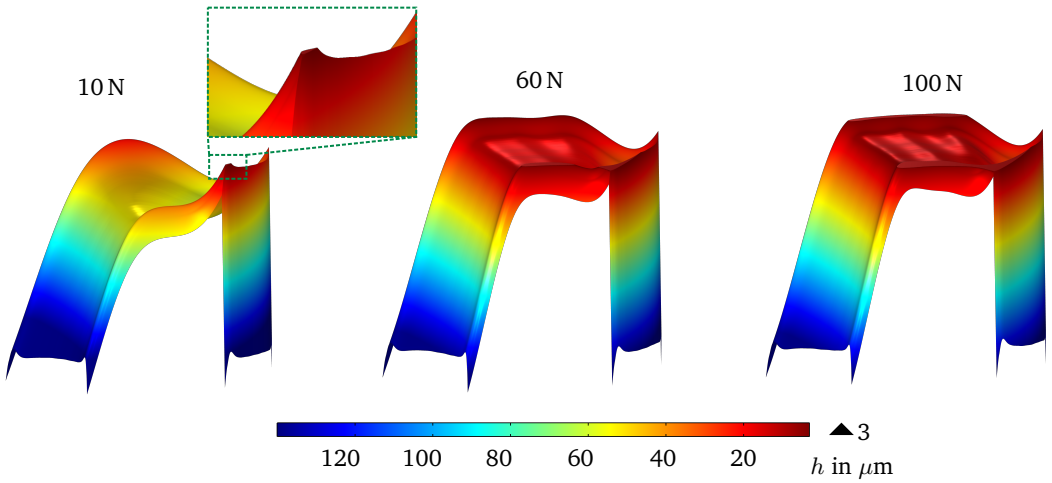

Figure 5.10.: Film height h during 3 running-in states ($H_{\mathrm{mixed}} = 3\,\mu\mathrm{m}, n = 120\,\mathrm{krpm}$).

5.3. Validation of Bearing Performance

In this section, the simulation results concerning bearing performance of the annular-shaped bearing topology are validated. The validation process involves the following investigations:

- Analysis of the performance map based on simulation results from the modified TEHD simulation model and measurements from the high-speed test rig
- Comparison of two top foils with different step heights s_{h}
- Examination of the wear pattern concerning bearing performance

The evaluation includes the power loss and load-carrying capacity of the high-speed test rig, which are compared to the simulation results, while considering uncertainties inherent in both simulation and experimentation.
For the first comparison, the top foil, called TF_1, investigated in Sec. 5.3.2, is used. Its input parameters are examined in Sec. 4.3.
To initiate the comparison, the top foil labeled as TF_1 is employed, which has been detailed in Section 5.3.2. The parameters associated with TF_1 are thoroughly examined in Section 4.3. A "performance map" (Fig. 5.11) is introduced for comparative purposes. This map depicts the experimental and simulation results with respect to power loss and thrust load at different rotational speeds. Specifically, considering 120 krpm, the maximum design speed, and 90 krpm, a speed where the bearing can handle substantial loads without excessive wear up to approximately 80 N.
At 90 krpm it is anticipated that, the bearing exhibits nearly half the friction losses compared to 120 krpm due to the expected quadratic correlation between spinning speed and power loss (refer to Eq. 2.28).
The side losses—discussed in Sec. 3.1.1—are taken into account and are added to the simulation results, which contribute with 25 W for 120 and 12 W for 90 krpm.
Notably, the presented experimental results represent mean values from five runs, accounting for a repetition error of 5%, including sensor errors discussed in Section 3.1.2. The estimated input uncertainty for the simulation results is approximately $\pm 5.5\%$, a derivation detailed in Section 4.4.
The simulation results are obtained as follows:

1. Simulation of run up to 120 krpm with $H_{\mathrm{min}} = 3\,\mu\mathrm{m}$ approach (compare Sec. 5.2).

Parameter	Value	Variation	Description
$\bar{s}_{\mathrm{h}}$	66 μm	$\pm 2\%$	Step height
$\bar{s}_{\mathrm{w}}$	600 μm	$\pm 6\%$	Step width
H_{bowl}	20 μm	$\pm 25\%$	Maximum bowl height
H_{coat}	12 μm	$\pm 25\%$	Maximum height of the coating accumulation

Table 5.1.: Input parameters for TF_2.

2. Simulation of wear until 100 N is reached. The wear pattern is stored into the variable $h_{\mathrm{wearstore}}$.
3. With disabled wear algorithm, all necessary load states for the two velocities are calculated. The stored wear pattern $h_{\mathrm{wearstore}}$ of the previous step is added to the local film height variable h.

Conversely, obtaining the experimental results involve:

1. Driving the running-in procedure discussed in Sec. 5.2.2.
2. After reaching 120 krpm and 100 N load, the operating point is held until a steady state is reached. Steady state can be determined by investigating temperature gradients of all measured temperatures in the test rig as well as the spinning speed controller reaching a stable state where the spinning speed variation is below 0.01 krpm.
3. Systematically decreasing the thrust load in 10 N increments, maintaining each point until steady state is reached. The output values are calculated and stored as average values over five seconds.
4. After reaching 30 N, the velocity is decreased to 90 krpm and the load is increased to 80 N. Step 3. is repeated until 30 N is reached.
5. Step 2. to 4. are repeated five times.

Based on this, the results of these measurements are discussed, comparing them to the simulation results, focusing on the top foil TF_1. A comprehensive examination of TF_1's geometric properties is available in Sec. 4.3.2. Fig. 5.11 presents the results for 90 krpm, demonstrating an almost linear behavior for both simulation and experiment across various operating points. While the average simulation result slightly exceeds the experimental counterpart, the experimental values remain within the simulation range when considering their uncertainty. Therefore, it can be concluded that the modeling uncertainties (refer to Fig. 2.10 and Fig. 2.11) are below the measurement system's resolution and input uncertainty range. This indicates that the model can predict the bearing behavior in the shown load range from 30 to 80 N and 90 krpm correctly.
Similar analysis applies to the results obtained at 120 krpm. Notably, load conditions exceeding 90 N exhibit a deviation from the near-linear trend observed at lower loads. The simulation and experimental results show slight deviations in the slope, with the experimental data indicating a more progressive change. Despite this, all measured points remain within the simulated uncertainty range. Consequently, the model accurately predicts the bearing's behavior within the provided range of 30 to 80 N and 120 krpm.

5.3.1. Step Height Variation

Subsequently, a step height variation is considered. This parameter variation is an essential element in simulating model validation to ascertain the parameter variability's impact. To assess this, the step height

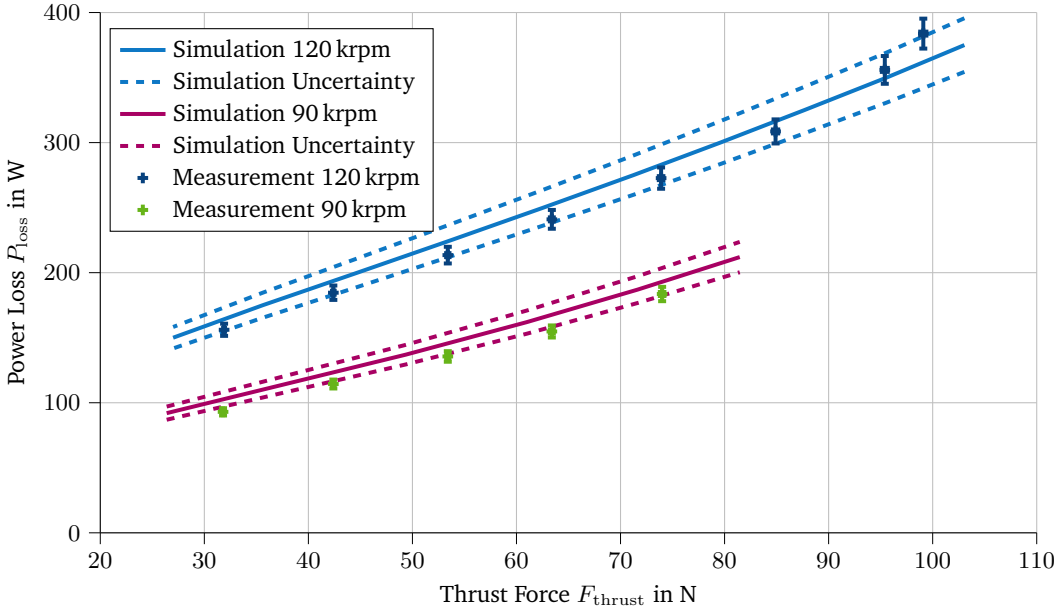

Figure 5.11.: Performance map TF_1 for 120 and 90 krpm with experimental and simulation results.

input parameter is modified, aiming to observe a consistent output relationship in both the simulation and real-world scenarios [76]. Since deviations can arise due to the stamping process, a feasible step height with acceptable accuracy across the pad is around $60\,\mu m$. A top foil—denoted as TF_2—is selected with a mean step height of $66\,\mu m$, contrasting with the TF_1 top foil featuring an average step height of $145\,\mu m$.

Table 5.1 compiles crucial parameters for TF_2. The results for both simulation and measurements are presented in Fig. 5.12 using a performance map at a speed of 120 krpm. The performance map reveals a nearly identical power loss between both top foils at loads around 30–50 N. However, higher loads unveil a discernible change in slope, with the difference peaking at 100 N, amounting to nearly 50 W. Consequently, it is evident that this altering input parameter induces corresponding changes in output for both simulation and experiment, affirming the model's predictive capability.

Additionally, the wear pattern in both simulation and experiment can be compared. Fig. 5.13 displays the simulated wear pattern for the top foil TF_2, alongside a microscopic image of the top foil. The deformation (v_{3T}) for both top foils (TF_1 and TF_2) is also presented. The higher step height of TF_1 contributes to greater deformation, aligning with the observations in Section 4.3.3. Consequently, TF_1 demonstrates a higher wear peak near the trailing edge, approximately $21\,\mu m$ compared to TF_2 with around $8\,\mu m$. Moreover, increased wear occurs at coating accumulations for TF_2, affirmed by the microscopic image. Thus, the simulation model accurately predicts the wear pattern for varying step heights.

5.3.2. Wear Pattern Sensitivity on AFTB Performance

Section 5.2.2 explores a decline in measured power loss due to increased wear during running-in experiments on the high-speed test rig. Here, this behavior is investigated using the simulation model, examining various running-in conditions. The simulation procedure largely follows the description in Sec. 5.3. However, there's a distinction in the spinning speed set in step 1, ranging from 120 to 50 krpm in increments of 10 krpm. The obtained wear results are used to establish a characteristic curve, ranging from 30 to 100 N. These conditions are compared at 120 krpm, and the resulting performance map is

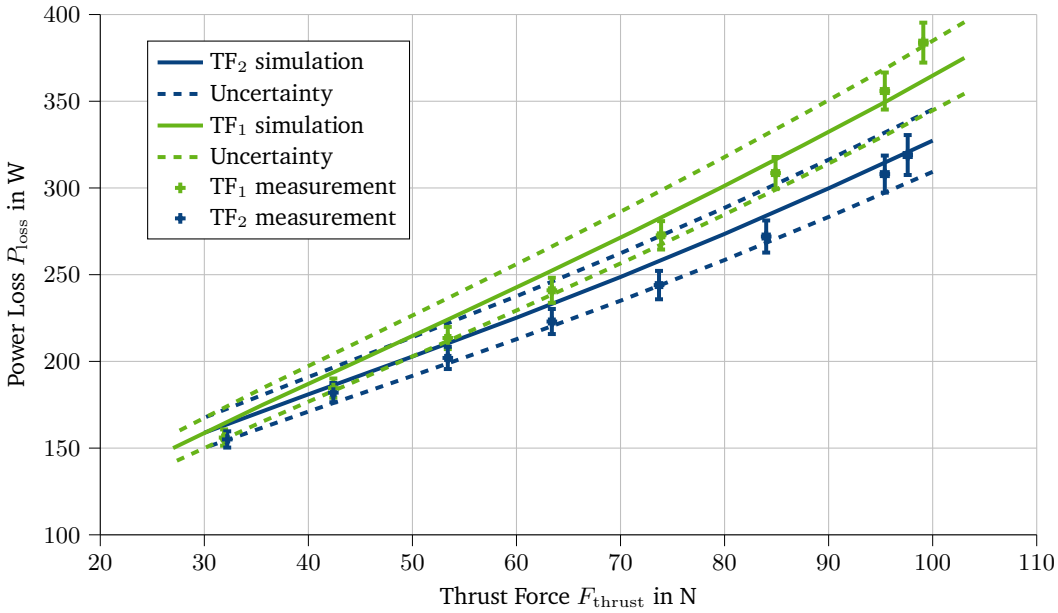

Figure 5.12.: Performance map for step height variation comparison at 120 krpm with simulation and measurement results for TF_1 and TF_2.

presented in Fig. 5.14a. Evidently, running-in conditions involving 100 N and 50 krpm yield improved performance in contrast to the 120 krpm running-in case. These differences are more pronounced at higher loads and diminish at loads below 50 N.
Therefore, it's reasonable to focus on the highest load case, as illustrated in Fig. 5.14b. This graph depicts the performance quantity Φ_{Loss}, derived from the loss divided by the load capacity, evaluated at 120 krpm on the left vertical axis. Additionally, wear volume is shown on the right vertical axis. The horizontal axis represents the running-in spinning speed for a 100 N load on the bearing. Analyzing the wear volume indicates an exponential increase as the running-in speed decreases. This trend aligns with expectations, as reduced running-in speeds necessitate a better bearing topology to sustain the same load, leading to increased wear. The maximum wear volume is observed at the last simulated point with 50 krpm carrying 100 N. This point demonstrates extensive wear on both the complete coating accumulation and portions of the coating layer within the pad's middle section, compensating for the top foil sagging. However, simulating lower speeds is unfeasible with this bearing design.
Focusing on performance at 120 krpm, it's evident that smaller wear leads to worse performance until a threshold, at around 80 krpm, beyond which no performance increase is detectable. This behavior can be explained by factors like advancing smoothing in of the film height disturbances caused by the coating accumulations. Below 80 krpm, the coating accumulations are smoothed in completely. In contrast, lower running-in speeds lead to greater sections of the bearing, reaching the limiting film height of $H_{\text{mixed}} = 3\,\mu\text{m}$, resulting in concurrent wear. However, this doesn't induce significant changes in the bearing's topology, such as an improved taper land ratio or smaller step size. For that purpose, substantial wear on the entire land section would be necessary.
This behavior is also examined using experimental results from the top foil run-in at 50 krpm, referred to as TF_3 hereafter. Notably, the bump foil remains consistent in this test setup. The simulation includes certain adjustments in TF_3's input, detailed in Table 5.2. This top foil features a slightly lower step height and smaller average coating distribution than the top foil discussed in Section 4.3.
Fig. 5.15 illustrates the resulting performance map for TF_3 through simulation and measurement results,

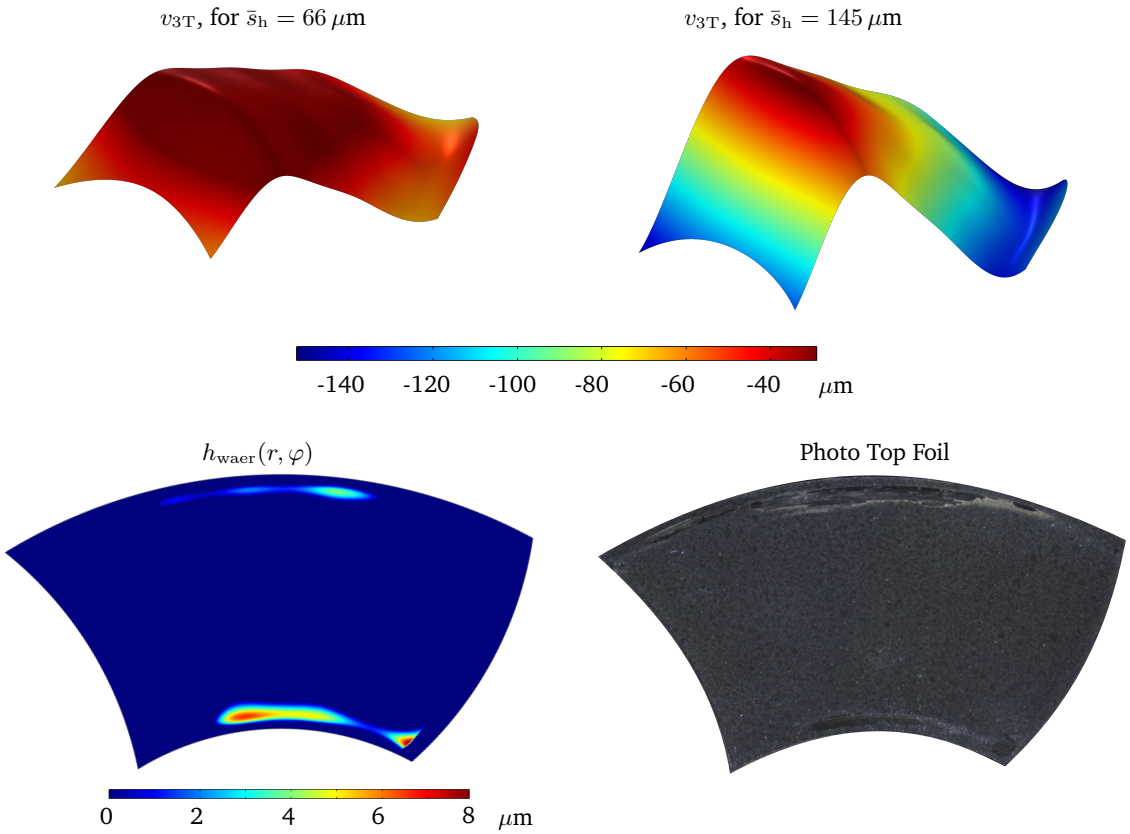

Figure 5.13.: Top foil deformations v_{3T} for TF_1 and TF_2 as well as simulated and measured wear pattern due to running-in for TF_2.

along with associated uncertainties, at 120 krpm. Additionally, simulation results for TF_1 are included for comparison. The figure shows that for lower loads, differences are minor, but higher loads exhibit an increased slope in TF_1's simulation results compared to TF_3. While experimental data demonstrates a slightly lower mean value for TF_3, it remains within the simulation's uncertainty range. The disparity at high load points signifies a significant difference and validates the self-optimizing behavior discussed in Fig. 5.14b. This reaffirms that the simulation model can adapt to varying conditions, as long as they're included as input parameters.
Fig. 5.16 presents simulation results for various conditions: a top foil with $h_{bowl}(r) = 0$ and $h_{coat}(r) = 0$ (called TF_1 undisturbed), standard running-in of TF_1, and a running-in condition with $F_{thrust} = 100\,N$ at $n_{r-in} = 60$ krpm. These simulations are performed at $n = 120$ krpm and $F_{thrust} = 100\,N$. The upper part of the figure depicts the wear pattern and its maximum height. The middle row shows the pressure distribution p resulting from the compressible Reynolds equation, presented as color on the film height

Parameter	Value	Variation	Description
$\bar{s}_h$	130 μm	$\pm 2\%$	Step height
$\bar{s}_w$	600 μm	$\pm 6\%$	Step width
H_{bowl}	15 μm	$\pm 25\%$	Maximum bowl height
H_{coat}	10 μm	$\pm 25\%$	Maximum height of the coating accumulation

Table 5.2.: Additional input parameters for TF_3.

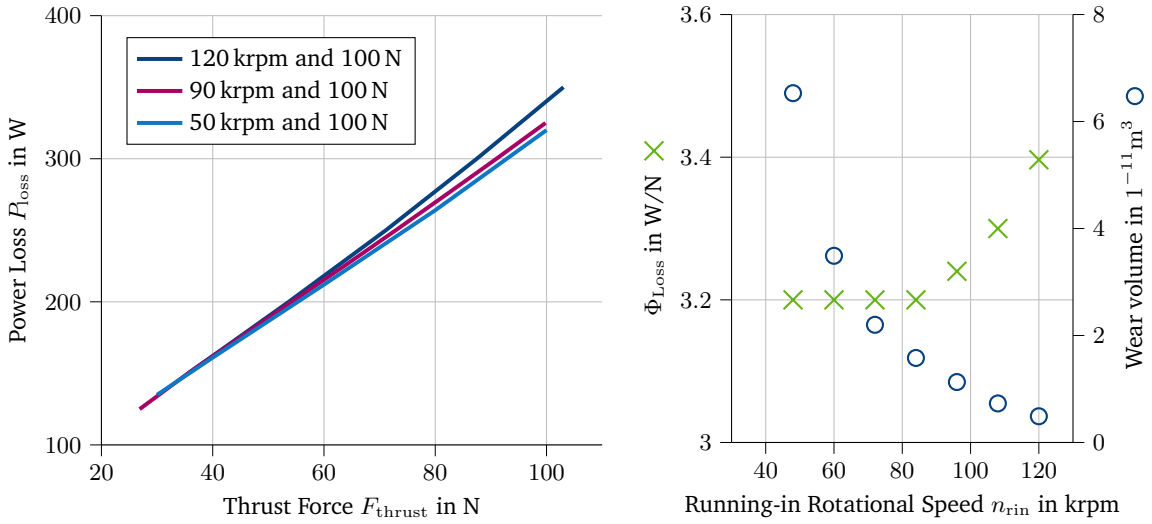

(a) Performance map for a top foil with different running-in speeds (without side losses).

(b) Wear volume and Φ_{Loss} for different running-in speeds (without side losses).

Figure 5.14.: Running-in speed's influence on bearing performance.

along the z-axis. The lower row presents the local shear stress $dM = \frac{-2\eta}{h}(x\,\frac{\partial v}{\partial z} - y\,\frac{\partial u}{\partial z})$ for the three cases. The subsequent observations are discussed in the following. Even for an undisturbed TF1, wear is evident at the inner radius r_{i} near the trailing edge within area II. The maximum wear height is 8 μm. The standard TF_1 configuration exhibits wear in all three areas described in Fig. 5.2, resulting in a maximum wear height of 21 μm. The third condition, with greater prominence and a maximum wear height of 30 μm near the trailing edge, similarly displays wear in these areas.

These varying wear conditions lead to distinct film height distributions, subsequently influencing the resulting pressure profiles. In the first condition, the bending of the top foil induces elevated deformation near the trailing edge—also the reason for wear in this location—creating a secondary, albeit smaller, taper land area within a pad. In this area, a peak pressure of 4 bar is observed. The primary taper part of the bearing generates a maximum pressure of approximately 2.5 bar. For the standard case, the coating accumulations result in similar behavior, but with additional pressure peaks at the coating accumulations near the inner and outer radii within the pad's center. In the third condition, the smoother coating layer leads to a more pronounced taper land topography. Pressure peaks are now evident at the connection to the bump arcs and at the trailing edge. These peaks are better distributed, with a maximum pressure peak of 2.6 bar. This behavior is reflected in the film quantity Φ_{Film}, which stands at 0.099 for the first case, 0.093 for the standard configuration, and 0.19 for the more aggressive running-in condition. The quantity remains nearly constant for the first two cases but almost doubles for the third, primarily due to a more even load distribution.

This behavior also results in differing shear stresses, affecting the deviation of calculated power losses as discussed in Fig. 5.14. The local shear stress, evaluated in the bottom row of Fig. 5.16, reveals that coating accumulations yield higher local shear stresses. Only the third condition, with a more even film height distribution, shows evenly distributed shear stresses. It's evident that defects in the top foil induce greater stress on the bearing, which can be offset through a more aggressive running-in procedure. However, a defect-free top foil with the current annular design, featuring a step height of around $150\,\mu\text{m}$, cannot undergo running-in without experiencing wear. This is due to the fact that the top foil is forced to bend towards the trailing edge as it is discussed in Sec. 4.3.3.

In conclusion, the bearing's performance—described by the performance quantity Φ_{Loss} and analyzed

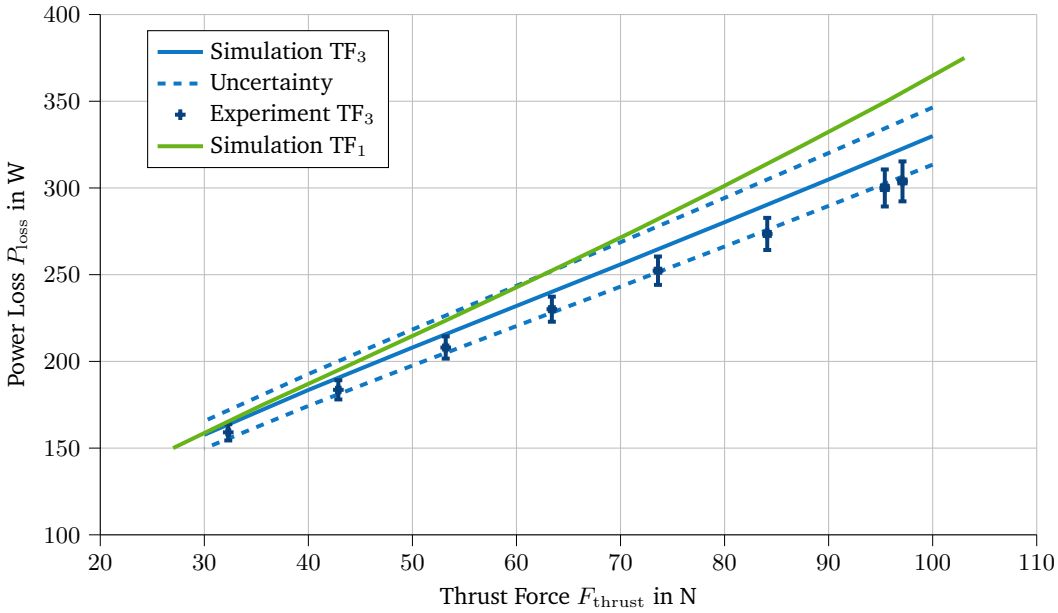

Figure 5.15.: Performance map of TF_3 used in running-in process with 50 krpm and 100 N. Compared to the simulation results of TF_1. All at 120 krpm.

through performance maps—demonstrates excellent validity and reproducibility in comparison to the experiments conducted in the test rig. This validation holds considering the provided boundary conditions and input parameters for both the bearing and its environment. Hence, it's evident that the bearing and its surroundings are accurately modeled within the established accuracy. Consequently, the simulation's predictive capability concerning bearing performance can be confidently asserted as validated.

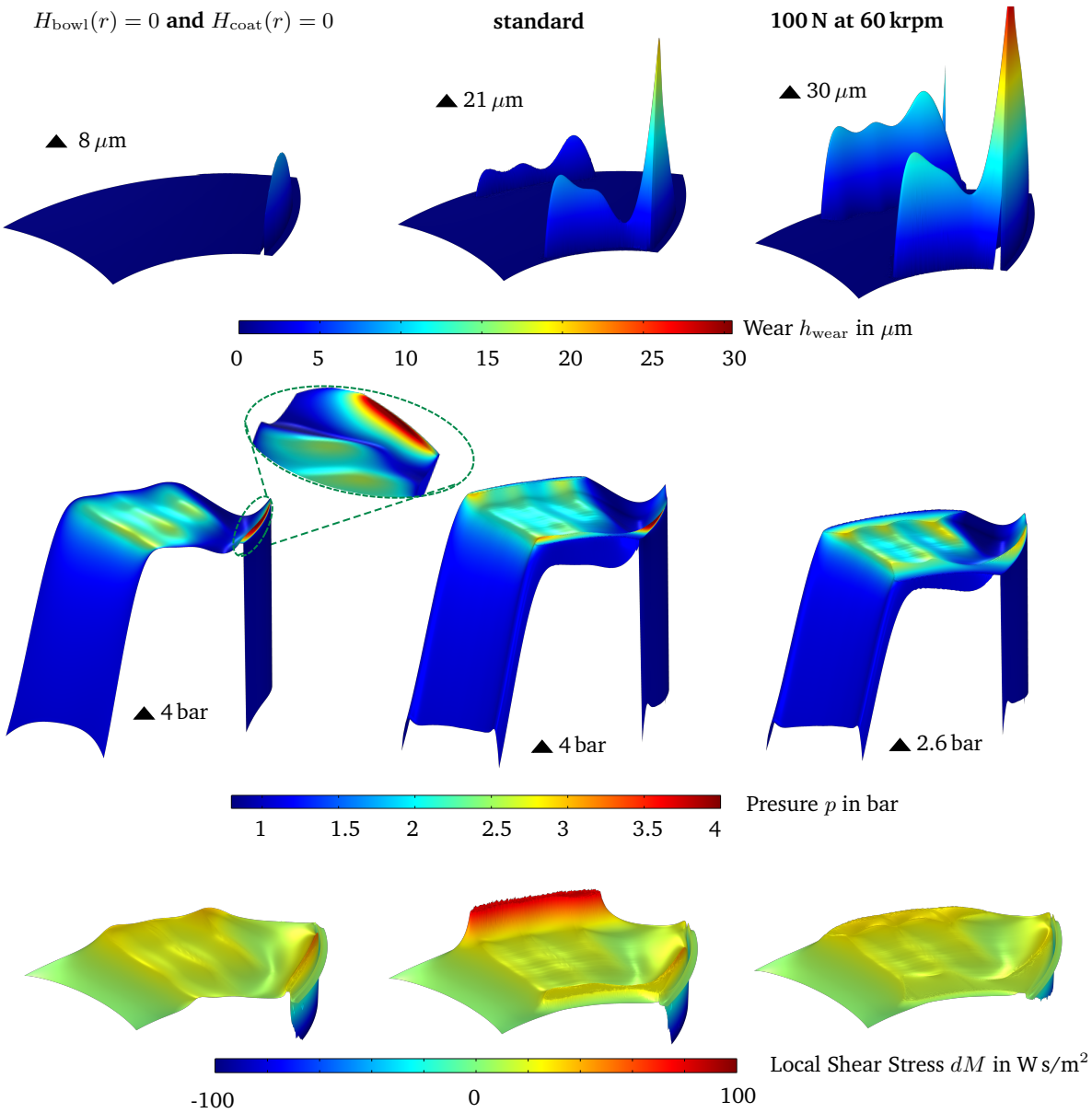

Figure 5.16.: Simulation results at 120 krpm and 100 N for TF_1 without defects (bowl height and coating distribution set to zero), standard running-in and running-in at 60 krpm.

5.4. Thermal Household Validation

For the purpose of design and optimization, the thermal balance of the bearing system holds particular significance and necessitates thorough validation (refer to Section 2.2.5). The validation process encompasses the following investigations:

- Examination of simulation results with specific focus on the simulated temperatures of the rotor disk T_{RD} and the air film T_{air}.
- Analysis of the principal heat path computed using the modified TEHD model.

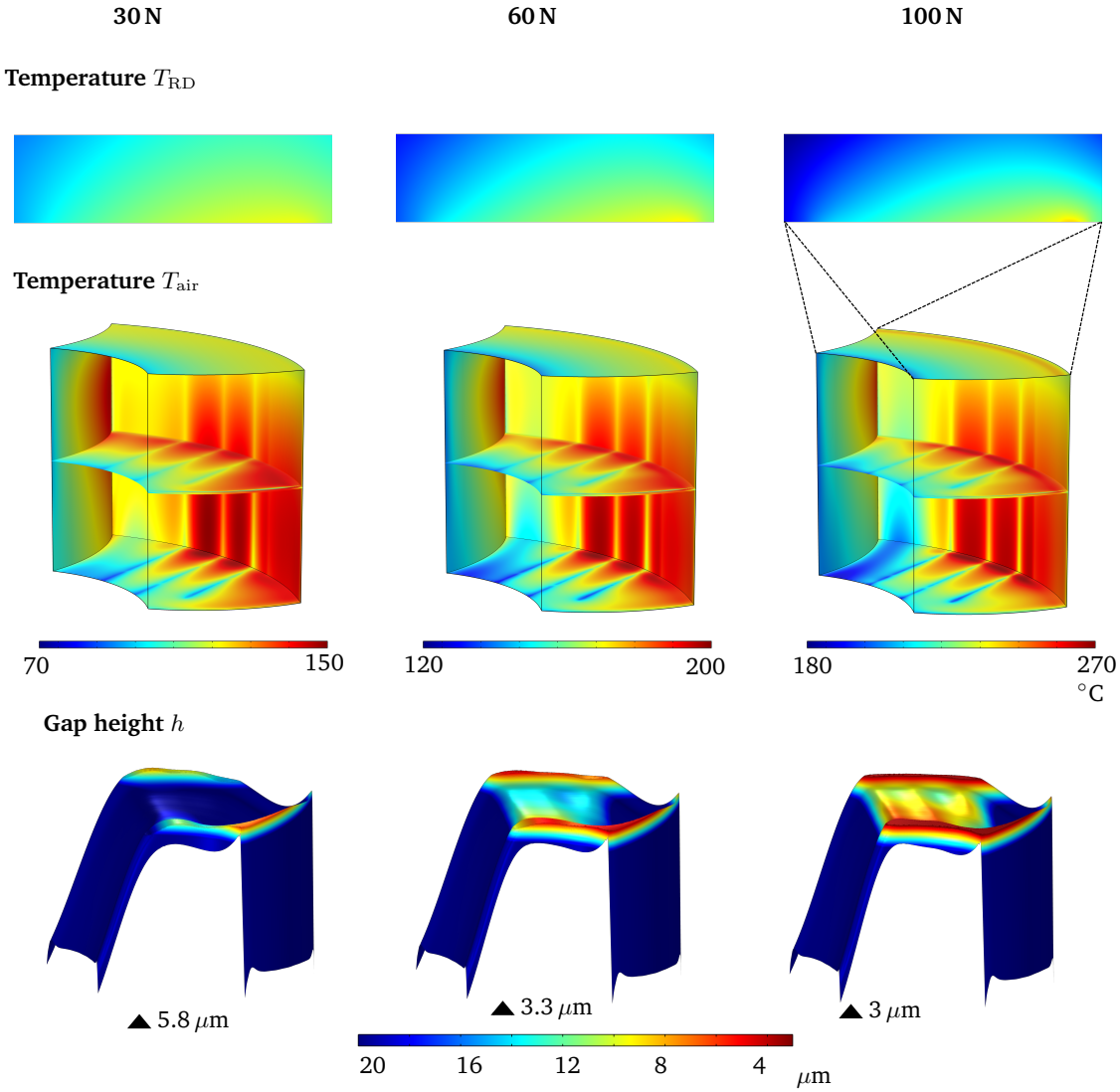

Figure 5.17.: Simulation results of the AFTB with focus on disk and air film temperatures, as well as local film heights, all for three load cases at 120 krpm.

- Comparison between the simulated modified thermal resistance model and measurements from the thermal resistance test rig.
- Comparison between temperatures of the bearing system derived through the modified TEHD model and measurements from the high-speed test rig.

Initially, simulation results for three load cases (30, 60, and 100 N represented in three columns) are examined at 120 krpm, post simulated running-in, in Fig. 5.17. These results for the top foil TF_1 were already investigated in Sec. 5.3 with respect to performance, and its input parameters are introduced in Sec. 4.3.2. The uppermost row of the figure presents the disk temperature T_{RD}, calculated through the heat diffusion equation (Equation 2.2). The subsequent row shows the air film temperature T_{air}, deduced using the modified three-dimensional energy equation Eq. 4.25. For enhanced comprehension of the existing gap height, the air film's height h is illustrated in the third row, derived via the compressible

Reynolds equation Eq. 2.3. Notably, the color bar for this row spans from 20 to $3\,\mu\mathrm{m}$, facilitating clearer representation of minute gap heights. It's worth noting that the maximum gap height across all three cases equals the step height s_h, amounting to $145\,\mu\mathrm{m}$.
Analysis of the rotor disk temperature T_RD indicates a more uniform heat distribution at lower loads compared to the 100 N case. However, the highest temperature consistently occurs at the same location, nearly at the outer diameter where the bearing gap interfaces the disk. Given that the generated heat has the highest density at the coating accumulations at the outer diameter, this is well-founded (compare Fig. 5.16).
The air film's temperature distribution (T_air) in the second row exhibits a relatively uniform pattern across the three load cases. Only the maximum and minimum temperatures escalate by approximately 50°C per 30 N increase in load. This pattern is reasonable, considering that generated heat is directly proportional to the thrust load at a given velocity (refer to Fig. 5.7a).The lowermost layer of T_air interfaces with the top foil. Heat sinks at the bump arc connections are discernible by lower temperatures, while regions with greater gap height in the taper region beyond the leading edge exhibit lower temperatures compared to areas with smaller gap heights.
The difference in the maximum temperature can be explained by assessing the gap height h in the third row of the figure. Given that the top foil undergoes a running-in process at a 100 N load case with H_mixed $=3\,\mu\mathrm{m}$, it becomes evident that the minimum gap height for this scenario is $3\,\mu\mathrm{m}$. The color bar for this row is tailored from 20 to $3\,\mu\mathrm{m}$ to accentuate smaller gap heights. Notably, the maximum gap height across all three cases remains consistent at the step height s_h. It is observable that the taper land-like film height reaches full development at 30 N. For the 100 N load case, the primary change involves a decrease in the distance between the top foil and the rotor disk, accompanied by slight top foil sagging. Gap heights below $8\,\mu\mathrm{m}$ manifest solely at the coating accumulations for all three load cases. Consequently, the bearing behavior remains largely unaltered between 30 N and 100 N in the simulation, with variations chiefly pertaining to the distance between the top foil and the rotor disk. Given that generated heat is inversely proportional to the gap height, greater heat generation occurs for higher loads.

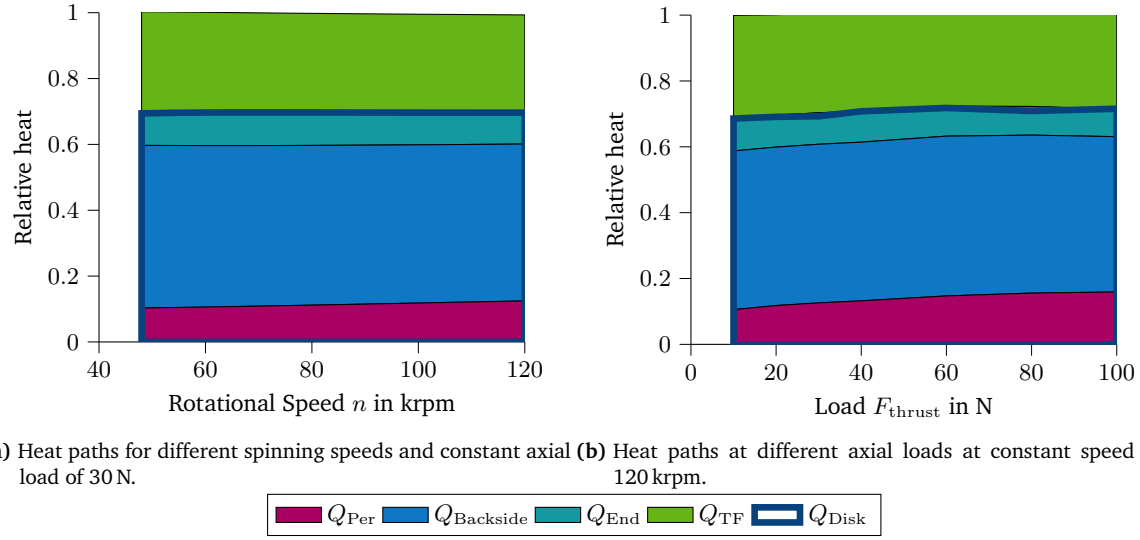

(a) Heat paths for different spinning speeds and constant axial load of 30 N.

(b) Heat paths at different axial loads at constant speed of 120 krpm.

Figure 5.18.: Heat flow paths relative to the power loss in the bearing gap.

Moreover, the bearing system can be assessed in terms of heat paths as explained in Sec. 2.2.5. The outcomes are presented in Fig. 5.18a and Fig. 5.18b, with varying rotational speeds n on the left side

and differing thrust loads F_{thrust} at a constant speed of $n = 120\,\mathrm{krpm}$ on the right side. The results are normalized by the generated power loss in the bearing, as per Eq. 2.28. The relative amount of heat is depicted for cumulative heat flow in the disk Q_{Disk}, comprising the heat over the periphery Q_{Per}, the heat over the rotor disk backside Q_{Backside}, and the rotor end Q_{End}. Likewise, heat influx into the top foil Q_{TF} is presented.
The summation of the aforementioned relative heats are consistently adding up to 1, underscoring their comprehensive description of heat flow within the bearing. Furthermore, it becomes apparent that there is minimal variation in the distribution of heat paths, regardless of changes in speed or load in both diagrams. The division between heat flow within the top foil and the rotor disk consistently is 0.3 to 0.7 across all cases.
This behavior can be attributed to alterations in power loss and heat fluxes into the disk and top foil. Notably, the film height undergoes the most significant change. As both power loss and heat fluxes are inversely proportional to the film height, there is no other dependency left and the correlation remains constant. Thus, the thermal characteristic of this bearing remains consistent across a wide parameter range at $\Phi_{\mathrm{TH}} = 0.3$. To validate these correlations, temperature gradients can be measured. One such gradient describes the thermal resistance of the foil package, an aspect explored in the subsequent section.

5.4.1. Thermal Resistance of the Bump Foil

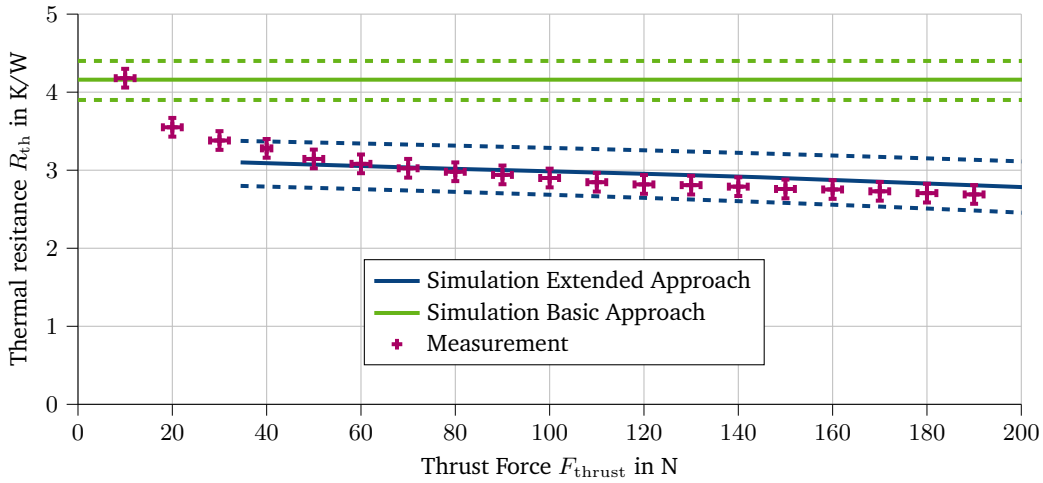

Figure 5.19.: Simulated thermal resistance of Lehn's approach and the extended approach of Sec. 4.2.3. Compared to measurements of the thermal resistance test rig.

The thermal resistance model is an analytical expression originally formulated in Lehn's dissertation [52] and subsequently expanded upon in Section 4.2.3. Given the absence of any existing validation of this thermal resistance model in the literature, and considering the introduced extensions, a specific emphasis is placed on the validation of this thermal resistance model.
Validation of the thermal resistance of the bump foil is conducted within its dedicated test rig, introduced in Section 3.2. For the purpose of comparing measured thermal resistance values with simulations, a simplified model is constructed, comprising solely the top foil and the lines at the bump contacts. The top foil is subjected to a constant heat flux, mirroring the conditions in the thermal resistance test rig. While the thermal resistance model outlined in Sec. 2.2.3, as formulated by Lehn [52], is applied to the contact lines, the extended model introduced in Section 4.2.3 is employed with a heat flux distributed over the entire top foil area. This extended model is therefore dependend on the deflection of the top

foil. The outcomes of the experimental measurements, alongside the simulation results, are depicted in Fig. 5.19. Here, the thermal resistance R_{th} is plotted on the vertical axis as a function of the thrust load F_{thrust} on the horizontal axis. The simulation uncertainties stem from the inherent variability of input parameters concerning the bump foil, such as radius and height, and are quantified at $\pm 6.25\,\%$. Similarly, measurement errors are provided for thrust load ($\pm 1\,\mathrm{N}$) and the measured thermal resistance ($\pm 2\,\mathrm{K} + 1.5\,\%$), as detailed in Section 3.2.2. Notably, the adjusted approach struggles to accurately predict thermal resistance values below thrust loads of 40 N due to the lack of alignment between the bump foil and the base plate, an aspect not accounted for in the simulation model for these specific scenarios (see Section 5.1 for further elaboration).
Because the basic thermal resistance model remains independent to thrust forces, it yields a constant value of $R_{\mathrm{th}} = 4.16\,\mathrm{K/W}$. Conversely, the extended approach factors in the thrust force, resulting in decreasing thermal resistance due to the diminishing distance between the top foil and the base plate as the load increases. The experimental data exhibit a marked decreasing trend at lower force values and display a discernible linear relationship beyond 45 N. Notably, this trend is adeptly captured by the simulated data originating from the new modeling approach. As such, it is deduced that the modification of the thermal resistance model stands as a substantiated expansion, leading to an overall reduction in thermal resistance, ranging from 17 % to 30 % between 40 and 100 N, compared to the basic model.

5.4.2. Temperature of the Bearing System

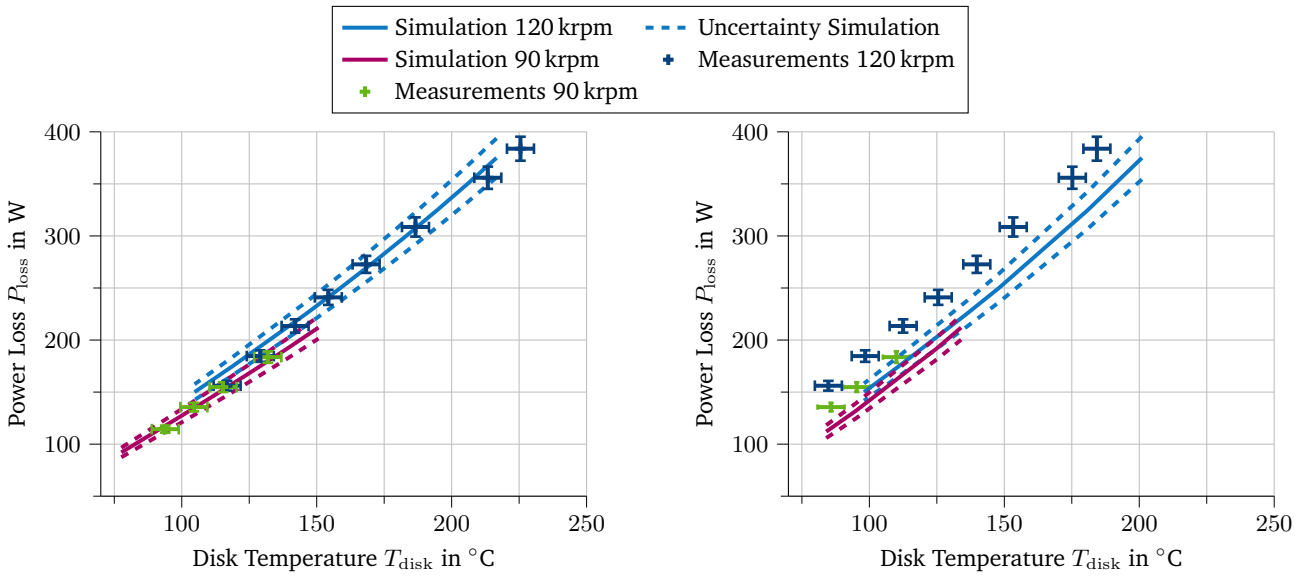

(a) Radial rotor disk temperature position $T_{\mathrm{disk},2}$.

(b) Axial disk temperature position $T_{\mathrm{disk},1}$.

Figure 5.20.: Rotor disk temperature validation. With measurements of the high-speed test rig and TEHD simulation results for 90 and 120 krpm.

To further validate the thermal household, the two pyrometer sensors in the high-speed test rig can be employed. Their calibration as well as their positions are described in Sec. 3.1.1. The measurements are again obtained from TF_1 and the test procedure described in Sec. 5.3. The outcomes are depicted in Fig. 5.20, where the temperature T_{disk} of the disk is plotted against power loss P_{loss} for two distinct rotational speeds. Fig. 5.20a pertains to the radial position $T_{\mathrm{disk},2}$ on the disk, whereas Fig. 5.20b corresponds to the axial position $T_{\mathrm{disk},1}$. The illustrated simulation uncertainty originates from power loss

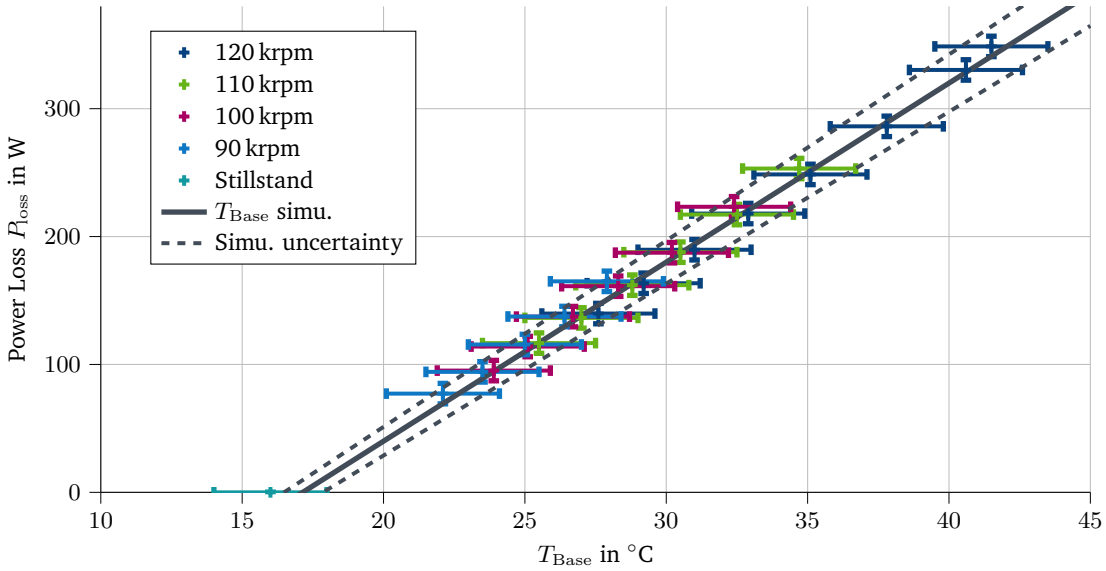

Figure 5.21.: Base temperature measurements for different speeds, compared to the simulated base plate temperature T_{Base}.

uncertainties. For measurements, factors encompassing repeatability error, temperature measurement accuracy, and torque measurement accuracy are taken into consideration.
The results distinctly demonstrate an almost linear correspondence between power loss and temperature for both positions and rotational speeds for simulation and experiment. This alignment is expected within the simulation context, given the thermal households dependency on the velocity and the load is small, as described in the introduction of this section and shown in Fig. 5.18. The fact that the measurement shows the same behavior, testifies to the validity of this relationship. In terms of absolute values, the comparison showcases strong agreement between measured and simulated radial position temperatures $T_{\mathrm{disk},2}$. However, for the axial position $T_{\mathrm{disk},1}$, a constant offset of approximately $10\,°\mathrm{C}$ is observed in the measured temperature when contrasted with the simulation results at the same position. This discrepancy can potentially be attributed to the intricate flow pattern stemming from the externally pressurized axial bearing, causing a less accurate approximation of flow behavior on the rear side of the rotor disk. Despite this offset, the measured and simulated values agree sufficiently, validating the simulation model for disk temperature, along with its corresponding boundary conditions.
Additionally, the base temperature is measured within the high-speed test rig. Drawing on the information provided in Section 4.2.3, wherein the thermal resistance between the cooling water in the base plate and the measurement point is characterized as 0.24 K/W, a straightforward correlation can be established:

$$Q_{\mathrm{TF}} = \Phi_{\mathrm{TH}}\, P_{\mathrm{loss}} = \frac{1}{R_{\mathrm{Base}}}\left(T_{\mathrm{base}} - T_{\mathrm{coolingwater}}\right) \tag{5.1}$$

$$P_{\mathrm{loss}} = \frac{1}{R_{\mathrm{Base}}\,\Phi_{\mathrm{TH}}}\,T_{\mathrm{Base}} - \frac{T_{\mathrm{coolingwater}}}{R_{\mathrm{Base}}\,\Phi_{\mathrm{TH}}} \tag{5.2}$$

Considering the quasi-constant nature of Φ_{TH} across a wide operational spectrum, the function $P_{\mathrm{loss}}(T_{\mathrm{Base}})$ can be deduced. The results, alongside with measured power loss, are displayed in Fig. 5.21, accounting for measurement and simulation uncertainties derived in Sec. 3.1.2 and 4.4. The simulated power loss and temperature align well with their measured counterparts, signifying the accurate modeling of heat transmission through the top foil. This, in turn, affirms the thermal resistance model's validity within the context of the proposed enhancement. Overall, the thermal equilibrium of the model demonstrates compelling agreement and reproducibility in relation to real-world conditions within the test rig, while

appropriately incorporating pertinent boundary conditions and input parameters of the bearing and its surroundings.
Given that all surrounding temperatures, including the disk temperature, and the base plate's temperature values, are within the measured values, it can be concluded that the air film energy equation is modeled correctly within the derived accuracy. Therefore, the thermal household is validated.

5.5. Summary and Conclusion

This chapter is related to the validation of the simulation model. It is structured into four sections, each addressing a distinct bearing characteristic as introduced in Section 2.4.2.
The first bearing characteristic examined pertains to stiffness Φ_{St}. The stiffness of the bump foil is compared with simulations, revealing inconsistent behavior between simulation and experiment. For loads higher 40 N, the simulated stiffness was shown to be higher compared to the experiments. For lower forces, the measurement results exhibit highly nonlinear behavior, attributed to the alignment processes of the bump foil on the base plate. Additionally, the influence of uncertain input parameters results in significant variability at approximately $\pm\,17.6\,\%$. The validation attempt of this bearing characteristic revealed modeling uncertainties, which prevented a successful validation of the stiffness.
Proceeding to the air film height characteristic Φ_{Film}, wear simulation and analysis are conducted. The onset of wear, characterized by the mixed lubrication limit H_{mixed}, is identified through comparison with literature and measurements. Alignment with WLI measurements confirms $H_{\mathrm{mixed}} = 3\,\mu\mathrm{m}$. Subsequently, the running-in process of the top foil is scrutinized. It is established that the novel wear algorithm is able to predict the coating layer's abrasion across various run-in stages.
The performance characteristic Φ_{Loss} (power loss divided by load) is the third bearing aspect examined. The comparison of simulated power loss and thrust load with measurements from the high-speed test rig, encompassing all relevant modeling facets outlined in Ch. 4, yields satisfactory congruence with $\Phi_{\mathrm{Loss}} \approx 3$ for $n = 120\,\mathrm{krpm}$. Furthermore, sensitivity analysis of wear patterns is conducted, affirming that augmented abrasion of the coating accumulation results in enhanced bearing performance. This underscores the necessity of thorough investigating simulation input parameters and expanding the simulation model to achieve such outcomes.
Lastly, the thermal equilibrium characteristic Φ_{TH} is addressed. Initial simulation outcomes are showcased, indicating that the simulated thermal quantity consistently approximates $\Phi_{\mathrm{TH}} = 0.3$ across a broad parameter spectrum, meaning that only 30 % of dissipated heat is transferred into the top foil. To substantiate the simulated findings, the extended thermal resistance model of the bump foils is juxtaposed with measurements from the thermal resistance test rig. The agreement between the extended model and the measurements is notably satisfactory. Furthermore, comparison of temperature measurements from the rotor disk and base plate in the high-speed test rig with simulation results leads to the conclusion that the extended model proficiently forecasts the bearing's thermal balance.
In essence, the validation process attests to the comprehensive nature of the simulation model. The simulation results demonstrate consistent alignment with measurements across various bearing characteristics. This, in turn, substantiates the model's reliability and its utility for further designs and optimizations.

6. Summary and Conclusion

In this thesis, the validation of a simulation model for an air foil thrust bearing through experimental results has been comprehensively presented. The primary objective of this research was to establish the validity of the simulation model by correlating its predictions with experimental data. The validation process focused on crucial characteristics of the bearing, including performance, thermal behavior, stiffness, and film height distribution. This summary encapsulates the key contributions and outcomes from each chapter of the thesis.

Chapter 2 introduced the context of air foil thrust bearings, delving into their historical development and highlighting the governing equations derived from prior work. It also provided insights into tribological systems and discussed the principles of model validation, emphasizing the importance of investigating both simulation and experimental uncertainties to successfully validate a simulation model or reveal modeling inaccuracies.

Chapter 3 then detailed the test rigs and measurement tools designed to validate the simulation model. A newly developed high-speed test rig capable of thrust bearing measurements under demanding conditions was introduced. The test rig is able to run at 120 krpm while applying 100 N of thrust load on the foil bearing. One special property of the test rig is the gimbal which enables an alignment of the bearing to the rotor disk. With the help of this test rig, power loss and temperature measurements were obtained with high precision. The repeatability error was found to be below 5%. Additionally, a specialized thermal resistance test rig and mechanical property measurement setups were presented, along with discussions on measurement capabilities and uncertainties.

The modeling and adjustment of the air foil thrust bearing were explored in Chapter 4. The chapter investigates the intricate components of the bearing, such as the rotor, bump foils, and top foil, with sensitivity analysis guiding the identification of key parameters. Geometric properties were determined through thorough measurements, and the model was extended to incorporate an extended thermal resistance model, as well as introducing a new wear algorithm. The presented wear algorithm can calculate running-in wear for hard-soft contacts with a fluid film in between. Furthermore, detailed CFD simulations were presented to calculate the heat transfer coefficient for the rotor disk. In addition to that, uncertainties arising from input variables were presented and summarized to provide simulation uncertainties for the validation in Chapter 5.

Finally, Chapter 5 concluded the validation process by focusing on four main bearing characteristics. The stiffness of the bump foil, air film height distribution, bearing performance, and thermal behavior were all validated through comparisons of simulation results with experimental data. The analysis revealed that the simulation model exhibited good agreement with empirical findings across these key aspects. The validation efforts extended to diverse parameters, wear patterns, and thermal conditions, demonstrating the robustness of the simulation model. In particular, the validation of wear patterns stresses the importance of incorporating running-in wear into the simulation model for this bearing design. Considering all model extensions, the calculated uncertainties of the input parameters, as well as measurement uncertainties, the performance, wear patterns, and thermal behavior of the bearing were thoroughly validated. However, it was found that the stiffness of the bearing was not fully represented by the simulation model due to the alignment process of the bump foils, making flat shell theory insufficient for simulating the stiffness of this bearing design. Nevertheless, the stiffness was found to be almost independent of the other bearing characteristics due to the rather stiff top foil.

In conclusion, this thesis successfully achieved its main objective of validating a simulation model for an air foil thrust bearing using comprehensive experimental investigations. The multi-step validation process, encompassing performance, thermal behavior, stiffness, and film height distribution, established the reliability and accuracy of the simulation model. The results have profound implications for understanding

the involved behavior of air foil thrust bearings and delivers the starting point for optimizing their performance in practical applications.
Furthermore, the sensitivity analysis and adjustments to the simulation model highlight the significance of model refinement and adaptation. The wear algorithm introduced in this work not only aids in simulating real-world wear patterns but also opens avenues for future research on wear-related phenomena in thrust bearings.
Future work can also focus on incorporating the alignment process of bump foils and their impact on the stiffness behavior of the bearing. Furthermore, a full bearing model, including all pads, could help gain an understanding of the bearing under misaligned conditions. In addition to these stationary bearing properties, future research could incorporate dynamic aspects and investigate the influence of the thrust bearing on the whole rotor bearing system.

Bibliography

[1] G. L. Agrawal. “Foil air/gas bearing technology—an overview”. In: 78682 (1997), V001T04A006. DOI: 10.1115/97-gt-347.

[2] M. Arghir and O. Benchekroun. “A New Structural Bump Foil Model With Application From Start-Up to Full Operating Conditions”. In: *Journal of Engineering for Gas Turbines and Power* 141.10 (2019). ISSN: 0742-4795. DOI: 10.1115/1.4044685.

[3] F. Balducchi, M. Arghir, and R. Gauthier. “Experimental analysis of the dynamic characteristics of a foil thrust bearing”. In: *Journal of Tribology* 137.2 (2015), p. 021703. DOI: 10.1115/1.4029643.

[4] F. Balducchi et al. “Experimental Analysis of the Start-Up Torque of a Mildly Loaded Foil Thrust Bearing1”. In: *Journal of Tribology* 135.3 (2013), p. 316. ISSN: 0742-4787. DOI: 10.1115/1.4024211.

[5] Y. Basar and W. B. Krätzig. *Mechanik der Flächentragwerke: theorie, berechnungsmethoden, anwendungsbeispiele*. Springer-Verlag, 2013.

[6] S Bauman. “An Oil-Free Thrust Foil Bearing Facility Design, Calibration, and Operation. NASA TM 2005-213568”. In: *National Aeronautics and Space Administration, Cleveland, OH* (2005).

[7] E. E. Bisson and W. J. Anderson. *Advanced bearing technology*. Vol. 38. Office of Scientific and Technical Information, National Aeronautics, 1964.

[8] H Block. “The Foil Bearings-A New Departure in Hydrodynamic Lubrication”. In: *Lubrication Engineering* 316 (1953).

[9] P. Bonello and H. M. Pham. “Nonlinear dynamic analysis of high speed oil-free turbomachinery with focus on stability and self-excited vibration”. In: *Journal of Tribology* 136.4 (2014), p. 041705. DOI: 10.1115/1.4027859.

[10] R. J. Bruckner. “Simulation and modeling of the hydrodynamic, thermal, and structural behavior of foil thrust bearings”. PhD thesis. 2004.

[11] T. A. Cable. “Experiments and Predictions with a Foil Thrust Bearing Supported by Metal Mesh Screen”. PhD thesis. Texas AandM University, 2020.

[12] R. Chen et al. “Research on the performance of foil thrust bearings under dynamic disturbances”. In: *Tribology International* 174 (Oct. 2022), p. 107744. DOI: 10.1016/j.triboint.2022.107744.

[13] H. Czichos and K.-H. Habig. *Tribologie-Handbuch: Tribometrie, Tribomaterialien, Tribotechnik*. Springer-Verlag, 2010.

[14] C. DellaCorte and M. J. Valco. “Load capacity estimation of foil air journal bearings for oil-free turbomachinery applications”. In: *Tribology Transactions* 43.4 (2000), pp. 795–801.

[15] C. DellaCorte, A. R. Zaldana, and K. C. Radil. “A systems approach to the solid lubrication of foil air bearings for oil-free turbomachinery”. In: *J. Trib.* 126.1 (2004), pp. 200–207. DOI: 10.1115/1.1609485.

[16] C. DellaCorte et al. “Performance and durability of high temperature foil air bearings for oil-free turbomachinery”. In: *Tribology transactions* 43.4 (2000), pp. 774–780. DOI: 10.1080/10402000008982407.

[17] J. R. Dickman. *An investigation of gas foil thrust bearing performance and its influencing factors*. 2010.

[18] D Dowson. “A generalized Reynolds equation for fluid-film lubrication”. In: *International Journal of Mechanical Sciences* 4.2 (1962), pp. 159–170. DOI: 10.1016/s0020-7403(62)80038-1.

[19] B. Dykas. “Factors influencing the performance of foil gas thrust bearings for oil-free turbomachinery applications”. PhD thesis. Case WEstern Reserve University, 2006.

[20] B. Dykas et al. “Design, fabrication, and performance of foil gas thrust bearings for microturbomachinery applications”. In: *Journal of Engineering for Gas Turbines and Power* 131.1 (2009).

[21] M. Eickhoff et al. “Analysis of Air Foil Thrust Bearings with Annular Top Foil Including Wear Prediction, Part I: Modeling and Simulation”. In: *Tribology International* (2022). DOI: https://doi.org/10.1016/j.triboint.2022.108174.

[22] K. Feng and S. Kaneko. “Analytical Model of Bump-Type Foil Bearings Using a Link-Spring Structure and a Finite-Element Shell Model”. In: *Journal of Tribology* 132.2 (Apr. 2010). 021706. ISSN: 0742-4787. DOI: 10.1115/1.4001169.

[23] M Fénot et al. “A review of heat transfer between concentric rotating cylinders with or without axial flow”. In: *International journal of thermal sciences* 50.7 (2011), pp. 1138–1155.

[24] S. A. Fricke. “Auswirkungen von Unsicherheiten auf die Validierung einer Mischreibungssimulation”. PhD thesis. 2019.

[25] Abdelrasoul M. G. and Shigehiko K. “Fluid Flow and Thermal Features of Gas Foil Thrust Bearings at Moderate Operating Temperatures”. In: *Proceedings of the 9th IFToMM International Conference on Rotor Dynamics*. Springer International Publishing, 2015, pp. 1223–1233.

[26] A. M. Gad and S. Kaneko. “A new structural stiffness model for bump-type foil bearings: application to generation II gas lubricated foil thrust bearing”. In: *Journal of Tribology* 136.4 (2014), p. 041701. DOI: 10.1115/1.4027601.

[27] A. M. Gad and S. Kaneko. “Performance characteristics of gas-lubricated bump-type foil thrust bearing”. In: *Proceedings of the Institution of Mechanical Engineers, Part J: Journal of Engineering Tribology* 229.6 (2015), pp. 746–762.

[28] A. M. Gad and S. Kaneko. “Tailoring of the bearing stiffness to enhance the performance of gas-lubricated bump-type foil thrust bearing”. In: *Proceedings of the Institution of Mechanical Engineers, Part J: Journal of Engineering Tribology* 230.5 (2016), pp. 541–560.

[29] S Gray, H Heshmat, and B. Bhushan. “Technology progress on compliant foil air bearing systems for commercial applications.” In: *BHRA Fluid Engng*. 1981.

[30] E. Guenat and J. Schiffmann. “Performance potential of gas foil thrust bearings enhanced with spiral grooves”. In: *Tribology international* 131 (2019), pp. 438–445.

[31] B. Hamrock;B.; Schmid S; Jacobson. *Fundamentals of Fluid Film Lubrication*. Second Edition. New York: CRC Press, 2004. DOI: 10.1201/9780203021187.

[32] H. Heshmat and W. Shapiro. “Advanced development of air-lubricated foil thrust bearings”. In: Okt (1982), pp. 1–6.

[33] H. Heshmat, J. A. Walowit, and O. Pinkus. “Analysis of Gas Lubricated Compliant Thrust Bearings”. In: *Journal of Lubrication Technology* 105.4 (1983), pp. 638–646. ISSN: 0022-2305. DOI: 10.1115/1.3254696.

[34] H. Heshmat et al. “Oil-free turbocharger demonstration paves way to gas turbine engine applications”. In: 78545 (2000), V001T04A008. DOI: 10.1115/2000-gt-0620.

[35] C. Hirsch. *Numerical Computation of Internal and External Flows (Second Edition)*. Second Edition. Oxford: Butterworth-Heinemann, 2007.

[36] P. Hryniewicz, D. H. Locke, and H. Heshmat. "New-Generation Development Rigs for Testing High-Speed Air-Lubricated Thrust Bearings". In: *Tribology Transactions* 46 (4 Jan. 2003). DOI: 10.1080/10402000308982663.

[37] P. Hryniewicz et al. "Structural properties of foil bearings: a closed-form solution validated with finite element analysis". In: *Tribology Transactions* 52.4 (2009), pp. 435–446.

[38] I Iordanoff. "Maximum load capacity profiles for gas thrust bearings working under high compressibility number conditions". In: (1998). DOI: 10.1115/1.2834589.

[39] I. Iordanoff. "Analysis of an Aerodynamic Compliant Foil Thrust Bearing: Method for a Rapid Design". In: *Journal of Tribology* 121.4 (1999), pp. 816–822. ISSN: 0742-4787. DOI: 10.1115/1.2834140.

[40] I. Iordanoff et al. "Effect of internal friction in the dynamic behavior of aerodynamic foil bearings". In: *Tribology international* 41.5 (2008), pp. 387–395. DOI: 10.1016/j.triboint.2007.09.010.

[41] Vrancik J. "Prediction of Windage Power Loss in Alternators". In: *National Aeronautics and Space Administration* (1968).

[42] T. H. Kim, M. Park, and T. W. Lee. "Design optimization of gas foil thrust bearings for maximum load capacity". In: *Journal of Tribology* 139.3 (2017), p. 031705.

[43] R. F. Klaass and C. DellaCorte. "The quest for oil-free gas turbine engines". In: *SAE Transactions* (2006), pp. 863–881. DOI: 10.4271/2006-01-3055.

[44] C-P R. Ku and H. Heshmat. "Structural stiffness and coulomb damping in compliant foil journal bearings: parametric studies". In: *Tribology transactions* 37.3 (1994), pp. 455–462. DOI: 10.1080/10402009408983317.

[45] G. D. Larue, S. G. Kang, and W. Wick. *Turbocharger with hydrodynamic foil bearings*. US Patent 7,108,488. 2006.

[46] N. LaTray and D. Kim. "Design of Novel Gas Foil Thrust Bearings and Test Validation in a High-Speed Test Rig". In: *Journal of Tribology* 142.7 (2020). ISSN: 0742-4787. DOI: 10.1115/1.4046412.

[47] N. T. LaTray and D. Kim. "A High Speed Test Rig Capable of Running at 190,000rpm to Characterize Gas Foil Thrust Bearings". In: (6112018). DOI: 10.1115/GT2018-77111.

[48] S. Le Lez, M. Arghir, and J. Frene. "Static and dynamic characterization of a bump-type foil bearing structure". In: (2007).

[49] D. Lee D.; Kim. "Thermohydrodynamic Analyses of Bump Air Foil Bearings With Detailed Thermal Model of Foil Structures and Rotor". In: *Journal of Tribology* 132 (2 2010). DOI: 10.1115/1.4001014.

[50] D. Lee and D. Kim. "Three-dimensional thermohydrodynamic analyses of Rayleigh step air foil thrust bearing with radially arranged bump foils". In: *Tribology Transactions* 54.3 (2011), pp. 432–448. DOI: 10.1080/10402004.2011.556314.

[51] Y.-B. Lee et al. "Thrust Bump Air Foil Bearings with Variable Axial Load: Theoretical Predictions and Experiments". In: *Tribology Transactions* 54.6 (2011), pp. 902–910. ISSN: 1040-2004. DOI: 10.1080/10402004.2011.606957.

[52] A. Lehn. “Air foil thrust bearings: A thermo-elasto-hydrodynamic analysis”. PhD thesis. TU Darmstadt, 2017.

[53] A. Lehn, M. Mahner, and B. Schweizer. “A thermo-elasto-hydrodynamic model for air foil thrust bearings including self-induced convective cooling of the rotor disk and thermal runaway”. In: *Tribology International* 119 (2018), pp. 281–298.

[54] A. Lehn, M. Mahner, and B. Schweizer. “Elasto-gasdynamic modeling of air foil thrust bearings with a two-dimensional shell model for top and bump foil”. In: *Tribology International* 100 (2016), pp. 48–59.

[55] L. Licht. “An experimental study of high-speed rotors supported by air-lubricated foil bearings—part 1: rotation in pressurized and self-acting foil bearings”. In: (1969). DOI: 10.1115/1.3554970.

[56] D. Lubell and D. Weissert. *Rotor and bearing system for a turbomachine*. US Patent 7,112,036. 2006.

[57] M. Mahner, A. Lehn, and B. Schweizer. “Thermogas-and thermohydrodynamic simulation of thrust and slider bearings: Convergence and efficiency of different reduction approaches”. In: *Tribology International* 93 (2016), pp. 539–554. DOI: 10.1016/j.triboint.2015.02.030.

[58] F. R. Menter. “Two-equation eddy-viscosity turbulence models for engineering applications”. In: *AIAA Journal* 32.8 (Aug. 1994), pp. 1598–1605. DOI: 10.2514/3.12149.

[59] Z. N. Nemeth. “Experimental evaluation of foil-supported resilient-pad gas-lubricated thrust bearing”. In: (1977).

[60] D.-J. Park et al. “Theoretical considerations of static and dynamic characteristics of air foil thrust bearing with tilt and slip flow”. In: *Tribology International* 41.4 (2008), pp. 282–295. DOI: 10.1016/j.triboint.2007.08.001.

[61] Z-C Peng and MM Khonsari. “Hydrodynamic analysis of compliant foil bearings with compressible air flow”. In: *J. Trib.* 126.3 (2004), pp. 542–546.

[62] T. Pronobis. “Dynamisches Verhalten von Rotoren in axialen Gasfolienlagern”. PhD thesis. 2021.

[63] K. Qin. “Development and application of multiphysics simulation tools for foil thrust bearings operating with carbon dioxide”. PhD thesis. 2017.

[64] K. Qin et al. “Development of a computational tool to simulate foil bearings for supercritical CO2 cycles”. In: *Journal of Engineering for Gas Turbines and Power* 138.9 (2016).

[65] M. Raymond M. ; Kasarda. “Windage Power Loss Modeling of a Smooth Rotor Supported by Homopolar Active Magnetic Bearings”. In: *Journal of Tribology* (2008). DOI: 10.1115/1.2806203.

[66] O. Reynolds. “IV. On the theory of lubrication and its application to Mr. Beauchamp tower’s experiments, including an experimental determination of the viscosity of olive oil”. In: *Philosophical transactions of the Royal Society of London* 177 (1886), pp. 157–234.

[67] M. Rieken, M. Mahner, and B. Schweizer. “Thermal Optimization of Air Foil Thrust Bearings Using Different Foil Materials”. In: *Journal of Turbomachinery* 142.10 (2020). ISSN: 0889-504X. DOI: 10.1115/1.4047633.

[68] D. Ruscitto, J. McCormick, and S. Gray. *Hydrodynamic air lubricated compliant surface bearing for an automotive gas turbine engine. I. Journal bearing performance*. 1978. DOI: 10.2172/7095892.

[69] K. Ryu and L. San Andrés. “Effect of Cooling Flow on the Operation of a HotRotor-Gas Foil Bearing System”. In: *Journal of engineering for gas turbines and power* 134.10 (2012). DOI: 10.1115/1.4007067.

[70] M. H. Sadd. *Elasticity: theory, applications, and numerics*. Academic Press, 2009.

[71] M. Salehi, H. Heshmat, and J. F. Walton. "On the frictional damping characterization of compliant bump foils". In: *J. Trib.* 125.4 (2003), pp. 804–813. DOI: 10.1115/1.1575774.

[72] M. Salehi, E. Swanson, and H. Heshmat. "Thermal features of compliant foil bearings—theory and experiments". In: *J. Trib.* 123.3 (2001), pp. 566–571.

[73] L. San Andrés and T. H. Kim. "Analysis of gas foil bearings integrating FE top foil models". In: *Tribology International* 42.1 (2009), pp. 111–120.

[74] L. San Andrés and T. H. Kim. "Thermohydrodynamic analysis of bump type gas foil bearings: a model anchored to test data". In: *Journal of Engineering for Gas Turbines and Power* 132.4 (2010).

[75] L. San Andrés, . Ryu, and P. Diemer. "Prediction of Gas Thrust Foil Bearing Performance for Oil-Free Automotive Turbochargers". In: *Journal of Engineering for Gas Turbines and Power* 137.3 (2015), p. 40. ISSN: 0742-4795. DOI: 10.1115/1.4028389.

[76] R. G. Sargent. "Verification and validation of simulation models". In: *Proceedings of the 2010 Winter Simulation Conference*. 2010, pp. 166–183. DOI: 10.1109/WSC.2010.5679166.

[77] S. Schlesinger. "Terminology for model credibility". In: *Simulation* 32.3 (1979), pp. 103–104.

[78] H. Schlichting and K. Gersten. *Boundary-layer theory*. springer, 2016.

[79] S. K. Shrestha, D. Kim, and Y. Cheol Kim. "Experimental feasibility study of radial injection cooling of three-pad air foil bearings". In: *Journal of Tribology* 135.4 (2013), p. 041703. DOI: 10.1115/1.4024547.

[80] K. Sim and T. H. Kim. "Thermohydrodynamic analysis of bump-type gas foil bearings using bump thermal contact and inlet flow mixing models". In: *Tribology international* 48 (2012), pp. 137–148.

[81] R. C. Smith. *Uncertainty quantification: theory, implementation, and applications*. Vol. 12. Siam, 2013.

[82] AF Stahler. *Analyzation, design, fabrication, and testing of a foil bearing rotor support system Quarterly technical report, period ending 21 Feb. 1966*. Tech. rep. 1966.

[83] R. Stribeck. *Kugellager für beliebige Belastungen*. Buchdruckerei AW Schade, Berlin N., 1901.

[84] A. Z. Szeri. *Fluid film lubrication*. Cambridge university press, 2010.

[85] A. Theile et al. "Analysis of air foil thrust bearings with annular top foil including wear prediction, Part II: Experimental investigations". In: *Tribology International* 188 (2023), p. 108742.

[86] B. Tower. "First report on friction experiments". In: *Proceedings of the institution of mechanical engineers* 34.1 (1883), pp. 632–659.

[87] B. Tower. "Second report on friction experiments". In: *Proc. Inst. Mech. Engrs.* 36 (1985), pp. 38–70.

[88] J. A. Walowit, J. N. Anno, and B. J. Hamrock. "Modern developments in lubrication mechanics". In: *ASME. J. of Lubrication Tech* (1977). DOI: 10.1115/1.3453088.

[89] F. White. *Viscous Fluid Flow*. Second Edition. New York: MCGraw-Hill, Inc., 1991.

[90] P. Wriggers and T. Laursen. *Computational contact mechanics*. Vol. 2. Springer, 2006. DOI: 10.1007/s00466-012-0730-x.

[91] F. Xu, J. Chu, and L. Sha. "Air foil thrust bearings with top foil sagging: Theoretical predictions and experiments". In: *Tribology International* 177 (Jan. 2023), p. 107995. DOI: 10.1016/j.triboint.2022.107995.

[92] Z. Xu et al. “Load-carrying characteristics of bump-type gas foil thrust bearings”. In: *International Journal of Mechanical Sciences* 244 (Apr. 2023), p. 108080. DOI: 10.1016/j.ijmecsci.2022.108080.

A. Appendix

Material Properties

Table A.1.: Material properties of bump foil, top foil, and the rotor.

Part (Material)	Parameter	Value	Description
Top Foil (Inconel 750)	E_{TF}	215 GPa	elastic modulus
	ρ_{TF}	8.2 g/cm^2	density
	ν_{TF}	0.3	Poisson's ratio
	λ_{TF}	12 W/mK	thermal conductivity
Bump Foil (Inconel 718)	E_{BF}	205 GPa	elastic modulus
	ρ_{BF}	8.2 g/cm^2	density
	ν_{BF}	0.3	Poisson's ratio
	λ_{BF}	12 W/mK	thermal conductivity
Rotor (1.4542)	α_{RD}	$11 \cdot 10^{-6}$ 1/K	thermal expansion
	E_{RD}	200 GPa	elastic modulus
	λ_{RD}	16 W/mK	thermal conductivity
	ρ_{RD}	7.8 g/cm^2	density

Air Film Properties

Viscosity of air:

$$\eta = -1.75 \cdot 10^{-}11 \cdot T_{\mathrm{air}}^2 + 5.68 \cdot 10^{-8} \cdot T_{\mathrm{air}} + 3.06 \cdot 10^{-6} \tag{A.1}$$

Thermal conductivity κ of air:

$$\kappa = -2.1 \cdot 10^{-8} \cdot T_{\mathrm{air}}^2 + 8.46 \cdot 10^{-}5 \cdot T_{\mathrm{air}} + 2.89 \cdot 10^{-3} \tag{A.2}$$

Heat capacity $c_{\mathrm{p},}$ at constant pressure of air:

$$c_{\mathrm{p}} = 2.43 \cdot 10^{-4} \cdot T_{\mathrm{air}}^2 - 0.077 \cdot T_{\mathrm{air}} + 1.008 \cdot 10^{3} \tag{A.3}$$

Density ρ is treated as an ideal gas defined as:

$$\rho = \frac{p}{R \cdot T_{\mathrm{air}}}, \tag{A.4}$$

with $R = 287.06\,\mathrm{J/(Kg{\cdot}K)}$ being the specific gas constant. These approximations are taken from Lehn [52].